

University of Granada
Andalusian Institute of Geophysics

Passive and Active Seismic Tomography of Volcanic Islands
São Miguel (Portugal) and Deception (Antarctica)

DISSERTATION

for the degree of
Doctor of Earth Sciences

presented by

Daria Zandomeneghi

on the recommendation of

Prof. Dr. Jesús M. Ibañez Godoy, examiner

Dr. Fco. Javier Almendros Gonzalez, co-examiner

University of Granada, 2007

Universidad de Granada
Doctorado en Ciencias de la Tierra
Instituto Andaluz de Geofísica

Tomografía Sísmica Activa y Pasiva en las Islas Volcánicas

São Miguel (Portugal) y Decepción (Antártida)

MEMORIA

para optar al grado de Doctor en Ciencias de la Tierra

presentada por

Daria Zandomeneghi

Fdo. Daria Zandomeneghi

V°B° de Director

V°B° del Director

Fdo. Dr. Jesús Ibañez Godoy

Fdo. Javier Almendros

Universidad de Granada, 2007

Index

| | |
|---|------------------|
| <i>Spanish Extended Abstract</i> | <i>1</i> |
| Esta Tesis | 1 |
| Tomografía y Volcanes | 3 |
| Tomografía Activa y Pasiva | 4 |
| Isla Decepción | 6 |
| Introducción | 6 |
| Experimento Sísmico | 7 |
| Resultados y Discusión | 9 |
| Conclusiones | 10 |
| São Miguel | 11 |
| Introducción | 11 |
| El experimento sísmico | 12 |
| Resultados y discusión | 14 |
| Conclusiones | 15 |
| Conclusiones Generales | 16 |
| <i>1. Tomography and Volcanoes</i> | <i>24</i> |
| 1.1. . Seismic Tomography | 24 |
| 1.2. Tomography and Volcanoes | 25 |
| 1.2.1. Importance of Tomographic Models | 26 |
| 1.2.2. General Interpretation of Vp and Vs Anomalies in Volcanoes | 28 |
| 1.2.3. Active and passive seismic tomography | 33 |
| 1.2.4. An example | 35 |
| Campi Flegrei | 37 |

| | |
|--|-----------|
| 1.3. References | 42 |
| 2. <i>Theory and Principles</i> | 46 |
| 2.1. Locating Earthquakes | 47 |
| 2.2. Velocity Model | 50 |
| 2.2.1. Theory Fundamentals | 51 |
| 2.2.1.1. Representation of Structure | 51 |
| 2.2.1.2. Traveltime Determination | 52 |
| 2.2.1.3. Inverse Problem | 56 |
| 2.2.1.4. Analysis of Solution Quality | 61 |
| 2.2.2. 1D Models | 66 |
| 2.2.3. 3D Model | 69 |
| 2.2.3.1. Benz's Method | 69 |
| 2.2.3.2. Toomey's Method | 71 |
| References | 75 |
| 3. <i>Central São Miguel</i> | 78 |
| Abstract | 78 |
| Extended Abstract | 80 |
| Introduction | 80 |
| Seismic Experiment | 81 |
| Results and Discussion | 83 |
| Conclusions | 84 |
| 3.1. The Question | 85 |
| 3.2. Tectonic Overview | 86 |
| 3.3. Previous Studies | 88 |
| 3.3.1. Geology | 88 |

| | | |
|-------------|--|------------|
| 3.3.2. | Hydrothermal and Geothermal Activity | 93 |
| 3.3.3. | Geochemistry | 95 |
| 3.3.4. | Gravimetry | 95 |
| 3.3.5. | Geodesy | 100 |
| 3.3.6. | Tectonics and Seismology | 102 |
| 3.3.7. | Resuming the ‘State of the Art’ | 107 |
| 3.4. | . Seismic experiment | 109 |
| 3.4.1. | Objectives | 109 |
| 3.4.2. | Institutions | 109 |
| 3.4.3. | Experiment Design | 110 |
| 3.4.4. | Station Types | 112 |
| 3.4.4.1. | Lennartz Marslite | 112 |
| 3.4.4.2. | MallAG | 113 |
| 3.4.4.3. | Local network | 114 |
| 3.4.5. | Data processing | 116 |
| 3.4.5.1. | Data Formats and Software | 116 |
| 3.4.5.2. | P and S Arrival Time Determination | 116 |
| 3.4.5.3. | Data Quality | 118 |
| 3.4.6. | Previous Results from the Experiment | 119 |
| 3.4.6.1. | Seismic data | 119 |
| 3.4.6.2. | Minimum 1D Velocity Model and High Precision Locations | 122 |
| 3.5. | 1-D Velocity Model | 123 |
| 3.5.1. | Method | 123 |
| 3.5.2. | Input Data | 123 |
| 3.5.3. | Tests | 126 |
| 3.5.4. | Results | 130 |
| 3.6. | Initial Locations | 136 |
| 3.6.1. | Method | 136 |
| 3.6.2. | Input Data | 136 |

| | | |
|-------------|--|------------|
| 3.6.3. | Results | 138 |
| 3.7. | 3-D Velocity Model | 142 |
| 3.7.1. | Method | 142 |
| 3.7.2. | Input Data | 142 |
| 3.7.2.1. | Data selection | 143 |
| 3.7.2.2. | Grid definition and parameter selection | 143 |
| 3.7.2.3. | Initial Model | 146 |
| 3.7.3. | Vp/Vs Ratio | 146 |
| 3.7.4. | Error | 146 |
| 3.7.5. | Resolution analysis and input tests | 148 |
| 3.7.5.1. | Checkerboard Test | 148 |
| 3.7.5.2. | Impulse Response Test | 156 |
| 3.7.5.3. | Reconstruction Test | 157 |
| 3.7.5.4. | Starting Models | 159 |
| 3.7.5.5. | Jackknife Test | 160 |
| 3.7.6. | Results | 161 |
| 3.8. | Discussion of Results and Conclusions | 169 |
| 3.8.1. | Low velocity regions | 170 |
| 3.8.2. | High velocity regions | 171 |
| 3.9. | Conclusions | 175 |
| | References | 177 |
| 4. | <i>Deception Island</i> | 180 |
| | Abstract | 180 |
| | Extended Abstract | 182 |
| | Introduction | 182 |
| | Seismic Experiment | 183 |
| | Results and Discussion | 185 |

| | |
|---|------------|
| Conclusions | 186 |
| 4.1. The Question | 187 |
| 4.2. Tectonic Overview | 188 |
| 4.3. Previous Studies on Deception | 192 |
| 4.3.1. Geology and Volcanology | 193 |
| 4.3.2. Structural Geology and Geodynamics | 199 |
| 4.3.3. Gravimetry and Magnetics | 201 |
| 4.3.4. Seismicity | 204 |
| 4.3.5. Seismic Structure | 209 |
| 4.3.6. Resuming the ‘State of the Art’ | 212 |
| 4.4. Seismic Experiment | 214 |
| 4.4.1. Objectives | 214 |
| 4.4.2. Institutions | 215 |
| 4.4.3. Experiment Design | 215 |
| 4.4.3.1. Air-gun Shooting Configuration | 217 |
| 4.4.3.2. Source Generation | 221 |
| 4.4.3.3. Signal Characteristics | 223 |
| 4.4.4. Station Types | 224 |
| 4.4.4.1. Lennartz Marslite | 225 |
| 4.4.4.2. Lennartz M24 | 225 |
| 4.4.4.3. mallAG | 226 |
| 4.4.4.4. OBS | 227 |
| 4.4.5. Data Processing | 228 |
| 4.4.5.1. Data Formats and Software | 228 |
| 4.4.5.2. Data Quality | 229 |
| 4.4.5.3. P Arrival Time Determination | 232 |
| 4.4.5.4. Input Format | 235 |
| 4.4.6. Other Results from the Experiment | 235 |

| | | |
|-------------|---|------------|
| 4.4.6.1. | Gravimetry | 236 |
| 4.4.6.2. | Magnetics | 236 |
| 4.4.6.3. | Bathymetry | 236 |
| 4.4.6.4. | Water Measurements | 239 |
| 4.5. | 3D Tomography | 240 |
| 4.5.1. | Method | 240 |
| 4.5.2. | Input | 241 |
| 4.5.2.1. | Grids Definition and Parameters Selection | 241 |
| 4.5.2.2. | Data Selection | 245 |
| 4.5.2.3. | Initial Model | 245 |
| 4.5.2.4. | Bathymetry | 246 |
| 4.5.3. | Error Definition | 251 |
| 4.5.4. | Resolution Analysis | 259 |
| 4.5.4.1. | DWS Definition | 260 |
| 4.5.4.2. | Checkerboard Test | 263 |
| 4.5.4.3. | Impulse Response Test | 275 |
| 4.5.4.4. | Reconstruction Test | 281 |
| 4.5.4.5. | Spike on Reconstructed Image | 283 |
| 4.5.4.6. | Shifted Grid Test | 285 |
| 4.5.5. | Starting Model | 286 |
| 4.6. | Results | 291 |
| 4.6.1. | Description of Results | 291 |
| 4.6.2. | More about the Result Quality | 300 |
| 4.6.2.1. | 2D Profiles | 300 |
| 4.6.2.2. | Bathymetry | 303 |
| 4.6.3. | Discussion of Results | 305 |
| 4.6.3.1. | A1 | 305 |
| 4.6.3.2. | A2 | 307 |
| 4.6.3.3. | A3 | 307 |

| | | |
|-------------|--------------------------------|------------|
| 4.6.3.4. | A4 | 308 |
| 4.6.3.5. | B1 | 308 |
| 4.6.3.6. | B2 | 310 |
| 4.6.3.7. | B3 | 310 |
| 4.7. | Conclusions | 312 |
| | References | 318 |
| 5. | <i>Conclusions</i> | 324 |
| | A Final Consideration | 331 |
| | References | 334 |
| | <i>Acknowledgements</i> | 335 |

Spanish Extended Abstract

Esta Tesis

El objetivo principal de esta tesis es representar la estructura interna de dos islas volcánicas: São Miguel (Islas Azores) y Decepción (Shetland del Sur, Antártida). Estas islas, más allá de las diferencias reconocidas en su tectónica y actividad volcánica, comparten dos aspectos fundamentales: las dos poseen una intensa actividad sísmica de origen volcánica y ambas tienen una estructura interna que es fundamentalmente desconocida. Estas características justificaron la realización de dos campañas sísmicas; un experimento tomográfico pasivo y uno activo, a São Miguel y Decepción respectivamente.

Los experimentos estaban principalmente dirigidos a la determinación de una imagen tomográfica de la estructura de velocidad de las islas, a través del estudio de los residuos temporales de las señales sísmicas. Como era de esperar, los dos experimentos presentaban problemas diferentes y entonces era necesario afrontarlos de dos formas distintas.

La diferencia fundamental consistió en elegir una técnica pasiva en Sao Miguel y una activa en Decepción. La razón principal de las dos alternativas estaba en el aspecto práctico de su realización. Mientras São Miguel presenta una infraestructura favorable al despliegue de una red sísmica y su manutención por un tiempo prolongado, con el fin de poder registrar la actividad sísmica natural; la isla Decepción, por su localización geográfica y condiciones climáticas, presenta mayores dificultades desde este punto de vista. Por tanto era más idóneo realizar una campaña corta e intensa, de sísmica activa, para estudiar una región tan lejana.

Estas opciones estaban además sostenidas en razones más estrictamente científicas. De hecho, São Miguel presenta una actividad volcano-tectónica natural muy elevada, de manera repetida se presentan enjambres sísmicos y sus focos están bien distribuidos en profundidad. Este tipo de sismicidad, como veremos, indicaba un experimento pasivo como la mejor estrategia para recopilar datos para una tomografía sísmica. Además esperábamos que esta actividad nos aportara información acerca de la estructura sísmica del volcán tanto con una distribución de V_p como de V_p/V_s . Es bien sabido que la razón V_p/V_s es una herramienta básica para determinar la presencia y distribución de los fluidos, y entonces su conocimiento es particularmente atractivo para una región que tiene una intensa actividad hidrotermal con explotación geotérmica. Como razón adicional la isla estaba simultáneamente monitorizada por la red sísmica local cuyos datos podían

ser fácilmente integrados con aquellos procedentes del experimento para obtener una considerable cantidad de datos sin un esfuerzo adicional.

Por otra parte, la isla Decepción es caracterizada por una actividad sísmica que es principalmente de largo periodo y por esto muy difícil de introducir en un estudio tomográfico. Por esta razón era posible recopilar en poco tiempo una importante base de datos de tiempos de primeras llegadas de ondas P recurriendo a fuentes artificiales. Además, un factor importante era dado por la geometría especial de la isla que la hace ideal para un experimento que combine fuentes activas de tierra y oceánicas.

La elección de una técnica específica implicaba que los datos obtenidos iban a requerir la aplicación de métodos de inversión tomográfica diferentes. La parte matemática del estudio tomográfico tenía que manejar problemas que variaban, entre otros, por el tipo de datos (ondas P y S contra solo ondas P), incógnitas de la inversión (terremotos contra disparos de aire comprimidos bien localizados), parametrización del modelo (fuentes sísmicas rodeadas por la estructura de la corteza contra fuentes en un medio líquido), etc.

Por estas razones, la estructura de la tesis refleja el ajuste del método tomográfico a la unicidad de la región estudiada. En el primer capítulo, introducimos el concepto de tomografía y los propósitos principales de su aplicación a las regiones volcánicas. Explicamos brevemente cual es el significado de las anomalías de velocidad y lo que nos dicen acerca de la estructura del volcán. Luego introducimos las principales técnicas y sus ventajas e inconvenientes. Aclaremos estos conceptos con un ejemplo de sus aplicaciones. En el segundo capítulo profundizamos el aspecto teórico de la tomografía y explicamos los principios básicos y la matemática que controla su aplicación. Nos centramos en los algoritmos que vamos a aplicar en nuestros experimentos, haciendo hincapié en las ventajas en cada caso. En el tercer capítulo, describimos el experimento de São Miguel, desde el trabajo de campo hasta los resultados tomográficos. En el cuarto capítulo, análogamente explicamos los detalles de la campaña sísmica de la isla Decepción. Comenzamos con la descripción de la campaña y a través de la selección y preparación de los datos, presentamos la imagen sísmica de la isla. Finalmente, en el quinto capítulo, resumimos los principales resultados tomográficos a la luz de un análisis comparativo de las diferentes técnicas tomográficas.

En esta óptica, además de la representación tomográfica de las dos islas, nos enfrentamos con las ventajas y los inconvenientes de las alternativas pasiva y activa. Los aspectos favorables y las desventajas relacionadas con la aplicación de estas técnicas son resaltados como resultado natural de este trabajo. Esperamos que la comparación final de sus resultados pueda mejorar el conocimiento del potencial tomográfico como herramienta para el conocimiento de los volcanes.

Tomografía y Volcanes

Los edificios volcánicos se encuentran normalmente localizados en regiones que son fuertemente heterogéneas respecto a la distribución de sus propiedades geofísicas. El marco geodinámico donde se ubican los volcanes puede ser muy complicado, con numerosos procesos tectónicos que actúan a escalas diferentes. Además, estas áreas suelen tener un historial de actividad volcánica variable y presentan una geología complicada. Estas heterogeneidades pueden estar relacionados con fenómenos de corta duración tales como la actividad geotérmica, erupciones y derrumbes y/o con estructuras más grandes y más estables, como en los procesos de alimentación del manto y las interacciones entre placas tectónicas. Esta evolución compleja tiene su evidencia geofísica en la extrema variabilidad de parámetros, del campo magnético y gravimétrico, del régimen de deformación y de las propiedades sísmicas, entre otros.

Este trabajo está particularmente enfocado en la heterogeneidad de la estructura sísmica, que puede ser evaluada cuantitativamente e interpretado a través de la tomografía sísmica. La distribución de los parámetros sísmicos se atribuye a una variación de las propiedades elásticas, composición, distribución de los fluidos, temperatura y presión, entre otros. A partir de estas variaciones es posible la determinación de la estructura interna. Esto constituye un paso fundamental para entender los sistemas magmáticos activos, y determinar la extensión de su región fuente. Además, estos conocimientos son fundamentales para la valoración de la evolución eruptiva y del riesgo volcánico.

Debido a su flexibilidad, la tomografía sísmica constituye una herramienta atractiva y útil. Por ejemplo, diferentes componentes de las ondas sísmicas son utilizados, incluyendo tiempos de primera llegada, amplitudes, espectrogramas, formas de ondas enteras o el campo de ondas en su totalidad. Además, se puede utilizar diferentes fases sísmicas en un gran rango de configuraciones fuentes- instrumentos de registro. Las fases más utilizadas en la tomografía sísmica incluyen una variedad de fases telesísmicas, ondas superficiales, modos normales, onda P y S de terremotos locales, y, entre las ondas internas, directas, reflectadas, refractadas y difractadas. Los instrumentos de registro pueden ser en línea o en una distribución tridimensional, las fuentes utilizadas ser naturales o artificiales, las escalas representadas cubrir el rango entre pocas decenas de metros y distancias globales, etc.

En concreto, la representación tomográfica obtenida a través de los tiempos de viaje de las ondas internas consiste en la reconstrucción de la estructura tridimensional del campo de velocidad/lentitud utilizando tiempos de llegada de las ondas P y S de fuentes naturales y/o artificiales. Si además las fuentes están localizadas en el interior del volumen a determinar, estamos en lo que denominamos 'Local Earthquakes Tomography' (LED)

La tomografía sísmica de los tiempos de llegada básicamente consiste en la manipulación de los retrasos (llamados residuos) entre tiempos de llegada observados y aquellos calculados in un modelo de velocidad de prueba, para evaluar mejoras al modelo mismo, hasta lograr la más razonable estructura de velocidad. En el caso específico de LED esto problema es bastante más complejo porqué la localización de las fuentes es sustancialmente desconocida, junto con la estructura de velocidad del medio donde los terremotos se localizan.

No obstante, la LED es la técnica básica para el estudio de las regiones volcánicas, donde se espera contar con una elevada actividad sísmica local, y donde también las heterogeneidades son de una escala que sólo pueden ser resueltas utilizando ondas P y S de terremotos locales. Evidentemente el principal objetivo del estudio tomográfico consiste en la localización y modelación de las zonas en donde existen material fundidos parcialmente y cámaras magmáticas.

Las estructuras volcánicas deben su heterogeneidad, entre otras razones, a (1) la variedad de las rocas que forman los complejos volcánicos (lavas masivas, lavas vesiculadas, cenizas consolidados, rocas piroclásticas no consolidadas, depósitos alterados, rocas no volcánicas, etc) (2) la presencia de sistemas de fracturas, en donde posiblemente existen fluidos en circulación de diferente origen y estado (gas/líquidos de derivación meteórica o volcánica, magma, etc.) (3) la presencia de volúmenes de roca frágil debilitada por repetidos episodios de ascenso de magma, perturbaciones térmicas, o colapsos de caldera (4) la presencia de fundidos parciales y/o totales o restos densos de intrusiones magmáticas a niveles más o menos superficiales por debajo de los edificios volcánicos.

Tomografía Activa y Pasiva

En los últimos años, la tomografía sísmica basada en los tiempos de llegada se viene aplicando de manera repetida para el estudio de los volcanes, con el fin de representar sus estructuras internas y mejorar el conocimiento de los procesos activos que acontecen durante las erupciones. En muchos casos, los experimentos sísmicos han sido de tipo pasivo. En

tiempos más recientes, se ha extendido el uso de los experimentos activos, en substitución o integración del registro pasivo de la actividad sísmica natural. Los datos para este tipo de estudios proceden de fuentes activas como explosiones en tierra o disparo de aire comprimido en agua.

En general, cuando se tiene que estudiar una región volcánica a través de la técnica tomográfica, ambos tipos de experimentos se deberían tener en cuenta. Es básico determinar las características de la información que se puede obtener en comparación con su coste, es decir, nos referimos, entre otros, a la calidad del resultado final frente a la razón entre esfuerzo y tiempo, y también al coste económico.

La estructura sísmica de un volcán puede representarse en detalle, pero con mucha dificultad, usando la técnica de la sísmica pasiva. En muchos casos esta técnica sufre, entre otros problemas, de una pobre distribución de fuentes, pobre conocimiento de los recorridos de los rayos sísmicos y de la localización de las fuentes mismas. Desde el punto de vista de la inversión tomográfica, la complejidad del problema matemático se ve incrementada porque, además de la estructura de velocidad, se tienen que determinar otros parámetros (localizaciones y tiempos origen) como incógnitas adicionales. Al mismo tiempo, la base de datos conseguida puede no ser adecuada en su tamaño porque las señales de tipo volcano-tectónico pueden ser pocas comparadas con otras señales volcánicas. Para recoger una cantidad suficiente de estos datos haría falta un largo periodo de registro. Esta última posibilidad implica inevitablemente unos costes adicionales de mantenimiento y el riesgo adicional de trabajar en zonas volcánicas más o menos activas.

Como alternativa, en los experimentos de sísmica activa se puede obtener una distribución óptima de fuentes artificiales y estaciones de registro. Esto puede garantizar una buena resolución lateral y una considerable cantidad de datos en poco tiempo. La mayor dificultad de la técnica activa está en la obtención de la distribución espacial de la razón V_p/V_s conjuntamente con V_p . Además, la profundidad máxima alcanzada por los rayos sísmicos difícilmente puede llegar a los niveles corticales más profundos. Finalmente, las campañas de sísmica activa implican un impacto económico y un esfuerzo de organización muy importante.

Isla Decepción

Introducción

Entender la isla volcánica de Decepción en su conjunto viene condicionado por el conocimiento limitado de su estructura interna. Su evolución y estado actual está siendo estudiado de manera continuada pero sin que hasta la actualidad se haya presentado información acerca de la distribución del material fundido, de la profundidad de los sedimentos y de la localización de los cuerpos intrusivos y zonas de fallas por debajo y alrededor de la isla, etc; los modelos de estructura de la isla presentan poco detalle. La isla Decepción está situada en un sistema tectónico regional complejo y su geoquímica y actividad sísmica no encajan en ninguna interpretación unitaria y coherente en el marco de la geodinámica regional. En este trabajo vamos a utilizar la tomografía sísmica para aportar información adicional y discutir las relaciones entre las imágenes obtenidas de las heterogeneidades sísmicas y otras observaciones geofísicas y geológicas.

La isla Decepción es un volcán activo localizado en el Estrecho de Bransfield entre la Península Antártica y las islas Shetland del Sur. Localizada en correspondencia con el límite occidental del centro de tres sub-cuencas que se ha podido dividir morfológicamente el Estrecho. La isla es un estratovolcán con forma de herradura de 15 km de diámetro y una bahía interna ocupada por el mar. Está compuesta de rocas que tienen una edad menor de 0.75 millones de años y con evidencia de erupciones históricas. (1842, 1967, 1969 y 1970). Las rocas piroclásticas, los aglomerados, los “tufos” y cenizas forman por lo menos el 80% de su volumen. La bahía interior (Port Foster) se ha formado, con mucha probabilidad, por la extensión pasiva progresiva de un sistema de fallas normales que cruzan la isla. De echo, los mapas estructurales y los perfiles de reflexión en el interior de Port Foster indican que la tectónica local está controlada entre otros, por dos sistemas de fallas principales: un sistema con dirección NE-SW, consistente con el régimen extensivo regional del Estrecho de Bransfield, que controla la alineación de los centros eruptivos del 1967 y 1970; el segundo sistema presenta orientación NNW-SSE, aproximadamente perpendicular al primero, observado en muchas fallas y probablemente controla la forma de la Costa Recta, la costa oriental de la Isla Decepción.

La actividad volcánica de la isla es, en el presente, elevada, e incluye una circulación hidrotermal intensa, una posible resurgencia del fondo de Port Foster y una intensa sismicidad, en donde se tiene, entre otros, señales volcano-tectónicas y de largo periodo. Estas observaciones junto con las anomalías gravimétricas y magnéticas y la alta atenuación sísmica indican la probable existencia de una cámara magmática superficial bajo Port Foster, emplazada en un medio fuertemente fracturado. La actividad volcano-tectónica, que se concentra en enjambres, como los de 1992 y de 1999, viene atribuida a la acción de los principales sistemas de fallas en la isla. Por otra parte, el mecanismo que origina la actividad de largo periodo se ha explicado a través de la interacción de agua de deshielo o procedente de acuíferos superficiales con rocas a alta temperatura, que se concentran a lo largo de los sistemas de fracturas permeables.

Recientemente, en enero de 2005, se realizó una campaña de tomografía sísmica de ondas P de alta resolución en el ámbito del proyecto *TOMODEC*. En esta tesis describimos el experimento sísmico, la recogida de datos, su análisis, la inversión tomográfica y su aplicación a nuestros datos. Presentamos una imagen preliminar de la estructura de velocidad de la isla Decepción de la región y sus alrededores. En base a estos resultados, proponemos un modelo estructural y evolutivo para Decepción en el marco de la tectónica regional.

Experimento Sísmico

El experimento sísmico fue planteado con el fin de obtener una imagen sísmica tridimensional de la Isla Decepción y de la región que la rodea. Se generaron disparos de aire comprimidos cada minuto siguiendo un esquema de malla en el interior de Port Foster y aproximadamente cada dos minutos a lo largo de tres anillos concéntricos alrededor de la isla. Además, se realizaron dos líneas largas de disparos cuyas direcciones cruzaban la isla: una orientada según la línea NNO-SSE y de unos 92 km de longitud, la otra aproximadamente perpendicular a la primera y de alrededor de 55 km.

Se desplegaron ochenta y cinco sismómetros en tierra y catorce de fondo marino (OBS) con el fin de registrar las señales emitidas por los cañones de aire comprimido. El esquema de disparo se repitió una segunda vez y algunas estaciones fueron colocadas en una posición diferente entre la primera y la segunda tanda de disparos para incrementar la cobertura de los rayos sísmicos. Las estaciones sísmicas fueron instaladas con una distancia mínima de 0.2 km usando sismómetros independientes y antenas sísmicas de gran apertura. También se desplegaron antenas sísmicas de corta

apertura. La distribución de las estaciones fue condicionada en gran medida por la presencia de glaciares, lagos, y barrancos. Los OBS fueron distribuidos en la bahía interior y en una configuración circular entorno a la isla. La mayor parte de las estaciones sísmicas fueron equipadas únicamente con sismómetros verticales, mientras 20 estaciones de tierra y los OBS tenían sensores de tres componentes. Los OBS además incluían un hidrófono. Aproximadamente se realizaron 6600 disparos de aire comprimido usando como plataforma el buque científico *Hespérides*, recolectándose un total de 120 Gbytes de datos. Además de los datos sísmicos, también se hicieron medidas de datos de gravimetría, magnetismo y batimetría multihaz a lo largo de las mismas líneas recorridas por el buque.

La base final de datos consistía de más de 70000 tiempos de llegada de ondas P, identificados y marcados en los registros sísmicos. Además, a cada lectura de tiempo de llegada se les atribuyó un error usando una combinación de picking manual y automático. Cada estación registró un promedio de ~1500 señales, y cada señal de disparo pudo ser identificada en más de 15 estaciones.

Los tiempos de viaje de la onda P fueron posteriormente invertidas utilizando el método de Toomey. Este método separa el problema directo, del calculo del tiempo teórico de viaje de la onda sísmica, con respecto al problema inverso, de determinación de la estructura de velocidad. Los tiempos de viaje y los recorridos aproximados de los rayos sísmicos hasta cada estación se calculan para cada nodo de una malla tridimensional utilizando la técnica del 'shortest-path'. El problema inverso se resuelve utilizando una técnica de LSQR y se regulariza a través de parámetros de amortiguamiento (damping) y suavizado (smoothing). Los parámetros para la estructura de velocidad vienen definidos en una malla regular tridimensional que es normalmente más espaciada que aquella utilizada para el trazado del rayo. Este método resultó especialmente útil para los datos del experimento de Decepción porque incluye la topografía, la batimetría y el trazado del rayo en una capa líquida como es nuestro caso, un experimento sísmico en ambiente oceánico.

En nuestra tomografía, invertimos los datos utilizando dos configuraciones de malla. La primera consiste en una malla centrada en la isla Decepción y de extensión 53 km y 52 km en dirección E-O y N-S respectivamente. La malla para el trazado del rayo presenta un espaciado de 250 m, mientras la de perturbaciones de velocidad un espaciado de 500 m; ambas se extienden hasta 12 km de profundidad. Para la segunda configuración, reducimos las dimensiones de la malla hasta 12 x 14 x 7 km alrededor de Port Foster y las del trazado del rayo y perturbaciones hasta 100 y 200 m respectivamente.

Evaluamos la estabilidad de la solución de nuestra inversión a través de tres tipos de pruebas. El modelo de velocidad inicial para la inversión se obtuvo como un promedio horizontal del resultado tomográfico 2D obtenido a nivel regional y a partir de datos procedentes del mismo experimento. Repitiendo las inversiones con modelos iniciales diferentes, derivados de otros experimentos sísmicos, pudimos averiguar que las imágenes finales de la estructura de velocidad no dependían del

modelo inicial introducido. Además exploramos un amplio abanico de posibilidades para los parámetros de amortiguamiento (damping) y suavizado (smoothing). Sus valores finales fueron elegidos para minimizar los residuos temporales simultáneamente de los tiempos de llegada, la 'rugosidad' y la variancia del modelo. En nuestra inversión los parámetros finales de regularización fueron: 30 para el parámetro de smoothing (horizontal y vertical, 20 para la configuración con malla de perturbaciones de 200m) y 100 para el damping. Finalmente, realizamos pruebas de tipo tablero de ajedrez, respuesta a anomalías puntuales y otros modelos hipotéticos para evaluar la resolución espacial y en amplitud de la imagen tomográfica. Estas pruebas nos sugirieron una resolución máxima central para una región de 40 x 40 km centrada en la isla Decepción entre la superficie y aproximadamente 5 km de profundidad.

Resultados y Discusión

Se obtuvo la convergencia de la inversión tomográfica a una solución estable con 6 iteraciones, cuando el residuo medio (RMS) de los datos se redujo de un 80%, desde 247 ms del modelo inicial hasta 52 ms. Para la configuración más pequeña (200 m de malla de perturbaciones), el resultado resultó estable con 6 iteraciones, con una reducción del RMS de 260 ms hasta 34 ms. Los resultados de ambas inversiones se utilizaron para interpretar la estructura de velocidad de Decepción y de la región donde se ubica.

La imagen tomográfica es altamente heterogénea con una variación lateral de velocidad sísmica de más de 2 km/s a 1 km de profundidad. Contrastes similares son presentes entre la superficie y 5 km de profundidad, a todas las escalas.

Las variaciones de velocidad de las ondas P difícilmente pueden explicarse usando una única interpretación, pero en el caso de Decepción nos ayuda la asociación espacial de muchas otras anomalías observadas con estructuras ya conocidas en otros estudios. Una zona de alta velocidad domina la región al NO de Decepción a todas las profundidades resueltas y está separada de las bajas velocidades de la isla a través de un gran gradiente lateral del parámetro velocidad (> 0.8 km/s en ~ 2 km) que está alineado con una dirección paralela a aquella del Estrecho de Bransfield. Esta anomalía tiene su máximo entre 1 y 3.5 km de profundidad, y no es homogénea horizontalmente. Dos de los tres máximos que destacan en el interior de esta anomalía deforman su contacto sur-oriental con las regiones confinantes. Ambas anomalías, la del Suroeste y la del Noreste se extienden fuera del límite de la alta velocidad global e indican un movimiento de cizalla a lo largo de un plano

con dirección NO-SE. La anomalía más pronunciada de baja velocidad yace en correspondencia de Port Foster, en todo el intervalo de profundidades resuelto por nuestra inversión. A 1 km de profundidad, la anomalía se alarga en la dirección NO-SE y su perturbación máxima excede en 1 km/s con respecto al modelo de velocidad inicial. Hasta 1.5-2.0 km de profundidad esta anomalía se debe a la presencia de sedimentos y está formada por varios máximos que coinciden con la posición de los centros eruptivos del 1967 y 1970. De todas formas, la amplitud y la profundidad de esta anomalía requieren la presencia de altas temperatura y fundidos parciales localizados por debajo de Port Foster a profundidades mayores de los 1.5-2 km aproximadamente. La presencia de una cámara magmática ha sido además sugerida por otros muchos estudios. Esta baja velocidad en el interior de Port Foster está parcialmente rodeada por una distribución de altas velocidades que aproximadamente sigue la costa y ocupa nuestra imagen tomográfica entre la superficie y 3 km de profundidad. Estas altas velocidades pueden corresponder a una fase antigua parecida a la de volcanso-escudo de las islas volcánicas, a un borde de caldera antecedente o a intrusiones magmáticas enfriadas a niveles corticales muy superficiales.

Muchas otras anomalías, de alta como de baja velocidad, se pueden explicar a través de la presencia de formaciones de origen volcánico y de origen sedimentaria, respectivamente. La amplia anomalía de baja velocidad localizada al Este de la Isla Decepción corresponde a un fondo marino donde se depositan sedimentos procedentes principalmente de la isla misma. Su forma general es altamente irregular aunque la posición de su máximo a 0.5 km de profundidad corresponde con la de la Costa Recta. Por otra parte, la forma y posición de la anomalía de alta velocidad posicionada al sur de Decepción son similares a un máximo aislado de anomalía gravimétrica de Bouguer y de anomalía magnética. Por estas razones, representan probablemente los restos de una intrusión enfriada. Otra anomalía de alta velocidad está centrada en Sail Rock, una estructura andesítica erosionada del fondo marino localizada al SO de la isla. En contraposición, una anomalía de baja velocidad que se extiende al oeste de Decepción puede relacionarse con una zona de intenso volcanismo de fondo oceánico, y puede ser la resultante de grandes depósitos de origen volcanso-clástico y/o de un sistema magmático activo.

Conclusiones

La imagen tomográfica de la isla Decepción y sus alrededores presenta una distribución de la velocidad de las ondas P caracterizada por fuertes contrastes laterales. Esta heterogeneidad se puede explicar con la presencia de un sistema magmático cortical por debajo de Port Foster, por cuerpos magmáticos enfriados, por partes de basamento cristalino y por

variaciones en los espesores de los depósitos sedimentarios. Muchas de estas estructuras presentan los efectos de direcciones principales NO-SE y NE-SO y pueden ser interpretadas en el marco de la tectónica regional. En la zona del estrecho del Bransfield, la tectónica está caracterizada por una extensión en dirección NO-SE que actúa en todo el Estrecho de Bransfield y otra dirección principal NE-SO también activa. El orden cronológico en el cual actúan los dos sistemas es de difícil determinación, pero la localización espacio-temporal de las erupciones, y el modelo de cámara magmática que se sugiere en este trabajo, nos indica la probable contemporaneidad de ambos sistemas.

São Miguel

Introducción

São Miguel es una isla volcánica densamente habitada, cuya actividad volcánica, aunque extensamente reconocida y estudiada en muchos aspectos, no se ha explicado en términos de un marco estructural más amplio. El principal objetivo de este trabajo es obtener información sobre la estructura de esta región volcánica a través de tomografía sísmica, y discutir la relación entre la imagen de las heterogeneidades sísmicas obtenida y otras observaciones geofísicas y geológicas.

El archipiélago de las Azores está formado por nueve islas volcánicas situadas alrededor de 38° N, 28° O, en el punto triple entre las placas Americana, Euroasiática y Africana. São Miguel es la isla mayor del archipiélago. Su estructura se caracteriza por sistemas de fallas con direcciones NO-SE y E-O. Los complejos volcánicos más importantes se encuentran en la intersección de estos alineamientos tectónicos. En la región central de São Miguel, las principales estructuras volcánicas son Fogo y Furnas. Ambas son volcanes centrales con una caldera sumital y una producción predominantemente traquítica. Furnas es el volcán más joven, y consiste en un complejo abrupto de caldera de 8 x 5 km, formado a lo largo de colapsos sucesivos. En los últimos 3000 años, la mayoría de las erupciones han sido freatomagmáticas, ocurriendo con un intervalo de recurrencia de 320 años. El edificio volcánico de Fogo tiene una elevación de unos 1000 m sobre el nivel del mar, y está compuesto de flujos de lava, domos y depósitos piroclásticos sobre un basamento submarino anterior.

Aunque ningún volcán de São Miguel ha entrado en erupción desde el siglo XVII, el área está sujeta a un alto grado de sismicidad. En los últimos años, la red sísmica regional ha registrado y localizado anualmente varios miles de terremotos en

la zona. Su origen está relacionado con la presencia de fallas con dirección ONO-ESE, que dominan la tectónica regional. Sin embargo, ocasionalmente ocurren enjambres de terremotos (de hasta 100 terremotos al mes), especialmente en la región central de São Miguel. El origen de estos terremotos se asocia con la actividad volcánica y/o geotérmica de la zona. Hasta ahora, no se han descrito evidencias de terremotos de largo periodo o tremor volcánico, quizás por la ausencia de instrumentación especializada. En cualquier caso, dada la intensa actividad hidrotermal que se observa en São Miguel, es muy probable que ocurran eventos de largo periodo.

Conjuntamente con la sismicidad, la presencia de extensos sistemas hidrotermales constituye otra evidencia de volcanismo activo en São Miguel. Estos sistemas sugieren la existencia de fuentes de calor bajo la caldera de Furnas o entre Fogo y la costa norte. Además, las fuentes hidrotermales y las fumarolas se distribuyen a lo largo de sistemas de fractura que cruzan Fogo y Furnas. La actividad más intensa coincide con alineamientos tectónicos E-O en Furnas y NO-SE en Fogo.

El experimento sísmico

En el marco del Proyecto Europeo *E_RUPTION*, se instaló en São Miguel una red sísmica temporal con la intención de expandir y completar la red permanente operada por el “Sistema de Vigilancia Sismológica dos Acores” (SIVISA). Esta red estuvo operativa entre el 4 de abril y el 15 de julio de 2003, e incluía instrumentos de corto periodo y de banda ancha, así como tres antenas sísmicas. El objetivo fundamental del proyecto consistía en cuantificar la sismicidad de la zona, y obtener datos apropiados para la elaboración de una tomografía sísmica de la región central de São Miguel. La base de datos existente, perteneciente al SIVISA, proporcionó información preliminar sobre la distribución de terremotos, que se utilizó para la planificación de la red temporal. Durante los tres meses de registro, se detectaron más de mil terremotos. La mayoría eran terremotos locales caracterizados por un tiempo S-P del orden de unos pocos segundos, y una magnitud-duración menor de 2.5. En promedio, ocurrieron unos 5-10 terremotos diarios, excepto entre el 26 y el 27 de abril, periodo en el que se registraron más de 160 terremotos en unas pocas horas.

El conjunto de datos de partida utilizado para la tomografía consistía en una lista de tiempos de llegada de fases P y S, determinados visualmente para 756 terremotos locales registrados en una red sísmica de 33 estaciones. Estos datos se

emplearon para calcular las localizaciones preliminares. El modelo inicial de velocidad se obtuvo mediante el código *VELEST*, usando una base de datos de 331 terremotos registrados en 26 estaciones. Con este programa determinamos la estructura de velocidad 1D que mejor ajustaba (en el sentido de los mínimos cuadrados) los tiempos de llegada observados. Como modelo de partida utilizamos la estructura de velocidad utilizada por SIVISA en las localizaciones de rutina. El modelo resultante era parecido, aunque en la parte más superficial (por encima de 4 km de profundidad) encontramos valores más bajos de velocidad. En este modelo 1D calculamos la posición de los terremotos mediante el programa *NLloc*, que proporciona una solución de máxima verosimilitud para el problema de la localización de la fuente

La parte principal del trabajo consistía en la determinación de la estructura tridimensional de velocidad de las ondas P y S para la región central de São Miguel, a través de la inversión tomográfica de los tiempos de llegada de terremotos locales. Este método separa el problema directo (cálculo del tiempo de viaje) del problema inverso (determinación de la velocidad). En el problema directo, se calculan los tiempos de viaje y las trayectorias aproximadas de los rayos mediante una técnica de diferencias finitas. Esta técnica es adecuada para el experimento en São Miguel, ya que puede resolver los fuertes contrastes de velocidad esperables en zonas volcánicas. El problema inverso se resuelve mediante un algoritmo LSQR, que incluye parámetros de suavizado que condicionan la variabilidad del modelo final, y proporciona una solución de mínimos cuadrados para la inversión de la matriz de perturbaciones de velocidad. Los parámetros del modelo se definen en una malla tridimensional de celdas cúbicas de lentitud constante, menos densa que la usada para el trazado del rayo. Tras varias pruebas con diferentes tamaños de celda, concluimos que el tamaño de celda óptimo era de 1 km. El tamaño de celda para la malla del cálculo del trazado del rayo utilizado en el problema directo para calcular los tiempos de viaje fue de 0.25 km.

Para realizar la inversión tomográfica, seleccionamos las llegadas de fases P y S pertenecientes a 289 terremotos locales registrados en una subred de 20 sismómetros. El modelo inicial de velocidad se pudo definir a partir del modelo 1D descrito. La resolución del procedimiento se comprobó mediante inversiones de datos sintéticos generados en modelos con anomalías de velocidad conocidas. Se utilizaron tests de tablero de ajedrez, de respuesta a anomalías puntuales, y de reconstrucción. Estas pruebas confirmaron que la resolución era adecuada en la zona central del dominio seleccionado, incluyendo las calderas de Fogo y Furnas, hasta una profundidad de unos 6 km, en correspondencia con la mayor densidad de rayos sísmicos que atraviesan las celdas en esa zona. También determinamos la influencia de la selección de los terremotos en el modelo final de velocidad. Para ello realizamos un test “jackknife”, en el que repetimos las inversiones usando diferentes subconjuntos de la base de datos de tiempos de llegada, obteniendo en todos los casos modelos muy parecidos. Finalmente, también introducimos perturbaciones en el modelo inicial, llegando siempre a modelos finales similares.

Resultados y discusión

La inversión tomográfica produjo una solución estable tras 10 iteraciones, con una reducción del RMS de los residuos de los tiempos de llegada de la onda P de 0.35 s en el modelo inicial a 0.13 s en el modelo final. Los resultados muestran la presencia de varias anomalías de velocidad de ondas P y S, que difieren de los valores iniciales hasta un 10%. Horizontalmente se aprecian contrastes importantes, que se reproducen en todo el rango de profundidades resuelto. Las anomalías principales mantienen su posición, cambiando ligeramente en intensidad. Esto significa que cualquiera que sea el mecanismo que produce las anomalías, se extiende hasta la profundidad máxima que hemos resuelto en nuestra inversión.

Los contrastes de velocidad observados en el medio están relacionados con depósitos piroclásticos, cuerpos intrusivos, campos geotérmicos, y con efectos tectónicos a diferentes escalas. Bajo la caldera de Furnas encontramos una anomalía de baja velocidad, que se mantiene estable hasta 6 km de profundidad. Las velocidades son del orden del 10% menores que en el modelo inicial, lateralmente homogéneo. Superficialmente, esta anomalía representa una indicación de la presencia de sedimentos volcanoclásticos de baja densidad, fuertemente alterados por la actividad hidrotermal. Estos productos incluyen pumitas, ignimbritas y depósitos de oleadas piroclásticas, cenizas freatomagmáticas, y fragmentos de domo. Sin embargo, la continuación de la anomalía en profundidad puede estar más bien relacionada con fracturación intensa del medio y/o áreas de alteración hidrotermal.

En la región NO del área de estudio, entre la caldera de Fogo y la costa norte, existe otra zona de baja velocidad. Esta anomalía negativa es más débil que la de Furnas, ya que no sobrepasa el 2-3% con respecto al modelo inicial. De hecho, aparece en una región periférica del volumen estudiado, donde la resolución del modelo es menor, por lo que debe ser interpretada con cierta reserva. En cualquier caso, su presencia apunta de nuevo a la actividad de un sistema geotérmico en una matriz de depósitos piroclásticos poco densos y porosos. Esta interpretación se confirma por la existencia en la zona del campo de Ribeira Grande, que constituye el principal campo geotérmico explotado en la actualidad en São Miguel.

Por el contrario, la región que se extiende entre el sur de Fogo y el noroeste de Furnas, a través de la zona de Congro, muestra anomalías de velocidad positivas de hasta un 10% por encima del modelo inicial. En realidad se pueden diferenciar dos subvolumenes dentro de esta zona anómala, separados por una banda más lenta. Esta zona central tiene la mayor

cobertura de rayos sísmicos, por lo que probablemente esta partición en dos regiones es una característica real de la estructura de velocidad. La región que separa los dos máximos coincide con la existencia de una zona sismogénica, altamente fracturada, que se ajusta al campo de esfuerzos tectónicos regionales, y ha sido sugerida por diferentes observaciones sismológicas. Los dos máximos se interpretan como depósitos densos y/o remanentes de intrusiones plutónicas. Esto significa que el volcán Fogo puede estar sobre los restos enfriados de una cámara magmática, como sugiere la ausencia de actividad magmática evidenciada por distintos estudios geofísicos y geoquímicos.

En cuanto a la razón V_p/V_s , tiende a ser baja en general en toda la región central de São Miguel, en concordancia con estudios sísmicos previos. Sin embargo, existen zonas con valores superiores e inferiores al valor promedio de 1.68 calculado para el área. La región central del volumen estudiado muestra una razón entre normal y alta, a todas las profundidades resueltas. Estos valores se extienden hacia el este, cerca de la zona de Furnas, y entre Fogo y la costa sur de São Miguel. Por otra parte, el extremo NNO del área de estudio y la región de Furnas están caracterizados por valores bajos de la razón V_p/V_s . Los valores más bajos ocurren en ambos casos a una profundidad de unos 2 km.

La distribución de la razón V_p/V_s concuerda con las interpretaciones realizadas a partir de la velocidad de la onda P. La comparación de ambas distribuciones espaciales es una potente herramienta para comprender la naturaleza del medio volcánico, en particular la presencia de fluidos. Combinando ambos resultados, la zona de Furnas queda definitivamente asociada con el desarrollo de un importante campo geotérmico dominado por la fase de vapor en el relleno piroclástico de la caldera. Por el contrario, el volumen magmático enfriado de Fogo actuaría como la ruta preferida para la circulación de fluidos, fundamentalmente agua líquida.

Conclusiones

La imagen tomográfica tridimensional de V_p y V_p/V_s obtenida para la región central de São Miguel muestra importantes variaciones laterales de velocidad, que se pueden atribuir al efecto del relleno sedimentario, la presencia de depósitos densos o restos de intrusiones plutónicas, la actividad de sistemas geotérmicos, etc. En este sentido, el modelo de velocidad constituye el marco de referencia en el que interpretar la actividad sísmica e hidrotermal de la isla. Este modelo está de acuerdo con las observaciones obtenidas a partir de otros estudios. Del mismo modo, concuerda con las tendencias

geodinámicas de la zona, que parecen influenciar la estructura de la isla a través de varios sistemas de fallas de afinidad regional.

Conclusiones Generales

En este trabajo nos hemos centrado especialmente en la heterogeneidad de la estructura sísmica, la cual puede ser puesta en evidencia a través de los estudios de tomografía sísmica.

Hemos tenido en consideración a dos islas volcánicas, São Miguel (Azores) y Decepción (Antártida), las cuales se caracterizan por una elevada sismicidad y actividad volcánica y la ausencia de un conocimiento en detalle de su estructura sísmica. Hemos modelado el interior de estos volcanes a través de la aplicación de dos técnicas tomográficas diferentes, basadas en experimentos pasivos y activos para São Miguel y Decepción, respectivamente. Hemos propuesto una interpretación de los resultados con el fin de relacionar su estructura interna con la actividad presente, y con otras observaciones geofísicas obtenidas en otros estudios.

Para el caso de São Miguel, hemos determinado la distribución tridimensional de velocidades de las ondas P y S mediante la inversión tomográfica de tiempos de llegada de terremotos locales. Para ello hemos usado lecturas de fases P y S de 289 terremotos registrados en una red sísmica de 20 estaciones. Los resultados nos presentan varias anomalías de velocidad, respecto a un modelo de partida, con buena resolución en los primeros 5-6 km. Estas perturbaciones son interpretadas en términos de depósitos piroclásticos, cuerpos intrusivos, campos geotérmicos y los efectos de la actividad tectónica. De manera concreta, se observa una zona de baja V_p en la caldera de Furnas, que pone en evidencia la acumulación de sedimentos volcanoclasticos y depósitos alterados geotérmicamente. Otra zona de baja velocidad se extiende en correspondencia con la zona altamente fracturada de Ribeira Grande, entre Fogo y la costa norte de la isla. Por otro lado, se han observado anomalías positivas muy intensas cerca de Fogo y Noroeste de Furnas. Estas anomalías han sido interpretadas en función de la existencia de depósitos volcánicos de alta densidad y de intrusiones plutónicas enfriadas. Las altas velocidades están separadas entre si por una región que presenta valores de V_p ligeramente más bajos, y que se corresponden con una región fracturada.

Estas interpretaciones han sido confirmadas y detalladas a través del estudio de la distribución espacial de la razón V_p/V_s . Esta relación se revela como una herramienta potente para entender la naturaleza de los fluidos puestos en juego en el estado volcánico actual de la región. Así, los bajos valores de V_p y V_p/V_s de Furnas se pueden asociar con la presencia de un campo geotérmico dominado por emisiones intensas de vapor en una caldera rellena de piroclastos. No se observan evidencias de magma en esta región. Por el contrario, la planta geotérmica de Ribeira Grande, entre Fogo y la costa Norte de la isla, está principalmente dominada por fluidos líquidos, como se observa consistentemente a través de nuestros resultados. Los restos fríos de la cámara magmática remanente de Fogo parecen que actualmente no presentan ningún tipo de indicación de actividad volcánica. Por contrario, los fluidos que parecen estar presentes son probablemente agua en el estado líquido.

La estructura de Decepción ha sido estudiada mediante la inversión de tiempos de llegada de ondas P generadas por fuentes activas. Se generaron más de 6600 disparos en el mar, y se registraron en 85 estaciones sísmicas sobre tierra y 14 sismómetros de fondo marino, que se distribuyeron en 119 posiciones diferentes. La inversión tomográfica tridimensional resuelve fuertes contrastes de velocidad hasta una profundidad de unos 5 km. La característica más remarcable de los resultados es la existencia de una región de baja velocidad bajo Port Foster, que viene interpretada como una región magmática extensa. En las zonas superficiales, esta zona se interpreta con la presencia de depósitos piroclásticos sedimentarios que rellenan la caldera. Las bajas velocidades E de Decepción corresponden a un fondo marino que está caracterizado por estructuras sedimentarias (barrancos, cordilleras y flujos de derrubios) hacia la Cuenca Central del Bransfield. Los valores de baja velocidad de P en una zona al SO de Neptuno Bellows pueden estar generados por los depósitos piroclásticos originados en antiguos conos volcánicos. La zona de baja velocidad del oeste de Isla Decepción son las evidencias de edificios volcánicos y sedimentos volcanoclásticos de gran espesor, anomalías térmicas o sistemas magmáticos activos.

También se observan zonas de alta velocidad. La anomalía más extensa se encuentra NO de la región y está compuesta por un conjunto de máximos. Esta anomalía indica la presencia de un basamento cristalino de corteza continental que se encuentra en correspondencia con el bloque de las islas Shetland del Sur. El contraste brusco con las zonas de baja velocidad en el SO tiene una tendencia bien definida en la dirección NE-SO, que es compatible con la tectónica regional de extensión en el Bransfield. Existe otra zona de alta velocidad en la zona de Neptuno Bellows, la posible posición del antiguo basamento de la Isla Decepción, lo que probablemente refleje el antiguo escudo del volcán. También se observa una anomalía de alta velocidad en el Sur de la Isla, y probablemente sea la imagen sísmica de un antiguo domo volcánico o intrusión, o la zona de ascenso del antiguo sistema de alimentación magmático de la isla. Hacia el oeste de la isla existe una

zona de anomalía de alta velocidad que probablemente sea la imagen sísmica del afloramiento conocido como Sail Rock, un edificio andesítico erosionado.

Como se observa, los modelos de velocidad de estas regiones volcánicas nos ofrecen una primera imagen de la estructura interna de dos zonas volcánicas activas que han sido estudiadas previamente con otras técnicas, pero que hasta ahora no se han podido interpretar en un marco volcano-tectónico más completo. En este sentido, nuestras estructuras sísmicas intentan establecer un modelo que permita interpretar las observaciones previas y así responder a numerosas preguntas planteadas por la curiosidad científica.

Es interesante además que parte de estas nuevas indicaciones estructurales se puedan relacionar con el contexto tectónico regional. Por esta razón estas imágenes tomográficas son una llave muy importante para las interpretaciones geodinámicas. En el caso de São Miguel, por ejemplo, es evidente el papel que juega el sistema de fracturas regional NO-SE, que atraviesa toda la región y que se puede considerar aún activo. El aporte magmático de los edificios volcánicos de São Miguel si es, a día de hoy, aún activo, solo está asociado a sistemas profundos, de alimentación magmático a gran escala. De igual manera la estructura sísmica de la Isla Decepción pone en evidencia la relación entre la evolución de la isla y la tectónica regional. Muchos de los resultados indican la presencia de dos sistemas de fallas dominantes, en las direcciones NE-SO y NO-SE, los cuales ya han sido reconocidos a gran escala en estudios anteriores. Estos sistemas han condicionado la historia volcánica de Decepción, sus erupciones pasadas, su emplazamiento y la evolución de la caldera, y la presente distribución de la sismicidad.

Se podrían hacer muchas más consideraciones acerca de la relación entre nuestras imágenes de estructura sísmica y el contexto tectónico regional, pero es obvio que esto va mucho más lejos de nuestros propósitos en este trabajo. En cualquier caso, hay muchos más aspectos que merecen la pena ser recordados de manera concisa.

Un conocimiento más profundo de las regiones volcánicas estudiadas posee muchas implicaciones prácticas. La situación de São Miguel clarifica perfectamente la importancia del conocimiento volcánico para objetivos tecnológicos. Desde hace años, la isla recibe una parte importante de su demanda energética a través de la explotación de sus plantas geotérmicas. Sobre la base de nuestros resultados, obviamente confirmamos la existencia de un campo geotérmico en Ribeira Grande, al norte de la isla, que ya está en explotación. Pero es igualmente interesante observar que nosotros sugerimos la presencia de un campo geotérmico de alta temperatura en la zona de Furnas, para el cual los fluidos en condiciones supercríticas podrían ser de interés económico (de lo que sabemos, sólo hace muy poco se ha planteado el estudio de esta área para su explotación económica). Por el contrario, la región del volcán de Fogo no parece una buena candidata para la prospección geotérmica. De manera similar, las fuertes anomalías térmicas observadas en Decepción y la

bien conocida circulación de abundante agua podría apuntar a la presencia de una posible reserva geotérmica que ha sido sub-estimada hasta ahora, y podría ser tenida en cuenta en el desarrollo sostenible y sin impactos de las bases Antárticas allí presentes. Pero de nuevo este punto va más allá de los objetivos de esta tesis y de las limitaciones impuestas por el Tratado Antártico.

Además, el conocimiento del estado actual y una posible visión de la evolución volcánica de estas islas tienen implicaciones importantes desde el punto de vista del diseño y gestión del riesgo volcánico. No podemos olvidar que São Miguel está densamente habitada, y la isla Decepción es visitada cada año por numerosos investigadores y decenas de miles de turistas. Nosotros podemos concluir, a partir de nuestro estudio, que para São Miguel Central, aparte del riesgo relacionado con la intensa actividad sísmica y la geotérmica, no existen evidencias de que pudiera haber actividad volcánica importante de una manera inminente. Para el caso de la isla Decepción, es obvio que la presencia de un volumen extenso de magma cerca de la superficie debe ser tenida en cuenta de manera muy cuidadosa.

La comparación entre las dos técnicas tomográficas aplicadas, los modelos de velocidad obtenidos y su importancia desde el punto de vista estructural nos permite generalizar los resultados de nuestras campañas con el fin de encontrar las fortalezas y debilidades de los experimentos de sísmica activa y pasiva. Se han observado muchas diferencias entre las dos técnicas, tanto en relación a los datos a analizar, como a los resultados obtenidos.

Desde un punto de vista cuantitativo, los experimentos de sísmica activa permiten obtener un conjunto de datos muy consistente en un intervalo de tiempo relativamente corto, mientras que las técnicas pasivas a menudo necesitan recoger los datos a lo largo de periodos de muchos meses/años. No siempre este es el caso, pues en regiones volcánicas se puede dar la presencia de enjambres sísmicos. Pero, en estos casos, las fuentes sísmicas suelen presentarse agrupadas en el espacio, y es evidente que no tienen gran interés desde el punto de vista tomográfico.

Este punto nos conduce a unos de los problemas más importantes, los relacionados con la calidad de los datos provenientes de los experimentos tomográficos, esto es, la cobertura espacial de las fuentes sísmicas y de las estaciones de registro. En el caso de utilizar la actividad natural, las fuentes sísmicas pueden estar agrupadas y no bien distribuidas a lo largo de la zona de estudio, ni con respecto a la posición de las estaciones. Este hecho desgraciadamente significa que los caminos seguidos por los rayos sísmicos son subparalelos, lo cual no añade mucha más información (fuentes en agrupamientos); o no pueden atravesar de manera completa el volumen que deseamos estudiar (una distribución no apropiada). De este modo la extensión lateral de la zona de posible estudio se reduce de manera significativa debido a la distribución no adecuada de los caminos de los rayos sísmicos. La capacidad que tiene los datos para distinguir objetos próximos, esto es, su capacidad de resolución, se reduce debido a estos tipos de distribución. La escala de las estructuras

resueltas también depende de la longitud de onda, la cual varía fuertemente entre eventos sísmicos, pero de forma general es mayor para las fuentes naturales que para los disparos artificiales. Existe otra dificultad que viene incrementada en el caso de bases de datos pobres de experimentos pasivos, y es más un hecho matemático. Está relacionada con el aumento de la no-linealidad del esquema de la inversión cuando se añade el problema de la localización de los terremotos. Es evidente que cuando se tiene pocos tiempos de viaje este problema está fuertemente indeterminado.

En el caso del experimento de São Miguel afrontamos la dificultad de tener una base de datos pequeña perteneciente a una campaña de campo de tres meses, en donde muchos terremotos estaban demasiado lejos de la región bajo estudio, o demasiado cerca entre ellos, en pequeños agrupamientos, o finalmente registrados sólo en pocas estaciones. Esta base de datos tan pobre nos ha obligado a verificar continuamente su calidad frente a las incertidumbres que pudiera introducir. A menudo la mejor estrategia ha sido reducir la cantidad misma de los datos de manera que no se introdujeran errores sistemáticos. Esto justifica que la fase de preparación de los datos fuera interminable, y que la continua selección y control de los resultados se hiciera con numerosos controles y pruebas, a lo largo de los primeros pasos de la inversión. La incertidumbre final en la estructura de velocidad resuelta pudo ser separada con dificultad del error debido a la imprecisa localización de los terremotos. Considerando todos estos factores, y en particular la final distribución y cantidad de datos, sólo fue posible obtener imágenes usando celdas de 1 km de ancho. Por tanto esta dimensión limita el tamaño de la estructuras menores que podríamos resolver e interpretar.

Por el contrario, en el experimento de la isla Decepción permitió obtener, en una campaña de dos semanas de duración, una gran cantidad de datos, perfectamente distribuidos a lo largo de la región de interés y con respecto a las posiciones de las estaciones de registro. La resolución lateral alta nos ha hecho posible obtener imágenes de pequeñas estructuras, tan grandes como algunas decenas de metros. Sólo ha sido necesaria una selección de los datos cuando aparece ruido sísmico sobre los sismogramas. En particular, las formas de onda se encuentran fuertemente afectadas por la llegada de la onda de agua, la cual es obviamente de mayor amplitud en las distribuciones fuente-receptor de fondo marino. Puesto que es conocida la posición de las fuentes, también el problema directo del trazado del rayo es considerablemente más fácil y se puede alcanzar más altos niveles de exactitud. En este caso, al menos con de fuentes marinas de aire comprimido, el cálculo de sus caminos sólo es complicado por, después de que los rayos sísmicos atraviesen las capas de agua, la localización de los puntos de entrada en la irregular superficie marina.

Sin embargo las técnicas pasivas presentan también ventajas notables. Primero, es posible reconocer y realizar modelos de velocidad con otras fases útiles. Por ejemplo, es extraordinaria la información procedente de la razón V_p/V_s , la cual es fácilmente observada en fuentes naturales. En el experimento de São Miguel hemos sido capaces de dibujar la distribución

de V_s , junto con la de V_p . Esto se ha revelado una información básica para la interpretación de las anomalías sísmicas y la distribución de los fluidos. Más aún, en la tomografía pasiva la ocurrencia de hipocentros profundos puede extender en profundidad de las dimensiones del volumen a resolver. Con experimentos de fuentes artificiales las fuentes sísmicas son superficiales y los caminos de los rayos atraviesan estructuras superficiales. En este caso, proporcionalmente a la extensión cubierta por los experimentos, la tomografía de São Miguel puede modelar estructuras más profundas con respecto a aquellas de la isla Decepción, cuyas raíces más profundas están aún pendientes de resolver.

Finalmente, pero no por último, una campaña de sísmica activa a menudo es resultado de una fase de preparación logística complicada, de una fase de campo delicada y de un considerable impacto económico. En el experimento de Decepción hubo que respetar un calendario muy estricto con el fin de desplegar el mayor número posible de estaciones sísmicas, y de manera simultánea a la generación de las señales. Obviamente esto implica coordinación y trabajo de muchos investigadores.

Por consiguiente, y como una de las principales conclusiones metodológicas de nuestra investigación, insistimos que nos es posible definir una técnica tomográfica preferida respecto a otra. Su selección depende fuertemente de las condiciones específicas y del objetivo del estudio. Existen diferentes ventajas y dificultades que los diferencian en la preparación y ejecución de las campañas de campo, la recogida final de datos y los análisis conclusivos. Obviamente, la mejor –y más difícil– estrategia es la de la integración de las dos técnicas. Por estas razones, es altamente deseable una mejora del conocimiento de la estructura sísmica de toda la isla de São Miguel. La organización de un experimento activo y el despliegue de antenas sísmicas revelarían la estructura completa de la isla con gran detalle. El uso de las antenas sísmicas densas sería la técnica que nos permitiría estudiar la actividad sísmica de largo periodo, que como hemos visto constituye una pieza que todavía falta en esta imagen. Por otro lado, para el caso de Decepción, los registros sísmicos obtenidos en el pasado se podrían integrar para obtener más información sobre las fases P y las S. Esto podría clarificar la distribución interna de los fluidos y ofrecer la imagen tomográfica de las estructuras más profundas. La cámara magmática podría ser fácilmente dibujada, junto con las zonas de actividad geotérmica y de circulación de fluidos. En estructuras de velocidad así detalladas, la sismicidad estudiada anteriormente, tanto de tipo volcano-tectónico o de largo periodo, podrían localizarse de manera precisa y dar explicaciones sobre su fuente. Finalmente, con un volumen grande de datos, los estudios tomográficos podrían ofrecer una representación de los cambios de la estructura sísmica de la isla durante su evolución en tiempos recientes, es decir, una tomografía sísmica 4D.

This Thesis

The main aim of this work is to image the internal seismic structure of two volcanic islands: São Miguel (Azores Islands, Portugal) and Deception (South Shetland Islands, Antarctica). Besides their differences, widely recognized in the tectonic and geodynamic perspective, the islands share two fundamental aspects: both host intense seismic activity of volcanic origin and both have an internal structure which is substantially unknown. These characteristics provided the motivation for two seismic surveys, a passive and an active experiment at São Miguel and Deception Island, respectively. The principal aim of both experiments was the final construction of a tomographic image of the velocity structure of the islands, throughout the study of the traveltimes residuals of recorded signals. As expected, the two experiments posed different problems and hence needed two different approaches.

The basic difference consisted in the choice of carrying out a passive experiment at São Miguel and an active one at Deception Island. The main reason of the two experimental alternatives arose from the practical concerns. While São Miguel has an infrastructure favourable to the deployment of a local seismic network and its maintenance for a relatively long period in order to record natural seismic activity, Deception Island, owing to its geographical location, presents greater logistical difficulties. Hence, a short, intensive, experiment was preferable to study this remote region.

These choices were further supported by more strictly scientific considerations. São Miguel has an intense natural volcano-tectonic activity, that is often temporally clustered, and well extended in depth. This kind of seismicity, as discussed below, suggested a passive experiment as the best strategy to collect data for a seismic tomography. Moreover, this activity was expected to yield information about the seismic structure of the volcano as V_p and also V_p/V_s distribution. It is well known that the knowledge of the V_p/V_s ratio is a basic tool in the determination of fluids distribution, and hence was particularly attractive in the application to a region which hosts intense hydrothermal and geothermal activity. As an

additional reason, the island was contemporaneously monitored by a local seismic network whose data could be easily integrated with those of the experiment in order to obtain a considerable amount of data without additional effort.

By contrast, Deception Island is characterized by a seismic activity which is mainly of long period type, and which is hardly introduced in a tomographic study. For this reason a significant database of P-wave first arrival times only could be collected in a short time by recurring to artificial sources. Furthermore, a remarkable factor was the rather unusual geometry of the island, that made it ideal for a combined land and marine high-resolution active source experiment.

The choice of a specific technique had to take into account that the obtained data possibly needed the application of different tomographic methods. The mathematical part of the tomographic study had to handle problems which vary, among others, for data type (P- and S-wave against only P-wave), inversion unknowns (earthquake sources against well located airgun shot sources); and model parameterization (seismic sources surrounded by the crustal structure against the water first layer for air-gun sources location).

Hence, the structure of this thesis reflects this attempt of adjusting the tomographic study to the uniqueness of the studied regions. In the Chapter One, we introduce the tomography concept and the main purposes of its application to volcanic regions. We briefly explain what velocity anomalies mean and what they suggest about the volcano structure. We then introduce the principal techniques and their advantages and drawbacks. We support these concepts with an example of their application. In the second chapter, we go deeper the theoretical aspect of the tomography and we explain the basic principles and the mathematics controlling its application. We closely focus on the algorithms we apply for our experiments, highlighting their main advantages in each case. In the third chapter, we describe the São Miguel experiment, from the field work to the tomography results. In the Chapter Four we give similar details of the Deception Island seismic survey. In both cases, we start with the field campaign, we describe the selection and preparation of data, and we present and interpret the seismic image of the island. Finally the fifth and final chapter summarize the main tomographic results of this thesis in the light of a comparative analysis of the two different experiments.

In addition to the main purpose of tomographic imaging for the two volcanic islands, in this work we evaluate the advantages and drawbacks of the active versus passive alternatives. Insight into the favourable aspects and inconveniences related to the application of these techniques is gained as natural result of our work. We hope that the final comparison of their performances can improve the knowledge of the tomography as tool for understanding volcanoes

1. Tomography and Volcanoes

1.1. Seismic Tomography

Seismic data represent one of the most valuable resources to investigate the earth structure. By them, several methods have been developed to derive information about the otherwise inaccessible earth interiors. Among these methods, seismic 3D tomography possibly represents the technique that more easily can image the seismic structure, and whose results can be more directly translated to a true picture of subsurface masses. Hence, since 1970s it has been applied in geological investigations, meanwhile its theory improved in the mathematical aspects and methodologies [Rawlinson and Sambridge 2001].

Seismic tomography is an intriguing tool of study due to its flexibility. For example, different components of the seismic waves may be used, including traveltimes, amplitudes, waveform spectra, full waveforms or the entire wave field. Moreover, different seismic phases can be used and in a variety of source-receiver configurations. The phases more successfully used in seismic tomography include a variety of teleseismic phases, local earthquake P and S waves, surface waves, normal modes, and, among body waves, direct, reflected, refracted, and diffracted waves. Receivers can be in-line or 3D, sources can be natural or artificial, resolved scales can span the whole range between few tents of meters and global distances (see, for example, several applications in *Seismic Tomography : theory and practice* [Iyer and Hirahara 1993].

In particular, seismic-imaging via body-wave traveltimes consists in the reconstruction of the three-dimensional velocity/slowness field by using P- and S-wave arrivals data from natural and/or artificial sources. If the seismic sources for such arrival-time study are located within the modelled volume, we are dealing with what we call Local Earthquakes Tomography (LET,[Kissling 1988]).

The seismic traveltime tomography basically consists in the manipulation of the misfits (commonly called residuals) between observed travel times and travel times calculated in a tentative model, to estimate improvements to the trial model itself, until the most likely velocity structure is reached [Thurber and Aki 1987]. In the specific case of Local Tomography this problem is significantly more complex, because the location of the seismic sources can be unknown, beside the seismic structure of the medium where they are located.

Nevertheless, the Local Traveltime Tomography is the approach at the base of the study of volcanic regions, where considerable local seismic activity is expected to occur and heterogeneities are at a scale easily resolvable by using of P and S-wave local earthquakes data [Foulger and Arnott 1993].

1.2. Tomography and Volcanoes

Volcanic regions constitute a challenging field of application for seismic tomography. At the same time they supply the fascination of their structural complexity and the benefits of an intense natural seismic activity.

The inner structure of volcanoes is expected to show highly heterogeneous seismic velocities properties. This is due, among other reasons, to (1) the variety of rocks forming the volcano complex (massive lavas, vesiculated lavas, consolidated tuff, unconsolidated pyroclastic rocks, altered deposits, non volcanic rocks), (2) the presence of dense fracture systems, possibly hosting circulating fluids of various origin and state (gas/liquids of volcanic or meteoric derivation, magma) (3) the presence of fragile rock volumes weakened by repeated episodes of magma ascent, by thermal perturbations or by caldera collapses (4) the occurrence of melt or partially melted bodies or dense remnant of magmatic intrusions both to shallow and deep levels behind the volcanic edifice.

To this complexity it has to be summed the additional difficulty provided by the small scale of such overlapping heterogeneities and the irregularity of their contacts and geometry. This complexity is particularly developed in volcanic areas because it is the physical imprint of the often irregular volcanic evolution and of a history of variable eruptive styles. Moreover, with respect to other geological settings, we may observe that the modelling of the seismic structure has to supply a mathematical representation of an extreme topography such as that in volcanic regions [Ripperger et al. 2003].

Nevertheless, in the last decade the seismic tomography on volcanoes has been providing images with an increasing resolution, where many goals are pursued at different scale (Chapter 1.2.1), also if the primary objective is to map the internal structure (1.2.1), with detailed information (1.2.2) depending upon the applied technique (1.2.3).

1.2.1. Importance of Tomographic Models

Several areas of active volcanism have been studied by both local earthquakes/active sources and teleseismic tomographic methods, to inspect their detailed shallow structure as well as their deep roots. Throughout a tomographic analysis, the volcano structure can be revealed as spatial distribution of several seismic parameters. Among them, this investigation allows to better define physical constrains such as velocity of P-wave, of S-wave, scattering and attenuation, and, from these, many other properties (rock density, temperature and pressure distribution, fluid presence and fracturing state, see 1.2.2). First of all, this information answers to modelling purposes. The first goal of tomographic studies is to map the location and size of zones of partial melt and crustal magma reservoirs [Iyer and Dawson 1993]. On one side, by using seismic signals with wavelengths of several kilometres, teleseismic tomography supplies information at great scale and so it is suitable for studying larger scale and deeper structures. On the other, the short wavelength of local earthquakes and explosions enable structures, such as feeding conduits, magma chambers, and zones of solidified magmatic intrusion, to be studied on the kilometre and sub kilometre scales. Obviously, the contemporary application of both methods is a powerful tool to resolve structures on a wide range of dimensional scales.

In addition, the tomographic study goes further into the scientific curiosity and permits to understand the volcano dynamics and evolution. In fact, from the structural status of its interiors, it is often possible (but difficult [Cañon-Tapia and

Walker 2004]) to provide clues about the evolution of the volcano in the framework of the general tectonics and about the origin of its magma. This means that the tomography is a tool not only to ‘see’ how volcanoes are inside, but, ultimately, to argue about why they are in such a way and how the Earth operates deep in its interiors.

We must take into account, moreover, that to localize and model seismic sources inside of volcanoes, it is necessary this kind of knowledge of the internal structure of the volcanic edifice. Due to lack of 3D models usually 1D structures are used to determine hypocenters of volcanic events and waveform modelling [Goldstein and Chouet 1994]. In contrast to usual earthquake seismology, however, we cannot expect a 1D layered medium as a good approximation at volcanic structure. Tomography is hence the best method to achieve a 3D image of the seismic velocity distribution in a volcano.

Obviously, the detailed knowledge of active regions as seismic properties of the propagation medium is important to understand the seismic signals used for eruption forecasting [Wegler and Luehr 2001]. This means that the knowledge of the volcano structure and dynamics improves the predictive chances in the hazard assessment. Considering that, the population density near volcanoes is typically high , worldwide [Smith 2004] the tomographic tool acquires relevance in terms of volcanic risk management.

To these considerations, we have to add the technological utility of what is more than a theoretical knowledge of volcanic areas. In fact, regions which host volcanic structures are often site of strong thermal anomalies that can be precisely imaged by a tomographic study. This technique, hence, becomes an additional tool for geophysical survey and prospecting. The main goal of this investigation resides in the use of geothermal resource as energy but thermal waters often contain sulphur, gold, silver, and mercury that can be recovered as a by-product of energy production [*Kious and Tilling 1996*].

1.2.2. General Interpretation of V_p and V_s Anomalies in Volcanoes

For volcanic areas, seismic tomography experiments yield velocity models highly variable, from surface to depth. In many cases, good correspondence is found between the tomographic results and structures known from geological and other geophysical studies (for example, in joint inversions with gravity data [Roy et al. 2005]). This provides confidence in the applied tomographic methods, and also gradually supplies an understanding of what 3D velocity anomalies geologically represent in volcanic areas.

As with teleseismic data, a primary goal of local earthquakes tomography in volcanic areas is to demonstrate whether or not magma accumulations exist and to delineate them if so [Iyer and Dawson 1993]. Roughly speaking, a magma chamber is a volume of molten or partially molten rock with physical properties, among which seismic velocity, significantly different from the surrounding host rocks: for this reason, it provides an ideal target for imaging via seismic tomography methods [Chouet 2003]. Low seismic velocities usually characterize magma reservoirs and are explained with near-solidus temperatures or with the presence of melt. On the opposite, high velocities are assigned to crystalline intrusives.

This picture is actually more complex because, also in presence of magma, the seismic properties of the medium depend on several factors (among them depth/lithostatic load, presence of fluids, porosity and fracturing, for example) and their variable combination [Winkler and Murphy 1995]. In addition, these factors have different effects above diverse seismic phases, and this makes not unique the interpretation of their velocity perturbations. In general P-wave tomographic images are available for many volcanoes, while S-wave or V_p/V_s models are limited to a few cases and attenuation of seismic waves (Q_p or Q_s) to even fewer [McNutt 2005].

Several reasons may account for the observed lateral changes in seismic velocities: (1) changes in lithology, fluid content (and state) (2) changes in texture, such as those due to development of cracks in the rock, or to large pore fluid volumes in fractured zones (3) changes in temperature and pressure (4) anisotropy in velocity distribution. This is an especially intriguing question, because also if it constitutes a practical assumption, the real Earth surely is not an isotropic medium. The seismic velocity anomalies should be interpreted keeping in mind the effects of anisotropy in addition to

isotropic lateral heterogeneities [Winkler and Murphy 1995]. The travel time residuals which cannot be explained by isotropic seismic tomography are probably attributable to anisotropy effect [Barclay and Solomon 1998; Dunn and Toomey 2001; Toomey et al. 2007].

Hence, the seismic velocities distribution has to be interpreted in a wide scenario, as it certainly is the effect of the combination of these changes, whose effects we know little about at present.

Many controlled laboratory [Boitnott and Bonner 1994; Bonner et al. 1998; Vinciguerra et al. 2005]; He and Schmitt, 2006) and theoretical modelling studies [Carcione et al. 2003; Cerney and Carlson 1999; Takei 2002; Winkler and Murphy 1995] concern the relationship between seismic velocity and rock properties, such as density-porosity, temperature and presence of partial melt. Usually laboratory measurements are conducted with wave frequencies much higher than common seismic frequencies and at room temperature and pressure. More reliable information proceeds from the application of tomography study at a great variety of volcanic setting, from volcanoes [Hansen et al. 2004; Patane et al. 2006] to calderas [Sherburn et al. 2003; Vanorio et al. 2005] to geothermal fields [Husen et al. 2004; Julian et al. 1996]), although the uniqueness of each situation has to be taken into account.

A number of studies have revealed the strict correspondence between seismic velocity and *lithology*. Commonly, lower values of V_p are observed in materials with high porosity, such as tuffs and pyroclastic deposits, in contrast with highly consolidated material, as granitic or metamorphic rocks [Lees and Wu 2000]. The presence of fractures similarly reduces the seismic velocity compared to intact rock [Fehler et al. 1998; Vinciguerra et al. 2005]. This picture is complicated by the hydrothermal alteration whose commonest effect is the lack of cohesion for the rock and a decrease of the values of seismic velocities, if compared with rock protolitha [Cerney and Carlson 1999]. On the opposite, also local effects of stiffening of the matrix by lithifications and microporosity reduction has been observed [Bonner et al. 1998].

In dry conditions, the *temperature* produces a decrease in velocity which is probably due to the softening of the rock matrix and to the increase in porosity which results from the different thermal expansion of minerals. Anyway, when partial melting is reached (see later), V_s decreases more strongly than V_p , because an increasing temperature mainly decreases the comprehensive shear modulus of the rock. This usually leads to an increase of V_p/V_s with temperature. This rise, more specifically, reaches infinity upon melting of the rock [Muller and Raab 1997]. However, V_p/V_s variations depending on temperature are still ambiguous [Christensen 1996] and are difficult to evaluate [Nakajima and Hasegawa

2003]. To convert velocity anomalies to variations in temperature, it can be assumed [Magde et al. 2000] a P-wave velocity reduction of $-0.5 \text{ m/s/}^\circ\text{C}$ at temperatures below $1000 \text{ }^\circ\text{C}$, $-2.0 \text{ m/s/}^\circ\text{C}$ at temperatures above $1000 \text{ }^\circ\text{C}$ (near the solidus).

The theoretical behaviour of rock with *melt* inclusions is fairly well understood, but there is no unique method to relate in situ velocities to the proportion of melt. An estimate of the variations of several seismic parameters, among which V_p and V_s , and their dependence on the model assumptions are given for olivine and pyroxene in upper mantle conditions of temperature and pressure. Main results shows that these seismic parameters can vary over a wide range: for example, for a 10% melt, V_p and V_s can vary by 10-40 % and 20-100 %, respectively, compared with values for solid rock, depending on the assumptions on the melt geometry and phase change mechanism [Mavko 1980]. Other experiments [Murace and Mc Birney 1973] measured temperature-dependent velocities in igneous rocks. Below $800^\circ\text{-}900^\circ\text{C}$ the compressional seismic wave velocity is nearly constant at about 5-6 km/s, then, when rocks are fully melted (1200°C), the velocity decreases by 50% to 2-3 km/s.

On the other hand, in fluid saturated rocks the effect of temperature on pore fluids properties enhances the dependence of P-wave velocity with temperature, because of changes of compressibility at fluid phase transitions. This doesn't affect the shear modulus of the rock: on S wave velocity the only observable effect depends on density changes. So, what we usually observe is a low V_p/V_s in gas-bearing rocks (i.e. high fluid compressibility) and high V_p/V_s in liquid-bearing formations (i.e. low fluid compressibility). This is coherent with the 'Biot' effect, which predicts that the bulk modulus of the pore fluid acts to stiffen the pores to the deformation of the compressional wave, thus increasing the compressional velocity. Instead, there is no similar effect on the shear modulus [Biot 1956]. The saturation state has also other effects on velocities of rock. Among them the development of local-flow of the fluid in the pore spaces, which produces a frequency dependence on the measured velocity; the frame weakening of the matrix rock and a density effect on the material [Boitnott and Bonner 1994]. Moreover, high fluid pressure induces a phase transition by opening cracks, thus leading the V_p/V_s ratio to decrease. Laboratory tests for sandstones [Wang et al. 1998] and granites [Vanorio et al. 2005] model the variation of V_p/V_s as a function of pore fluid temperature and pressure to higher temperature and pressure. V_p/V_s increases moving from gas to liquid conditions, but, if crack opening occurs, there is a sudden lowering of the value for gas conditions, while the ratio grows if the rock persists liquid-saturated.

The effects of *pressure* on V_p is that of an overall increase with depth [Cerney and Carlson 1999], but it should be considered the effective pressure in spite of the lithostatic load, so taking into account the pore pressure [Carcione et al. 2003; He and Schmitt 2006] Moreover, V_p/V_s increases with pressure in saturated rocks as cracks close [Vinciguerra et al. 2005], and it has to be considered that lithostatic pressure and ductile flow are likely to close pores in the lower crust [Muller and Raab 1997].

Listed below (**Table 1**) are the general differences in V_p and V_s in porous and cracked rocks containing the listed fluids relative to the same rocks under laboratory-liked conditions [Sanders 1993].

| Seismic parameter | Water(saturated) | Steam+Water | Partial melt |
|-------------------|-------------------|--------------|--------------|
| V_p | Larger | Much smaller | Smaller |
| V_s | Unchanged/smaller | Smaller | Much smaller |
| V_p/V_s | Larger | Smaller | Larger |

Table 1 *Variations of some seismic parameters in porous or cracked rocks filled by different fluids.*

While the importance of fluid compressibility in changing V_p/V_s has been widely studied, the effect of *pore geometry* on the ratio has been identified but poorly quantified. Even for the same fluid the sign of the V_p and V_p/V_s change cannot be predicted without specifying the pore geometry. In general sense, when the porosity and liquid content are held constant, thinner voids (cracks) lower the seismic velocities significantly more than spherical pores or vesicles [Cerney and Carlson 1999]. But for V_p and V_s separately considered, a change in liquid content or in the pore aspect ratio (indicator of the shape; ~ 1 for spherical shapes, and $\ll 1$ for thin shapes) can have the same effects. However, the ratio $d\ln V_s/d\ln V_p$ is independent of the liquid content and is sensitive to changes in pore geometry. Hence, it can be used for determining the actual pore geometry in the Earth's interior [Takei 2002]. Broadly speaking, a decrease of this velocities logarithmic ratio is associated with an increase of the aspect ratio. For crustal conditions, it has been showed [Nakajima et al. 2001] that low V_p and low V_p/V_s can be caused by inclusions of H_2O with a relatively large aspect ratio and that low V_p and high V_p/V_s is almost surely caused by melt inclusions.

The general framework of these relationships can be used to decide which seismic parameter is the most efficient in an experiment aimed to imagine a particular crustal environment. For example, in ancient volcanic regions, the V_p alone can be indicative of relic magma chamber, while adjunctive V_p/V_s measurements are needed to distinguish between a region of partial melt and regions of geothermal fluids [Nakajima et al. 2001]. Interestingly, V_p/V_s ratio is very sensitive to factors that may change with time: parameters like the degree of fracturing, the gas content, and the amount of partial melt can vary significantly with time, compelling the generation of 'real time' or 4D-tomographic models [Patane et al. 2006].

1.2.3. Active and passive seismic tomography

In the last decades, first arrival time tomography has been applied to imagine the interiors of volcanic edifices and to gain a better knowledge in the processes acting during an eruption. In most cases the seismic experiments carried out in volcanic areas have been of passive type, with local earthquakes as sources. This is the case, among others, for Vesuvio [De Natale et al. 2004; Scarpa et al. 2002], Campi Flegrei [Vanorio et al. 2005], Taupo [Sherburn et al. 2003], Kilauea [Hansen et al. 2004] and Piton de la Fournaise [Nercessian et al. 1996].

Recently, active seismic experiments have spread out, substituting or sustaining contemporary passive data recording. More often, the information from these surveys have been used to integrate the previous knowledge of the volcano seismic structure. Active tomography have been done at the cited volcanoes, i.e.: Vesuvio [Zollo et al. 2002], Campi Flegrei [Zollo et al. 2003], Taupo [Harrison and White 2006], Kilauea [Morgan and Zelt 2006] and Piton de la Fournaise (Lankar, 1997). The input data for these studies are body wave arrivals from active sources, borehole explosions on land or airgun shots offshore.

Hence, when a volcano has to be investigated by seismic tomography means, both techniques have to be carefully considered, in terms of their advantages and related problems. Several aspects should be taken into account, regarding the information accessible by using each technique and its cost, in terms of resolution, time-consuming, and economic impact.

Generally, the detailed structure of the volcano edifice is hard to image with natural seismicity because it suffers, among other problems, from a poor distribution of sources, poorly knowledge of ray geometry and source locations. The *distribution* of seismic events below many volcanoes is uneven. If local sources (the volcano earthquakes) are strongly clustered, most of the seismic rays travel parallel across the region of interest and do not sample it in a homogeneously distributed pattern, as expected by crisscrossing seismic paths. From the point of view of *the inversion formalism*, the complexity of the mathematical problem is increased because source parameters (location and origin time) have to be found out together with the velocity structure, so augmenting the unknowns' number. For the same reason, the non-linearity of the inversion scheme raises simultaneously with the uncertainty of the source location (see Chapter 2.2.1.). As additional problem of the passive tomography, the database available is often inadequate in its *amount*. In fact, the seismic activity of

many volcanoes is low, as number and magnitude of volcano-tectonic earthquakes, if compared with other types of volcanic signals (such as tremor, long period, explosions). This implies that data of a large time interval have to be gathered together to collect a considerable amount. This is quite a common approach to obtain a considerable dataset, to finally perform a high resolution tomography, as needed to imagine small volcanic structures. Unfortunately, this procedure can join together data that possibly are not 'compatible'. Observations proceeding from several years of natural seismic activity probably are due to a seismic structure that has been evolving in that interval, and hence they cannot testify a true, unique structural state. Last, but not least, active volcanoes poses serious *practical problems* in the maintenance of a stable station network to record natural seismic activity for a long period. Beside the intrinsic risk of working in active volcanic areas and consign it expensive instruments, volcanoes have often extreme topography and are located in hardly accessible regions.

One possible way to circumvent some of these problems is to use active seismic sources and deploy a dense seismic array of stations above and around the volcano, in order to gain the necessary sources-receivers *distribution*. By artificially establishing the positions of seismic stations and artificial sources, it can be easily gained a stable and well distributed ray paths coverage. Hence, the first notable advantage of this method stays in the good lateral and temporal resolution which is possible to gain. Moreover, this kind of experiment guarantees a considerable *amount* of data in a short interval of time. For this property, unlikely passive experiments, they return data as in a snapshot of the seismic structure, steady only for a short interval. Furthermore, the recourse to active sources in local seismic tomography is considered really efficient from the *mathematical point* of view because their use minimizes the complication that inversion tomography finds in the location of natural sources in an unknown velocity structure.

On the opposite, the *signal* produced in these experiments frequently only permits a P-wave first arrival tomography (beside, eventual waveform studies or the use of vibrators as surface wave sources), which does not supply any indication on V_s/V_p ratio distribution. Another major problem in using explosions or airgun shots can be given by the occurrence of natural seismicity. Usually shot positions are few and not repeatable. If the signal is disturbed by a volcanic event, which are often in the same frequency range, the data of this shot can probably not be used in the inversion. But the greatest difficulty in active tomography relates with the spatial distribution of ray paths in *depth*: typically, seismic waves do not travel deep and final resolution can be as high as desired but constrained to shallower crustal levels. Finally, an active source experiment imposes a critical evaluation of the planning difficulties and *economic* impact, especially when source

firing implies a larger number of stations, their deployment in wild regions, the use of a large amount of explosive, ship managing and eventually drilling.

1.2.4. An example

Plenty of tomography studies applied at volcanic areas have been carried out during last years. Their results obviously depend on the uniqueness of each situation, and here we can only outline the commonest conclusions obtained. Both high and low velocity anomalies have been detected inside volcanic edifices or across volcanic areas. In general, the following relationships are by far prevalent in the literature:

- (1) high velocity with high-strength magmatic rocks : cumulates, dike structures, frozen magma chambers. (Etna [Aloisi et al. 2002; Patane et al. 2002; Villaseñor et al. 1998]; Vesuvio [De Natale et al. 2004]; Ascension Island [Evangelidis et al. 2004]; Kilauea [Haslinger et al. 1999]; Tungurahua [Molina et al. 2005]; Piton de la Fournaise [Nercessian et al. 1996]; Unzen [Ohmi and Lees 1995]; Vesuvio [Scarpa et al. 2002]; Taupo volcanic zone [Sherburn et al. 2003]; Bandai [Yamawaki et al. 2004]
- (2) high velocity with caldera rim formations (Rabaul caldera [Finlayson et al. 2003]; Campi Flegrei [Judenherc and Zollo 2004; Vanorio et al. 2005; Zollo et al. 2003]
- (3) low velocity with partial melt volumes, magma chambers (Rabaul caldera [Finlayson et al. 2003]; Kilauea [Haslinger et al. 1999]; Yellowstone [Husen et al. 2004]; Ridge segments [Magde et al. 2000]
- (4) low velocity with low density deposits (Ascension Island [Evangelidis et al. 2004]; Toba caldera [Masturyono et al. 2001]; Taupo volcanic zone [Sherburn et al. 2003]; Bandai [Yamawaki et al. 2004]; Campi Flegrei [Judenherc and Zollo 2004]
- (5) low velocity with thermally altered, highly fractured, geochemically modified volumes (Etna [Aloisi et al. 2002]; Redoubt [Benz et al. 1996]; Tungurahua [Molina et al. 2005]; Piton de la Fournaise [Nercessian et al. 1996]; Unzen [Ohmi and Lees 1995]; Spurr [Power et al. 1998]
- (6) high Vp/Vs with partial melt volumes, magma in variable amount (Nevado del Ruiz [Londono and Sudo 2003]; Toba caldera [Masturyono et al. 2001], Onikobe volcanic area [Nakajima and Hasegawa 2003]
- (7) high Vp/Vs with water-filled fractures (Vesuvio [Scarpa et al. 2002]); Campi Flegrei [Vanorio et al. 2005]
- (8) low Vp/vs with gas-filled fractures rocks (Kilauea [Hansen et al. 2004]; Yellowstone [Husen et al. 2004]; Nevado del Ruiz [Londono and Sudo 2003]; Onikobe volcanic area [Nakajima and Hasegawa 2003], Etna [Patane et al. 2006; Patane et al. 2002]; Campi Flegrei [Vanorio et al. 2005]

In few cases these results have been obtained using both tomographic techniques, active and passive, in the same volcanic region.

Among these few cases, we consider of special interest the application to Campi Flegrei caldera, for its structural analogy with several tectonic features of our studied regions. This is a remarkable example of tomography carried out at a volcanic caldera with strong geothermal activity, in a sea-facing setting, and a complex history of tectonic evolution.

Campi Flegrei

Campi Flegrei is a resurgent caldera located 15 km west of Naples, Southern Italy. Its formation is related to two main explosive eruptions (37-39000 and 12000 ybp,[Civetta et al. 1997]), followed by other smaller eruptions until the most important recent event which occurred in 1538. Since then, the caldera has been sinking, apart two resurgence episodes in 1970-72 and 1982-1984. An intense hydrothermal activity is observed in the zone, delineating the limits of ancient calderas rims. This activity motivated the onset of geothermal explorations and boreholes perforation in the zone.

The structure of the caldera has been studied with local earthquakes tomography (Aster and Meyer, 1988). The seismic image revealed the structure of a caldera filled by a few km thick layers of volcanic deposits, with low V_p , high V_p/V_s and high P-wave attenuation. The possible presence of a magma reservoir at about 4-5 km of depth was suggested instead by extrapolation at depth of temperature data and teleseismic observations [Ferrucci et al. 1992].

An active seismic survey was carried out in the gulfs of Naples and Pozzuoli to better constrain the seismic structure of this caldera, during September, 2001 [Zollo et al. 2003]. About 5000 shots were fired and 62 sea bottom and 72 land seismometers were deployed in the area. A total of 90000 P-wave first arrival times were introduced in the inversion algorithm. The resolved volume extended to a depth of 3.5 km for wider structures, with inversion cells of 0.25 to 1 km of dimensions. The most prominent resolved structure (**Figure 1.1**) is an arc-like high P-wave velocity anomaly ($V_p=3.5-4.0$ km/s) which is interpreted as a caldera rim and whose existence is confirmed by a positive gravity anomaly. It is detected at about 0.8-2 km depth, with a diameter of about 8-12 km and a height of 1-2 km. According to stratigraphic data, the rim is likely formed by solidified lavas or/and tuffs with interbedded lava. The presence of melt is excluded due to the velocity range of the tomographic image, at least until the limit of resolved depths.

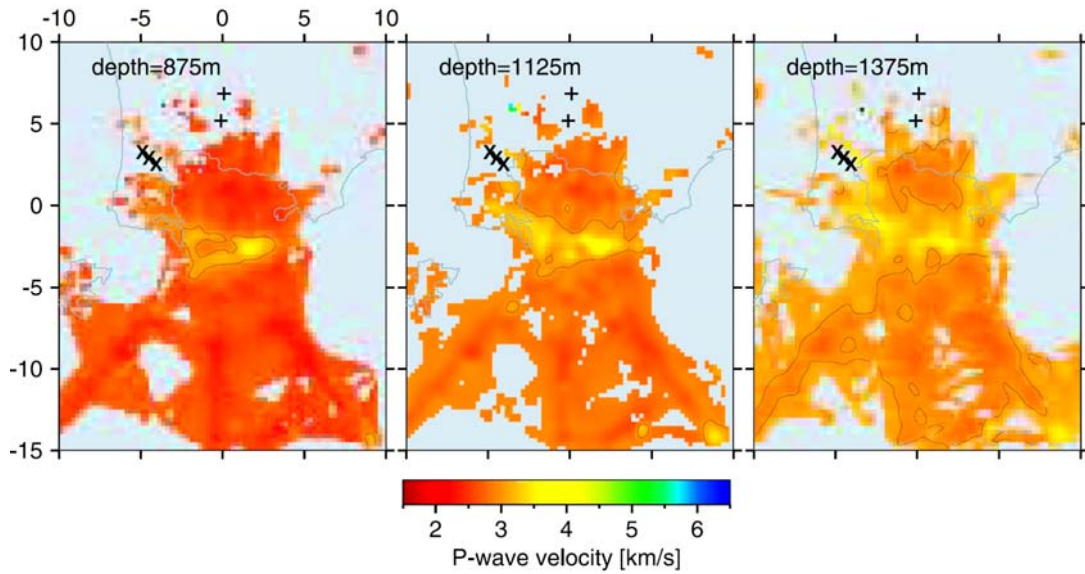


Figure 1.1 Map view of P-wave velocity at three different depths (875 m, 1125 m and 1375 m, from left to right). The coastline is outlined in gray. The crosses indicate positions of geothermal wells. From Zollo et al. (2003)

To the same dataset was later [Judenherc and Zollo 2004] included that proceeding from a previous experiment in the Vesuvio area. The amount of raypaths crossing the region increased (to a total of 95000 observations) and the cell dimension for the tomographic inversion was 0.25 km for the caldera zone. The maximum depth for resolved structures in the caldera reaches 2 km. The velocity distribution is compared with in situ density and lithology analyses, and the geological structure of the area is determined (**Figure 1.2**). The high velocity perturbation (+0.5/1 km/s) marking the caldera rim is confirmed between 0.75 and 2 km of depth. , and it is associated with a density around 2.4 g/cm^3 ($V_p > 3.5 \text{ km/s}$) and trachytic lavas and tuffites with interbedded lavas. The infilling shows otherwise a density of about 2.2 g/cm^3 ($V_p < 3 \text{ km/s}$), and it is mainly composed by pyroclastic rocks, tuffs and chaotic tuffites. The collapse dimension of the caldera

is estimated around 1.2 km. Interestingly, normal faults affecting the underlying carbonatic basement (at 3-4 km depth) are imaged. They are observed as vertical offset of the >5.5 km/s velocity contour and are interpreted as preferred routes for magma upwelling, in the absence of a resolved shallow reservoir.

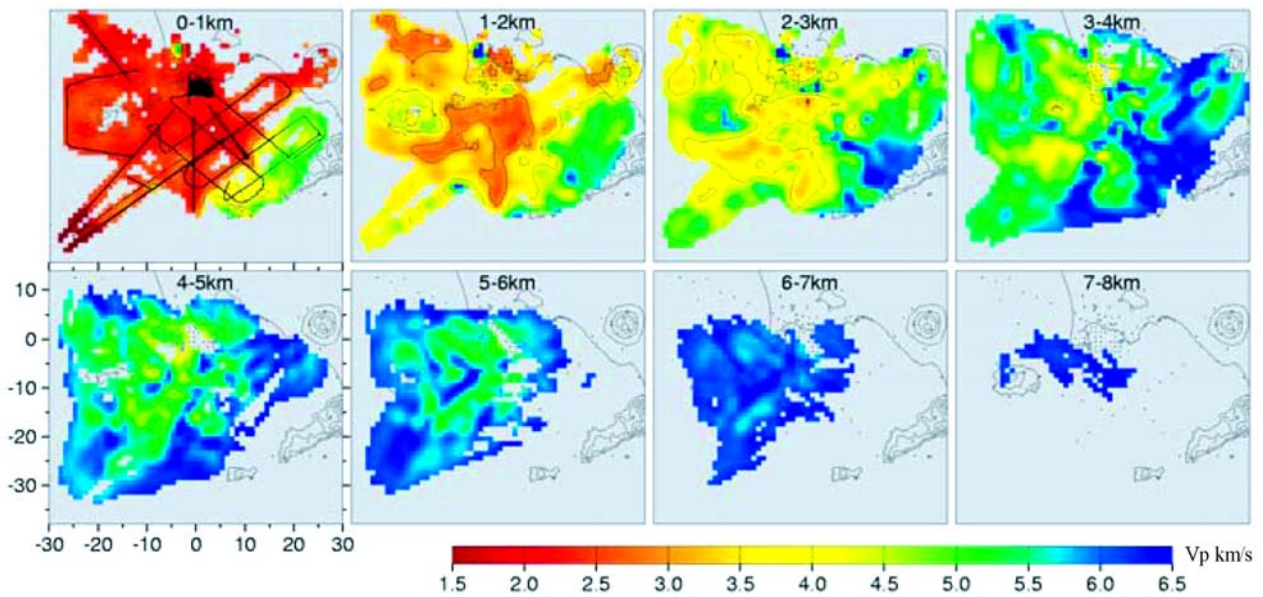


Figure 1.2 Map view of P-wave velocity at several depths (indicated in figures as top and bottom depths). The topography is outlined in gray with contour interval of 500m. The black lines indicate shot locations. From Judenherc et al. (2003)

A 3D seismic traveltime tomography of the same area was performed few years later [Vanorio et al. 2005] by inverting simultaneously P-wave and S-wave first arrival times for both velocity and hypocenter locations with 462 microearthquakes data. The grid spacing was 0.5 km and the resolved volume extended 5-6 km in depth. The map of V_p (**Figure 1.3**) and of the $V_p \cdot V_s$ product shows a high value ($V_p > 4.8$ km/s and $V_s > 2.8$ km/s) horseshoe-shaped located at 2

km of depth. Again, this anomaly is indicated as the on-land remainder of the caldera rim, whose below-sea-level had been detected by the active tomography [Zollo et al. 2003]. As adjunctive results, a low velocity anomaly (V_p between 1.7 and 3.8 km/s, V_s between 1.0 and 2.5 km/s) dominated at surface by caldera-infilling material is imaged within the high velocity. To understand this anomaly, the ratio V_p/V_s is imaged. It reveals a centered high V_p/V_s at 1.5 km of depth surrounded by a low V_p/V_s which shows a flat feature at 4 km depth beneath the city of Pozzuoli. The interpretation for this low V_p/V_s anomaly indicates this zone as a overpressured gas-bearing rocks at supercritical conditions. The low ratio, moreover, lets exclude the presence of melt down to 4-5 km depth. In contrast, the shallower higher V_p/V_s anomaly at 1 km suggests the presence of rocks containing fluids in the liquid phase.

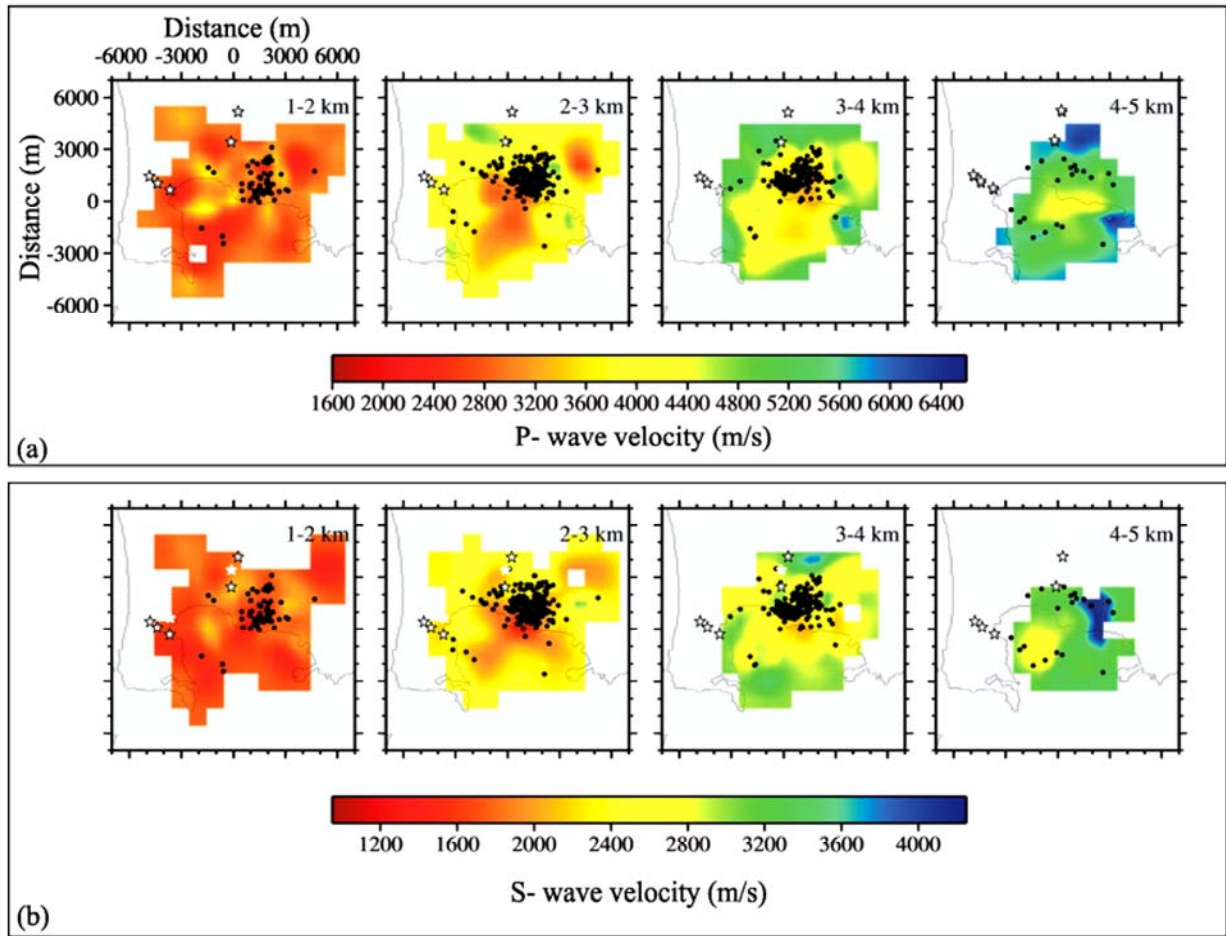


Figure 1.3 Map view of P-wave velocity (a) and S-wave velocity (b) at four different depth intervals. The coastline is outlined in gray. The black circles and black stars indicate earthquakes and well locations. From Vanorio et al. (2005).

1.3. References

- Aloisi, M., Cocina, O., Neri, G., Orecchio, B., and Privitera, E., 2002, Seismic tomography of the crust underneath the Etna volcano, Sicily: *Physics of the Earth and Planetary Interiors*, v. 134, p. 139-155.
- Barclay, A. H., and Solomon, S., 1998, Seismic Structure and crustal magmatism at the Mid-Atlantic Ridge, 35N: *Journ. Geophys. Res.*, v. 103, p. 17827-17844.
- Benz, H. M., Chouet, B. A., Dawson, P. B., Lahr, J. C., Page, R. A., and Hole, J. A., 1996, Three dimensional P and S wave velocity structure of Redoubt Volcano, Alaska: *J. Geophys. Res.*, v. 101, p. 8111-8128.
- Biot, M. A., 1956, Theory of propagation of elastic waves in a fluid-saturated porous solid: I. Low-frequency range, II. Higher frequency range: *J. Acous. SOC. Amer.*, v. 28, p. 168-191.
- Boitnott, G. N., and Bonner, B. P., 1994, Characterization of rock for constraining reservoir scale tomography at the Geysers geothermal field: *Nineteenth Workshop on Geothermal Reservoir Engineering*, p. 231-236.
- Bonner, B., Robert, J., Duba, A., and Kasameyer, P., 1998, *Laboratory Studies of Geyser Rock and Impacts on Exploration*, Lawrence Livermore National Laboratory.
- Cañon-Tapia, E., and Walker, G. P. L., 2004, Global aspects of volcanism: the perspectives of “plate tectonics” and “volcanic systems”: *Earth-Science Reviews*, v. 66, p. 163–182.
- Carcione, J. M., Helbig, K., and Helle, H. B., 2003, Effects of pressure and saturating fluid on wave velocity and attenuation in anisotropic rocks: *International Journal of Rock Mechanics & Mining Sciences*, v. 40, p. 389–403.
- Cerney, B., and Carlson, R. L., 1999, The effect of cracks on the seismic velocities of basalt from site 990, Southeast Greenland Margin: *Ocean Drilling Program Results*.
- Civetta, L., Orsi, G., Pappalardo, L., Fisher, R. V., Heiken, G., and Ort, M., 1997, Geochemical zoning, mingling, eruptive dynamics and depositional processes-the campanian ignimbrite, Campi Flegrei caldera: *J. Volc. Geotherm. Res.*, v. 75, p. 183-219.
- Chouet, B. A., 2003, *Volcano Seismology: Pure Appl. Geophys.*, v. 160, p. 739-788.
- Christensen, N. I., 1996, Poisson’s ratio and crustal seismology: *J. Geophys. Res.*, v. 101, p. 3139-3156.
- De Natale, G., Troise, C., Trigila, R., Dolfi, D., and Chiarabba, C., 2004, Seismicity and 3-D substructure at Somma-Vesuvius volcano:evidence for magma quenching: *Earth Planet. Sci. Lett.*, v. 221, p. 181-196.
- Dunn, R. A., and Toomey, D. R., 2001, Crack-induced seismic anisotropy in the oceanic crust across the East Pacific Rise (9°30’N): *Earth Planet. Sci. Lett.*, v. 189, p. 9-17.
- Evangelidis, C. P., Minshull, T. A., and Henstock, T. J., 2004, Three-dimensional crustal structure of Ascension Island from active source seismic tomography.: *Geophys. J. Int.*, v. 159, p. 311-325.
- Fehler, M., House, L., Scott-Phillips, W., and Potter, R., 1998, A method to allow temporal variation of velocity in travel-time tomography using microearthquakes induced during hydraulic fracturing: *Tectonophysics*, v. 289, p. 189-201.
- Ferrucci, F., Hirn, A., Virieux, J., De Natale, G., and Mirabile, L., 1992, P-sv conversions at a shallow boundary beneath Campi Flegrei caldera (Naples, Italy): Evidence for the magma chamber: *J. Geophys. Res.*, v. 97, p. 351-359.

- Finlayson, D. M., Gudmundsson, O., Itikarai, I., Nishimura, Y., and Shimamura, H., 2003, Rabaul volcano, Papua New Guinea: seismic tomographic imaging of an active caldera: *Journ. Volc. Geotherm. Res.*, v. 124, p. 153-171.
- Foulger, G. R., and Arnott, S. K., 1993, Local tomography: volcanoes and the accretionary plate boundary in Iceland, *in* Iyer, H. M., and Hirahara, K., eds., *Seismic Tomography: Theory and practice*, London, Chapman & Hall.
- Goldstein, P., and Chouet, B., 1994, Array measurements and modelling of sources of shallow volcanic tremor at Kilauea volcano, Hawaii: *J. Geophys. Res.*, v. 99, p. 2637-2652.
- Hansen, S., Thurber, C., Mandernach, M., Haslinger, F., and Doran, C., 2004, Seismic velocity and attenuation structure of the East Rift Zone and South flank of Kilauea volcano, Hawaii.: *Bull. Seism.Soc.Am*, v. 4, p. 1430-1440.
- Harrison, A., and White, R. S., 2006, Lithospheric structure of an active backarc basin: the Taupo Volcanic Zone, New Zealand: *Geophys. J. Int.*, v. 167, p. 968-990.
- Haslinger, F., Kissling, E., Ansoerge, J., Hatzfeld, D., Papadimitriou, E., Karakostas, V., Makropoulos, K., Kahle, H. G., and Peter, Y., 1999, 3D crustal structure from local earthquake tomography around the Gulf of Arta (Ionian region, NW Greece): *Tectonophysics*, v. 304, p. 201-218.
- He, T., and Schmitt, D., 2006, P and S- wave velocity measurements and pressure sensitivity analysis of AVA response, CSPG-CSEG-CWLS Convention.
- Husen, S., Smith, R. B., and Waite, G. P., 2004, Evidence for gas and magmatic sources beneath the Yellowstone volcanic field from seismic tomographic imaging: *Journal of Volcanology and Geothermal Research*, v. 131, p. 397-410.
- Iyer, H. M., and Dawson, P. B., 1993, Imaging volcanoes using teleseismic tomography, *in* Iyer, H. M., and Hirahara, K., eds., *Seismic tomography: Theory and practice*, London., Chapman & Hall.
- Iyer, H. M., and Hirahara, K., 1993, *Seismic tomography : theory and practice*: London ; New York, Chapman & Hall, xvii, 842 p. p.
- Judenherc, S., and Zollo, A., 2004, The Bay of Naples (southern Italy): Constraints on the volcanic structures inferred from a dense seismic survey: *J. Geophys. Res.*
- Julian, B. R., Ross, A., Foulger, G. R., and Evans, J. R., 1996, Three dimensional seismic image of a geothermal reservoir: The Geysers, California: *Geophys.Res. Lett.*, v. 23, p. 6685-6688.
- Kious, J. W., and Tilling, R. I., 1996, *The Dynamic Earth:the story of plate tectonics*: General Interest Publications, Bernan Assoc., 76 p.
- Kissling, E., 1988, Geotomography with local earthquakes data: *Rev.Geophys.*, v. 4, p. 659-698.
- Lees, J. M., and Wu, H., 2000, Poisson's ratio and porosity at Coso geothermal area, California: *J. Volcanol. Geotherm. Res.*, v. 95, p. 157-173.
- Londono, J. M., and Sudo, Y., 2003, Velocity structure and a seismic model for Nevado del Ruiz Volcano (Colombia): *Journal of Volcanology and Geothermal Research*, v. 119, p. 61-87.
- Magde, L. S., Barclay, A. H., Toomey, D. R., Detrick, R. S., and Collins, J. A., 2000, Crustal magma plumbing within a segment of the Mid-Atlantic Ridge, 35° N: *Earth Planet. Sci. Lett.*, v. 175, p. 55-67.
- Masturyono, R., McCaffrey, D., Wark, S., Roeker, F., Ibrahim, G., and Sukhyar, 2001, Distribution of magma beneath the Toba caldera complex, north Sumatra, Indonesia, constrained by three-dimensional P wave velocities, seismicity, and gravity data: *Geochem. Geophys. Geosyst.*
- Mavko, G. M., 1980, Velocity and attenuation in partially molten rocks: *J. Geophys. Res.*, v. 85, p. 5173-5189.
- McNutt, S. R., 2005, *Volcanic Seismology*: *Annu. Rev. Earth Planet. Sci.*

- Molina, I., Kumagai, H., Le Pennec, J.-L., and Hall, M., 2005, Three-dimensional P-wave velocity structure Tungurahua Volcano, Ecuador: *J. Volc. Geotherm. Res.*, v. 147, p. 144-156.
- Morgan, J. K., and Zelt, C. A., 2006, 3D seismic velocity structure of Hawaii from onshore-offshore tomography.
- Muller, H. J., and Raab, S., 1997, Elastic wave velocity of granite at experimental simulated partial melting conditions: *Phys. Chem. of the Earth*, v. 22, p. 93-96.
- Murace, T., and Mc Birney, A. R., 1973, Properties of some common igneous rocks and their melt at high temperatures: *Geol. Soc. Am. Bull.*, v. 84, p. 3563-3593.
- Nakajima, J., and Hasegawa, A., 2003, Tomographic imaging of seismic velocity structure in and around the Onikobe volcanic area, northeastern Japan: implications for fluid distribution: *Journal of Volcanology and Geothermal Research*, v. 127, p. 1-18.
- Nakajima, J., Matsuzawa, T., Hasegawa, A., and Zhao, D., 2001, Seismic imaging of arc magma and fluids under the central part of northeastern Japan: *Tectonophysics*, v. 341, p. 1-17.
- Nercessian, A., Hirn, A., Lepine, J. C., and Sapin, M., 1996, Internal structure of Piton de la Fournaise volcano from seismic wave propagation: *J. Volc. Geotherm. Res.*, v. 70, p. 125-143.
- Ohmi, S., and Lees, J. M., 1995, Three-dimensional P- and S-wave velocity structure below Unzen volcano: *J. Volc. Geotherm. Res.*, v. 65, p. 1-26.
- Patane, D., Barberi, G., Cocina, O., De Gori, P., and Chiarabba, C., 2006, Time-Resolved Seismic Tomography Detects Magma Intrusions at Mount Etna: *Science*, v. 313, p. 821-823.
- Patane, D., Chiarabba, C., Cocina, O., De Gori, P., Moretti, M., and Boschi, E., 2002, Tomographic images and 3D earthquake locations of the seismic swarm preceding the 2001 Mt. Etna eruption: Evidence for a dyke intrusion: *Geophys. Res. Lett.*, v. 29.
- Power, J. A., Villaseñor, A., and Benz, H. M., 1998, Seismic image of the Mount Spurr magmatic system: *Bull. Volcanol.*, v. 60, p. 27-37.
- Rawlinson, N., and Sambridge, M., 2001, Seismic travelttime tomography of the crust and lithosphere: *Advances in Geophysics*, v. 46, p. 81-197.
- Ripperger, J., Igel, H., and Wasserman, J., 2003, Seismic wave simulation in the presence of real volcano topography: *Journ. Volcan. Geotherm. Res.*, v. 128, p. 31-44.
- Roy, L., Sen, M. K., McIntosh, K., Stoffa, P. L., and Nakamura, Y., 2005, Joint inversion of first arrival seismic travelttime and gravity data: *J. Geophys. Res.*, v. 2, p. 277-289.
- Sanders, C. O., 1993, Local earthquakes tomography: attenuation-theory and results, *in* Iyer, H. M., and Hirahara, K., eds., *Seismic tomography: Theory and practice.*, London, Chapman & Hall.
- Scarpa, R., Tronca, F., Bianco, F., and Pezzo, E. D., 2002, High resolution velocity structure beneath Mount Vesuvius from seismic array data: *Geophys. Res. Lett.*
- Sherburn, S., Bannister, S., and Bibby, H., 2003, Seismic velocity structure of the central Taupo Volcanic Zone, New Zealand, from local earthquake tomography: *Journal of Volcanology and Geothermal Research*, v. 122, p. 69-88.
- Smith, K., 2004 *Environmental Hazards: assessing risk and reducing disaster*: Routledge.
- Takei, Y., 2002, Effect of pore geometry on Vp/Vs: From equilibrium geometry to crack: *J. Geophys. Res.*, v. 107, p. 10.1029/2001JB000522.
- Thurber, C., and Aki, K., 1987, Three-dimensional seismic imaging: *Ann. Rev. of Earth and Planet. Sci.*, v. 15, p. 115-139.

- Toomey, D. R., Joussetin, D., Dunn, R. A., Wilcock, W. S. D., and Detrick, R. S., 2007, Skew of mantle upwelling beneath the East Pacific Rise governs segmentation: *Nature*, v. 446, p. 409-414.
- Vanorio, T., Virieux, J., Capuano, P., and Russo, G., 2005, Three dimensional seismic tomography from P wave and S wave microearthquake travel times and rock physics characterization of the Campi Flegrei Caldera.: *J. Geophys. Res.*, v. 110.
- Villaseñor, A., Benz, H. M., Filippi, L., De Luca, G., Scarpa, R., Patanè, G., and Vinciguerra, S., 1998, Three-dimensional P-wave velocity structure of Mt Etna, Italy: *Geophys. Res. Lett.*, v. 25, p. 1975-1978.
- Vinciguerra, S., Trovasto, C., Meredith, P. G., and Benson, P. M., 2005, Relating seismic velocities, thermal cracking and permeability in Mt. Etna and Iceland basalts: *Int. Journ. Rock Mech. Min. Sc.*, v. 42, p. 900-910.
- Wang, Z., Cates, M. E., and Langan, R. T., 1998, Seismic monitoring of a CO₂ flood in a carbonate reservoir: A rock physics study: *Geophysics*, v. 63, p. 1604-1617.
- Wegler, U., and Luehr, B. G., 2001, Scattering behaviour at Merapi volcano (Java) revealed from an active seismic experiment: *Geophys. J. Int.*, v. 145, p. 579-592.
- Winkler, K. W., and Murphy, W. F., 1995, Acoustic velocity and attenuation in Porous Rocks. *Rock Physics and Phase Relations. A handbook of physical constants.*, *Agu reference shelf*, p. 20-34.
- Yamawaki, T., Tanaka, S., Ueki, S., Hamaguchi, H., Nakamichi, H., Nishimura, T., Oikawa, J., Tsutsui, T., Nishi, K., Shimizu, H., Yamaguchi, S., Miyamachi, H., Yamasato, H., and Hayashi, Y., 2004, Three-dimensional P-wave velocity structure of Bandai volcano in northeastern Japan inferred from active seismic survey: *Journal of Volcanology and Geothermal Research*, v. 138, p. 267-282.
- Zollo, A., D'Auria, L., De Matteis, R., Herrero, A., Virieux, J., and Gasparini, P., 2002, Bayesian estimation of the 2D Pvelocity models from active seismic arrival time data: imaging of the shallow structure of Mt Vesuvio (Southern Italy) *Geophys. J.Int.*, v. 151, p. 566-582.
- Zollo, A., Judenherc, S., Auger, E., D'Auria, L., Virieux, J., Capuano, P., Chiarabba, C., de Franco, R., Makris, J., Michelini, A., and Musacchio, G., 2003, Evidence for buried rim of Campi Flegrei caldera from 3-d active seismic imaging: *Geophys.Res. Lett.*, v. 30.

2. Theory and Principles

Seismic waves have the ability to sample the Earth's elastic (and anelastic) properties where they propagate, and seismic tomography is the basic tool to reveal the structure of the medium crossed by their propagation paths. The propriety whose heterogeneity is revealed, depends on the wave type considered. For surface waves variations are observed in the dispersion, for free oscillations in the resonance frequencies. For body waves the travel times are typically the subject of study. Moreover, there are several different methods to image the structure of Earth's interiors. In all of them, complex algorithms must manage, with mathematical tools, the intrinsic complexity of natural phenomena [Thurber and Aki 1987].

In the following, we introduce only the general principles of seismic *traveltime* tomography, with few mathematical baselines. We focus on the concepts of model parameterization, on the techniques to determine traveltimes, the inversion schemes and some methods to analyze solution robustness. We then furnish some additional details for these codes that we use in our work and which are specially suited for seismic traveltime tomography using *local earthquakes* data.

Before coping with the seismic structure determination, we introduce the *earthquake location* problem. Actually, precise earthquakes locations constitute a basic requirement for the study of the seismicity of a region. But at the same time, they respond to a primary requisite for tomography applied to local seismic data of natural origin. In these cases, as we are going to see later, the definition of the seismic structure implies the solution of two coupled problems, i.e. earthquakes location and seismic velocity definition [Kissling 1988]. As preliminary conditions to solve the tomographic problem, both an earthquakes location and a starting velocity model not too different from the true ones are required. From here, the need for precise hypocenters determination and the development of algorithms able to quickly supply them as starting locations to the tomography code.

2.1. . Locating Earthquakes

The earthquake location problem in a known velocity structure is a typical inverse problem. Here, for each earthquake there are four unknowns (t_0 , x , y , z), while data are represented by arrival times for P and S-waves in several stations. The problem, as introduced since Geiger work (1910, [Haslinger 1998]) is resolved by minimizing the travel time residuals, ΔT , intended as differences between observed arrival times (T_{obs}) and predicted arrival times (T_{pre}), calculated for an assumed velocity model. The approach followed by the Geiger's method requires, with the starting velocity structure, also a first guess for the hypocenters parameters. Several comprehensive discussions for the earthquake localization problem can be found in literature [Lay and Wallace 1995].

In principle, four observations would be enough to solve the determination of the four parameters of one earthquake, being the four unknowns included in each observation. In reality the observed traveltimes are affected by errors and, to obtain an estimate as close as possible to the true solution of the system, the number of data has to be greater than the number of unknowns, four in this case.

Moreover, the problem itself is not linear: the travel time T_{obs} is a function of the four hypocentral parameters $T_{obs} = f(t_0, x, y, z)$ but f normally cannot be expressed as a linear combination of independent functions each dependent on only one hypocentral parameter. This means that these parameters cannot be independently resolved (for example, there is coupling between depth and origin time). Direct solutions of nonlinear problems are not possible. To solve this kind of problem, usually they have to be linearized and iteratively solved. But to do that, the initial guess has to be as close as possible to the true solution.

The earthquake location algorithm implemented in *NLloc* location programs package [Lomax et al. 2000] follows a probabilistic formulation of the inversion [Tarantola 1987; Tarantola and Valette 1982]. This formulation relies on the use of probability density functions to express our knowledge about the values of parameters. In earthquakes location, the unknowns are the hypocentral coordinates and the origin time; the observed data are a set of arrival times and the theoretical relation between them gets predicted traveltimes. With the assumption that theoretical relationship and observed arrival time have Gaussian uncertainties, Tarantola and Valette show that it is possible to evaluate analytically the probability density function or the misfit function, which can be expressed by

$$g(\mathbf{x}) = [\mathbf{t}_0 - \mathbf{h}(\mathbf{x})]^t (\mathbf{C}_t + \mathbf{C}_T)^{-1} [\mathbf{t}_0 - \mathbf{h}(\mathbf{x})] \quad (1)$$

where $g(\mathbf{x})$ is the misfit function, \mathbf{x} is the vector of hypocentral coordinates, \mathbf{t} is a set of observed arrival times, \mathbf{h} is a set of predicted travel times. \mathbf{C}_T and \mathbf{C}_t are covariance matrices of theoretical and observed times. The exponential of this misfit function makes part, multiplied by a $\rho(\mathbf{x})$ density function of prior information on the model parameters, of the expression for the posterior density function (*PDF*). It represents a complete, probabilistic solution to the location problem, including information on uncertainty and resolution. This solution doesn't require a linearized theory and the resulting *PDF* may be irregular and multi-modal because the forward calculation involves a non-linear relationship between hypocenter location and travel times. Actually, the travel times between each station and all nodes of an x , y , and z spatial grid are calculated once using a 3D version of the Eikonal finite-difference scheme [Podvin and Lecomte 1991], and later stored as travel time grid files. The forward calculation reduces to retrieving the travel times from the grid files and calculating the misfit function, i.e. the function which represents the distance between observed and calculated traveltimes. In this way, the 4D problem of hypocenter location becomes a 3D search over x , y , z , space.

This *PDF* function is determined systematically over a 3D space by an oct-tree importance sampling algorithm. It recursively subdivides and samples cells in 3D space to generate a cascade of sampled cells, considering the *PDF* values of the cell centre as leading factor to successive subdivisions. The probability that an earthquake location is in a given cell I is approximately

$$P_i = V_i PDF(x_i) \quad (2)$$

where V_i is the cell volume and x_i is the coordinates of the cell centre. The procedure starts with a global sampling of the full space on a coarse grid; then the cell with the largest probability P_{max} is obtained and subdivided into 8 child-cells, and the process is repeated for the child-cell with the P_{max} . This recursive procedure converges rapidly, producing an oct-tree structure of cells specifying location *PDF* in 3D space (**Figure 2.1**). The oct-tree procedure samples a larger number of cells in the regions of higher *PDF* and thus through the distribution of the visited cells gives an approximate idea of the *PDF* values importance and a useful and compact representation of the *PDF* itself.

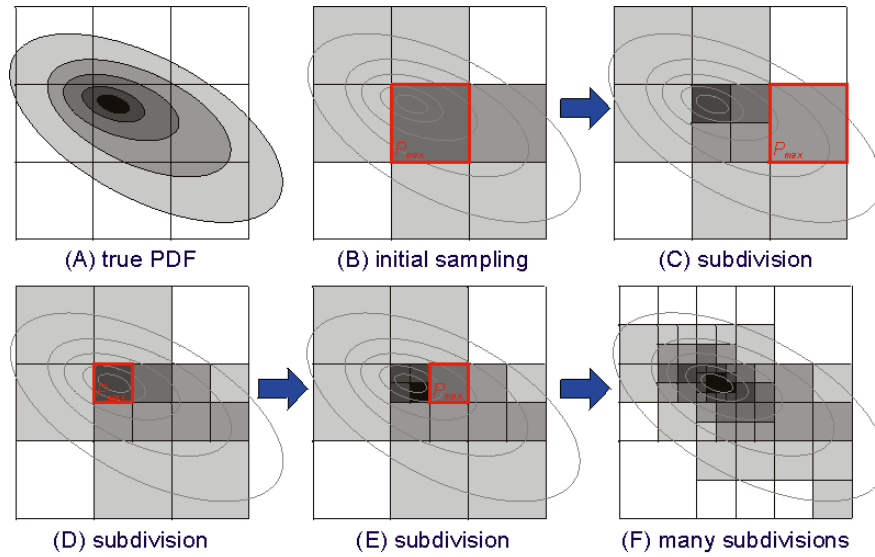


Figure 2.1 Oct-tree sampling. The algorithm searches recursively the cells with the highest Probability Density Function in a 3D space. Only 2D section are represented. From Lomax et al.(2000).

2.2. *Velocity Model*

If enough independent data (observations from a set of earthquakes) are available, it becomes feasible adding more unknown parameters to the system of linear equations made up for each hypocenter location, like velocities of the medium. This finally lets us introduce our tomography problem. In the case of seismic signals proceeding from artificial bursts, the location unknowns are obviously spared as they are fixed and the exploration is for the velocity structure alone.

With the introduction of these extra parameters, the non-linearity of the problem is additionally increased and also the mathematical complexity of its solution. Usually, the location and velocity problems are not contemporaneously solved, and, instead, a stepwise approach is used [Thurber 1983]. The two inverse problems are separated and separately solved. The basic principles of location problem solution have already been described in Chapter 2.1. In the following, we focus on the velocity structure problem. In particular, we are interested to both the inversions for 1D and 3D velocity model.

As we said, the strong non linearity of the 3D velocity inversion algorithm requires, besides precise starting locations for earthquakes, a 1D velocity structure to use as initial model. The perturbations which lead to the final 3D model are calculated with respect to this starting structure. This is the reason why, to introduce the inversion problem for velocity structure, we start with the 1D case. Although the mathematics poses different problems, the basic concepts are the same both for the 1D and 3D analysis. This means that the theoretical guidelines we have to familiarize with, are valid independently of the desired degree of complexity.

We begin by introducing some basic concepts and then we apply those principles specifically to our inversions schemes. We explain the *VELEST* computation routine for the Minimum 1D [Kissling 1988; Kissling 1995], and then we introduce the basics of the inversion codes used to obtain a 3D velocity structure. In this case, two algorithms are showed, based on different mathematical approaches, i.e. those of Benz [Benz et al. 1996] and of Toomey [Toomey et al. 1994].

2.2.1. *Theory Fundamentals*

This introduction to the fundamentals of seismic traveltime tomography is based on some papers that are milestones for the comprehension of the tomographic problem [Iyer and Hirahara 1993; Kissling 1988; Lay and Wallace 1995; Nolet 1987; Rawlinson and Sambridge 2001; Thurber and Aki 1987; Zhao 2001] and which we refer to for further details.

The steps required to produce a tomographic image are:

- (1) Model parameterization. A set of parameters has to be defined to model the seismic structure.
- (2) Forward calculation. Given a set of trial model parameters, a procedure is defined for the calculation of the model data (traveltimes)
- (3) Inversion. The model parameters have to be adjusted in order to fit the model data to the observed data
- (4) Analysis of solution robustness. The quality of the result is evaluated through covariance and resolution matrix from linear theory or on practical synthetic tests.

2.2.1.1. *Representation of Structure*

The seismic structure we want to solve (as its variations of P or S wave velocities) has to be parameterized in order to be mathematically handled. Velocity variations can be defined by a set of interfaces whose geometry is varied until the representation goes closer to the true structure, as a set of constant velocity layers, blocks or nodes. Constant velocity blocks are simple to define but they introduce velocity discontinuities between adjacent blocks [Humphreys and Clayton 1988]. Hence, an alternative is to define velocities at the vertices of a rectangular grid together with a specified interpolation function [Kissling et al. 2001; Thurber 1983]. These interpolation functions are used to calculate the velocity at any point within a rectangular grid of nodes, ensuring that the velocity field is continuous throughout the model volume while the velocity gradient can change from cell to cell. A common function is the tri-linear interpolation function (Thurber, 1988):

$$v(x, y, z) = \sum_{i=1}^2 \sum_{j=1}^2 \sum_{k=1}^2 v(x_i, y_j, z_k) \left(1 - \left| \frac{x - x_i}{x_2 - x_1} \right| \right) \left(1 - \left| \frac{y - y_j}{y_2 - y_1} \right| \right) \left(1 - \left| \frac{z - z_k}{z_2 - z_1} \right| \right) \quad (3)$$

(where $v(x_i, y_i, z_i)$ are the velocities at the eight grid points surrounding (x, y, z)) or higher order functions such as Cubic cardinal spline and Cubic B-splines. To have a more flexible representation, rather than use a block or grid parameterization, it could be used also a scheme in which velocity is discretized in the wavenumber domain rather than the spatial domain. A spectral representation of slowness distribution can be obtained by using a truncated Fourier series based on position and wavenumber vectors [Wang and Pratt 1997].

2.2.1.2. Traveltime Determination

If data for seismic tomography are traveltimes, we need to calculate them in the parameterized model, to solve the so called *forward problem*. The traveltime t of a ray in a continuous velocity medium $v(\mathbf{x})$ is

$$t = \int_L \frac{1}{v(\mathbf{x})} dl \quad (4)$$

where the integral of differential path length dl is done along the L ray path, \mathbf{x} is the position vector and v is the velocity. This equation is non-linear because the integration path depends on the velocity, as we are going to see later. For an elastic medium, the propagation of the seismic wavefronts can be described by the Eikonal equation, which is

$$(\nabla_{\mathbf{x}} T)^2 = 1/[v(\mathbf{x})]^2 \quad (5)$$

(with T traveltime of the wavefront) and which is subject to the high frequency assumption: the wavelength of a seismic wave should be much less than the length scale of the velocity variations of the medium through which it passes. If we

describe, in spite of the wavefront position, the position of a point \mathbf{x} of constant phase on the wave as $\mathbf{x} = \mathbf{x}(T)$, we can talk of ray paths, by definition normal to wavefronts (**Figure 2.2**). The ray equation is obtained from the Eikonal equations and used to describe ray path geometry:

$$\frac{d}{dl} \left(\frac{1}{v(\mathbf{x})} \frac{d\mathbf{x}}{dl} \right) = \nabla \left(\frac{1}{v(\mathbf{x})} \right) \quad (6)$$

The Fermat's Principle is a consequence of this equation and states that of all the paths that join two points in a velocity medium, the true ray path will be stationary in time. This means that a ray connection g two fixed points follows the path with the shortest traveltime:

$$\delta \int_L \frac{1}{v(\mathbf{x})} dl = 0 \quad (7)$$

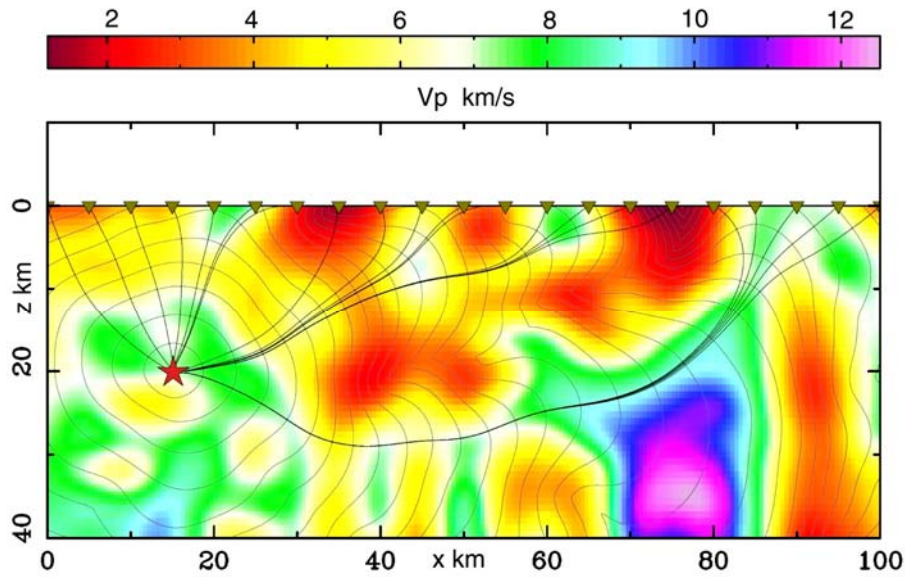


Figure 2.2 Ray paths and wavefronts. Wavefronts are the thin grey lines, rays the black lines perpendicular to the wavefronts. Wavefronts are represented at 0.5 s intervals. From Rawlison and Sambridge (2001).

In traveltimes tomography, the determination of travel times is performed traditionally through *ray tracing methods* (Shooting, Bending Pseudo-bending or analytical methods) but there are also wavefront tracking schemes such as finite difference solutions of the Eikonal equation and those that follow the network/graph theory, which makes direct use of the Fermat's principle.

Shooting and Bending methods essentially solve an initial value and two points boundary problem, respectively, by tracing trial ray paths and respecting the Fermat's Principle and the Snell's Law at model interfaces [Cerveny 1987]. In the Pseudo-bending method the complexity is augmented by introducing a perturbation scheme where ray paths are precisely traced by short integration steps in a continuous 3D medium [Um and Thurber 1987].

Otherwise the travel time can be found by considering the propagation path of the entire wavefront. The Eikonal equation is solved with *finite-difference solutions* on a regular grid [Ammon and Vidale 1993; Vidale 1990]. Here the traveltimes between a grid point and the surrounding nodes is determined by the Eikonal equation where the differential

terms of $(\partial T/\partial x)$ type are represented along the three directions by means of finite differences and using Huygen's principle for this finite difference approximation [Podvin and Lecomte 1991]. This means that each point reached by the wavefront is considered itself a new source of waves extending in all directions. The point of global minimum traveltimes along the perimeter of the points processed so far is used as the next source to locally expand the solution region. As the method tracks the wavefront but not the ray, the paths can be obtained by starting at the source and following the maximum traveltimes gradient up to the receiver.

The main difficulties with the Eikonal grid-based methods are there where the true wavefront is not differentiable, as happen in complex velocity media, where the gradient can have discontinuities. Anyway, this has been partially resolved with formulations based on weak solution of the Eikonal equations, which means an approximate solution that can be not differentiable everywhere. Moreover, finite-difference schemes only locate first arrivals and they need a densely sampled model to accurately calculate traveltimes, with exigent demand of power and memory.

For these reasons, *network methods* have been introduced [Moser 1991; Toomey et al. 1994]. They directly utilize Fermat's principle to find the path of the first arrival ray between source and receiver. A grid of nodes is use to parameterize the velocity model and a network (or graph) is formed by connecting neighboring nodes with traveltimes path segments. The first arrival path is that, between source and receiver, with the least traveltimes. The model can be formed by constant velocity blocks with nodes at the interfaces. The connection paths do not cross any block boundaries and so the traveltimes t is related to the path l through the slowness values s as $t = s l$. Instead if the model is represented by velocity nodes, the network nodes can coincide with them and the traveltimes can be given by the slowness at the two connected nodes: $t = l (s_1 + s_2) / 2$. Then, the only problem is to locate the path of minimum traveltimes among all the possible paths between source and receiver. The problem can be further simplified by changing arc extremes. In fact, the traveltimes is calculated from the source to all the points of the graph. As for this calculation there is reciprocity with respect to ray extremes, it is computationally preferable to consider stations as starting positions in spite of true sources.

Main problems with this method are related to the finite node spacing that can be unable to fully represent the velocity structure and with the range of angles which can be only a poor approximation to the true ray path. Increasing nodes number and connectors augments too much the time consumption. But the method is able to always find first arrivals and can work in really complex media .

2.2.1.3. *Inverse Problem*

Given a representation of an elastic property of the subsurface, such as velocity, and/or hypocentral locations, by a set of parameters \mathbf{m} , a relationship can be found between these model parameters and data, e.g. traveltimes:

$$\mathbf{d} = \mathbf{g}(\mathbf{m}) \quad (8)$$

which constitutes the basis of the tomography. For an observed dataset \mathbf{d}_{obs} and an initial model \mathbf{m}_0 , \mathbf{g} is the functional which describes the relation between model and data while the difference $\mathbf{d}_{\text{obs}} - \mathbf{g}(\mathbf{m}_0)$ gives an indication of how well the current model predictions \mathbf{m}_0 satisfy the observed data \mathbf{d}_{obs} .

The inverse problem is hence the manipulation of \mathbf{m} through operations of the type:

$$\mathbf{m} = \mathbf{m}_0 + \Delta\mathbf{m} \quad (9)$$

in order to minimize the difference between observed (\mathbf{d}_{obs}) and predicted (\mathbf{d}_{calc}) data (traveltime residuals). In other words, we want to obtain a value for $\Delta\mathbf{m}$ which can minimize the difference $\mathbf{d}_{\text{obs}} - \mathbf{d}_{\text{calc}}$.

$\mathbf{g}(\mathbf{m})$ can be linearized by a Taylor expansion in series. Neglecting the second and higher orders:

$$\mathbf{g}(\mathbf{m}) \approx \mathbf{g}(\mathbf{m}_0) + \mathbf{G} \Delta\mathbf{m} \quad (10)$$

where $\mathbf{g}(\mathbf{m})$ contains the \mathbf{d}_{obs} , $\mathbf{g}(\mathbf{m}_0)$ contains the calculated \mathbf{d}_{calc} in the model \mathbf{m}_0 and \mathbf{G} is the Jacobi-matrix of partial derivatives $\partial g_i / \partial m_j$ evaluated at \mathbf{m}_0 .

If we consider the traveltime residuals ($\Delta\mathbf{d}$) we can write down the same system as

$$\Delta\mathbf{d} \approx \mathbf{G} \Delta\mathbf{m} \quad (11)$$

At this point, the problem is reduced to evaluate that perturbation to the model ($\Delta\mathbf{m}$) we need to fit the calculated data \mathbf{d}_{calc} to the observed data \mathbf{d}_{obs} . This fitting can never be perfect for mathematical as for physical reasons. From a mathematical point of view the non linearity of $\mathbf{g}(\mathbf{m})$ prohibits the exact solution of the (10) and from a physical point of view, the errors on the data and the impossibility to truly represent the real earth with a model, prevent the perfect fit of \mathbf{d}_{obs} and \mathbf{d}_{calc} .

A way to solve this inverse problem is through *Backprojection methods*. These methods can be used to calculate the model perturbation (for example, slowness perturbation) in (11) by iteratively mapping traveltimes residuals into slowness perturbation along the ray paths until the data are satisfied. Two well known Backprojection techniques are the Algebraic Reconstruction Technique (ART) and the Simultaneous Iterative Reconstruction Technique (SIRT). These schemes are quite complex and their explication goes beyond the purpose of this work (cfr. references [Rawlinson and Sambridge 2001])

Alternatively, as in the *Gradient methods*, if we formulate the inverse problem as that of minimizing an objective function consisting of the data residual term (and one or more regularization terms) and if we assume that $\mathbf{d}_{\text{obs}} \approx \mathbf{g}(\mathbf{m})$ of equation (8) has a Gaussian distribution, we are trying to minimize (cfr also (10))

$$\mathbf{E}(\mathbf{m}) = \mathbf{g}(\mathbf{m}) - \mathbf{g}(\mathbf{m}_0) - \mathbf{G} \Delta\mathbf{m} \quad (12)$$

This can be also written as an objective function with several terms Among them, there is the term $\Psi(\mathbf{m})$ which measures the difference between the observed and predicted data.

$$\Psi(\mathbf{m}) = \|\mathbf{g}(\mathbf{m}_i) - \mathbf{d}_{\text{obs}}\|^2 \quad (13)$$

and $\mathbf{g}(\mathbf{m}_i)$ gives the estimated of data \mathbf{d}_{calc} after the perturbation to the model.

If uncertainty estimates have been made for the observed data (on picking errors) then more accurate data are given a greater weight in the objective function by writing $\Psi(\mathbf{m})$ as

$$\Psi(\mathbf{m}) = (\mathbf{g}(\mathbf{m}_i) - \mathbf{d}_{\text{obs}})^T \mathbf{C}_d^{-1} (\mathbf{g}(\mathbf{m}_i) - \mathbf{d}_{\text{obs}}) \quad (14)$$

where \mathbf{C}_d is the data covariance matrix. Actually it is a data weighting matrix more than a data covariance matrix because it reflects the uncertainty associated with the data.

Another regularization term is included in the objective function to take into account that not all model parameters are well constrained by data (underdetermined problem). This term has the form

$$\Phi(\mathbf{m}) = (\mathbf{m} - \mathbf{m}_0)^T \mathbf{C}_m^{-1} (\mathbf{m} - \mathbf{m}_0) \quad (15)$$

with \mathbf{C}_m a priori model covariance matrix, which is a true model weighting matrix whose entries reflect the statistical uncertainties of the initial model

The third regularization term is the minimum structure solution term $\Omega(\mathbf{m})$ which attempts to find an acceptable trade off between satisfying the data and finding a model with the minimum of structural variation:

$$\Omega(\mathbf{m}) = \mathbf{m}^T \mathbf{D}^T \mathbf{D} \mathbf{m} \quad (16)$$

This last equation introduces \mathbf{D} as matrix of spatial partial derivatives that simulate a continuously varying velocity field when the velocity parameters are constant velocity blocks or other crude representations.

At this point, the objective function becomes:

$$\mathbf{S}(\mathbf{m}) = \frac{1}{2} [\Psi(\mathbf{m}) + \varepsilon \Phi(\mathbf{m}) + \eta \Omega(\mathbf{m})] \quad (17)$$

with ε damping factor and η smoothing factor.

As \mathbf{g} is non-linear, the minimization of (17) requires an iterative approach:

$$\mathbf{m}_{n+1} = \mathbf{m}_n + \delta\mathbf{m} \quad (18)$$

now, the perturbation is applied to the model to minimize $S(\mathbf{m})$ and obtain \mathbf{m}_{n+1} and then the new ray path and traveltimes are calculated in the new model. These iterations stop when $S(\mathbf{m})$ is minimized or the changes at each iterations are sufficiently small.

A way to measure the data fit is given by the normalized χ^2

$$\chi^2 = \left(\frac{1}{N} \right) \sum_1^N \left[\left(\mathbf{d}^i - \mathbf{d}_{obs}^i \right) / \sigma^i \right]^2 \quad (19)$$

with N number of traveltimes (i) and σ^i traveltime weight/uncertainty. Its square root is, with the addition of a weight factor, the same as the common output of inversion programs, commonly called RMS (Root Mean Square).

There are several techniques to minimize $S(\mathbf{m})$. For example, the *Gauss-Newton method* obtains the \mathbf{m}_{n+1} by finding the minimum of the tangent paraboloid to $S(\mathbf{m})$ at \mathbf{m}_n and so updating the model in each iteration.

In another technique, that of *Damped Least Squares*, we again consider the equation (17), and write it considering the linearized equivalence at each iteration $\delta\mathbf{d} = \mathbf{G} \delta\mathbf{m}$ (cfr (11)) and residuals as

$$S(\mathbf{m}) = \frac{1}{2} \left[(\mathbf{G} \delta\mathbf{m} - \delta\mathbf{d})^T \mathbf{C}_d^{-1} (\mathbf{G} \delta\mathbf{m} - \delta\mathbf{d}) + \varepsilon \delta\mathbf{m}^T \mathbf{C}_m^{-1} \delta\mathbf{m} + \eta \delta\mathbf{m}^T \mathbf{D}^T \mathbf{D} \delta\mathbf{m} \right] \quad (20)$$

where the functional to be solved is

$$\mathbf{F}(\mathbf{m}) = \mathbf{G}^T \mathbf{C}_d^{-1} (\mathbf{G} \delta\mathbf{m} - \delta\mathbf{d}) + \varepsilon \mathbf{C}_m^{-1} \delta\mathbf{m} + \eta \mathbf{D}^T \mathbf{D} \delta\mathbf{m} = 0 \quad (21)$$

This has the solution, for no smoothing ($\eta = 0$) and damping unitary (\mathbf{C}_d and \mathbf{C}_m represent the known a-priori error statistics):

$$\delta \mathbf{m} = [\mathbf{G}^T \mathbf{C}_d^{-1} \mathbf{G} + \mathbf{C}_m^{-1}]^{-1} \mathbf{G}^T \mathbf{C}_d^{-1} \delta \mathbf{d} \quad (22)$$

which is called the Damped Least Squares (DLS) solution to the inverse problem [Aki et al. 1977]. As equation (21) shows, the damping and the smoothing factors are applied to the model perturbations. These can be, as here, the difference with respect to the previous iteration: in this case the strategy is called *creeping*. If instead, as in the Gauss-Newton method, they are applied to the model itself, or to the difference with respect to the first starting model, then the strategy is called *jumping*.

The same (22) is equivalent, with the formulation as a set of normal equations, to minimize the (20) by finding the least squares solution of the system:

$$\begin{bmatrix} \mathbf{C}_d^{-1/2} \mathbf{G} \\ \sqrt{\varepsilon} \mathbf{C}_m^{-1/2} \\ \sqrt{\eta} \mathbf{D} \end{bmatrix} \delta \mathbf{m} = \begin{bmatrix} \mathbf{C}_d^{-1/2} \delta \mathbf{d} \\ \mathbf{0} \\ \mathbf{0} \end{bmatrix} \quad (23)$$

And this is equivalent to solve (22).

The solution of (22) depends on its dimensions. For small problems it is often used the Singular Value Decomposition (SVD). It can handle matrices singular or nearly singular, which is often the case in tomographic problems, with a direct solution and produces covariance and resolution estimates quite directly.

For models with a large number of parameters, iterative techniques are more practical. Conjugate gradients and LSQR (Least Squares with QR decomposition), a variant of the conjugate gradient algorithm, are probably the most commonly used method to solve linear systems of type (22) with a large number of unknowns [Nolet 1985].

Both SVD and LSQR solvers can be used to solve (22) or (23) because they can be applied to non-squares matrix and solve the equations in the least-squares sense.

At this point it is interesting to note that the general formulas have considered as model parameters both the earthquakes location and the velocity model. To facilitate computational handling of this inversion, parameter separation was incorporated [Thurber 1983; Thurber 1992], where $\mathbf{G} \delta \mathbf{m}$ is split into a part containing only velocity model parameters and

one containing only hypocentral parameters, without sacrificing their formal coupling solution. This means that (11) can be written as:

$$\Delta \mathbf{d} = \mathbf{G} \Delta \mathbf{m} = \mathbf{H} \Delta \mathbf{h} + \mathbf{V} \Delta \mathbf{v} \quad (24)$$

where $\mathbf{H} \Delta \mathbf{h}$ contains the hypocentral part and $\mathbf{V} \Delta \mathbf{v}$ the velocity part. Using the QR-decomposition [Lawson and Hanson 1974] a reduced set of equations is obtained

$$\Delta \mathbf{d}' = \mathbf{V}' \Delta \mathbf{v} \quad (25)$$

which can be solved to calculate $\Delta \mathbf{v}$. Then the hypocentral corrections are estimated with the updated velocity model in a sole inversion for location ($\Delta \mathbf{d}'' = \mathbf{H}' \Delta \mathbf{h}$).

2.2.1.4. Analysis of Solution Quality

The solution of the tomographic inversion is not complete without an estimate of the robustness of the result itself. The resolution of any specific tomographic image is dependent on the dataset and tomographic technique used, and can fundamentally be determined following two approaches: the first assumes linearity of the inversion and offers a mathematical expression for the resolution; the second admits the difficulty related with the non-linear nature and recurs to empirical tests

2.2.1.4.1. Resolution.

As we have showed in (21) in the case that the smoothing is null

$$\varepsilon \mathbf{C}_m^{-1} \delta \mathbf{m} = -\mathbf{G}^T \mathbf{C}_d^{-1} (\mathbf{G} \delta \mathbf{m} - \delta \mathbf{d}) \quad (26)$$

If we add $\mathbf{G}^T \mathbf{C}_d^{-1} \mathbf{G} \delta \mathbf{m}$ to both sides of the equation, we obtain

$$[\mathbf{G}^T \mathbf{C}_d^{-1} \mathbf{G} + \varepsilon \mathbf{C}_m^{-1}] \delta \mathbf{m} = -\mathbf{G}^T \mathbf{C}_d^{-1} \delta \mathbf{d} \quad (27)$$

If

$$\delta \mathbf{m} = \mathbf{R} \delta \mathbf{m}_{\text{true}} \quad (28)$$

with \mathbf{R} resolution matrix that expresses the relationship between calculated solution and true solution and if

$$\delta \mathbf{d} = \mathbf{G} \delta \mathbf{m}_{\text{true}} + \zeta \quad (29)$$

with $\zeta = 0$ because we admit we can fully represent the true structure with the final model, hence comparing (20) and (21) we obtain (a part the sign)

$$\mathbf{R} = [\mathbf{G}^T \mathbf{C}_d^{-1} \mathbf{G} + \varepsilon \mathbf{C}_m^{-1}]^{-1} \mathbf{G}^T \mathbf{C}_d^{-1} \mathbf{G} \quad (30)$$

Which is the expression for resolution matrix, which ranges between 0 and 1. for $\mathbf{R} = 1$ the model is completely resolved and $\delta \mathbf{m} = \delta \mathbf{m}_{\text{true}}$. If $\mathbf{R} \neq 1$ then the model parameter estimates represent weighted averages of the true model parameters

2.2.1.4.2. Synthetic Tests

The previous approach has a principal difficulty in the fact that the \mathbf{R} matrix is derived from linear theory and lacks meaning when the non-linearity of the problem increases. In fact, the influence of systematic and random errors on the final results is hard to quantify owing to the nonlinear nature of seismic tomography, the difficulty of quantifying noise in the input data, and the effect of parameterization.

A number of empirical methods of uncertainty estimation is used to ensure that only robust, well-constrained features of the final model are interpreted. They are based on the definition of artificial models with known distribution, dimension, and intensity of anomalies. The procedure presents two steps: first we solve the direct problem to determine synthetic travel times and then we use those data as input for the inversion. The source-receiver geometry and inversion parameters have to be as close as possible to those used for the real data. The ray paths can be the same as in the solution model only if the solution is fully linearized, while they are only similar for iterative non-linear solutions. The comparison of the final model with the initial (known) model provides a qualitative indication about the resolving capabilities of code and data. Regions where the recovered model closely matches the input model are considered well resolved. However, the degree of recovery is sensitive to the geometry and intensity of the synthetic anomalies, a fact that has to be also pondered for the interpretation of the tests.

The *Checkerboard test* is a widely applied technique [Zelt 1988] to establish lateral velocity resolution for 3D seismic data. The checkerboard consists of vertical columns of alternating positive and negative velocity anomalies superimposed on the final/starting/homogeneous model. Several geometries, cell sizes, polarities are usually attempted. Usually between 5 and 10% variation is considered large enough to provide a perturbation greater than that expected as noise of the final RMS but as small as not to modify too much the ray paths from those in the final model. Anyway, also stronger anomalies, up to 20% have been applied [Evangelidis et al. 2004; Walck 1988]. Moreover, in our experience smoothed boundaries between anomalies perform better in the ray tracing phase because it has not to manage critical regions (as sharp contrasts or caustics).

In this procedure, traveltimes are computed for each checkerboard model using the real experimental geometry and random noise is added to the calculated travel-times, proportional to the observed uncertainty of data. Then, using the final velocity model as starting model, the travel times are inverted to recover the checkerboard. The evaluation of the semblance

between the known and the recovered checkerboard is usually presented by considering the ratio between the final recovered model and the known structure (recovery rate). Obviously, values close to 1 indicate well resolved regions.

The *Spike test* is another synthetic test used to assess the resolution by examining inversion of synthetic data for models with isolated anomalies positioned in key localities (i.e. regions of high geological interest). Moreover, it is equivalent to determining the point spread function for the single anomalous model cell [Humpreys and Clayton 1988]. It provides a sense of model fuzziness and streakiness at selected points and lets practically approaching the smearing problem, i.e. the way an anomaly spreads to adjacent nodes [Schurr et al. 2003].

The *Reconstruction test* [Zhao et al. 1992] is otherwise used with the aim of taking into account the non-linearity of the inversion in the obtained model and not that of a synthetic structure, such as in the Checkerboard test. The ray path geometry used is equal to that produced by the inversion of the real data in the linearized inversion. As easily understood, the conditions in which this test is performed are the closest to the true situation we can assemble: direct (ray tracing) and inverse (perturbation elaboration) problems are managed as in the true case. For this reason, this test can offer us the best indications about the fraction (as quality and quantity) of starting anomalies that the code is able to rebuild. Hence, this indication is especially useful in the interpretation of anomalies intensity.

A statistical technique such as the known *Jackknife test* [Lees and Crosson 1989] is also used to derive estimates of model parameter uncertainty. In this technique, repeated inversions are carried out, say k of them, with $1/k$ of the data randomly deleted, obtaining a set of solutions m_j from a set of 'pseudo-inversions'. The pseudo-inversions thus are considered to represent that information, about the model, which would be given by that portion of the data that has been removed. The properties of the results of the pseudo-inversions are used to estimate the model variance. Actually, the strong advantage of this method is that it does not require an estimate of noise in the data to assess the uncertainty in the resulting model because the noise itself contributes to the variance in the derived models.

Finally, last but not least, an examination of the *ray coverage* either directly or by means of weighted measures of ray sampling performance (for example Derivative Weight Sum [Kissling 1988]) provides another qualitative perspective on the solution quality.

2.2.1.4.3. *Error Definition*

In fitting a model to data it is necessary to know how much of the data variance can be attributed to stochastic processes, as opposed to unknown seismic structure [Barclay and Solomon 1998]. In the assumption of a final model which completely fits the data, this uncertainty represents how good this fitting is due to difficulties which don't depend on the code. Beside the Jackknife test, it can be obtained by summing up the variances of the individual sources of error we deal with. Among main sources of error there are sources (both passive, earthquakes, and active, as shots) and receiver positions, clock corrections and arrival time picking. For more complicated codes, other sources of error are the effect of bathymetry/topography, at the point where the wave penetrates the seafloor for active tomography or where the topography is rough and 'air wave' have to be avoided. This aspect cannot be separated from another uncertainty source, i.e. accuracy of ray tracing method, and of code operation, whose quality is hard to define for performances in complex structures.

2.2.2. 1D Models

The 1D model we look for is called Minimum 1D model [Kissling 1988] because it is the 1D model that leads to the smallest possible uniform location error for a large set of well-locatable events. This minimum 1D model is the result of an iterative inversion process which incorporates available a-priori information into the definition of the layering and the initial velocities. In other words, the Minimum 1D is the optimum model for earthquakes location for the data set from which it is inferred. Beside such earthquakes location improvement, the calculation of the Minimum 1D model has another application: to provide an initial model for 3D tomography. The Minimum 1D velocity model is the most appropriate initial 1D model for the 3D inversion and the 3D velocity deviations from this model should be evenly distributed with zero mean [Haslinger 1998; Kissling et al. 1994].

The Minimum 1D computation is done with the program *VELEST* [Kissling 1988; Kissling 1995; Kissling et al. 1994]. *VELEST* is a FORTRAN routine, running under UNIX operating systems that has been designed to derive 1D velocity models. Actually, it is set to solve the coupled hypocenter-velocity problem for local earthquakes, quarry blasts and shots. The final model consists of a layered 1D velocity model and station corrections. The starting velocity model and the reference station are introduced as a priori information, regarding the stratification of the area under study (velocities and layer thicknesses) and central station with nearly continuous recording. The forward problem is then solved by ray tracing from source to receiver, computing the direct, refracted and (optionally) the reflected rays passing through the 1D model. The code uses a Bending method (Chapter 2.2.1.2) through a geometrically one-dimensional layered Earth model, which approximates the true ray path by bending according to the local velocity field. The inverse problem is solved by full inversion of the dampest least squares matrix in the equation (see equation (22))

$$\delta \mathbf{m} = [\mathbf{G}^T \mathbf{C}_d^{-1} \mathbf{G} + \varepsilon \mathbf{C}_m^{-1}]^{-1} \mathbf{G}^T \mathbf{C}_d^{-1} \delta \mathbf{d} \quad (31)$$

where \mathbf{G} is the Jacobi matrix, \mathbf{G}^T is the transposed Jacobi matrix and ε is the damping parameter. The solution to the coupled problem is obtained iteratively, each iteration consisting of solving both the complete forward and inverse problem

once (**Figure 2.3**). As usual, solution quality is checked through the difference between calculated travel times and observed travel time, i.e. misfit function. The RMS misfit is provided as result of the inversion process.

Due to the intrinsic ambiguity of the inverse problem, the final solution is only the small part of a large output of statistics, which are given in order to evaluate such ambiguity. This statistics is useful in the search of the optimum control parameters that must be set and adjusted during the previous process of inversion 'preparation'. As seen, in the case of the coupled problem with local earthquakes data, it is possible to have several local RMS minima. In such situations, the solution by an iterative algorithm strongly depends on the initial conditions. For this reason, the application of the *VELEST* algorithm is a trial and error process (for different initial models, layer thickness, hypocentral parameters and inversion control parameters), where it is critical to search for different solutions with minimal misfits.

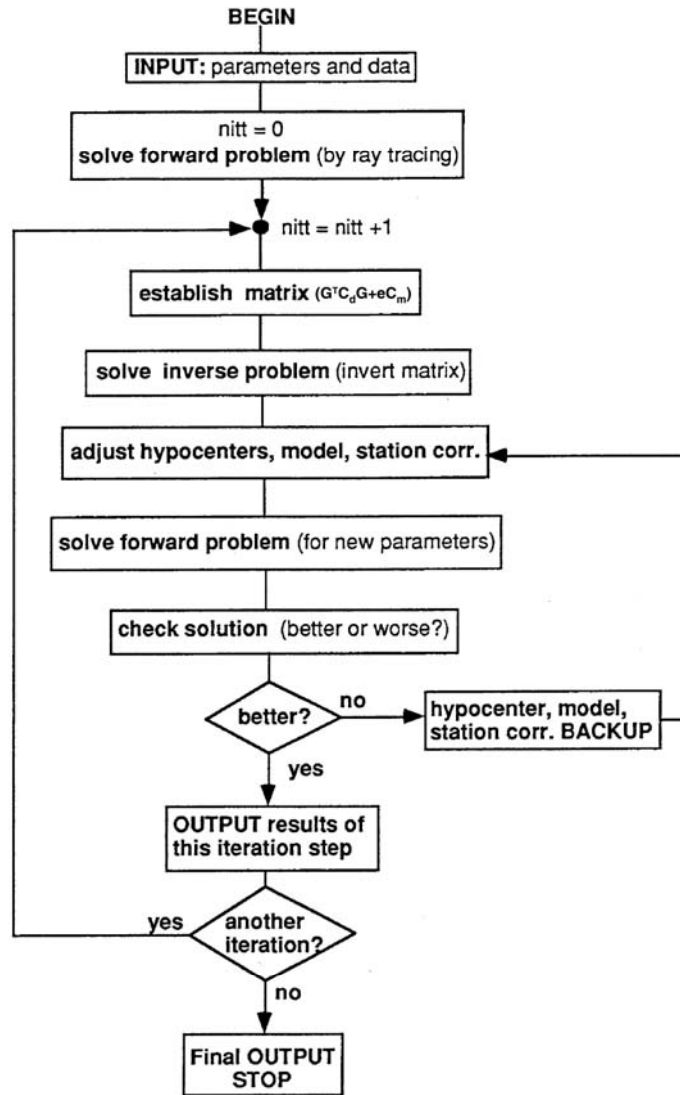


Figure 2.3 Flux diagram of the solution scheme for tomographic inversion of the program VELEST. The main printed output of VELEST reflects this procedure and provides detailed information about main steps. From Kissling, (1995).

2.2.3. 3D Model

2.2.3.1. Benz's Method

This method has been developed for local earthquakes arrival time data, to simultaneously determine both the three-dimensional velocity structure and earthquakes locations. It has been applied to numerous volcanoes such as Redoubt Volcano [Benz et al. 1996], Mount Spurr Volcano [Power et al. 1998], Mt. Etna [Villaseñor et al. 1998], Mt. Vesuvio [Scarpa et al. 2002]. In fact, in the method first-arrival times for local earthquakes are computed using a finite-difference technique, which allows for flexible parameterization of the velocity model and hence shows good performance in presence of complex structures and sharp contrasts.

To make the inversion problem tractable, the location and velocity structure inversion problems are separated, by managing one by one the slowness and hypocenter perturbations. Separation of parameters is achieved using an orthogonal transformation matrix, multiplying it with the matrix of hypocenter partial derivatives, and so leaving the velocity partial derivative matrix alone. As said, in this method, traveltimes are calculated using a finite difference technique [Podvin and Lecomte 1991]. The method estimates the travel time wave front (isochron) by solving the Eikonal equation across a finite-difference grid of rectangular, constant velocity cells. Standard formulations of the arrival time tomography problem require knowledge of the ray length within each cell sampled by a source-receiver pair, which is not explicitly known from finite difference computations [Rawlinson and Sambridge 2001]. So, rays are found by backtracking along the perpendicular to the wave front (the steepest path) from source to receiver.

The hypocentral partial derivatives, i.e. the solution to the direct problem in the location step, are calculated using a standard approach [Thurber 1986], while the earthquakes hypocenters are finally determined using a damped least squares expression of the problem and solving through a SVD algorithm. Assuming many stations recorded the earthquake, this produces a least squares correction for the earthquakes location and time. If fewer than the user-determined number of stations recorded the earthquake, or if the solution is poorly determined as indicated by small singular values, the

earthquake is discarded from the inversion. Station corrections are not used because they are considered to represent near-station geology features and are hence investigated.

Simultaneously, perturbations to slowness are computed with a Gradient method similar to the Damped Least Squares solution by using an LSQR solver [Power et al. 1998] with smoothing parameters conditioning the final model roughness and which provides a least squares solution to the inversion of the velocity perturbations system with accuracy comparable to Singular Value Decomposition (SVD) and efficiency comparable to back projection techniques [Benz et al. 1996] (Chapter 2.2.1.3).

Moreover, constraint equations are used to minimize artifacts due to the model parameterization: the model roughness is controlled by the requirement that the Laplacian of the slowness field must vanish. So, a set of smoothness constraint equations are build of the form

$$6u_{i,j,k} = (u_{i-1,j,k} + u_{i+1,j,k} + u_{i,j-1,k} + u_{i,j+1,k} + u_{i,j,k-1} + u_{i,j,k+1}) = 0 \quad (32)$$

where $u_{i,j,k}$ are the slowness values in an i, j, k cell and $u_{i\pm 1, j\pm 1, k\pm 1}$ are slowness in the adjacent cells.

So, the matrix system to solve, for the de-coupled problem and in terms of slowness perturbations, becomes (cfr equation (22)):

$$\begin{bmatrix} \mathbf{G}' \\ \sqrt{\eta} \mathbf{D}' \end{bmatrix} \delta \mathbf{u} = \begin{bmatrix} \delta \mathbf{d}' \\ 0 \end{bmatrix} \quad (33)$$

With $\delta \mathbf{u}$ is now the slowness perturbations vector; $\delta \mathbf{d}'$ traveltimes residuals, eventually modified by the earthquake location step; \mathbf{G}' matrix of partial derivatives of traveltimes with respect to slowness changes (i.e. matrix containing the length increments $d\mathbf{l}$ per cell sampled by a ray path); \mathbf{D}' set of smoothness-constraint equations and η that plays the role of controlling the trade-off between model roughness and data misfit reduction. The selection of the different terms in this constraint equation let control the degree of smoothness in the three different directions.

In addition, the relative rates of velocity and hypocenter convergence can be controlled by the user by varying the number of LSQR iteration, allowing exploration of the nonlinear trade-off between the two parameters [Hole et al. 2000].

2.2.3.2. *Toomey's Method*

Tomography of regions highly heterogeneous on short length scales as volcanic islands or oceanic ridges, with rough seafloors and complex topographies, needs a densely parameterized model to calculate both ray paths in the forward problem and perturbations to the starting velocities in the inverse problem [Barclay and Solomon 1998].

While a densely gridded model can better represent the heterogeneous medium, especially for the travel time calculation, it introduces a huge number of parameters and, hence, of unknowns. This number usually exceeds the number of available data, usually seismic delay times. For this reason, a common choice for tomographic method used in these tectonic setting is to separate the forward and inverse problem by using two different grid scales.

Toomey's method [Toomey et al. 1994] mostly applied to the study of oceanic regions [Barclay and Solomon 1998; Barclay and Toomey 2003; Barclay et al. 2001; Barclay and Wilcock 2004; Canales et al. 2000; Dunn and Toomey 2001; Magde et al. 2000; Tian et al. 2000; Toomey et al. 1998; Toomey et al. 2007], also approaches the tomographic problem by separating the solution and parameterization of the forward and inverse problem. It solves the traveltimes calculation following the graph or network theory [Moser 1991]. As seen (Chapter 2.2.1.2), by managing the medium through a nodal representation, traveltimes are calculated assigning times to the arcs connecting the graph and looking for the shortest path. This representation lets consider complex models, because node density can be increased to the limits of structural features and can lead to an accurate travel time calculation. Moreover, topography can be taken in account by shearing vertically the columns of nodes, following the seafloor relief. Due to reciprocity of traveltimes calculation stations are considered starting positions in spite of the sources.

A main feature of the code is to manage the tomographic problem with a hypothesis-testing approach, letting the user to choose and change the values of several parameters. What we obtain is actually a preferred model, where the code is only a tomographic tool to find out the most reasonable structure. This 'solution' of the inverse problem is completely meaningful in seismic tomography problem, where unknowns always exceed the data number and model uniqueness is an unfeasible aim.

The slowness perturbations are linearly related to the traveltimes residuals as in (11) or, more specifically, (25), and they are defined by linear interpolation between model values α_i at a set of parametric nodes ($i=1, \dots, m$). Interpolation weights are introduced to relate the perturbations to those parametric nodes that are immediately adjacent to the position \mathbf{x}

$$\delta \mathbf{u}(\mathbf{x}; \alpha_1, \alpha_2, \dots, \alpha_m) = \mathbf{w}_i(\mathbf{x}) \alpha_i(\mathbf{x}) \quad (34)$$

The advantage of this representation stays in the fact that the number of perturbational nodes $\alpha_i(\mathbf{x})$ is typically less than the number of nodes used to define $\mathbf{u}(\mathbf{x})$. The direct problem is solved in a densely gridded, complex, model of $\mathbf{u}(\mathbf{x})$ values, while the inverse problem is limited to finding velocity adjustments in the less detailed structure a one, two, or three dimensions.

The traveltimes derivative with respect to an individual parametric nodal value is the length of the path influenced by parameter α_n and weighted by the linear interpolation coefficient:

$$\frac{\partial t_k}{\partial \alpha_n} = \int_L w_n ds \quad (35)$$

and the equation (11) for each iteration is

$$\delta \mathbf{d} = \mathbf{G} \delta \mathbf{m} \quad (36)$$

where $\delta \mathbf{d}$ is a vector of travel time delays, $\delta \mathbf{m}$ is a vector made with the α_n , and \mathbf{G} is the Frechet matrix (which, in a finite dimensional space is the same as the Jacobi matrix) of partial derivative of traveltimes with respect to perturbational values, as in (35).

This is treated as a Damped Least Squares solution after stabilizing by additional constraints including penalties on the Euclidean size and roughness of the model vector $\delta \mathbf{m}$. The functional to minimize is quite similar to equation (20), a part the introduction of separated smoothing factors for the vertical and horizontal directions:

$$s^2 = \delta \mathbf{d}^T \mathbf{C}_d^{-1} \delta \mathbf{d} + \lambda_p \delta \mathbf{m}^T \mathbf{C}_p^{-1} \delta \mathbf{m} + \lambda_v \delta \mathbf{m}^T \mathbf{C}_v^{-1} \delta \mathbf{m} + \lambda_h \delta \mathbf{m}^T \mathbf{C}_h^{-1} \delta \mathbf{m} \quad (37)$$

where the all λ s permit to weight the importance of individual constraints. \mathbf{C}_d is the data covariance matrix, a diagonal matrix whose elements are each an estimate of the variance in the arrival time observations. \mathbf{C}_p is a model covariance matrix and introduces a penalty function. This is a tool to enforce prior knowledge of the model, in fact it is a diagonal matrix of the products of the value of each parameter of the prior model for its prior uncertainty: it is the same as \mathbf{C}_m in the general case (15) and so λ_p correspond to the damping factor \mathcal{E} of (20).

\mathbf{C}_v , \mathbf{C}_h , are again model covariance matrices but weighted through smoothing factors, different for the vertical and horizontal directions (where, moreover, depends on position). They, hence, roughly correspond to the term with η of equation (20). They allow a systematic search for the best fitting model as a function of smoothing length (cfr also (16)). In this method, moreover, these smoothing constraints are normalized by the prior slowness model. Instead of calculate the inverse of the smoothing matrices \mathbf{C}_v , \mathbf{C}_h , the smoothing constraints are applied as additional equations ins the inverse problem. Here, they take the form of an equation where model perturbations are weighted depending on the distance they have from the considered node. There is a decay parameter, defined separately for each coordinate direction, which expresses the length inside which, from the model parameter, the weight is non-zero.

The matrices equations are then located in a system similar to (23)

$$\begin{bmatrix} \mathbf{C}_d^{-1/2} \mathbf{G} \\ \lambda_p \mathbf{C}_p^{-1/2} \\ \lambda_v \mathbf{C}_v \\ \lambda_h \mathbf{C}_h \end{bmatrix} \delta \mathbf{m}_{i+1} = \begin{bmatrix} \mathbf{C}_d^{-1/2} \delta \mathbf{d} \\ -\lambda_p \mathbf{C}_p^{-1/2} \delta \mathbf{m}_i \\ -\lambda_v \mathbf{C}_v \delta \mathbf{m}_i \\ -\lambda_h \mathbf{C}_h \delta \mathbf{m}_i \end{bmatrix} \quad (38)$$

which is solved with LSQR method. A single iteration consists of solving the forward ray-tracing problem; evaluating $\delta \mathbf{d}$, \mathbf{G} , the elements of the left hand side matrix and of the right hand side in (38); solving for a new set of model perturbations; and applying these perturbations to the slowness model.

These regularization are used to constraint the perturbations with respect to the starting model, this means, with a *Jumping strategy*. In this way, on subsequent iterations, it tries to make the perturbation the negative of the sum of the previous perturbations, which is equivalent to saying that it tries to make the total perturbation zero, which is equivalent to saying that it is trying to keep the final result close to the starting model.

References

- Aki, K., Christoffersen, A., and Husebye, E. S., 1977, Determination of the three-dimensional seismic structure of the lithosphere: *J. Geophys. Res.*, v. 82, p. 277-296.
- Ammon, C. J., and Vidale, J. E., 1993, Tomography without rays: *BSSA*, v. 83, p. 509-528.
- Barclay, A. H., and Solomon, S., 1998, Seismic Structure and crustal magmatism at the Mid-Atlantic Ridge, 35°N: *Journ. Geophys. Res.*, v. 103, p. 17827-17844.
- Barclay, A. H., and Toomey, D. R., 2003, Shear wave splitting and crustal anisotropy at the Mid-Atlantic Ridge, 35°N: *J. Geophys. Res.*
- Barclay, A. H., Toomey, D. R., and Solomon, S. C., 2001, Microearthquake characteristics and crustal Vp/Vs structure at the Mid Atlantic Ridge, 35 N: *J. Geophys. Res.*, v. 106, p. 2017-2034.
- Barclay, A. H., and Wilcock, W. S. D., 2004, Upper crustal seismic velocity structure and microearthquake depths at the Endeavour Segment, Juan de Fuca Ridge: *Geochem. Geophys. Geosyst.*
- Benz, H. M., Chouet, B. A., Dawson, P. B., Lahr, J. C., Page, R. A., and Hole, J. A., 1996, Three dimensional P and S wave velocity structure of Redoubt Volcano, Alaska: *J. Geophys. Res.*, v. 101, p. 8111-8128.
- Canales, J. P., Detrick, R. S., Lin, J., and Collins, J. A., 2000, J. Pablo Canales, Robert S. Detrick, Jian Lin, and John A. Collins): *J. Geophys. Res.*, v. 105, p. 2699-2719.
- Cerveny, V., 1987, Ray tracing algorithms in three dimensional laterally varying layered structures, *in* nolet, G., ed., *Seismic Tomography: with applications in global seismology and exploration geophysics*, Dordrecht, D. Reidel, p. 99-133.
- Dunn, R. A., and Toomey, D. R., 2001, Crack-induced seismic anisotropy in the oceanic crust across the East Pacific Rise (9°30'N): *Earth Planet. Sci. Lett.*, v. 189, p. 9-17.
- Evangelidis, C. P., Minshull, T. A., and Henstock, T. J., 2004, Three-dimensional crustal structure of Ascension Island from active source seismic tomography.: *Geophys. J. Int.*, v. 159, p. 311-325.
- Haslinger, F., 1998, Velocity structure, seismicity and seismotectonics of the Northwestern Greece between the Gulf of Arta and Zakynthos, *ETH* 188 p.
- Hole, J. A., Brocher, T. M., Klemperer, S. L., Parsons, T., Benz, H., and Furlong, K. P., 2000, Three-dimensional seismic velocity structure of the San Francisco Bay area: *J. Geophys. Res.*, v. 105, p. 13859-13874.
- Humphreys, E., and Clayton, R. W., 1988, Adaptation of back projection tomography to seismic traveltime problems.: *J. Geophys. Res.*, v. 93, p. 1073-1085.
- Iyer, H. M., and Hirahara, K., 1993, *Seismic tomography: theory and practice*: London ; New York, Chapman & Hall, xvii, 842 p. p.
- Kissling, E., 1988, Geotomography with local earthquakes data: *Rev. Geophys.*, v. 4, p. 659-698.
- , 1995, *Velet, Users guide*, Internal report, Zurich, Institute of Geophysics.
- Kissling, E., Ellsworth, W. L., Eberhart-Phillips, D., and Kradolfer, U., 1994, Initial reference models in local earthquake tomography: *J. Geophys. Res.*, v. 99, p. 19635-19646.

- Kissling, E., Husen, S., and Haslinger, F., 2001, Model parameterization in seismic tomography: a choice of consequence for the solution quality: *Phys. Earth Planet.Int.*, v. 123, p. 89-101.
- Lawson, C. L., and Hanson, R. J., 1974, *Solving Least Squares Problems*: Englewood Cliffs, Prentice-Hall, 340 p.
- Lay, T., and Wallace, T., 1995, *Modern Global Seismology*: International geophysics series, v. 58.
- Lees, J. M., and Crosson, R. S., 1989, Tomographic inversion for three-dimensional velocity structure at Mount St. Helens using earthquake data: *J. Geophys. Res.*, v. 94, p. 5716-5728.
- Lomax, A., J., Virieux, J., Volant, P., and Berge, C., 2000, Probabilistic earthquake location in 3D and layered models: Introduction of a Metropolis-Gibbs method and comparison with linear locations, *in* Thurber, C. H., and Rabinowitz, N., eds., *Advances in Seismic Event Location*, Amsterdam, Kluwer.
- Magde, L. S., Barclay, A. H., Toomey, D. R., Detrick, R. S., and Collins, J. A., 2000, Crustal magma plumbing within a segment of the Mid-Atlantic Ridge, 35°N *Earth Planet. Sci.Lett.*, v. 175, p. 55-67
- Moser, T. J., 1991, Shortest path calculation of seismic rays: *Geophysics*, v. 56, p. 271-284.
- Nolet, G., 1985, Solving or Resolving inadequate and noisy tomographic systems.: *J. Comp. Phys.*, v. 61.
- , 1987, *Seismic tomography : with applications in global seismology and exploration geophysics*: Seismology and exploration geophysics: Dordrecht, Holland ;Norwell, MA, U.S.A., D. Reidel ; Kluwer Academic Publishers (USA,Canada), 386 p. p.
- Podvin, P., and Lecomte, I., 1991, Finite difference computation of traveltimes in very contrasted velocity models: a massively parallel approach and its associated tools: *Geophys. J. Int.*, v. 105, p. 271-284.
- Power, J. A., Villaseñor, A., and Benz, H. M., 1998, Seismic image of the Mount Spurr magmatic system: *Bull. Volcanol*, v. 60, p. 27-37.
- Rawlinson, N., and Sambridge, M., 2001, Seismic traveltime tomography of the crust and lithosphere: *Advances in Geophysics*, v. 46, p. 81-197.
- Scarpa, R., Tronca, F., Bianco, F., and Pezzo, E. D., 2002, High resolution velocity structure beneath Mount Vesuvius from seismic array data: *Geophys.Res. Lett.*
- Schurr, B., Asch, G., Rietbrock, A., Trumbull, R., and Haberland, C., 2003, Complex patterns of fluid and melt transport in the central Andean subduction zone revealed by attenuation tomography: *Earth Planet. Sci. Lett*, v. 215, p. 105-119.
- Tarantola, A., 1987, *Inverse problem theory: methods for data fitting and model parameter estimation*: Amsterdam, Elsevier, 613 p.
- Tarantola, A., and Valette, B., 1982, Inverse problems-quest for information: *J Geophys*, v. 50, p. 159-170.
- Thurber, C., 1986, Analysis methods for kinematic data from local earthquake.: *Rev.Geophys*, v. 24, p. 793-805.
- Thurber, C., and Aki, K., 1987, Three-dimensional seismic imaging: *Ann. Rev. of Earth and Planet. Sci.*, v. 15, p. 115-139.
- Thurber, C. H., 1983, Earthquake locations and three dimensional crustal velocity structure in the Coyote lake area, central California: *J. Geophys. Res*, v. 88, p. 8226-8236.
- , 1992, Hypocenter-velocity structure coupling in local earthquake tomography: *Phys. Seismol. Soc. Am.*, v. 75, p. 779-790.
- Tian, T., Wilcock, S. D., Toomey, D. R., and Detrick, R. S., 2000, Seismic heterogeneity in the upper crust near the 1991 eruption site on the East Pacific Rise, 9 50' N: *Geophys. Res.Lett*, v. 27, p. 2369-2372.
- Toomey, D. R., Wilcock, W. S. D., Solomon, S. C., Hammond, W. C., and Orcutt, J. A., 1998, Mantle Seismic Structure Beneath the MELT Region of the East Pacific Rise from P and S Wave Tomography: *Science*, v. 280, p. 1224-1227.
- Toomey, D. R., Joussetin, D., Dunn, R. A., Wilcock, W. S. D., and Detrick, R. S., 2007, Skew of mantle upwelling beneath the East Pacific Rise governs segmentation: *Nature*, v. 446, p. 409-414.

- Toomey, D. R., Solomon, S. C., and Purdy, G. M., 1994, Tomographic imaging of the shallow crustal structure of the East Pacific Rise at 9 30' N: *J. Geophys. Res.*, v. 99, p. 24135-24157.
- Um, J., and Thurber, C., 1987, A fast algorithm for two points seismic ray tracing.: *Bull. Seism.Soc.Am*, v. 77, p. 972-986.
- Vidale, J. E., 1990, Finite-difference calculations of traveltimes in three dimensions: *Geophysics*, v. 55, p. 521-526.
- Villaseñor, A., Benz, H. M., Filippi, L., De Luca, G., Scarpa, R., Patanè, G., and Vinciguerra, S., 1998, Three-dimensional P-wave velocity structure of Mt Etna, Italy: *Geophys. Res. Lett.*, v. 25, p. 1975-1978.
- Walck, M. C., 1988, Three-dimensional $V_p=V_s$ variations for the Coso region, California,: *J. Geophys. Res.*, v. 93, p. 2047-2052.
- Wang, Y., and Pratt, R. G., 1997, Sensitivities of seismic traveltimes and amplitudes in reflection tomography: *Geophys. J. Int.*, v. 131, p. 618-642.
- Zelt, C. A., 1988, Lateral velocity resolution from three dimensional seismic refraction data: *Geophys. J.Int.*, v. 135, p. 1101-1112.
- Zhao, D., 2001, New advances of seismic tomography and its applications to subduction zones and earthquakes fault zones: a review: *The Island Arc*, v. 10, p. 68-84.
- Zhao, D., Hasegawa, A., and Horiuchi, S., 1992, Tomographic imaging of P and S wave velocity structure beneath northeastern Japan: *J. Geophys. Res.*, v. 97, p. 19909-19928.

3. *Central São Miguel*

Abstract

The island of São Miguel (Azores Archipelago) is located in a complex geodynamical setting, in the triple junction zone among the American, Eurasian and African plates. The structure of São Miguel is characterized by fault systems of regional affinity mainly trending NW-SE and E-W. The most important volcanic complexes are located at the intersection of these tectonic lineaments. In Central São Miguel, the main volcanic structures are those of Fogo and Furnas. Both are central volcanoes with a summit caldera and a dominantly trachytic production. Furnas is the youngest volcano and consists of a steep-sided, 8x5 km caldera complex formed during several collapses. In the last 3000 years, most eruptions were phreato-magmatic and occurred with an average recurrence interval of 320 years. The Fogo volcanic edifice rises to an elevation of ~1000 m above sea level, and is composed by lava flows, domes and pyroclastic deposits over an older submarine lava basement.

Between April 4 and July 15, 2003, a temporary seismic network including short-period and broad-band instruments, as well as three small-aperture seismic antennas, was deployed in São Miguel to expand and complete the permanent network. The main goal of the project was to quantify the seismicity of the zone and possibly collect an appropriate database to elaborate a tomographic image of Central São Miguel. The existing database of the regional network provided information about the distribution of seismicity in the region. This information was used to plan the deployment of the new seismic network, which was maintained for a three months period for logistic reasons. During this period, the instruments recorded

more than one thousand earthquakes. Most of them were local earthquakes characterized by S-P times smaller than a few seconds and with magnitude-durations lower than 2.5. The daily average was 5-10 earthquakes per day, except for a single swarm in April 26-27 when more than 160 earthquakes occurred in a few hours.

We determined the three-dimensional distribution of P- and S-wave velocities for Central São Miguel Island (Azores, Portugal) by tomographic inversion of local earthquake arrival times. We used P- and S-phases from 289 earthquakes recorded by a network of 20 seismometers. The model shows good resolution in the shallowest 5-6 km, as illustrated by different resolution tests. There are several velocity anomalies, interpreted as pyroclastic deposits, intrusive bodies, geothermal fields, and the effects of tectonics. A low V_p zone marks Furnas caldera, probably evidencing volcanoclastic sediments with development of intense geothermal activity. Another low V_p zone extends in correspondence of the highly fractured area between Fogo and the north coast. Conversely, strong positive anomalies are found south of Fogo and northwest of Furnas. They are interpreted in terms of high-density deposits and remnants of a plutonic intrusion. These interpretations are supported by distribution of V_p/V_s , and are consistent with previous geological, geochemical, and geophysical data.

Extended Abstract

Introduction

São Miguel is a densely inhabited volcanic island whose volcanic activity, although widely recognized and studied, has not been explicated in a more complete picture of structural knowledge. The main aim of this work is to obtain information on the structure of this volcanic region via seismic tomography and to discuss the relationship between the obtained image of seismic heterogeneities and other geophysical and geological observations.

The Archipelago of Azores consists of nine volcanic islands located at about 38°N and 28°W, in the triple junction zone among the American, Eurasian and African plates. The largest island is São Miguel. The structure of São Miguel is characterized by fault systems mainly trending NW-SE and E-W. The most important volcanic complexes are located at the intersection of these tectonic lineaments. In Central São Miguel, the main volcanic structures are those of Fogo and Furnas. Both are central volcanoes with a summit caldera and a dominantly trachytic production. Furnas is the youngest volcano and consists of a steep-sided, 8x5 km caldera complex formed during several collapses. In the last 3000 years, most eruptions were phreato-magmatic and occurred with an average recurrence interval of 320 years. The Fogo volcanic edifice rises to an elevation of ~1000 m above sea level, and is composed by lava flows, domes and pyroclastic deposits over an older submarine lava basement.

Although São Miguel volcanoes have not erupted since the 17th century, the area is subject to seismicity. In the last years, thousands of earthquakes have been annually recorded and located around São Miguel Island by the regional seismic network. Their origin is mostly related to approximately WNW-ESE fault systems dominating the regional tectonics. However, occasional clusters of earthquakes comprising up to 1000 earthquakes per month are also detected, especially in Central São Miguel. The origin of these earthquakes is commonly associated to the volcanic and/or geothermal activity of the zone. Until now, no evidences of long-period earthquakes or volcanic tremor have been reported by the no-specialized

seismic instrumentation deployed over the area. Anyway, considering the extensive geothermal activity in São Miguel, long period events of hydrothermal origin are likely to occur. Together with seismicity, the presence of vigorous hydrothermal systems provides another indication of active volcanism in São Miguel. In fact, they possibly point to the existence of heat sources in depth, as below Furnas caldera or between Fogo volcano and the north coast. Thermal springs and fumaroles are distributed along fault systems crossing Fogo and Furnas. The most intense thermal activity coincides with an E-W tectonic lineament in Furnas and a NW-SE fault system in Fogo.

Seismic Experiment

Between April 4 and July 15, 2003, in the framework of the European Project *E_RUPTION*, a temporary seismic network including short-period and broad-band instruments, as well as three small-aperture seismic antennas, was deployed in São Miguel to expand and complete the permanent network operated by “Sistema de Vigilância Sismológica dos Açores” (SIVISA). The main goal of the project was to quantify the seismicity of the zone and possibly collect an appropriate database to elaborate a tomographic image of Central São Miguel. The existing database of SIVISA provided information about the distribution of seismicity in the region. This information was used to plan the deployment of the new seismic network, which was maintained for a three months period for logistic reasons. During this period, the instruments recorded more than one thousand earthquakes. Most of them were local earthquakes characterized by S-P times smaller than a few seconds and with magnitude-durations lower than 2.5. The daily average was 5-10 earthquakes per day, except for a single swarm in April 26-27 when more than 160 earthquakes occurred in a few hours.

Our starting data set consisted of visually-picked arrival times for P and S phases associated with 756 earthquakes, recorded in a seismic network of 33 stations. They mostly had a time difference between arrivals of P and S waves smaller than 3 s, and were hence considered as local earthquakes. The data were accurately selected to be used to obtain an initial 1D velocity model and preliminary earthquakes locations.

A preliminary 1D velocity model was obtained using the code *VELEST* and a database of 331 earthquakes observed in 26 stations. This code determined that velocity structure where calculated travel times best fitted the observed phase arrivals, in a least-square sense. To calculate our 1D model, we started with the velocity model used in routine locations by

SIVISA. We obtained a 1D model which mostly differed from the Azorean between surface and 4 km of depths and roughly presents lower velocities.

We then obtained a location for 426 of the initial earthquakes of the studied region, in the previously obtained 1D model. We used the code *NLloc*, which provided a maximum-likelihood solution for the source location problem and highly precise hypocenters positions.

As main part of this work, we determined the three-dimensional distribution of P- and S-wave velocities for Central São Miguel by tomographic inversion of local earthquake arrival times with the code of [Benz et al. 1996]. This method separates the forward problem of travel-time calculation from the inverse problem of velocity determination. In the forward step, travel times and approximate ray paths are calculated by using a finite-difference technique. In particular, this technique is well suited for the São Miguel experiment because it can manage strong lateral velocity contrasts, which are expected to be present, as in most volcanic regions. The inverse problem is solved by using a LSQR solver, with smoothing parameters conditioning the final model roughness. It provides a least squares solution to the inversion of the velocity perturbations matrix. The model parameters for velocity structure are defined on a regular three-dimensional grid of constant-slowness cubic cells that is sparser than the grid used for the ray tracing. After several tests with different cell-sizes, we selected a 1-km cell as the optimum dimension for our inversion. A denser grid of 0.25 km was used in the direct problem to calculate arrival times with an accurate ray path tracing.

We used P- and S-phases from 289 earthquakes recorded by a sub-network of 20 seismometers. The depth-dependent starting velocity model was that obtained in the previous 1D tomography inversion. The data and code resolution were checked by performing synthetic inversions such as in the checkerboard tests, impulse response test and reconstruction tests. They confirmed a good resolution in the centre of the domain, including Fogo and Furnas calderas, to a depth of 6 km, in correspondence with largest ray paths lengths and densely crisscrossed grid cells. We also measured the control exerted on results by the initial database selection by performing a Jackknife test, whose result indicated the independence of the final model. The effects of the starting model choose were assessed by repeating the inversions using starting models slightly different from our true initial model. We could hence establish that the images were not dependent on the starting model.

Results and Discussion

Convergence of the tomographic inversion to a stable solution was obtained after 10 iterations when, for P phase arrival times calculated with respect to the initial 1D velocity model, we observed a RMS reduction from 0.35 to 0.13 s. In the final result, there are several P- and S-wave velocity anomalies, which differ from the starting values up to 10%. In the vertical distribution of heterogeneities, we observe that the overall positions of the model contrasts do not strongly vary with depth. The main anomalies remain in their positions, slightly changing in intensity. This means that whatever mechanisms produce the velocity variations, they extend all the way down to the maximum depth resolved by our inversion.

The main velocity contrasts are interpreted as evidences of pyroclastic deposits, intrusive bodies, geothermal fields, and the effects of the tectonics acting at different scale. We imaged a low-velocity anomaly in the Furnas zone, stable down to 6 km depth. The velocity values are over 10% lower than those of the starting model. This wide anomaly evidences the presence of volcanoclastic, low density sediments, strongly altered by geothermal activity. These products include pumices, ignimbrite and surge deposits, phreatomagmatic ashes, and dome materials. However, while this explanation can be referred to the shallow layers, the continuation of the anomalies in depth may be associated with intensely fractured and/or hydrothermally altered areas.

Another zone of low velocity is situated in the NW region of the studied area, between Fogo caldera and the north coast. This negative anomaly is weaker than the SE anomaly, and never surpasses the 2-3% value. Moreover, it stands in a peripheral region of our volume and for this reason it is pointed out by our resolution tests as tentative. Again, a geothermal system embedded in porous, low-density pyroclastic deposits could be the origin of this low V_p zone, as supported by the presence of the Ribeira Grande geothermal field, the main geothermal area currently exploited in the island.

On the contrary, the region extending from the south of Fogo to the northwest of Furnas, across the Congro area, shows a positive anomaly, around 10% in its strongest value. This anomaly is actually constituted by two sub-volumes, in the NE and SW extremes, separated by a slower zone. The Central São Miguel zone has the highest ray coverage and thus this partition in two sub-regions is probably a real feature of the velocity structure. The region which presents lower V_p between the two maxima confirms the existence of the faulted, seismogenetic, zone that matches the regional tectonic stress field and is pointed out by several seismological observations. Instead, the two maxima are interpreted in terms of high-

density deposits and/or remnants of a plutonic intrusion. The Fogo volcano could stand as a chilled remnant of a magma chamber, as confirmed by the lack of evidence of magmatic activity from geophysical and geochemical surveys.

With respect to the V_p/V_s ratio, we observe that in Central São Miguel it tends to be low, in agreement with the results of previous seismic studies. Nevertheless, with respect to the value of 1.68 roughly derived for the whole area, both higher and lower values are retrieved by our inversion. A central, normal or slightly high ratio volume stands in the whole depth range. These high values extend eastward, closer to the Furnas area and between Fogo and the south coast. Low V_p/V_s can be observed in the north-northwest part of our volume and in the Furnas caldera zone. The lowest V_p/V_s ratios in both regions are found at about 2 km depth.

The V_p interpretations are supported by this V_p/V_s distribution, which reveals as a powerful tool to understand the nature of fluids involved in the actual volcanic state of the region. Hence, the low V_p of Furnas can be definitely associated with the development of an intense vapour-dominated geothermal field in pyroclastic caldera-infilling. On the opposite, the chilled remnant of the Fogo magma chamber would act as preferred pathways for circulating fluids, mostly water as liquid phase.

Conclusions

A three-dimensional seismic V_p and V_p/V_s tomographic image of Central São Miguel shows strong lateral velocity variations that can be attributed to sediment infilling, geothermal fields, high density deposits and/or remnants of a plutonic intrusion. In this sense, the velocity model establishes a base to better interpret the actual seismic and geothermal activity of the island. Moreover, the velocity model fits with observations from other studies and with the regional geodynamics, whose action seems to influence the structural setting of the island with the presence of several fault systems of regional affinity.

3.1. *The Question*

Inhabited volcanic areas, where even a small eruption could produce considerable losses, pose important problems in terms of hazard. This consideration motivated an European Union-sponsored project intended to quantify the present-day seismicity of various quiescent volcanoes in populated regions [Saccorotti et al. 2004].

One of the sites selected by the *E_RUPTION* project was São Miguel, where a seismic survey was carried out in the period April to July 2003. As target zone for study it was selected that region extending between two wide calderas, Fogo and Furnas, which hosts important seismic activity and also several vigorous geothermal fields. The regional network provided information about the distribution of seismicity in the region. This information was used to plan the deployment of the new seismic network, which was maintained for a three months period for logistic reasons. In this optics, the survey was intended to clarify the actual state of this seismogenetic region and possibly collect an appropriate database to elaborate a tomographic seismic image of central São Miguel. Moreover, it was intended to figure out the main features of the geothermal fields, their seismicity and internal structures.

In particular in our work, seismic data recorded during the experiment have been used to determine the three-dimensional seismic velocity structure of the central region of São Miguel. We then try to establish relationships between the distribution of seismic velocity and the volcanic structures of Central São Miguel. Hence, with the velocity model, we integrate the actual knowledge about this volcanic area, densely inhabited and, hence, of great interest. The actual features of geothermal fields are delineated and, as unforeseen result, the tendency of their development is outlined.

3.2. Tectonic Overview

The nine volcanic islands of the Azores Archipelago lie between 37° to 40° N and 25° to 31° W, in the triple junction region of the American, Eurasian and African plates (**Figure 3.1**). The western group (Flores and Corvo Islands) is located in the stable American Plate, whilst the Central (Faial, Pico, S. Jorge, Graciosa and Terceira Islands) and Eastern (São Miguel and Sta. Maria Islands) groups lie in a complex region [Fernandes et al. 2006]. The three main tectonic structures affecting the evolution of this zone are: (1) The Mid-Atlantic Ridge (MAR) which passes among the western islands (Flores/Corvo and Faial) with a N10° direction to the north of latitude 38°50'N and between N10° and N20° to the south. (2) The East Azores fracture Zone which has a roughly E-W direction and extents from the MAR to Gloria Fault to the east (a right-lateral strike slip fault between Azores and Gibraltar). (3) The Terceira Rift. This is a regional leaky transform [Madeira and Ribeiro 1990] extending more than 500 km until the Gloria fault, and oriented about N125° [Jonsson et al. 1999]. The Terceira Rift starts from the northern portion of the MAR and passes through the two northern islands of Graciosa and Terceira [Guest et al. 1999], until crossing also São Miguel Island. The Africa-Europe plate boundary in this region is probably coincident with this transform, which is considered in slow spreading, with a full rate of 4 mm/yr in the N75°E direction, according to the NUVEL-A global plate motion model [Jonsson et al. 1999]. The ENE-WSW extension is confirmed by detailed bathymetric surveys conducted within the Azores Archipelago [Lourenço et al. 1998; Miranda et al. 1998]. It has been proposed [Lourenço et al. 1998] that the Azores domain constitutes a diffuse plate boundary acting both as an oblique, ultra-slow spreading centre and a transfer zone accommodating dextral differential shear motion. Conversely, Olivet (as cited by [Gente et al. 2003]) proposed that alternate episodes of transform and spreading activity have been active in the Azores region for the last ~20 Myr. Finally, no clear evidence for a discrete triple junction has been found west of Faial island, where the diffuse plate boundary separating Eurasia and Africa intersects the MAR [Gente et al. 2003].

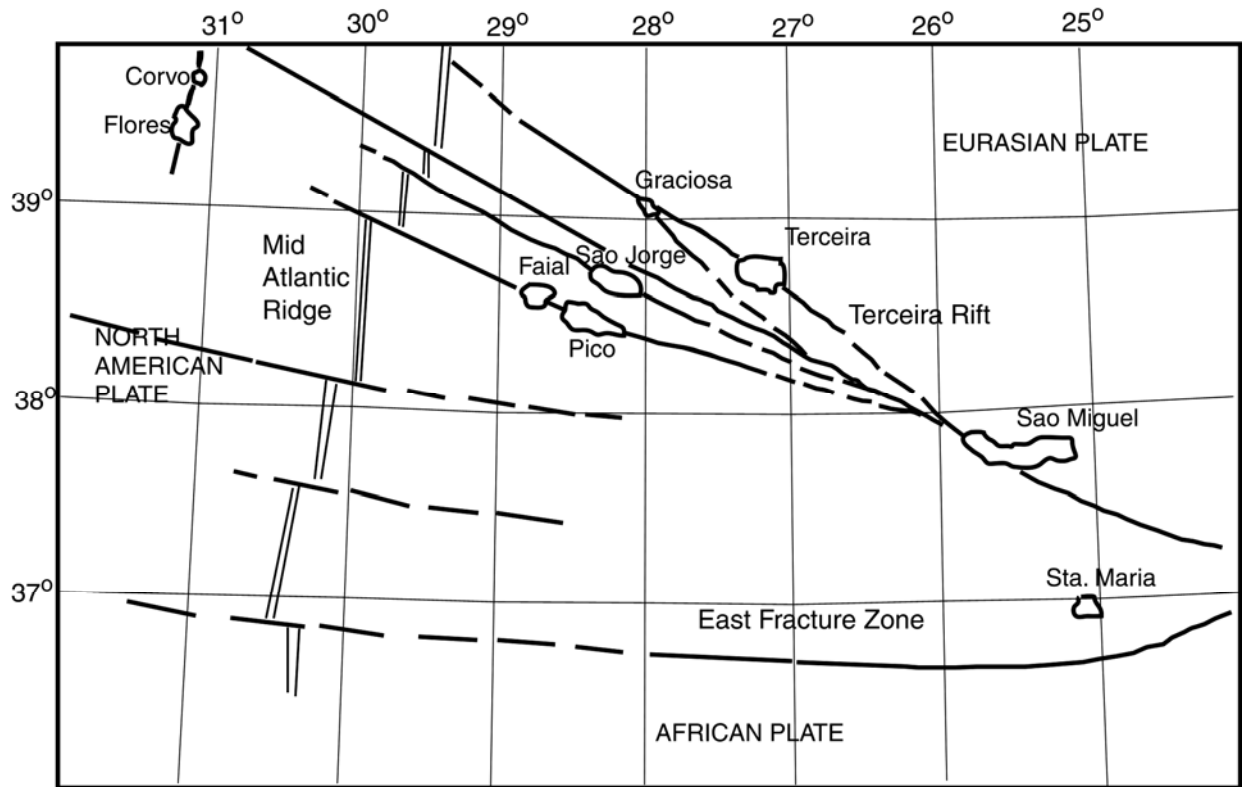


Figure 3.1 Regional tectonics of Azores Archipelago. The sketch shows main tectonic lineaments and faults (black lines), the island coastlines, the tectonic plates boundaries and their motion directions. Modified from Forjaz (1984).

3.3. Previous Studies

3.3.1. Geology

São Miguel, the largest island of Azores Archipelago, is a broadly oblong east-west oriented island about 63 km long and 8-15 km wide, and lies near the extremity of the islands chain, 400 km from the MAR crest. Its tectonics match the regional geodynamic framework for the Azores sector. Several tectonic structures, which mainly affect the centre and the western regions of the island, show approximately NW-SE and E-W directions (**Figure 3.2**). For example, the Ribeira Grande and Moisteros graben, together with faults in Congro area, are oriented WNW-ESE and correspond to the orientation of the regional Terceira Rift. Other well-known fractures have a W-E trend [Cruz 2003].

The geology of São Miguel is controlled by these structures of regional affinity, as well. The main volcanic features are clearly influenced by directions analogous to those described for the general tectonics. For example, numerous calderas are located at the intersection of great scale tectonic lineaments [Gandino et al. 1985; Haase and Beier 2003]. Thermal springs and fumaroles are distributed along fault systems NW-SE trending [Ferreira and Oskarsson 1999]. Seven [Cruz 2003; Forjaz 1984] or six [Gandino et al. 1985; Johnson et al. 1998] volcanic complexes have been recognized in the island: Sete Cidades, Picos, Fogo, Achada, Furnas, Povoação and Nordeste.

The oldest volcanic edifice was that of the Nordeste shield volcano. Later, activity spread westward, ending in the Picos sector, which constitutes the most recent volcanic complex. However, hydrothermal manifestations nowadays occur mainly in three active stratovolcanoes: Fogo, Furnas and, in lower extent, Sete Cidades. They are central volcanoes with a dominant trachytic production. During the last 5000 years, their activity showed 57 eruptions, mainly central and explosive, with an output of 4.6 km³ of dense rock, which constitutes a higher production with respect to the average erupted material calculated for the previous activity (0.01km³ per century in the last 4x10⁶ years)[Cruz 2003].



Figure 3.2 Sketch of São Miguel Island, with location names and main calderas and faults above the Digital Earth Model. Lakes are shaded in gray. The NE-SW linear feature is an artefact of the digital model. Tectonics from Camacho et al. (1997) and Digital Model topography from British Columbia University database (2007)

Sete Cidades is an active central volcano with an approximately circular summit caldera. The major fracture system reflects the regional tectonic regime: the Moisteros graben, a NW-SE tectonic structure on the NW flank, is considered a sub-aerial segment of the Terceira Rift. This structure crosses the caldera and controls the location of various scoria cones.

The main eruptive centres have their locations where these faults intersect the other important system which has a main W-E orientation. The eruptive activity started $2 \cdot 10^5$ ybp, alternating lava flows and mostly trachytic volcano-clastic production, with both pyroclastic flows and surges. Three important phases of caldera collapse occurred: 3.6, 2.9 and $1.6 \cdot 10^4$ ybp. Around 5000 ybp the intra-caldera activity changed from magmatic to mainly hydro-magmatic, with 17 eruptions, the last of which occurred 700 ybp and strongly affected the geomorphology of the zone.

Picos is a volcanic system located between Sete Cidades and Fogo. It constitutes a fissural system with a NW-SE direction, and probably is the SE prolongation of the fault system of Sete Cidades, with more than 200 cinder cones coexisting with trachytic domes, and tuff and pumice cones. The oldest known deposits are of 5000 ybp; while the youngest belongs to the historical eruption of 1652.

Fogo volcano is a distinctive cone, about 1000 m high, with a summit caldera about 3 km across and 300 m deep. The main faults on the northern flanks of the volcano have dominant NW-SE and NNW-SSE directions, which possibly reflect the orientation of the Ribeira Grande graben and which are marked by several scoria cones and domes. A group of E-W faults is also present; their intersections with the NW-SE tectonic alignment probably constitute the original location of the main edifice [Guest et al. 1999]. Fogo edifice built over an older submarine lava basement, sampled at a depth of 950 m, with an apparent age of about $2.8 \pm 1.4 \cdot 10^5$ years [Muecke et al. 1974]. The later activity built the edifice through accumulation of lava flows, domes and pyroclastic deposits, mainly of trachytic nature. In the last 4000 years, the growth of the volcano was dominated by explosive eruptions, intercalated with more effusive eruptions on satellite centres on its flanks. Two major caldera forming eruptions have been identified, 46500 and 26500 ybp, while one more recent took place in the last 15000 years. The most recent eruptions are dated 1563 and 1564 AD [Cruz 2003].



Figure 3.3 The caldera of Fogo in a NW to SE view. Photo by Jesús Ibañez (2003)

The ancient *Nordeste* shield of eastern São Miguel comprises lower basalts and final deposits of trachytic composition. The $^{40}\text{Ar}/^{39}\text{Ar}$ age determination obtain an age between 7.8 and 8.8 10^4 years, in contrast to previous attributed K-Ar ages of 1 to 4 $\cdot 10^6$ years. So, the eastern part of São Miguel would be almost contemporaneous to the western portion of the island [Johnson et al. 1998].

Furnas is the youngest of the three stratovolcanoes, and consists of a steep-sided, 8 x 5 km wide, caldera structure. To the east and north, where it lacks an own well-defined structure, it is built on the outer flanks of the Povoção lava complex. On the southern side, its flanks form the coastal cliffs, while to the west they show a constructive structure. The most important fracture systems cross the volcanic massif with a WNW-ESE trend and a normal dip-slip component, as extensional fractures parallel to the Terceira Rift [Guest et al. 1999]. The orientation of several valleys suggests that an E-W system of faults, parallel with the main axis of the island, is also active. Another important fracture system consists of conjugate faults with N-S and (N)NE-(S)SW trends. The NW-SE system seems to control the structural weakness of the

edifice, locating main caldera limits. Anyway, the convergence of the different structural systems is considered responsible of the positions of the main eruptive centres [Guest et al. 1999].



Figure 3.4 The caldera of Furnas in a NW to SE view. Photo by Jesús Ibañez (2003)

Furnas volcano formed mainly $10-1.2 \cdot 10^4$ ybp by voluminous eruptions of trachytic pumice [Moore 1990], alternating episodes of magmatic and phreato-magmatic activity of plinian and sub-plinian magnitude, forming deposits of interbedded ash and lapilli. In the last 3000 ybp several eruptions, mainly phreatic intra-caldera, occurred, with an estimated average time interval of 370 years, while for the last four eruptions, less than 200 years separated each of them. The volcanic centre summit subsided in several stages of caldera collapse that explain the origin of the depression of Furnas village and Furnas Lake. ^{14}C dates aged the $3 \cdot 10^4$ ybp and the $1.0-1.2 \cdot 10^4$ ybp ignimbrites produced during paroxysmal eruptions that proceeded that collapses. There have been two historic eruptions at Furnas volcano, one in 1439-1443 AD, east of Furnas Lake, in the Gaspar crater, and the other in 1630 AD, south of this lake [Guest et al. 1999].

| Year | Description Name or Location |
|-----------|---|
| 1439? | Pico de Ferraria?-Sete Cidades |
| 1439-43 | Pico do Gaspar- Furnas |
| 1563/1564 | Lagoa do Fogo, Pico do Sapateiro (Queimado), Pico de Da Guiomar, Monte Oscuro |
| 1630 | Lagoa Seca-Furnas |
| 1652 | Picos do Fogo I and II |
| 1713 | Pico das Camarinhas |

Table 1 Main historical eruptions in São Miguel Island, modified from Escuer (2006).

3.3.2. *Hydrothermal and Geothermal Activity*

Most of Portugal's geothermal exploration, and all of its exploitation for electric power generation, has been in the Azores Islands. In 2001, four areas having potential for geothermal power generation had been identified in São Miguel: Mosterios (5 MWe); Ribeira Quente (10 MWe); Furnas (80 MWe); and Ribeira Grande (80 MWe) [Huttrer 1996] (Figure 3.2). Geothermal exploration and research evidence two main active fields, in the Ribeira Grande-Fogo and Furnas regions. In these fields, local tectonics seem to control subsurface flow and the alignment of fumaroles and thermal springs [Cruz 2003].

Surface thermal manifestations at Fogo volcano are mainly associated with a NNW-SSE fault system in the northern slope of the volcano, which is probably associated to the Ribeira Grande graben. There are fumarolic grounds and water springs. Chemical analysis of fumaroles [Ferreira and Oskarsson 1999] shows CO₂ (>89 mol %) as main constituent, with H₂S and N₂ as minor constituents (<1 mol %). Ground waters have a composition ranging the whole interval between

meteoric waters, without volcanic contribution, and more volcanic input, with more CO₂-rich waters. Temperatures of hot springs are between 30 and 90 °C, but vary depending on different degree of mixing with rainwater. Several models have been proposed for the Ribeira Grande geothermal field [Carvalho et al. 2006; Gandino et al. 1985; Muecke et al. 1974]. They coincide in the importance of a secondary porosity (that porosity created through alteration of rocks by processes such as fracturing and geochemical modification) and in the presence of both liquid and two-phase aquifers. This geothermal field would be connected to a reservoir between Fogo and the northern coast, hosted by highly fractured, and pyroclastic rocks. The reservoir temperature would reach a maximum of 230-245°C at depths between 800 and 1300 m [Carvalho et al. 2006]. The heat source could be a magma chamber under Fogo volcano or, especially for deeper levels of the field, a regional heat anomaly [Gandino et al. 1985; Ritsema and Allen 2003; Silveira et al. 2006]. Actually, two power plants, with five production and one reinjection well, exploit the productive field of the Ribeira Grande sector (**Figure 3.5**).



Figure 3.5 The geothermal power plant on the northern slope of Fogo. Photo by Jesús Ibañez (2003).

At Furnas, the intense fumarolic activity, mainly concentrated along E-W lineaments, evidences the presence of a shallow aquifer at 100-200 m depth, at temperature of about 160°C. The fumarolic field shows stable composition with CO₂ (95-99% of dry gasses) and minor amounts of H₂S, N₂, Ar, O₂, H₂, CH₄ and probably stable temperature in time. From modelling of the hydrogen-methane relation, a heat source at 750 °C has been inferred, i.e. close to the solidus temperature for the local trachytic rocks [Ferreira and Oskarsson 1999]. This heat source is probably the plutonic remnants of the most recent volcanism below the center of the caldera, although there are no clear signs of direct magmatic contribution in the discharge composition [Cruz et al. 1999].

3.3.3. *Geochemistry*

The geochemistry of the Azores region is complex and has been interpreted as broadly consistent with a hotspot origin for the Azores platform [Haase and Beier 2003; Johnson et al. 1998]. Geochemically, São Miguel is particularly unusual, with strong intra-island heterogeneities [Beier et al. 2006; Jonsson et al. 1999]. Stable isotope and trace element data show a gradual change trending west-east across the island: they are consistent with a MORB-like depleted mantle source in lava flows in the west (related to the MAR emissions) and with an enriched mantle source and higher degrees of partial melting in flows in the east [Johnson et al. 1998]. The variability of the magmas can be due to relatively small mantle diapirs underlying São Miguel, in contrast to a large mantle plume of other hot spot-related islands. Tectonic extensional structures in the lithosphere would dominate the ascent of the magma, imposing the observed variability [Ritsema and Allen 2003; Widom 2003].

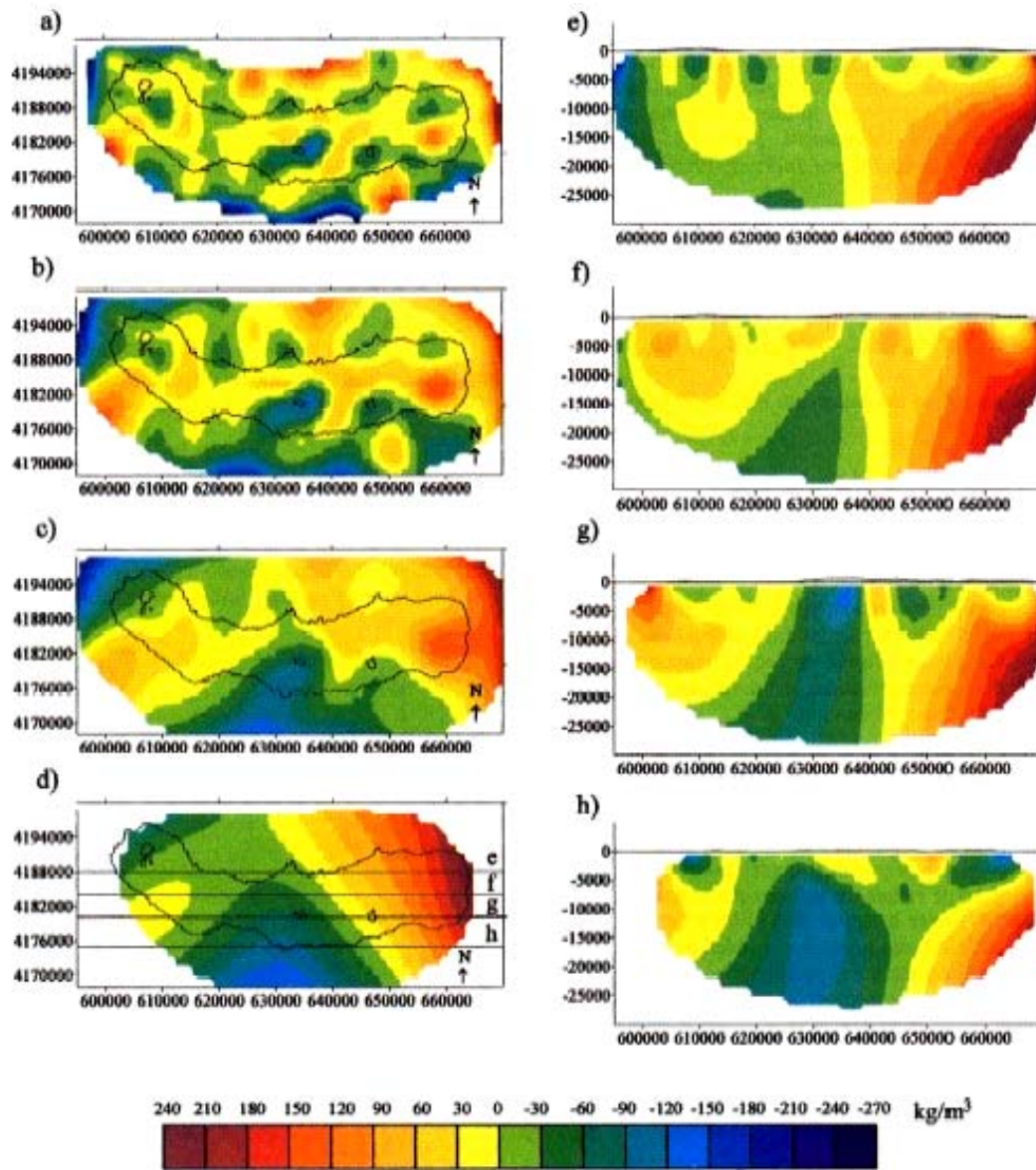
3.3.4. *Gravimetry*

Density structures, and subsurface masses associated to volcanic activity, have been modelled across the island as gravity anomalies [Camacho et al. 1997]. In fact, the gravimetric inversion technique is based on the adjustments of a

three-dimensional model of cubes of unknown density that represents the island subsurface. The global model proposed for the island also includes the individuation of deep masses (**Figure 3.7**). Minima from 20 km in depth, marking an azimuth of 120° are related to the tectonic pattern of the spreading centre of the Terceira Rift. These minima, approaching the surface, tend to disappear and are substituted by several superficial low density areas connected to the recent volcanism. At 8 km of depth, the strongest minima are limited to few areas, such as Fogo and Furnas (see **Figure 3.2** for locations). Likewise, the minimum persists in the Moisteros graben zone, possibly connected to the active fault system. At shallower depth others minima are observed in the area of Povoação and Sete Cidades. They are associated with zones of fissures, hydrothermal alteration or magmatic chambers. Especially for Sete Cidades, Fogo, Furnas, magmatic chambers are imaged at depths of 4-5 km or shallower. Maxima in the same range of depths are also modelled, being the most remarkable of them the ones of Nordeste and Congro. They correspond to old basaltic shields or partly solidified magmatic bodies.

Figure 3.6 Adjusted model of anomalous density contrast of Sao Miguel obtained from gravimetric inversion. Horizontal sections: (a) $z = -1000\text{m}$. (b) $z = -4000\text{ m}$. (c) $z = -8000\text{ m}$. (d) $z = -20000\text{ m}$. Vertical sections W-E in UTM coordinates: (e) $y = 418800$. (f) 4184000 . (g) $y = 4180000$. (h) $y = 417000$. Contour interval of 30 kg/m^3 . Modified from Camacho et al. (1997). 

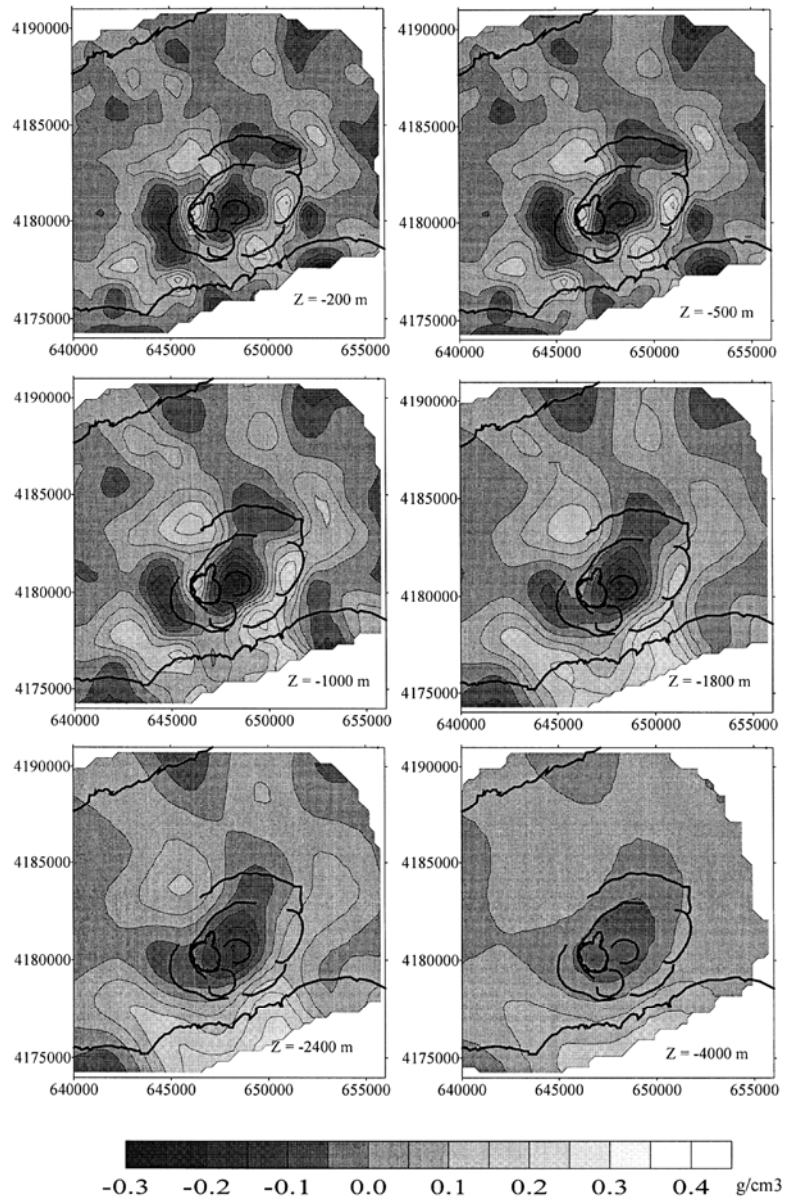
3 - Central São Miguel



The spatial distribution of anomalous bodies inside Furnas caldera (**Figure 3.7**) has been evidenced by removing the regional trend [Montesinos et al. 1999]. There are two important shallow, low density anomalies. One of them is in correspondence of Pico do Gaspar, east of Furnas Lake, which was the site of the 1439-43 eruption. At shallow levels, this anomaly is interpreted as a low-density silicic caldera infill, mainly due to collapse processes. In depth, this anomaly shifts toward the Furnas Caldera, to the north, which was the centre of the 1630 eruption. It has been suggested the existence of magma accumulation below the caldera, responsible for both the 1439-1443 and 1630 eruptions. The other anomaly is located on the outer western caldera wall, west of Furnas Lake. It has a SE-NW elongated shape. It could represent volcanic products from several eruptions which occurred after the formation of the main caldera from radial and concentric fractures. The main positive anomalies correspond to basaltic areas of high density, on the southern coast of Furnas and locally at the base of the eastern caldera wall, east of Pico do Gaspar.

Figure 3.7 Adjusted model of density anomaly of Furnas area obtained by gravimetric inversion. Depths of horizontal section are indicated in figure. Modified from Montesinos et al. (1999). 

3 - Central São Miguel



3.3.5. *Geodesy*

The Global Positioning System (GPS) has been used to measure a network of station on Furnas volcano edifice during 1993 and 1994 [Sigmundsson and Tryggvason 1995]. Strain analysis indicates areal dilatation of 0.84 ± 0.40 μ strain/y for the volcanic edifice (**Figure 3.8**). This deformation is explained as a slight inflation of the volcano. The location of the centre of inflation is located in the northern part of the caldera, and the size of the affected area suggests a depth for it of more than 1 km. It can be explained both with fluid accumulation in a deep hydrothermal system beneath the caldera or increase pressure for magma flowing toward shallow depth.

A GPS Survey during 1997 [Jonsson et al. 1999] confirms this trend, outlining that rates of deformations are low (< 7 mm/y). Anyway, another hypothesis, beside the inflation of Furnas Caldera, is suggested for the observed deformation pattern. It invokes a combination of two processes: plate divergence between the Eurasian and Africa plates (with a 75% of the 4 mm/y full plate spreading accommodated over the 10 km width of São Miguel) together with a deflation of the Furnas caldera.

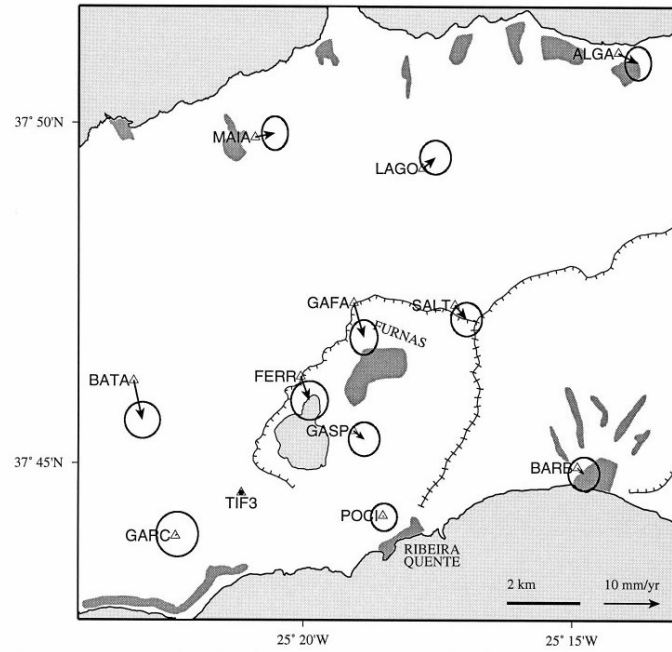


Figure 3.8 Horizontal displacement rates for 1993-1997. The TIF3 station is used as a reference station for the Furnas volcano network. Error ellipses indicate 95% confidence level. Modified from Jonsson et al. (1999).

GPS stations at Fogo shows displacements toward its caldera, indicating slight deflation of the volcano (**Figure 3.9**). The deflation is referred to several processes such as pressure decrease in a shallow magma chamber beneath Fogo, or extraction of hot water and steam by a geothermal plant in the north of the volcano edifice [Jonsson et al. 1999]

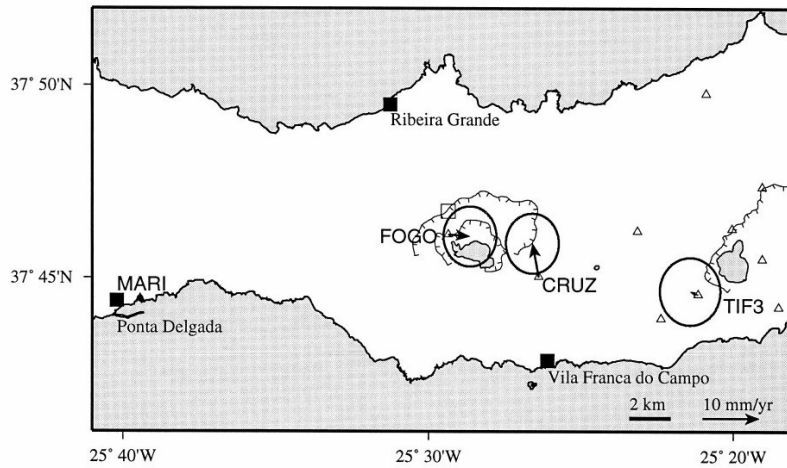


Figure 3.9 Horizontal displacement rates for 1993-1997. The MARI station is used as a reference station for the Fogo volcano network. Error ellipses indicate 95% confidence level. Solid squares are main towns. An open square denotes a geothermal power plant that is located about 1 km north of the station Fogo. Modified from Jónsson et al. (1999).

3.3.6. Tectonics and Seismology

Several investigations in São Miguel have evidenced the importance of the regional control on the distribution of tectonic elements [Cruz 2003; Gandino et al. 1985; Haase and Beier 2003; Miranda et al. 1998]. A recent study [Trota et al. 2006] indicates that the west and the east parts of the island are moving apart along the existing faults towards the WNW and ESE, respectively, to accommodate the regional tectonic plate motions. Such local displacement would evidence the strike slip component of the global motion, compatibly with part of the focal mechanisms calculated in the area (**Figure 3.10**) [Buform et al. 1988] and the existence of strike-slip faulting with two main orientations of 110-120°N and 140-150°N observed in the bathymetry [Lourenço et al. 1998].

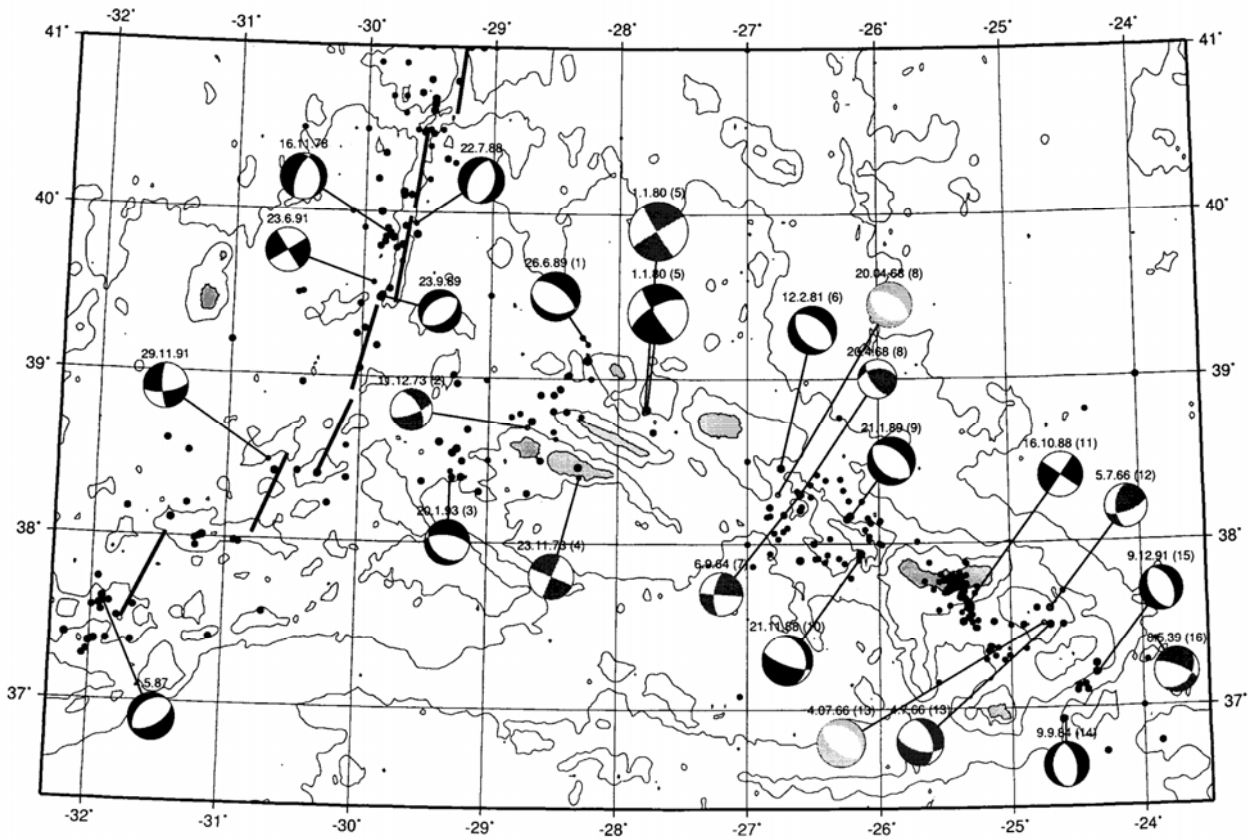


Figure 3.10 Seismicity map ($M > 4.0$) and focal mechanisms in the Azores region from 1928 to 1998. From Buforn et al. (1998). Focal mechanism symbols are shaded in different gray depending on the original database source

In this setting, Central São Miguel constitutes one of the most active seismogenic region in the Azores and it is crossed by different fault systems, mostly trending NW-SE and E-W. The local seismic network records an average of a few thousand earthquakes per year, only partly located (**Figure 3.11**). A substantial number of them are swarms of local, low-magnitude earthquakes located in the area between Fogo and Furnas [Escuer Tello 2006; Gongora et al. 2004].

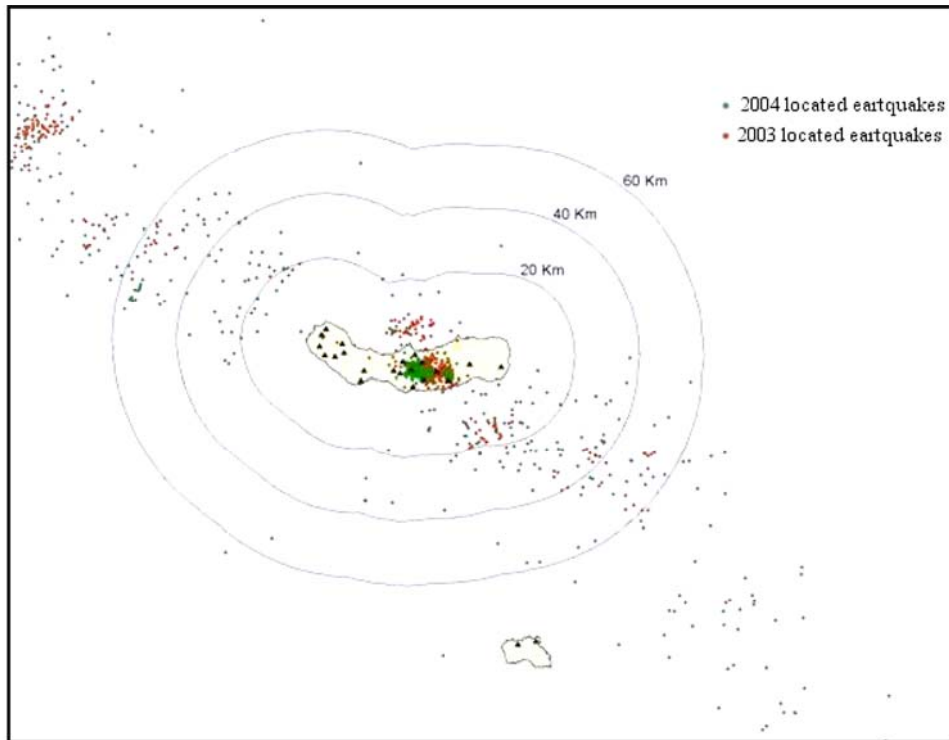


Figure 3.11 Located earthquakes and seismic stations (triangles) by University of Azores and SIVISA seismic network (Wallenstein, personal communication)

Although the tectonic control seems important, to explain the observed deformation in São Miguel, it has to be addressed additional local deformation, possibly of volcanic origin [Trota et al. 2006]. Moreover, a recent work [Luis 2006], using data from the ISC catalogue for the period 2001-2004, shows that most seismic swarms in Central São Miguel do not fit an Omori law. Furthermore, the time-magnitude relations demonstrate that they have no associated main-shock events. These results suggest that the swarms are not generated by a tectonic-driven main-shock/after-shock mechanism.

The most likely explanation is that Central São Miguel earthquake swarms have a volcano-tectonic origin. This fact is supported by preliminary analyses of the seismicity recorded during the 2003 *E_RUPTION* seismic survey (see later).

These analyses reveal a relationship between microearthquake swarms and local fault systems in Central São Miguel [Bonagura et al. 2004; Silva et al. 2005]. The widespread distribution of epicenters between Fogo and Furnas and the spatio-temporal evolution of the seismicity were attributed to the presence of hydrothermal fluids within pre-existing tectonic faults. Also the Global Volcanism Program, which includes an on-line summary of main activity of São Miguel island (<http://www.volcano.si.edu/world/volcano.cfm?vnum=1802>), further confirms the occurrence of swarms of microearthquakes beneath the NE flank of Fogo in May 1983, and later during 1988.

The relationship between seismic activity and hydrothermal circulation has been widely confirmed [Dawson et al. 1985]. An average V_p/V_s ratio of 1.53 and 1.62 has been obtained by using local and regional earthquake data, respectively, recorded during a temporary seismic survey in 1983. This estimate pointed to values lower than the global average for crustal rocks, which is close to 1.73 [Chatterjee et al. 1985]. Moreover, P-wave arrival time delays for seven regional earthquakes have been calculated by fitting the arrival times to plane wavefronts. Positive delays are located mostly around Fogo volcano, which suggests the presence of a low-velocity volume roughly centered at Fogo (**Figure 3.12**). Both the low V_p/V_s ratio and the presence of low-velocity regions, possibly indicated extended active geothermal systems in Central São Miguel.

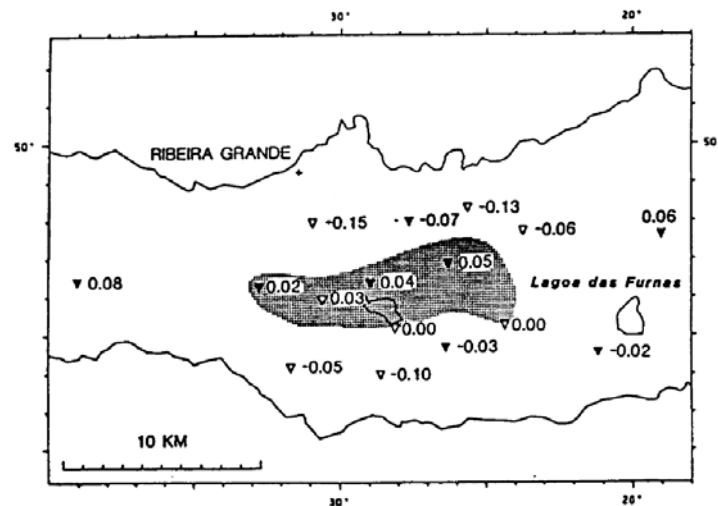


Figure 3.12 average plane-wave residuals using 7 regional events. The stippled area outlines the area of positive (delayed) residuals. Modified from Dawson et al. (1985).

Nevertheless, the occurrence of long-period events and volcanic tremor has not been reported so far in the area. These earthquakes are produced by the resonance of fluid-filled cavities within the volcanic medium [Chouet 2003]. Given the extensive geothermal activity in São Miguel, small amplitude, long-period seismicity of hydrothermal origin is likely to occur. It has been probably un-detected up to now, due to the lack of specialized instrumentation (i.e. seismic antennas [Almendros et al. 1999]) and/or adequate coverage near the geothermal areas. Recent improvement of instrumentation, with the deployment of a small aperture seismic array in the zone of Congro (A. Montalvo, personal communication), is expected to return interesting information about long-period seismic activity. Interestingly, the lack of noticeable volumetric, fluid-related seismic sources in São Miguel, which could be detected by the local network, probably indicates that massive magma transport is not occurring in the area.

In the 70s, seismic profiles were carried out with geothermal interest in Azores, in order to study the shallow structure [Senos and Nunes 1976]. A total of 20 explosions in São Miguel Island and 30 in Terceira Island were recorded by a seismic array of 35 stations. The profiles show a strong heterogeneity of velocity structure at shallow levels, especially in geothermal areas (**Figure 3.13**). For example, below Furnas the contours marking different velocities deflect toward greater depths, indicating lower velocities. Based on these studies, a 1D seismic crustal model (“Terra Açores”, TAC) was deduced for the hypocentral location routine of University of Azores [Escuer Tello 2006].

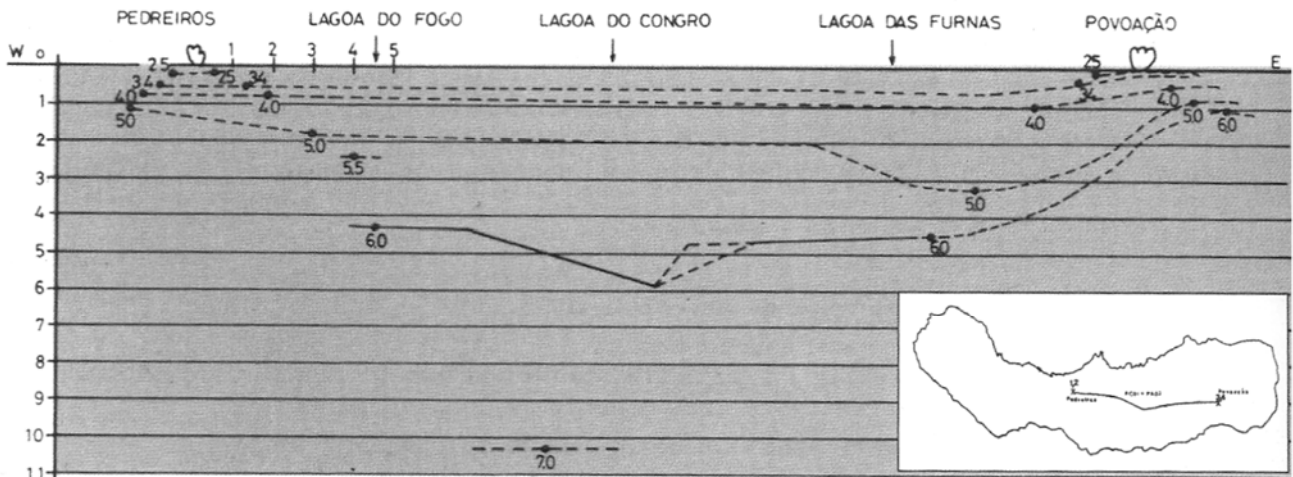


Figure 3.13: Seismic profile across Central São Miguel, as indicated in the small box in the corner. Modified from Escuer, (2006).

3.3.7. Resuming the ‘State of the Art’

Although Central São Miguel volcanoes have not erupted since the 17th century, the area is subject to seismicity. Its origin is mostly related to the approximately WNW-ESE fault systems dominating the regional tectonics [Buform et al. 1988; Madeira and Ribeiro 1990]. However, occasional clusters of earthquakes, detected in Central São Miguel [Escuer Tello 2006; Luis 2006], are commonly associated with the volcanic and/or geothermal activity of the zone. Actually, together with seismicity, another indication of active volcanism is the presence of vigorous hydrothermal systems. Thermal springs and fumaroles are distributed along fault systems crossing Fogo and Furnas [Cruz 2003; Ferreira and Oskarsson 1999]. This hydrothermal circulation points to the possible existence of heat sources in depth, for example below Furnas caldera [Camacho et al. 1997]. The study of gravity anomalies in Central São Miguel relates density contrasts to the existence of magmatic bodies in depth (as below Furnas and Fogo) and to deposits both of high and low compactness at surface

[Montesinos et al. 1999]. Geodetic surveys reveal a deflation for Fogo zone while do not supply a clear indications for Furnas situation [Jonsson et al. 1999; Sigmundsson and Tryggvason 1995]. Both the presence of magma and geothermal systems are indicated as responsible of an unclear deformation regime [Trota et al. 2006].

3.4. . *Seismic experiment*

3.4.1. *Objectives*

At present, little is known about São Miguel seismicity, almost in comparison with geology, geochemistry and other geophysical disciplines. As far as it is known, most of the local earthquakes are associated to brittle shear failures along several tectonics lineaments affecting the island. However, the direct role of magmatic-hydrothermal fluids in controlling these signals is not excluded, especially for those active areas located in the proximity of well established geothermal fields. The *E_RUPTION* experiment was aimed to multiple objectives, which included a precise earthquake location, the identification of the source mechanisms and the relationship with geothermal processes and the recognition of volcanic signals such as tremor or long period events. Beside the attempt to quantify the seismic activity of long period by using specialized instrumentation [Cipollini 2002], their proximity of geothermal power plants to the inhabited areas of Furnas and Ribeira Grande increased the interest toward the study both of natural and induced seismicity. Finally, among main goals, there was the elaboration of a seismic velocity model for the region.

After a short presentation of the field work carried out during the experiment, in this work we describe that part of the São Miguel study directed to the precise earthquake location and the elaboration both of a 1D and 3D tomographic velocity models for the studied region

3.4.2. *Institutions*

The database used for this work proceeds by the field part of the experiment which took place with the collaboration of several European institutions. As parts active in the field deployment and data collection, we can remember (with number

and type of provided instruments): (1) IAG, Instituto Andaluz de Geofísica, Granada, Spain (1+3 small aperture seismic array of mallAG type). (2) IGN , Instituto Geografico Nacional, Santa Cruz de Tenerife, Spain. (3) INGV, Istituto Nazionale di Geofisica e Vulcanologia, Naples, Italy (11 stations of Marslite type)(4) MNSN, Museo Nacional de Ciencias Naturales, Madrid, Spain. (5) UAC, Universidade dos Açores, São Miguel, Portugal (with 21 stations of diverse types).

3.4.3. *Experiment Design*

Between April 4 and July 15, 2003, a temporary network of 14 stations equipped with both short-period and broad-band instruments, as well as three small-aperture seismic antennas, was deployed in São Miguel to expand and complete the permanent network operated by University of Azores [Saccorotti et al. 2004].

The region object of study was covered with a dense net of stations, with a station density of 0.03 station/km² for the whole island and 0.1 station/km² for the central part of the island (Central São Miguel). The zone between Furnas and Fogo, in fact, was designed for the denser network because it was that pointed out by the regional seismic monitoring as the most active. Moreover, abundant and vigorous geothermal fields widen in this region and constitute a further reason of interest.

Station positions were selected on the base of their isolation and accessibility, taking in account that most locations were affected by rain flood during spring season. The total number of recording seismic stations was 33, but data of some of them had to be excluded from our study due to different reasons. For example, among stations (see **Figure 3.14**):

(1) PSM (not in **Figure 3.14**): it was located outside São Miguel. (2) SE2, SE3, SE4, SEA: they were located in the western São Miguel, far from the central studied area. The inclusion of data proceeding from these stations would increased the extension of the investigated region in order to include them, without carrying much more information to our knowledge (as we are going to see, this would increase the unknowns number with respect to the data number). (3) AZ22: no useful picking were retrieved from this station. (4)AZ23: no data proceeded from this station, probably due to bad performance.

3 - Central São Miguel

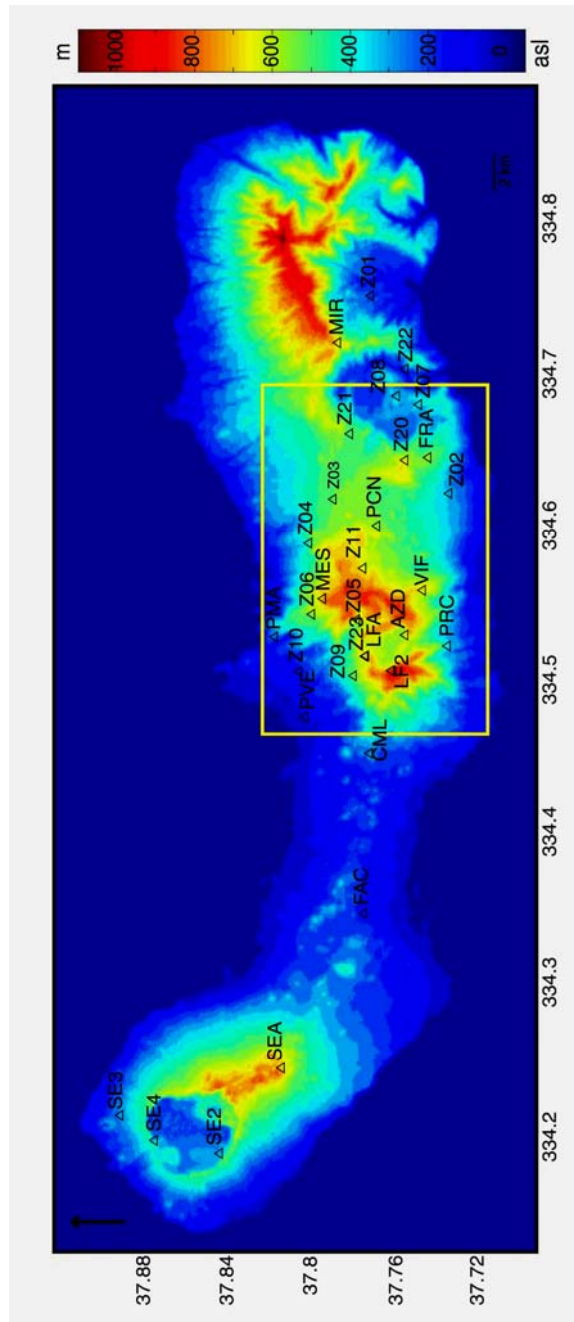


Figure 3.14 Topographic map of São Miguel Island, with location of stations deployed for the seismic experiment. A square marks the area selected for the 3D velocity inversion. The colour interval corresponds to 50 m

3.4.4. Station Types

The seismic stations owed to different institutions and were of different type and technical characteristics (**Table 3**). Thirty-three seismic stations recorded in continuous mode during the *E_RUPTION* seismic experiment. They were distributed among 10 Lennartz Marslite, 1 maliAG (actually 4, see later), 1 M24 and 20 ‘variegated’ types (from home-made stations to analogical stations) of the local seismic network.

3.4.4.1. Lennartz Marslite

The Marslite seismic stations are data acquisition systems of 20 bits of dynamical range working with three channels. They have one separate ADC for each channel, with a sampling rate of 125 Hz. The preamplifiers work on all three inputs simultaneously and can be set up by the user. There is a preamplifier with four 12 dB steps. Since digitisation always takes place at a fixed sampling rate of 4 kHz, the digital data stream need to be decimated to the final sampling interval, after the signal has been digitally low-pass filtered by a FIR (Finite Impulse Response) filter. The system is completed with a GPSlite time signal receiver. The recording is on rewriteable magneto-optical disks of 540 Mb, in binary format. The acquisition systems were programmed to record in continuous mode. The power supply was provided from an external unstabilized 12 V DC supply, later stabilized and changed to the required voltages by the system.

They were equipped with either short period or broad band instruments. The short period seismometers (Z01, Z02, Z03, Z04) were Lennartz LE-3Dlite MkII 1 s natural frequency. The broad band seismometers were Guralp CMG40T, 0.016-50 Hz natural frequency (Z09, Z10) and Lennartz LE-3Dlite 20 s (Z05, Z06, Z07, Z08)).

3.4.4.2. *MallAG*

The mallAG modules are high resolution (24 nominal bits) with an acquisition system that can work with a maximum of 12 sensors, in array configuration. The sample frequency was configured to 100 s/s and the ganancy to 1. Data acquisition is performed by 4 SEISAD18 plates, each of them managing 3 analogic channels. The plates are synchronized thanks to a PLL plate, whose time pulse is supplied by a GPS (Garmin 35-HVS) connected with a serial port. Digital data from 4 plates are passed to a commercial PC (Lippert Cool Roadrunner II) with low energy consumption, and are finally stored on a 30 GB USB hard disk. In addition, the system has a hard disk of 10 GB for the operating system and the temporary storing of a data buffer that is transferred to the external hard disk every 6 hours. The central control of the process is achieved by means of a low power industrial PC, which works under Windows 98. The acquisition program is Seislog, a free software developed by the University of Bergen (Norway), configured for continuous recording performance. The acquisition software generates files in SEISAN [Havskov and Ottemoller 1999] format, with ring buffers size of 10 minutes, characterized by a timing info in the header of each packet.

Physically, the mallAG systems are composed of a plastic suitcase which contains the adquisition system and which has to be connected through military-grade connectors to an antenna for the reception of the GPS signal and to a 'knot' where cables from several channels can be handed without risk for the acquisition system. The same case is connected to 12 V batteries for the power supply.

The array modules used as antennas were supplied with vertical L-28B Mark Products sensors, preamplified and with 4.5 Hz natural frequency. Electronic extension allow all the sensors to achieve a flat response curve in the 1-50 Hz frequency interval. In this manner, their response is almost identical to other 1Hz commercial sensors, being their cost much lower. Some of them were equipped with three-component L-4C Mark Products sensors, without preamplifier.

These stations were deployed as both dense seismic antennas and three component independent station. As antennas, they showed a discontinuous operation. Main problems were due both to physical weakness of these systems, aggravated by extreme weather conditions and to inability of the aquisition system to manage a huge amount of data, as proceeding from the 12 channels of the array continuously recording. These difficulties mostly affected the timing systems, which was unable to synchronize data. For these reasons data from 3 antennas, also if still useful for waveform-based analysis, have to

be rejected for any study where absolute time is an essential assumption, such as in a first-arrival tomography. In this sense, we decided not to use mIIAG data except for those records proceeding from the independent station with only 3 channels configured (AZD). This system, actually, performed well in the field and its data, after laboratory checks, have been introduced in this work.

3.4.4.3. Local network

Azorean seismic stations belonged to the regional network controlled by SIVISA and to the 'seismic mobile instruments' of the University of Azores. These last modules were equipped either with commercial data logger (Lennartz M24) or manufactured systems (16 bits instruments, by Ramon Ortiz; SEISAD18, by LSV laboratories). They are equipped with short period sensors (Lennartz LE3D; Mark L-28 or Sprengnether S-6000, all fixed to 4x gain) and programmed to continuous recording in different format (see **Table 2**).

| Station Name | Z20 | Z21 | Z22 | Z23 |
|------------------|---------------|-----------------|---------------|--------------------------|
| Data Logger | Lennartz M24 | R.Ortiz 16 bits | SEISAD 18/LSV | SEISAD 18/LSV |
| SamplingRate (s) | 0.01 | 0.02 | 0.01 | 1.01 |
| Sensor | Lennartz LE3D | 3D Mark L-28 | 3D Mark L-28 | 3D Sprengnether S6000 |
| f (Hz) | 1 | Extended 1 Hz | Extended 1 Hz | Extended 0.2 Hz |
| Data format | GSE | SIS | SEISLOG | SEISLOG |

Table 2 Technical characteristics of seismic stations deployed by UAC as temporary network.

The other stations belonged to the seismic network of SIVISA. Those stations whose data we used were analogical stations. They were equipped with short period sensors (Lennartz LE3D; Mark L-4 or Sprengnether S-6000, all fixed to 4x gain and

extended to 1 Hz) vertical or three components and with high ganancy. Sampling rate were 62.5 s/s [Escuer Tello 2006; Gongora et al. 2004].

| Sensor name | C | f_0 | Dam | Mass | Rg | CDR | Rc | G | K | Dyn | Mov |
|--------------------|---|---------|-------|------|------|------|----|-----|------------|-----|-----|
| Sprengnether S6000 | 3 | 2.0 | | 0.5 | 280 | | | 45 | 0.44 | | |
| Mark L28 B1 | 1 | 4.5 | 0.48 | 0.02 | 395 | | -- | 35 | -- | | 2.0 |
| Mark L4C | 1 | 1.0 | 0.28 | 1.0 | 5500 | 8905 | | 276 | | | |
| Sensor name | C | f-range | Out V | In V | I | G | W | | Resolution | Dyn | |
| Guralp CMG-40T | 3 | 0.03-50 | 10 | 12 | 50 | 3200 | 5 | | > NLNM | 145 | |
| Lennartz LE-1D | 1 | 1.0-80 | -- | 12 | 3 | 400 | 1 | | 3nm/s,1Hz | 120 | |
| Lennartz LE-3D/20s | 3 | 0.05-40 | | 12 | 50 | 1000 | 7 | | 2nm/s,1Hz | | |

Table 3 Overview of sensors used for the seismic experiment. *C*: Number of components; f_0 : natural frequency (Hz); *Dam*: open circuit damping; *Mass*: Mass (Kg); *Rg*: generator coil resistance (ohm); *CDR*: critical damping resistance (ohm); *Rc*: calibration coil resistance (ohm); *G*: generator constant (V/ms^{-1}); *K*: calibration coil motor constant (N/A); *Dyn*: dynamic range (dB); *Mov*: free motion of the mass (mm). *f-range*: frequency range in which the response is flat (Hz); *Out V*: max voltage out (V); *In V*: supply voltage (V); *I*: current used (mA); *G*: generator constant (V/ms^{-1} or V/g); *W*: weight of sensor (kg); *Resolution* can be given in nm/s, or whether the noise is above or below NLNM (New Low Noise Model) for most of the pass band. Modified from [Havskoz and Alguacil 2004]

3.4.5. *Data processing*

3.4.5.1. *Data Formats and Software*

One major difficulty in the early stages of this work arose because data from different recording systems had to be merged for a joint analysis. Data from Marslite stations were recorded as binary and stored as SAC files [Goldstein et al. 2003]. On the other side, data of maliAG were originally recorded in a system format easily converted and managed as SEISAN format. Also data of local network were returned in a SEISAN format, but dimension (i.e. time duration), headers and file names were completely different.

The selected common format was SAC, due to its handy nature, to the complete information contained in the header and the widespread diffusion of the processing software for its analysis. Moreover, this software combines several tools for seismological data processing under a LINUX/UNIX environment.

As we are going to explain in the following chapters, data selection for quality and location implies that from the starting database of 756 earthquakes observed among 33 stations, we considered 331 earthquakes in 26 stations to obtain the starting 1D model (Chapter 3.5). In this model, only 426 earthquakes found an optimized location (Chapter 3.6), and finally only 289 had location jointly inverted with the 3D velocity model, distributed among 20 stations (Chapter 3.7).

3.4.5.2. *P and S Arrival Time Determination*

With the help of this analysis package, we analyzed the records of seismicity and manually determined the P- and S-wave arrival times on the waveforms. S arrivals were picked on the horizontal components.

The recognized earthquakes mostly had a time difference between the arrival of P and S waves smaller than 3 s, and were hence considered as earthquakes of local type (**Figure 3.15**). Regional and tele-seismic events were found out as well, on

the base of their P-S difference timing, and on the waveforms and spectral content. Only local earthquakes were taken into account for our analysis.

Observation weights, both for P and S phases, were assigned according to the INGV standard procedure: 0, 1, 2, 3, 4 are assigned respectively to time errors <0.02, 0.02-0.05, 0.05-0.1, 0.1-0.2 and >0.2 s. First motion polarities for P arrivals were determined only for those phase onset were they were clear, this means, usually for 0, 1, 2 weights.

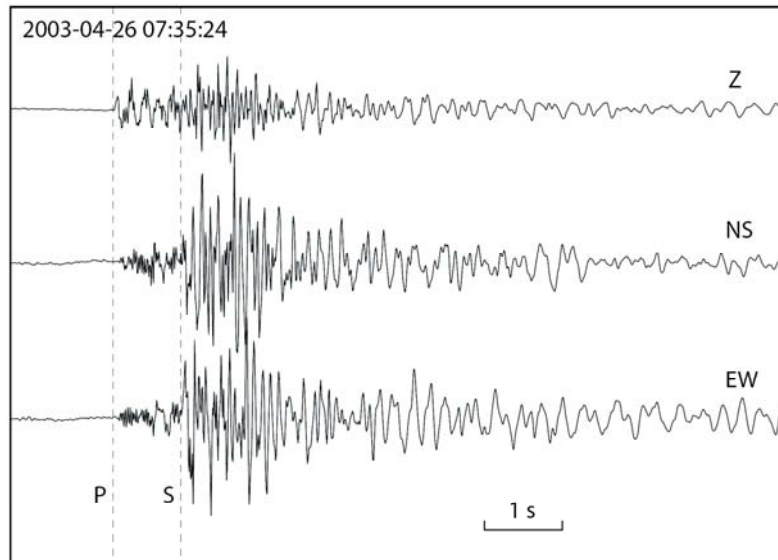


Figure 3.15 Example showing the original seismograms recorded in a short period, three-component station. Starting time of record and P and S-phase arrivals are also indicated.

3.4.5.3. *Data Quality*

Several steps lead to the final 3D tomography, through (1) a data selection. (2) a search of high precision earthquake locations and (3) of a starting velocity model.

The first and main difficulty was the selection of input data. In fact, we observed that:

(1) The natural activity was intense but of low magnitude, and so hardly recorded by the whole seismic network. For the same reason, the quality of recorded signals was often low, with low signal-to-noise ratio, and hence un-useful waveforms.

(2) The data record continuity was often interrupted: bad weather conditions damaged stations, and before they could be repaired, some hours of record were lost.

(3) As seen in the previous section, seismic stations were of different type and with different configuration. For example, the regional network was mostly of one component, there were both short period and broad band stations, the sample rate was not the same for all digitalizers, and periods of functionality were interrupted and often did not overlap for different stations).

And, as from a tomographic point of view, we considered as additional difficulties:

(4) The earthquakes strongly clustered between Fogo and Furnas, while nearby regions were characterized by medium-to-low seismic activity. Earthquakes mostly occurred as swarm, features which (see chapter about 3D inversion method) adds unknowns to the inversion without carrying much more information.

(5) Many stations belong to the regional network of seismometers, with an architecture planned for the seismic surveillance. This means that this configuration was not the optimum to record the seismic activity that took place during the survey. Stations were not homogeneously dispersed around and above the studied area, often too far from it and with low amplification characteristics.

(6) Last but not least: data belong to several organizations. Too much time has to be wasted to collect them and related information, such as station characteristics, location, formats.

This means that data had to be severely checked for their quality, and considered by their technical variability. Data were accurately selected, in order to introduce only high quality input and to make the studied volume of reasonable dimensions with respect to the information amount. The starting database was often re-checked, re-selected and limited by an increasing severity of selective parameters. In such a way, direct consequences of this selection are the robustness of

results but also the reduction of input data amount. For all these reasons, we take special care of testing the effect of starting database on the analysis results.

3.4.6. Previous Results from the Experiment

3.4.6.1. Seismic data

During the survey, the seismic network recorded more than one thousand earthquakes. Part them was used for preliminary studies aimed to the definition of activity style and the most notable features of the local seismicity.

Among main conclusions, a volcano-tectonic seismicity of local origin was recognized with magnitude-durations lower than 2.5 (**Figure 3.16**)[Chouet 2003]. An average rate of 5-10 earthquakes per day was detected, except for a single swarm in April 26-27, when more than 160 earthquakes occurred in a few hours (**Figure 3.16**).

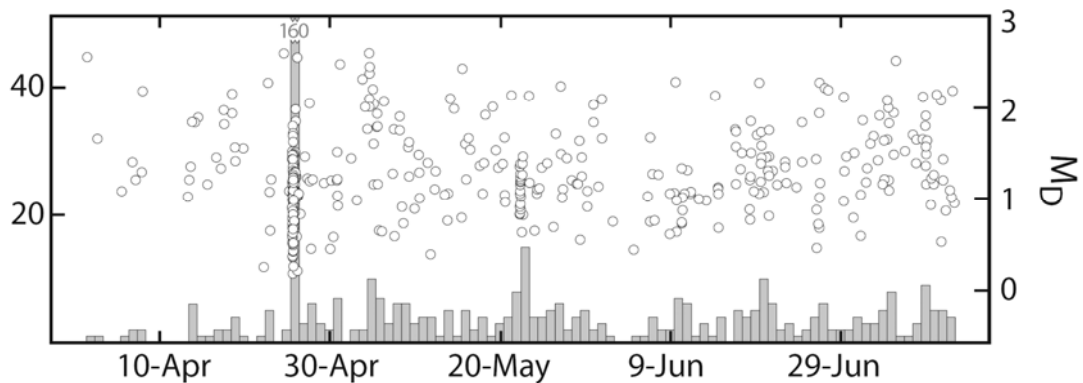


Figure 3.16 Histogram of the daily number of earthquakes recorded by the temporal network during the 2003 seismic experiment at São Miguel. On the same figure, the magnitude-duration values for the same events are indicated. From Saccorotti et al. (2004).

This clustered activity was analyzed by [Saccorotti et al. 2004] and [Bonagura et al. 2004] (**Figure 3.17**). In a preliminary earthquake location, the major seismogenetic zone was located in a small volume NE of the summit Fogo crater, at depths ranging between 1 and 6 km bsl. The temporal pattern of energy release did not show the typical main shock-aftershock sequence. The Principal Component Analysis and hypocenter-collapsing techniques (Best Estimate Method) offered indications about the significant planes of earthquake location and were consistent with the focal mechanisms obtained from P-wave polarities. There was a major NW-SE striking, SE dipping fault affecting the eastern slope of the Fogo edifice. The widespread part of epicentres otherwise indicated a complex pattern of faulting, probably related to an intense fluid circulation of hydrothermal origin. Moreover, these fault segments were indicated as possible sites for hydrothermal explosions. This study also analyzed the V_p/V_s ratio with a modified Wadati technique, and resolved a value around 1.7 for Central São Miguel. The explanation for this low value again pointed to the development of geothermal activity and circulation of boiling fluids.

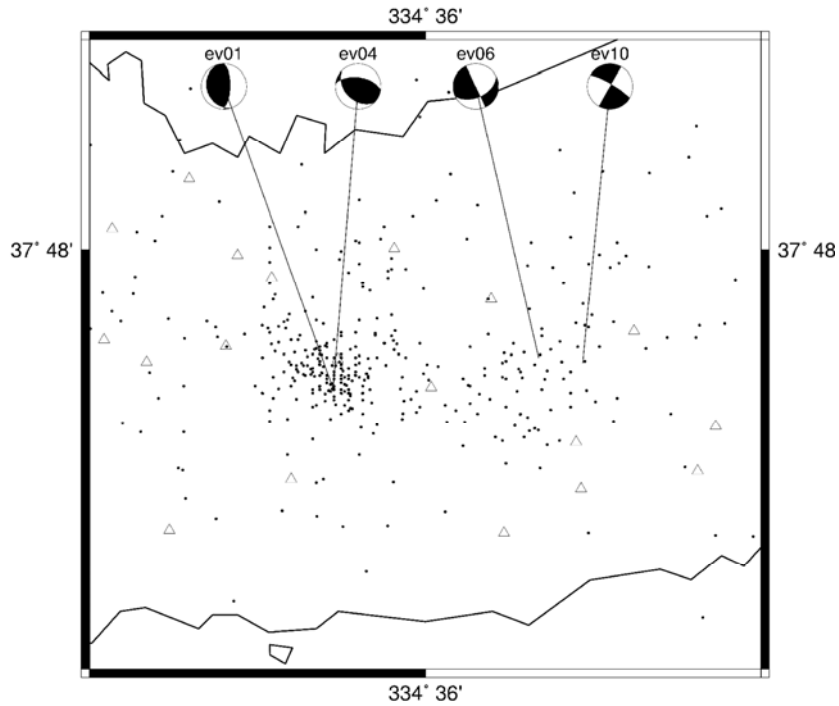


Figure 3.17 Fault-plane solution obtained from P-wave polarity data of the four best-located events. Dots are epicentres corresponding to a selected subset of hypocenters. From Bonagura et al. (2004).

Through a cross-correlation analysis, six different groups of multiplets have been identified [Silva et al. 2005], with a correlation coefficient as high as to justify their affiliation to the same seismic family of earthquakes. For each family the dominant frequency was determined, around 7-9 Hz. Considering typical P-wave velocities, wavelength on the order of 300 to 600 m were observed. The data also suggested that, for each family, the hypocenters spanned maximum distances in the order of 75-150 m. The highly modified waveforms for some families among different stations, pointed to a strong influence of the propagation structure in shaping the spectral features.

3.4.6.2. *Minimum 1D Velocity Model and High Precision Locations*

The work which preceded the elaboration of a 3D tomography implied an accurate input preparation. When the starting database is of reduced dimension, this groundwork is definitely vital. For the same reason so much time was dedicated both to the elaboration of the starting 1D model and precise earthquake locations.

Hence, main steps in the database preparation included, after the visual P and S-phase arrival picking (Chapter 3.4.5.1) (1) calculation of a 1D velocity model. We used the *VELEST* [Kissling 1995] algorithm and preliminary earthquakes locations(Chapter 3.5). (2) a precise earthquakes location. We used the *NLloc* software algorithm [Lomax et al. 2000] and the previously obtained 1D velocity model (Chapter 3.6).

The detailed explication of the used software is presented in the Theory section (Chapter 2).

3.5. 1-D Velocity Model

3.5.1. Method

After the selection of data and the picking of P- and S-wave arrival times, we needed a velocity model to use as starting structure for the 3D inversion. This starting model, called *minimum 1D model*, is usually a simple one-dimensional model which is ‘translated’ in the three-dimensional version to be enclosed in the 3D inversion. It is recommended [Kissling et al. 1994] to consider as natural starting point for a 3D inversion, a model that itself represents the least squares solution to the linearized relationship that relates travel times residuals and adjustments to the hypocentral and velocity parameters. This preliminary 1D velocity model was obtained using the code *VELEST*, that determines the velocity structure where calculated travel times best fit the observed phase arrivals (Chapter 2.2.2).

3.5.2. Input Data

The inversion for the Minimum 1D model needed a starting model and preliminary starting location as well. As starting velocity model, *a-priori* model, for São Miguel Island, we used the model TAC ('Terra Açores'). This is the velocity model commonly used by SIVISA to routine earthquake locations, obtained from seismic profiles [Senos and Costa 1978]. It is a simply velocity model of few layers of increasing P wave velocity with depth (**Table 4**).

| DEPTH | V _p | V _s |
|-------|----------------|----------------|
| 0.0 | 2.40 | 1.43 |
| 0.5 | 4.10 | 2.44 |
| 2.2 | 5.40 | 3.21 |
| 5.4 | 6.80 | 4.05 |
| 11.9 | 7.80 | 4.64 |

Table 4 TAC velocity model from seismic profiles, as used by the national geological service SIVISA. Depths are in km, velocities, for P-wave (V_p) and S-wave (V_s) in km/s.

We used only P-phases to obtain the minimum 1D model, as they had good onset in seismograms and small picking errors. The dataset was hence formed by a subset of the 426 located earthquakes provided by the location program in the TAC model (**Figure 3.18**), obeying precise quality conditions: 180° as maximum gap (angular distance, centered in the epicenter, between two seismic stations,) This is the gap which allows earthquakes to be well located by surrounding stations, without alignment with them, which would introduce uncertainty in location along the perpendicular direction.; 7 as minimum number of picked phases (to ensure at least 4 P-wave arrival times); 1 as maximum RMS (root mean square) after their preliminary location. After this selection, earthquakes used for the 1D velocity inversion were 331, with a 2500 observations, among 26 stations.

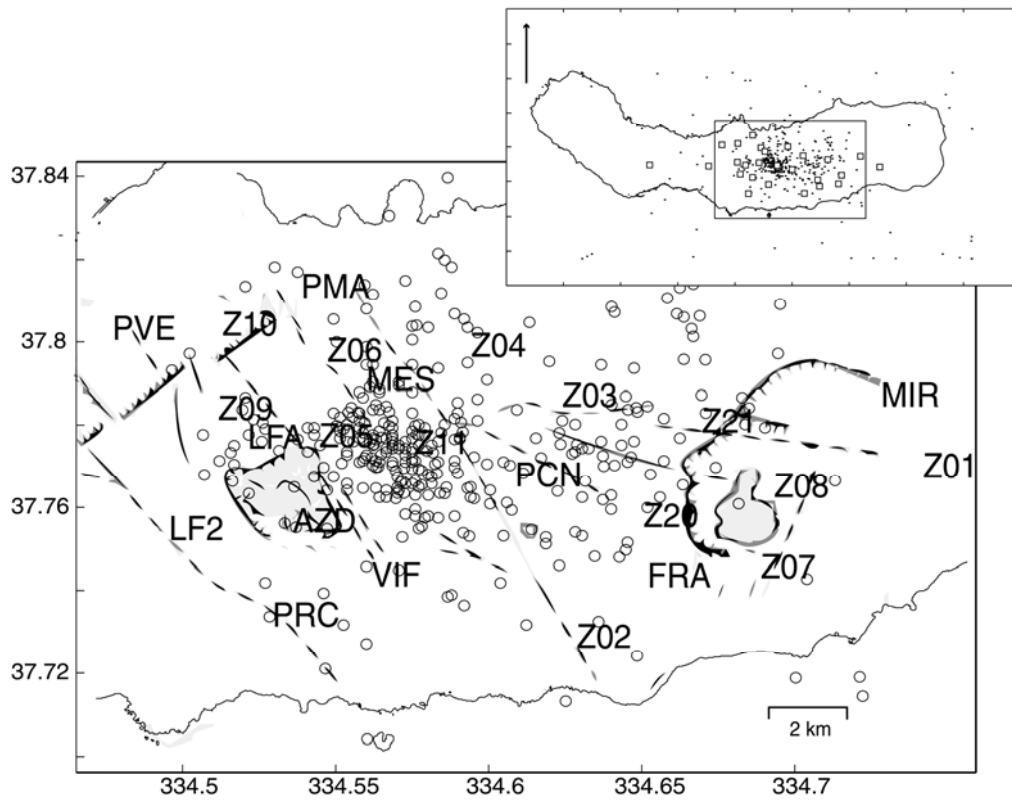


Figure 3.18 Zoom on seismogenic area in Central São Miguel, with preliminary located earthquakes (TAC model (circles) and main inferred tectonic lineaments. Caldera lakes are shaded in grey. Seismic stations are indicated with capital letters.

We choose as reference station the station Z11. In fact, the reference station should have a large number of observations with good coverage in azimuth and hypocentral distances. This guarantees that 3D effects on the ray paths to that station compose a well controlled average, and that relative differences in station corrections are meaningful in terms of 3D velocity structure interpretation and ray paths direction. Our Z11 was located close to the centre of the network and showed good and nearly-continuous records.

The geographic reference system used Cartesian coordinates obtained from the projection of the 1972 ellipsoid (WGS72) to an x-y axes reference system. The short distance conversion was based on the equivalence one minute of latitude = 1.8499 km; one minute of longitude = 1.4684. We selected an inversion process based on 5 iterations, with low damping for location and velocity's changes (0.1 as damping of origin time, x, y, and z coordinates and station correction, and a value of 1.0 for velocity model), alternating each time one location-and-velocity inversion with one only-location inversion.

3.5.3. Tests

As the calculation of the minimum 1D is a trial and error process for different starting assumptions (Chapter 2), we had to perform several tests to check the effects of these guesses on the final result. We analyzed the influence of the starting model (in our case, it is the TAC a-priori model) for the one-dimensional velocity structure inversion. So, we test different starting models, in terms of thickness and velocity values.

Since *VELEST* does not automatically adjust layers thickness, the appropriate layering of the model had to be found, using a damping value for velocity corrections which was low enough to permit to these values floating ($V_{\text{theta}} = 0.1$), in spite of affect other parameters (for example locations). After parameterizing the a-priori model in many layers, between -1 and 12 km depth, we observed how layer thickness affected results, in an every-2 km-layering, an every-1 km-layering and a 0.5 km one. We then chose as best model that which shows the lowest RMS. As result, we obtained that the optimum model presents layers of 1 km thickness. When we further joined together those, among layers, with the same velocity value, to reduce unknowns number, the RMS shows a reduction from 0.0791 to 0.0061 s.

As additional test, we investigated the initial structure assumption by modifying the starting a-priori model. We considered a new model with extremely low crustal velocities and another one with extremely high ($\pm 10\%$ with respect to the true model) and the same depths for gradient changes. What we observe (**Figure 3.19**) is that these results broadly converged toward the same values in the layers within well-resolved depth range. This suggests that there is not a strong control of the starting structure on the final models.

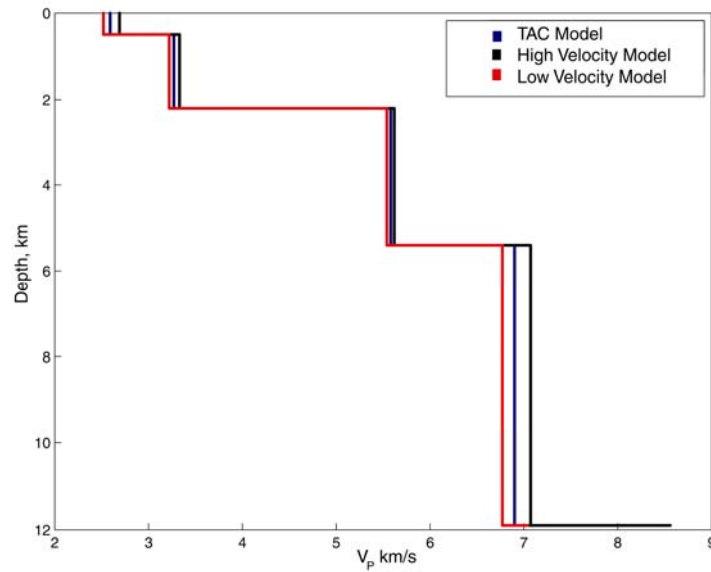


Figure 3.19 Final 1D velocity distributions for three different starting structures: result of the TAC model (blue line), result of a high velocity starting model (black line) and of a low velocity starting model (red line).

Nevertheless, to further test the dependence of results on the starting model, we made inversions starting from 100 different velocity models where each layer showed a random difference (maximum 10%) with respect to the TAC model, which was taken in turn of 0.5 km-thickness-layering, of 1 km-thickness-layering and finally of 2 km-thickness-layering. We observe (**Table 5**) how standard deviations of results are low especially for the 1 km-layering model, and especially in the more densely crossed layers (approximately until 6 km depth). This means that, for these layers, we do not expect strong variations depending on the starting models, almost for 1 km-thickness layers and at depths ranging from 1 to 6 km depth (**Figure 3.20**).

3 - Central São Miguel

| DEPTH | True model | Average Model | Standard Deviation | True Model | Average Model | Standard Deviation | True Model | Average Model | Standard Deviation |
|--------|------------|---------------|--------------------|------------|---------------|--------------------|------------|---------------|--------------------|
| 1.00 | 2.63 | 2.57 | 0.089 | 2.66 | 2.64 | 0.173 | 2.77 | 2.74 | 0.353 |
| 0.00 | 2.63 | 2.63 | 0.071 | 3.17 | 3.18 | 0.101 | 3.40 | 3.48 | 0.109 |
| -0.50 | 4.20 | 4.21 | 0.031 | | | | | | |
| -1.00 | 4.20 | 4.24 | 0.05 | 4.46 | 4.47 | 0.036 | | | |
| -1.50 | 4.20 | 4.24 | 0.05 | | | | | | |
| -2.00 | 5.06 | 5.04 | 0.123 | 4.91 | 4.91 | 0.036 | 5.39 | 5.38 | 0.061 |
| -2.50 | 5.22 | 5.23 | 0.083 | | | | | | |
| -3.00 | 5.41 | 5.43 | 0.077 | 5.40 | 5.4 | 0.032 | | | |
| -3.50 | 5.56 | 5.58 | 0.082 | | | | | | |
| -4.00 | 5.56 | 5.75 | 0.134 | 6.41 | 5.51 | 0.108 | 5.90 | 5.95 | 0.117 |
| -4.50 | 5.59 | 5.93 | 0.225 | | | | | | |
| -5.00 | 5.63 | 5.96 | 0.207 | 6.58 | 6.6 | 0.053 | | | |
| -5.50 | 6.84 | 6.73 | 0.244 | | | | | | |
| -6.00 | 6.88 | 6.9 | 0.165 | 6.85 | 6.88 | 0.102 | 6.85 | 6.86 | 0.194 |
| -6.50 | 6.88 | 6.98 | 0.108 | | | | | | |
| -7.00 | 6.88 | 7.03 | 0.108 | 6.86 | 7 | 0.106 | | | |
| -7.50 | 6.88 | 7.08 | 0.109 | | | | | | |
| -8.00 | 6.88 | 7.12 | 0.101 | 6.86 | 7.08 | 0.117 | 6.85 | 6.97 | 0.185 |
| -8.50 | 6.88 | 7.19 | 0.108 | | | | | | |
| -9.00 | 6.88 | 7.24 | 0.099 | 6.86 | 7.17 | 0.132 | | | |
| -9.50 | 6.88 | 7.27 | 0.098 | | | | | | |
| -10.00 | 6.88 | 7.29 | 0.1 | 6.87 | 7.24 | 0.128 | 6.86 | 7.11 | 0.214 |
| -10.50 | 6.88 | 7.32 | 0.088 | | | | | | |
| -11.00 | 6.89 | 7.33 | 0.088 | 6.87 | 7.28 | 0.132 | | | |
| -11.50 | 6.89 | 7.36 | 0.084 | | | | | | |
| -12.00 | 7.80 | 7.8 | 0.371 | 7.80 | 7.84 | 0.366 | 7.80 | 7.81 | 0.391 |

Table 5 Starting model/layering test. Depths (column 1); results from true velocity models (a-priori TAC structure) (“true model” of columns 2, 5, 8); mean velocities (“Average Models” of columns 3, 6, 9) and standard deviations (“Standard deviation” of columns 4, 7, 10) for 100 results in three tests (0.5 km, 1 km and 2 km layering thickness, as in table).

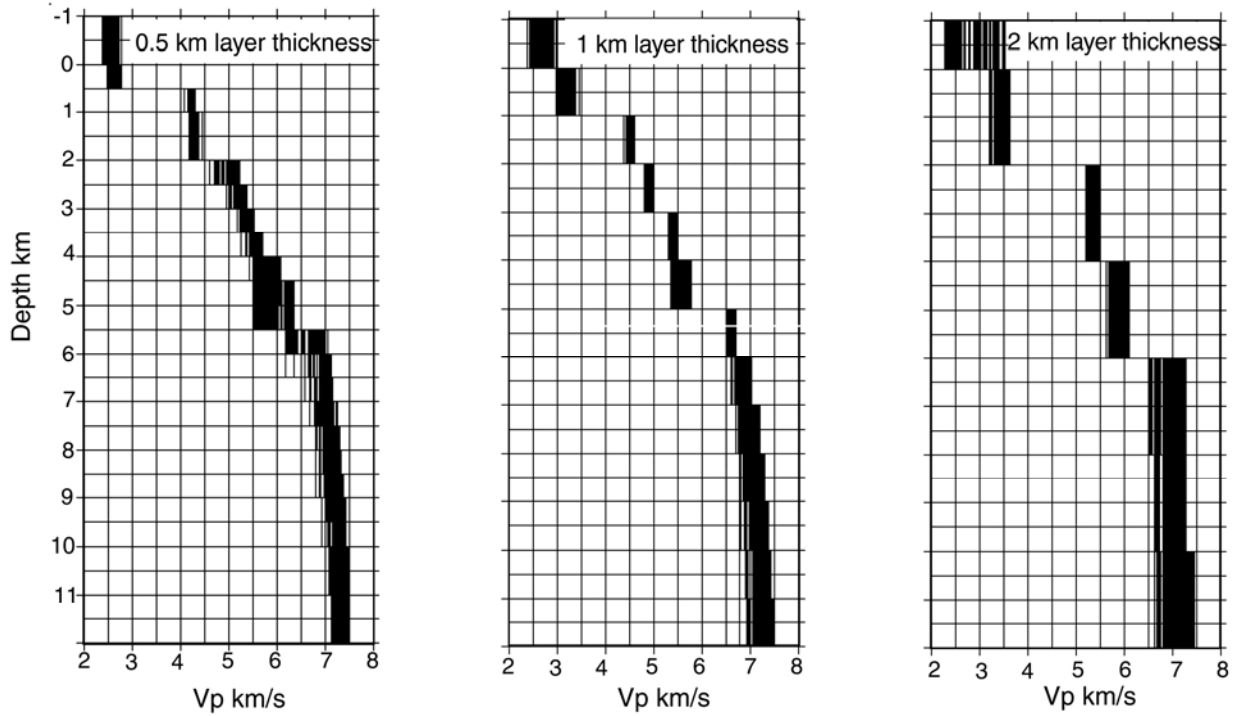


Figure 3.20 P-waves velocity distributions after velocity inversion starting each time from 100 models which have random variations of maximum $\pm 10\%$ in velocity with respect to the 0.5 km thickness layers (upper left figure); 1.0 km thickness layers (upper right figure) and 2.0 km thickness layers (lower figure) starting models.

3.5.4. Results

In the calculated minimum 1D velocity model, the RMS reduced from 0.044 to 0.018 s. The average displacement of earthquakes was 0.021 km (standard deviation 0.0413) in x, 0.021 km (0.0376) in y and 0.074 km (0.2083) in z direction, indicating that through the selection of parameters we balanced, during the inversion, the changes in velocity structure with those in hypocenter positions.

We must note that the model tested as Minimum 1D (**Table 6**) slightly differed from that we used later as starting velocity structure for 3D inversion. This depends on the dataset, which was slightly smaller due to the successive addition of data. These new data changed only slightly the velocity model and were supposed to have improved test quality.

| DEPTH km | -1.00 | 0.00 | 1.00 | 2.00 | 3.00 | 4.00 | 5.00 | 6.00 | 7.00 | 8.00 | 9.00 | 10.00 | 11.00 | 12.00 |
|------------------------|-------|------|------|------|------|------|------|------|------|------|------|-------|-------|-------|
| V _p km/s | 2.58 | 2.58 | 3.83 | 5.26 | 5.46 | 5.46 | 6.76 | 6.77 | 6.78 | 6.79 | 6.80 | 6.80 | 6.80 | 7.80 |

Table 6 Minimum 1D velocity model. Depths and corresponding velocities are reported

Comparing the TAC model with the new Minimum 1D, the most striking observation is about the change of velocity for the depths between surface and 4 km, and substantially equal for greater depths. This result can reflect the similarity of the starting model with the optimum at these depths, or the incapability of the one dimensional inversion to adjust velocity structure at depths scarcely sampled.

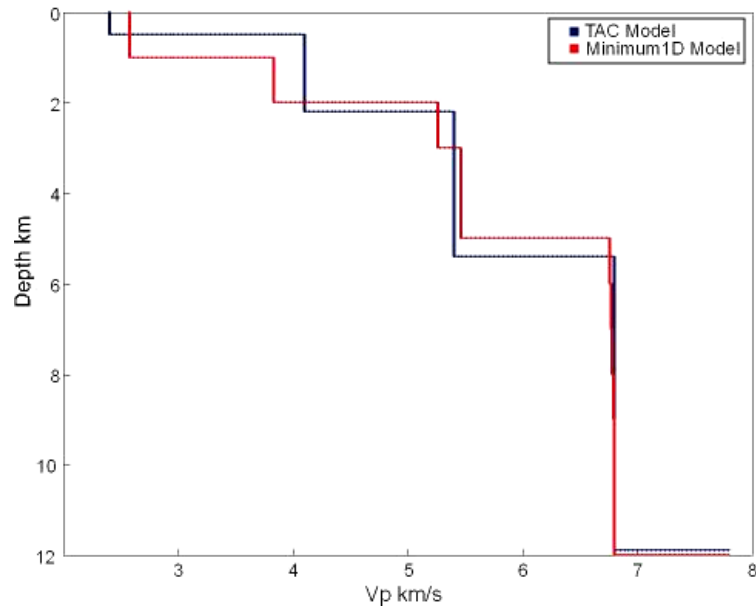


Figure 3.21 One-dimensional velocity models: TAC model, used in routine network location (blue line); Minimum 1D derived from our data (red line).

An advantage of VELEST is its extensive output, which allows a detailed analysis of the 1D inversion result (**Table 7**). We observe that most earthquakes are located between 1 and 10 km of depth, with a maximum between 6 and 10 km of depth (**Figure 3.22**). Due to this earthquakes distribution, and velocity layering, the number of rays crisscrossing these layers shows an increase from 6 km toward the surface. Hence, the maximum of resolution can be expected for these depths. The values indicated by columns 9 (XYKM) and 10 (ZKM) of the table specify the average ray lengths, as horizontal and vertical paths respectively.

3 - Central São Miguel

| NLAY | TOP | BOTTOM | VEL | NHYP | NREF | %LEN | NHIT | XYKM | ZKM | RFLX |
|------|-------|--------|------|------|------|------|------|------|-----|------|
| 1 | -1 | 0.00 | 2.58 | 0 | 0 | 0.0 | 2499 | 0.3 | 0.5 | 0 |
| 2 | 0.00 | 1.00 | 2.58 | 36 | 0 | 0.0 | 2605 | 0.3 | 1.0 | 0 |
| 3 | 1.00 | 2.00 | 3.83 | 14 | 49 | 15.9 | 2515 | 0.6 | 1.0 | 0 |
| 4 | 2.00 | 3.00 | 5.26 | 9 | 112 | 62.2 | 2330 | 1.1 | 0.9 | 0 |
| 5 | 3.00 | 4.00 | 5.46 | 14 | 1 | 0.8 | 2177 | 0.9 | 1.0 | 0 |
| 6 | 4.00 | 5.00 | 5.46 | 32 | 0 | 0.0 | 2107 | 0.7 | 0.9 | 0 |
| 7 | 5.00 | 6.00 | 6.76 | 43 | 32 | 21.1 | 1831 | 1.3 | 0.9 | 0 |
| 8 | 6.00 | 7.00 | 6.77 | 50 | 0 | 0.0 | 1438 | 0.9 | 0.9 | 0 |
| 9 | 7.00 | 8.00 | 6.78 | 56 | 0 | 0.0 | 1037 | 0.7 | 0.8 | 0 |
| 10 | 8.00 | 9.00 | 6.79 | 48 | 0 | 0.0 | 582 | 0.5 | 0.6 | 0 |
| 11 | 9.00 | 10.00 | 6.80 | 17 | 0 | 0.0 | 204 | 0.4 | 0.6 | 0 |
| 12 | 10.00 | 11.00 | 6.80 | 8 | 0 | 0.0 | 74 | 0.3 | 0.7 | 0 |
| 13 | 11.00 | 12.00 | 6.80 | 1 | 0 | 0.0 | 18 | 0.3 | 0.8 | 0 |
| 14 | 12.00 | -- | 7.80 | 0 | 0 | 0.0 | 0 | 0.0 | 0.0 | 0 |

Table 7 Statistics of the resulting Minimum 1D P-wave velocity model. NHYP, number of hypocenters in this layer; NREF, number of head-waves in this layer; %len, % of "refracted km" in this layer with respect to all refracted km; NHIT, number of rays passed through this layer; xy-km, average horizontal ray length (km) in layer; z-km, average vertical ray length (km) in layer; RFLX, number of reflections at bottom of this layer

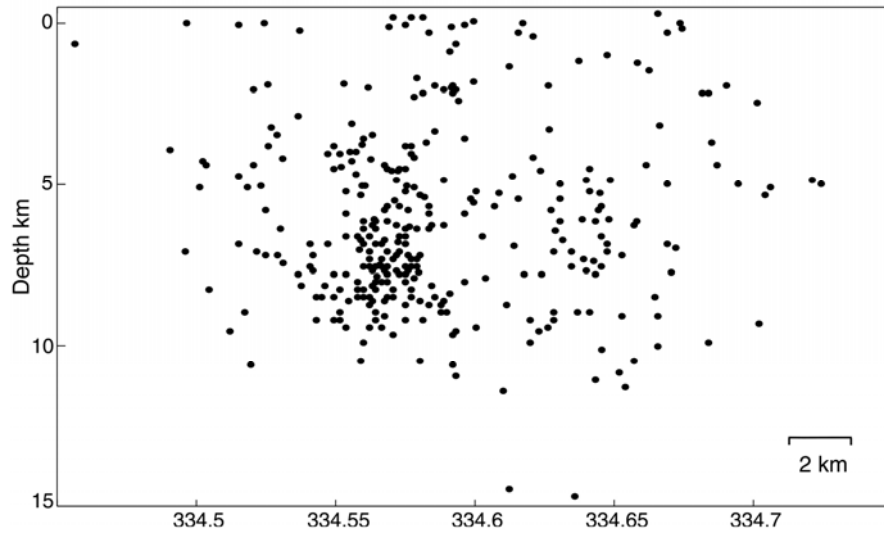


Figure 3.22 Position of hypocenters as located during 1D velocity inversion by VELEST program. The longitude is indicated along the horizontal axis.

Station residuals were the average values for the azimuthally and radially varying time delays at these stations, relative to the near-surface velocities of the Minimum 1D model. In teleseismic studies these travel time delays at stations are the main data to be interpreted, as seismic velocity anomalies distribution with respect to the azimuth of the incoming wave fronts. With local earthquake data the azimuthal and radial dependences are never as uniform for all stations as for the teleseismic data, and more when hypocenters are well distributed over the area. Anyway, we observed stations delay distribution in the minimum 1D and again after the precise earthquakes location (Chapter 3.6.3). In that step, these values are 'cleaned up' by, among others, location inaccuracies and hence delays can be related more directly to anomalies of the 1D model with respect to the true velocity 3D structure.

With the preliminary location in the Minimum 1D, residuals at stations probably represent several errors in conjunction with traveltimes misfits. To partly minimize these errors, we considered differences of misfit at stations with respect to the reference station (AZ11, in the centre of the network), and we called them 'delays'. These delays show an irregular distribution as sign and value (**Table 8**). Their values usually depend on the relationship between station position and

hypocenters distributions, because for stations which were lightened from a wide range of azimuth and distances, effects of local anomalies of velocity tend to be averaged. In our case, we observe (**Figure 3.23**) that there was an increase of negative delays for stations on the network east and north-west side, where surface geology (Chapter 3.3.1) does indicate the presence of low density (i.e. slow seismic P-wave) deposits of pyroclastic origin. We would either expect positive delays. Assuming that the Minimum 1D is the best model we can refer to, this discrepancy could be due to several reasons, among which (1) we were not lighting shallow velocities through these delays, so, no relationship existed between traveltimes and outcrops (2) we were managing data strongly affected by time errors, of various origins (3) the reference stations stayed itself above a strongly anomalous region. We will consider again the delays distribution after the precise earthquake locations.

| STATION | RESIDUAL | DELAY |
|---------|-------------|---------|
| Z01 | 0.0459(9) | -0.0033 |
| Z02 | 0.022(244) | -0.0058 |
| Z03 | 0.0204(257) | 0.0004 |
| Z04 | 0.0208(290) | -0.0009 |
| Z05 | 0.0201(206) | -0.0004 |
| Z06 | 0.0217(254) | 0.0005 |
| Z07 | 0.0259(89) | -0.0041 |
| Z08 | 0.0241(151) | -0.0063 |
| Z09 | 0.0206(46) | -0.0056 |
| Z10 | 0.0234(60) | -0.0072 |
| Z11 | 0.0235(142) | 0.0000 |
| Z20 | 0.0206(43) | 0.0014 |
| Z21 | 0.0199(55) | -0.0043 |
| AZD | 0.0209(178) | 0.0031 |
| CML | 0.0231(9) | -0.0002 |
| FAC | 0.0194(5) | -0.0041 |
| FRA | 0.0199(34) | 0.0004 |
| LFA | 0.0202(58) | 0.0033 |
| LF2 | 0.0170(2) | -0.0063 |
| MES | 0.0199(79) | 0.0066 |
| MIR | 0.0229(42) | 0.0069 |

3 - Central São Miguel

| | | |
|-----|-------------|---------|
| PCN | 0.0197(90) | 0.0015 |
| PMA | 0.0219(2) | -0.0039 |
| PRC | 0.0291(2) | -0.0073 |
| PVE | 0.0202(14) | -0.0063 |
| VIF | 0.0195(138) | 0.0036 |

Table 8 Station residuals and delays as calculated by Velest code. 'STATION' station name; 'RESIDUAL', average residual at station. In parenthesis, number of samples. 'DELAY' final delay with respect to the reference station AZ11

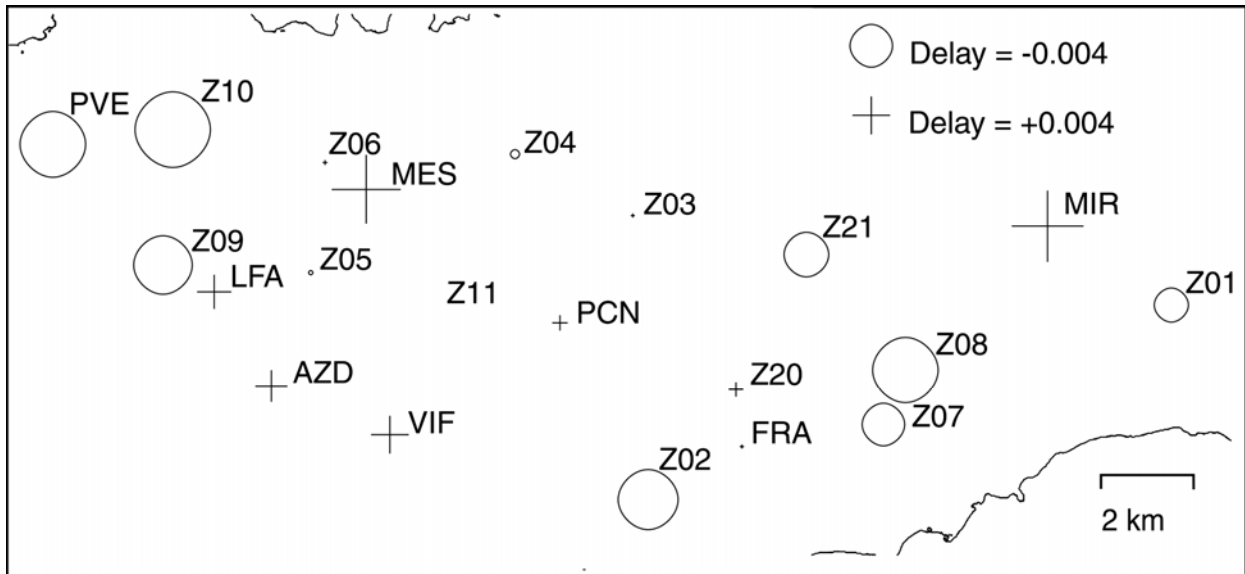


Figure 3.23 Station delays with respect to reference station Z11. We consider as delays the difference between average residuals at stations (see table), and that obtained for Z11, in seconds. Stations with few data are not reported.

3.6. Initial Locations

3.6.1. Method

The use of seismic data for the elaboration of a 3D velocity model strongly depends on accurate earthquake locations. This means that the validity of the iterative solution of the linearized problem for earthquake location and velocity structure depends on the quality of the initial estimate of model parameters, and among those the hypocenters locations.

Earthquakes locations were calculated with the program package *NLloc*, which constitutes a probabilistic, non-linear search in a 3D model (actually in a 1D model, represented as 3D grid). It systematically produces a misfit function, over a 3D, x, y, z spatial grid. The maximum likelihood (or minimum misfit) is pointed out as the ‘optimal’ hypocentre (Chapter 2.1)

3.6.2. Input Data

NLloc used a flat earth, rectangular, left-handed, x, y, z coordinates system, with kilometric unit distance, obtained with a Lambert transformation in the WGS-84 ellipsoid. First, the horizontally layered model with constant velocities in each layer was converted into a 3D model for the calculation of travel times. The travel time structure was parameterized by a 2D grid of 61 nodes on lateral sizes and 31 in depth, 1 km in spacing. Essentially the value found at each grid node was the slowness (i.e.1/velocity) multiplied by the grid spacing, until a time measure (in seconds). The location grid covered a central region of 60 km E-W, 30 km N-S and 30 km of depth and it was fully contained within the 3D travel time grid. The nodes were 61, 31, 31 in x, y, z direction respectively. Starting with 10 cells in the x and y directions and 4 in depth, the oct-tree procedure could lead to a maximum of 10000 nodes, with 0.01 km of size for the final sub-grid.

Location procedure involves P and S arrival time (Chapter 3.4.5.2). A V_p/V_s ratio of 1.68 was introduced, as inferred from a Wadati diagram of our data [Saccorotti et al. 2004]. In the parameters selection we imposed as conditions: (1) a minimum number of 7 traveltimes for each locatable earthquake (2) a maximum gap of 180° . (See Chapter 3.5.2 for more details). (3) a maximum RMS of 2.0 s. This last parameter was no restrictive to attempt the location of as more hypocenters as possible, taking into account that an analogous parameter had to be more selective in the input data for 3D inversion.

Records belonged to 26 stations, deployed in the area selected for traveltimes computation. Not the whole database from deployed stations was used. This was partly due to stations position: for example stations SE2, SE3, SE4, SEA were far from the seismically active zone. So, to include them, we should extend to unreasonable dimensions the 2D traveltimes grid in terms of time consumption (one huge file of traveltimes is calculated for each station (**Figure 3.24**) but also the velocity grid, in terms of unknowns number (each node of the slowness grid represents an unknown). As velocity model, we introduced the Minimum 1D as calculated by the *VELEST* (Chapter 3.5.4), which used the same traveltimes database and the TAC velocity model, as starting structure.

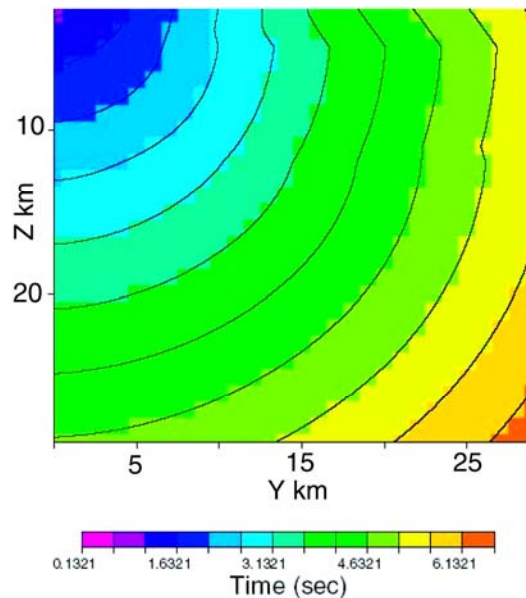


Figure 3.24 Example of travel time values as calculated for the reference station (Z11), as stored by the *NLloc* software. As the velocity model is 1D, this scheme does not change in x-axis with respect to y-axis.

3.6.3. *Results*

With the minimum 1D model 426 earthquakes were located to obtain accurate starting location for the 3D tomography and to yield an overview of the seismicity of the study area during the experiment (**Figure 3.25**). Each station managed an average of 72 P-wave traveltimes, which broadly indicates the average number of earthquakes located by each station. After location, the average value of calculated residuals for P phases at each station was 0.0043 s (with a standard deviation of 0.3207). The distribution of earthquakes is not homogeneous and events mostly cluster in the central region, between 334.5 and 334.67 degree of longitude E, 37.82 and 37.75 of latitude N. In cross sections, seismicity is clearly confined in the upper 10 km of the crust.

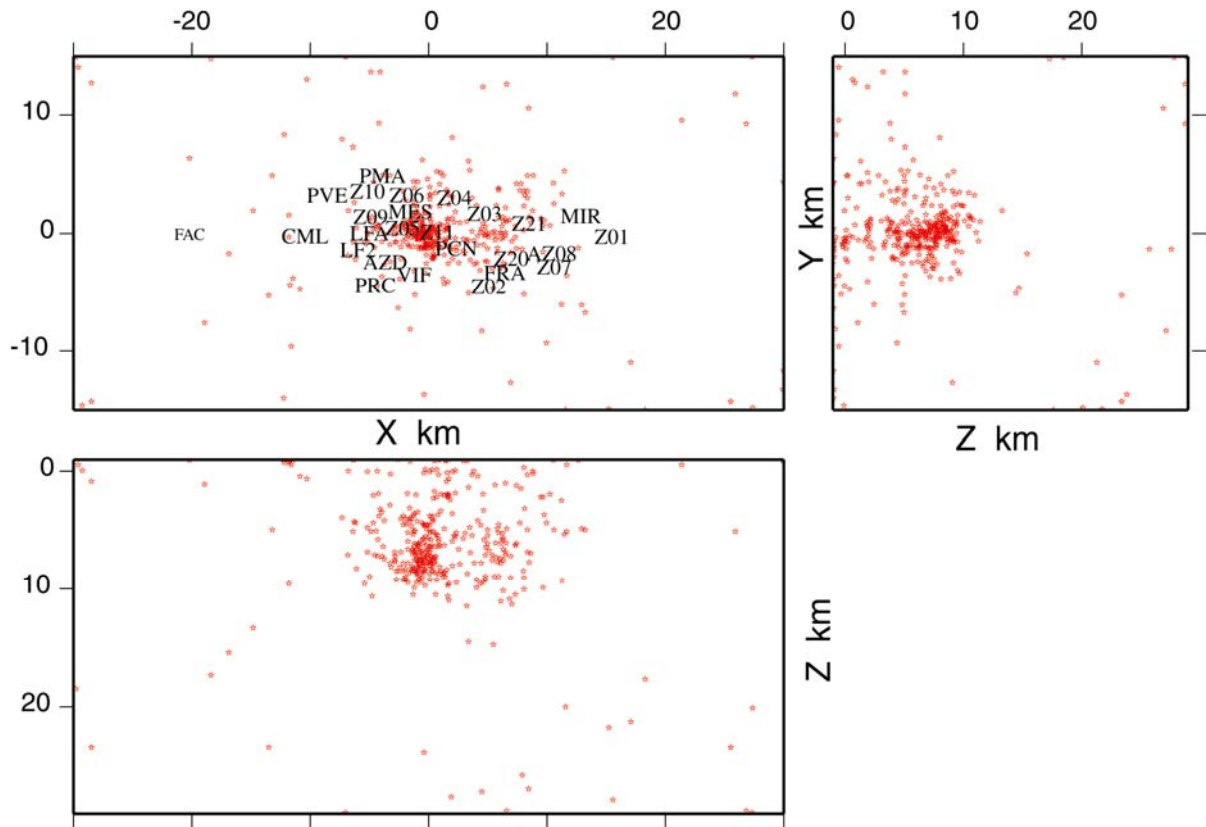


Figure 3.25 Earthquake hypocenters projected on the three planes as resulting from the NLloc location in the Minimum 1D velocity model.

We again analyzed station residuals because they represented the final values calculated in the minimum 1D velocity model for optimized locations. Other factors could however affect these stations residuals, such as errors in their location and systematic timing problems, together with punctual geological anomalies. If we could ignore all of these factors, residuals at each station could roughly point to lateral heterogeneities, only evidenced by the 3D velocity tomography. For this strong relationship with local velocity structure, we considered residuals at each station without comparison with the

reference station. In this sense, negative values corresponded to true velocities faster than those of the model, positive to true velocity slower than the model (**Table 9**).

We observe from the mapped distribution of residuals (**Figure 3.26**) that the highest positive are those of stations Z07, Z10, Z20, MES. For some of them, as discussed in the geological introduction to Central São Miguel (Chapter 3.3.1), this could be actually due to the presence of material with velocities lower than those of layer 1 in the Minimum 1D model. On the opposite, the presence of materials with higher than layer 1 velocities (in model 1D) could justify residuals at Z21, PCN, VIF, Z11, AZD, Z03, Z05, LFA, Z09. Other stay really close to the limits of studied area (MIR, PVE) and are doubtful. If we calculated the distribution of station delays with respect to the AZ11 station, at least for these station with enough traveltimes, we would observe (cfr *VELEST* results) negative delays for stations located in the Furnas zone and in that region between Fogo and the north coast.

| | | | | | | |
|--------|----------------|----------------|-----------------|----------------|----------------|-----------------|
| STN | Z01 | Z01 | Z02 | Z02 | Z03 | Z03 |
| Phase | P | S | P | S | P | S |
| AveRes | 0.523704(5) | -0.301460(5) | -0.033606 (183) | -0.021937(172) | -0.052931(181) | -0.037840 (176) |
| | Z04 | Z04 | Z05 | Z05 | PRC | PRC |
| | P | S | P | S | P | S |
| | -0.024330(199) | -0.093171 (18) | -0.056730(152) | -0.072720(149) | -0.036798(1) | -0.689291(1) |
| | Z06 | Z06 | Z07 | Z07 | Z08 | Z08 |
| | P | S | P | S | P | S |
| | 0.020626(180) | 0.041470(175) | 0.413516(63) | 0.759152(39) | -0.022921(116) | 0.090737(82) |
| | Z09 | Z09 | Z10 | Z10 | PMA | |
| | P | S | P | S | P | |
| | -0.040606(38) | 0.020245(32) | 0.172820(51) | 0.261095(48) | -1.271606(1) | |
| | Z11 | Z11 | Z20 | Z20 | Z21 | Z21 |
| | P | S | P | S | P | S |
| | -0.029619(80) | 0.327158(74) | 0.182200(33) | 0.321811(33) | -0.160235(36) | -0.073784(35) |
| | FRA | LFA | LFA | LF2 | MES | MES |
| | P | P | S | P | P | S |
| | -0.019421(29) | -0.058298(47) | -1.340479(1) | 0.258740 (2) | 0.040930(64) | 0.186842(52) |
| | AZD | AZD | CML | FAC | VIF | |
| | P | S | P | P | P | |
| | -0.029725(150) | 0.206696(131) | 0.079123(8) | 0.546332(3) | -0.1024(114) | |
| | MIR | PCN | PCN | PVE | PVE | |
| | P | P | S | P | S | |
| | 0.003321(34) | -0.117499(77) | 0.017485(73) | -0.073840(12) | -0.025846(12) | |

Table 9 Station average residuals for different phases as calculated by NLloc code. 'STN' station name; 'Phase' considered seismic phase; 'AveRes' average residual. In parenthesis, the number of traveltime data is reported.

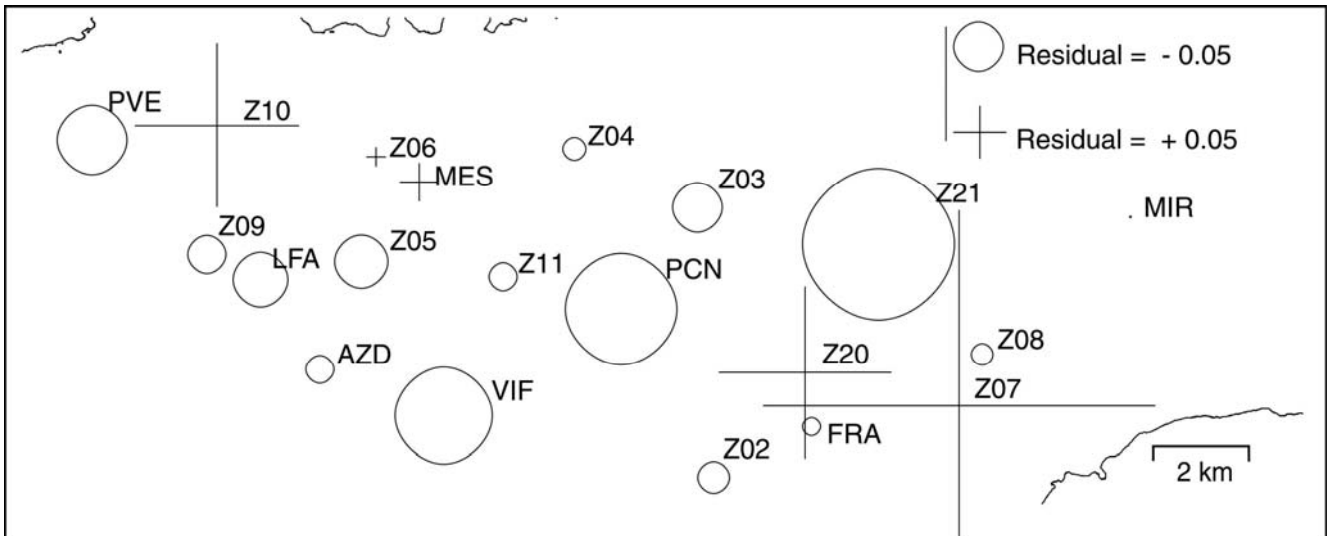


Figure 3.26 Traveltimes residuals at stations as resulting from the NLloc program. Negative residuals correspond to true velocities faster than those of the model, positive delays to true velocities slower than the model. Values in seconds. The areas selected is the same as in **Figure 3.23**. Only stations with sufficient traveltime data were considered,

3.7. 3-D Velocity Model

3.7.1. Method

We chose the seismic tomography code of [Benz et al. 1996] to calculate the 3D velocity structure of Central São Miguel. As seen (Chapter 2.2.3.1) the method allows for the simultaneous inversion of the 3D-P-wave velocity structure and earthquake locations and shows a good performance in the solution of the direct problem by using a finite-difference technique. Hence, the method is particularly well suited for application to a region where large lateral velocity contrasts are likely to occur.

3.7.2. Input Data

We already analyzed the preparation of (1) a Minimum 1D velocity starting model (Chapter 3.5) and (2) high precision starting locations (Chapter 3.6).

Next steps to perform the 3D inversion, were (3) data (traveltimes) choice, through a selection of stations and earthquakes (4) model parametrization and definition of best dimensions (5) parameters selection (6) starting model selection (7) uncertainty evaluation (8) resolution tests.

3.7.2.1. *Data selection*

Among the 427 earthquakes relocated in the Minimum 1D model, for the 3D inversion we selected 289 earthquakes with (1) a minimum of 6 phase readings (2) a maximum gap of 180° (3) a maximum offset between stations and earthquakes of 20 km, and (4) a minimum distance between hypocenters of 0.4 km. We decide to 'decluster' the database because swarms of earthquakes considerably increase the number of unknowns, without providing any further information about the structure. Their ray paths, in fact, approximately cross the same cells. The distance we selected (0.4km) takes into account both the error supplied by the location program and the grid dimension for the traveltimes calculation (0.25 km).

The final database consisted of 2197 P-wave and 1786 S-wave traveltimes, recorded in 20 stations, located within the selected area.

3.7.2.2. *Grid definition and parameter selection*

A 20 x 12 x 11 km volume centered at -25.426 W and 37.774 N, extending from 1.5 km above sea level to a depth of 9.5 km, was selected for the tomographic inversion. The volume was parameterized with a grid of constant-slowness cubic cells. After several tests with different cell sizes, we selected a 1-km cell as the optimum dimension for our inversion. It represented a good trade-off between travel time RMS, model resolution, and ray coverage [Benz et al. 1996]. It is the smallest spacing that produces excellent image fidelity without serious loss of resolution due to a poor sampling by seismic rays (**Figure 3.27**). A denser grid of 0.25 km, obtained by linear interpolation of the 1 km grid, was used in the direct problem to calculate arrival times with an accurate ray path tracing.

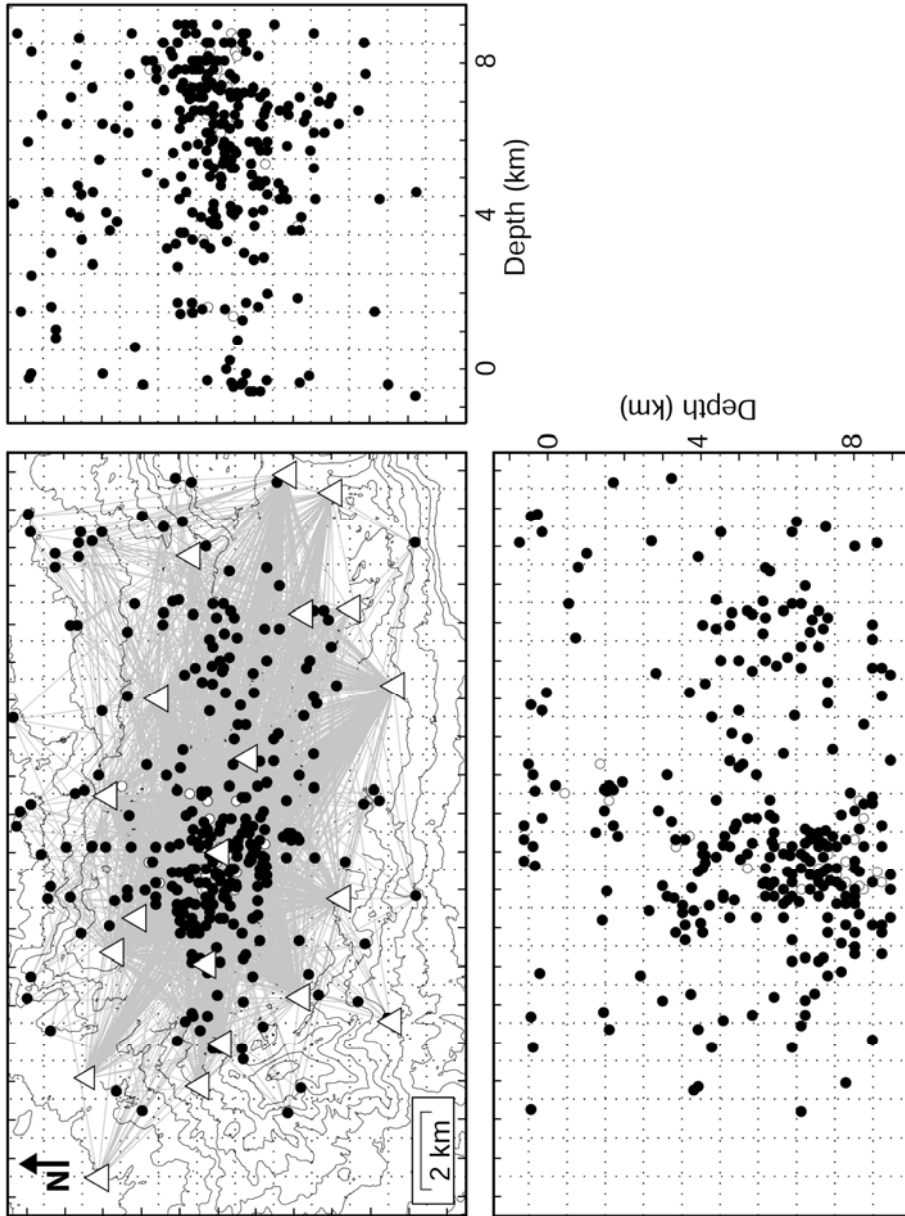


Figure 3.27 Stations (triangles) and earthquakes (black lines) used for the 3D inversion, projected on the horizontal plane and N-S and W-E vertical planes. P-wave paths (gray lines) and unused earthquakes (white circles) are also indicated. Grid parameterization (dotted lines) and 100-m topography contours are represented.

The selection of the smoothing parameter was based on minimizing the final RMS without introducing instabilities or increasing the model roughness due to modelling of the noise. Moreover, we observed that low smoothing results in a decrease of the number of ray paths that the model was able to adjust. The best balance between RMS and number of rays was achieved for a smoothing value of 60 (**Figure 3.28**).

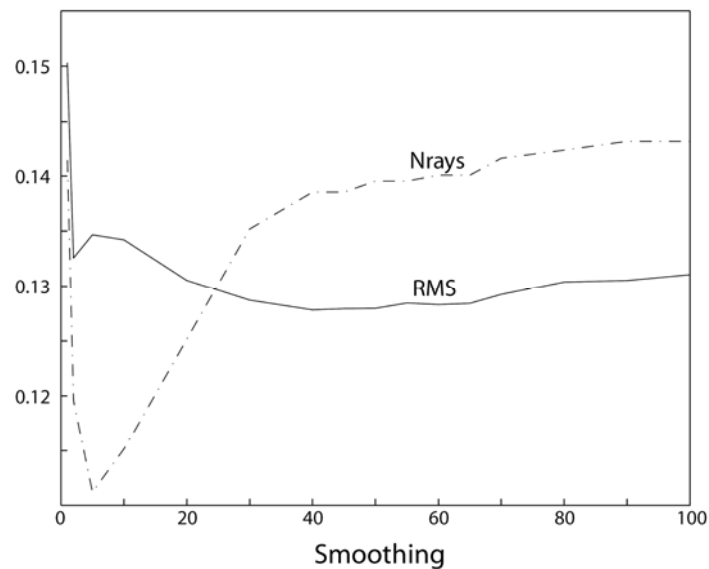


Figure 3.28 Distribution of final RMS and total number of used P-wave ray paths against smoothing values. Note that the number of rays is divided by 15000.

3.7.2.3. *Initial Model*

The starting structure for this inversion was the 3D version of the Minimum 1D velocity model as calculated in the Chapter 3.5.4. This means that we parameterized the 1D model by a three dimensional grid of nodes, as the code for the 3D inversion requires. In this model the code is solving the direct problem of traveltime calculation, by interpolating the wider grid (node distance of 1 km) to the denser one (0.25 km) Furthermore, we introduce the V_p/V_s ratio of 1.68, resulting from previous work on the same database [Saccorotti et al. 2004].

3.7.3. *V_p/V_s Ratio*

The inversion code does not allow for variations of the V_p/V_s ratio across the model. Therefore, we used an indirect approach to obtain the 3D V_p/V_s distribution. We separated the source location and velocity determination problems and estimated independent velocity models for P- and S-wave velocities. We assumed that the hypocenters were fixed at the locations determined by our final, full-dataset inversion. To make comparable the resulting velocity models, we selected only those earthquakes with both P- and S-wave travel times. Then, we performed two independent inversions for velocity: (1) we used the P-wave travel times to obtain the P-wave velocity model; and (2) we used the S-wave travel times as first arrivals for the S-wave velocity model. The initial S-wave model is derived from the starting 1D velocity model for the P-wave and a V_p/V_s of 1.68. The V_p/V_s model is calculated as the ratio between the obtained P and S velocity models.

3.7.4. *Error*

As introduced in the Chapter 2 about the analysis of solution quality for inversion tomography, as we deal with seismic arrival on waveforms, we must know as best as possible the magnitude and distribution of (1) the 'picking error' (time-

.uncertainty in identifying the seismic arrival on waveform); (2) the 'timing error' (time-uncertainty in the timing system of the instrument) and (3) 'position accuracy' (space-error in location of stations, also translatable in time-uncertainty). The final data we need, i.e. the arrival times, have to be considered together with the summed effects of these errors.

(1) We have already indicated the time accuracy of the manual picking, with values highly conservative. The average of the weights was 1.41, which means, following the weight-to-seconds equivalence of *INGV* (Italy), an average error in seconds of about 0.071.

(2) The timing error depends on seismic station characteristics and GPS timing capabilities. Usually the clock drift is assumed to be negligible. In our case, after finding out timing problems for the mallAG stations, used as arrays, we decided not to use those data whose time system could introduce a considerable timing error.

(3) The station location uncertainty was quantified with an elevation and a horizontal error. Most station location were determined by high precision GPS location procedures with respect to a landmark of known position. For this kind of measure the predicted error stands around 10 cm of error . For few stations we used hand Magellan GPS, where errors depend both on satellites' condition and instrument use. For our experience, based on repetition of some measures during previous campaigns, the average error is never greater than 20 m. The location errors , as distance, were converted in uncertainties in time assuming velocity of 2.58 km/s at stations (given by the Minimum 1D model) and basing calculation on a typical ray with a horizontal ray parameter of 0.27 s/km (a ray impinging with an angle of 45 with respect of the normal axis to surface, which is probably less). In general, the change in travel time due to as small shift in position can be quantified as $\delta t = \delta x \cdot \cos(\beta) / V$, where β is the angle between ray path and x_i axis and V is the velocity. If we accept, as conservative option, an average land station horizontal error of 20 meters, this value can be traslated in a timing uncertainty of 5 ms.

The final predicted uncertainty is determined by summing the variances of all error sources. In the final value of about 71 ms strongly prevails the picking error.

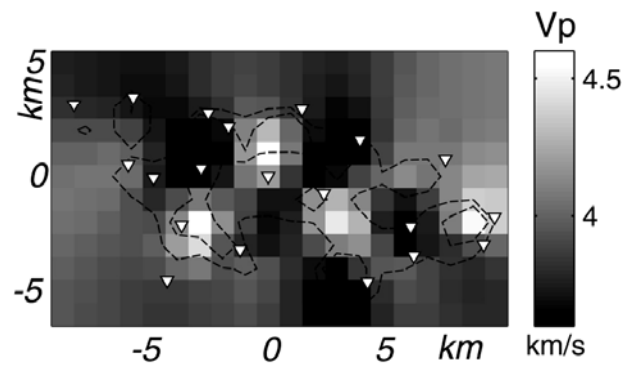
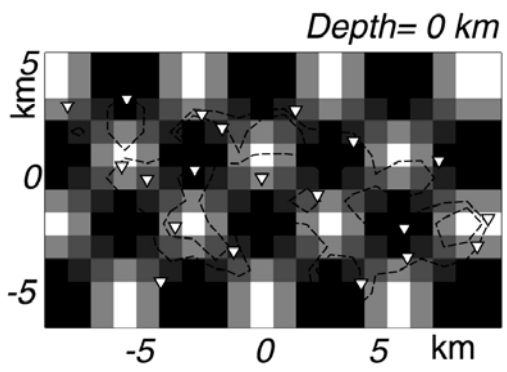
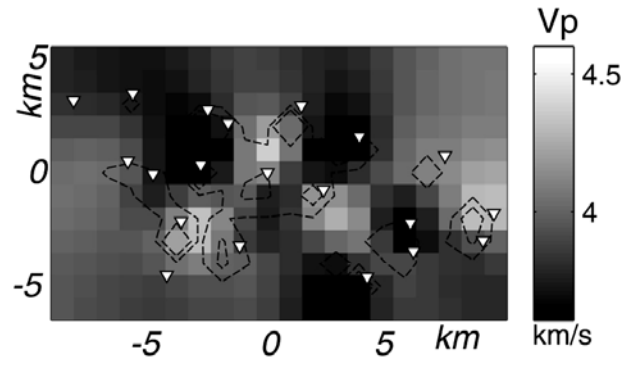
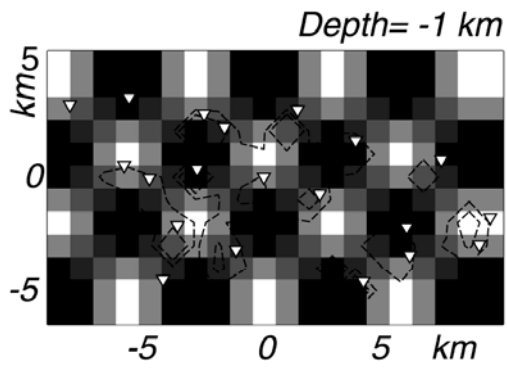
3.7.5. *Resolution analysis and input tests*

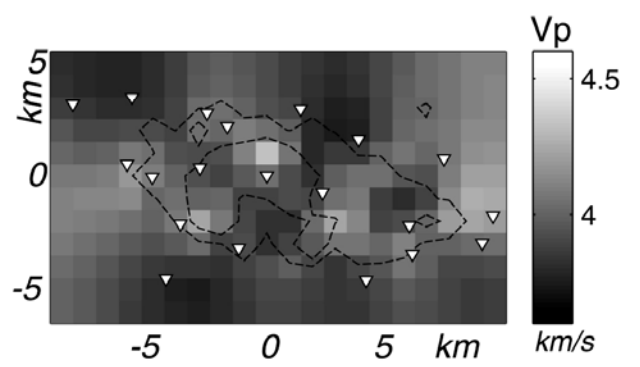
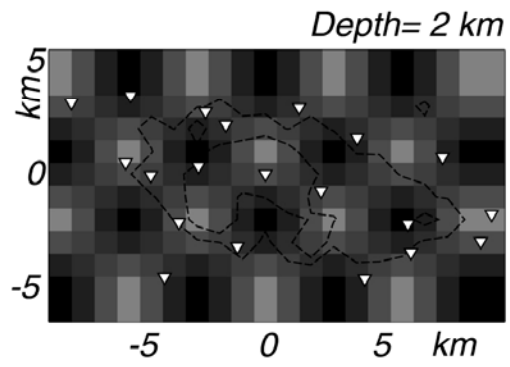
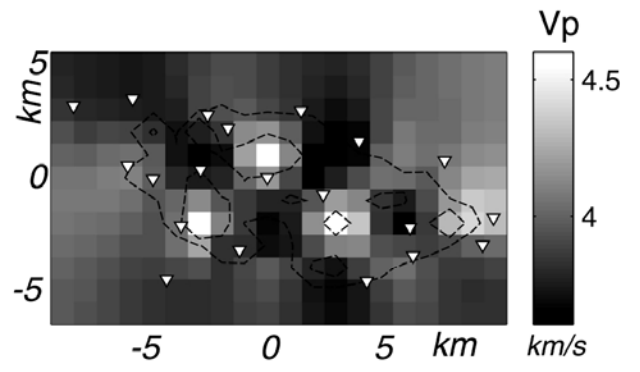
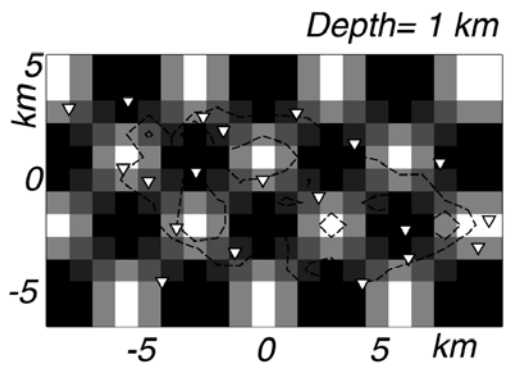
The influence of systematic and random errors on the final results can be quantified by using empirical methods of uncertainty estimation. Their results indicate the well-constrained regions of the final model, and the anomalies effectively present in the velocity field. Among resolution tests, we defined synthetic models to perform checkerboard tests [Zelt 1988] and impulse response tests [Humphreys and Clayton 1988]. We also used the final velocity model to carry out a reconstruction test [Zhao et al. 1992].

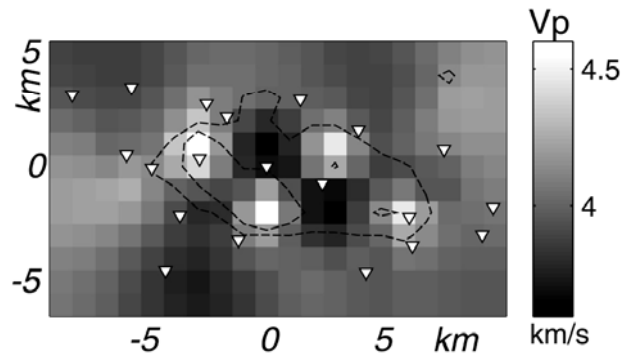
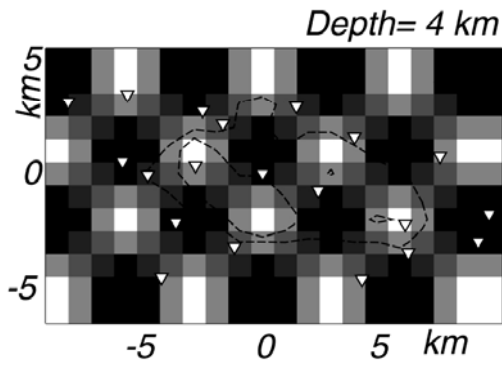
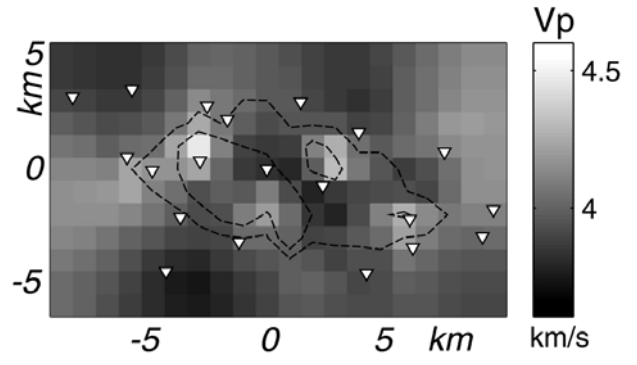
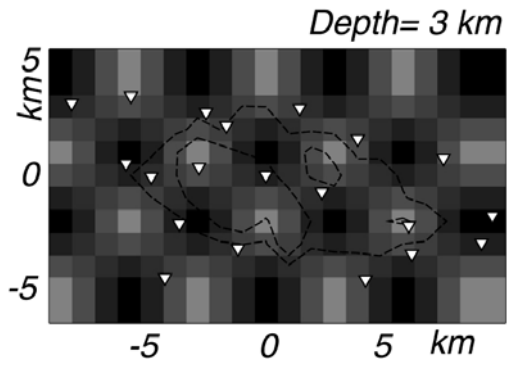
3.7.5.1. *Checkerboard Test*

We built a smoothed checkerboard model characterized by alternated positive and negative anomalies of $\pm 20\%$ with respect to an initial homogeneous model of 4 km/s. The anomaly dimensions were 3 x 3 x 4 km. In this model, we calculated synthetic travel times. A 4 km/s homogeneous half-space was used as starting velocity structure for the inversion of the synthetic database.

In **Figure 3.29** we show the results of the checkerboard test for horizontal sections every km between -1 and 6 km of depth. Contours indicate the total ray path length contained in each 1 x 1 x 1 km cell: lines corresponding to 10 and 40 km are plotted. The central region, with the highest ray coverage, is better reproduced. The original anomalies are well imaged in this area to a depth of 5-6 km, where cells are still densely crisscrossed. Also where the anomaly pattern is reproduced, the intensities are generally underestimated.







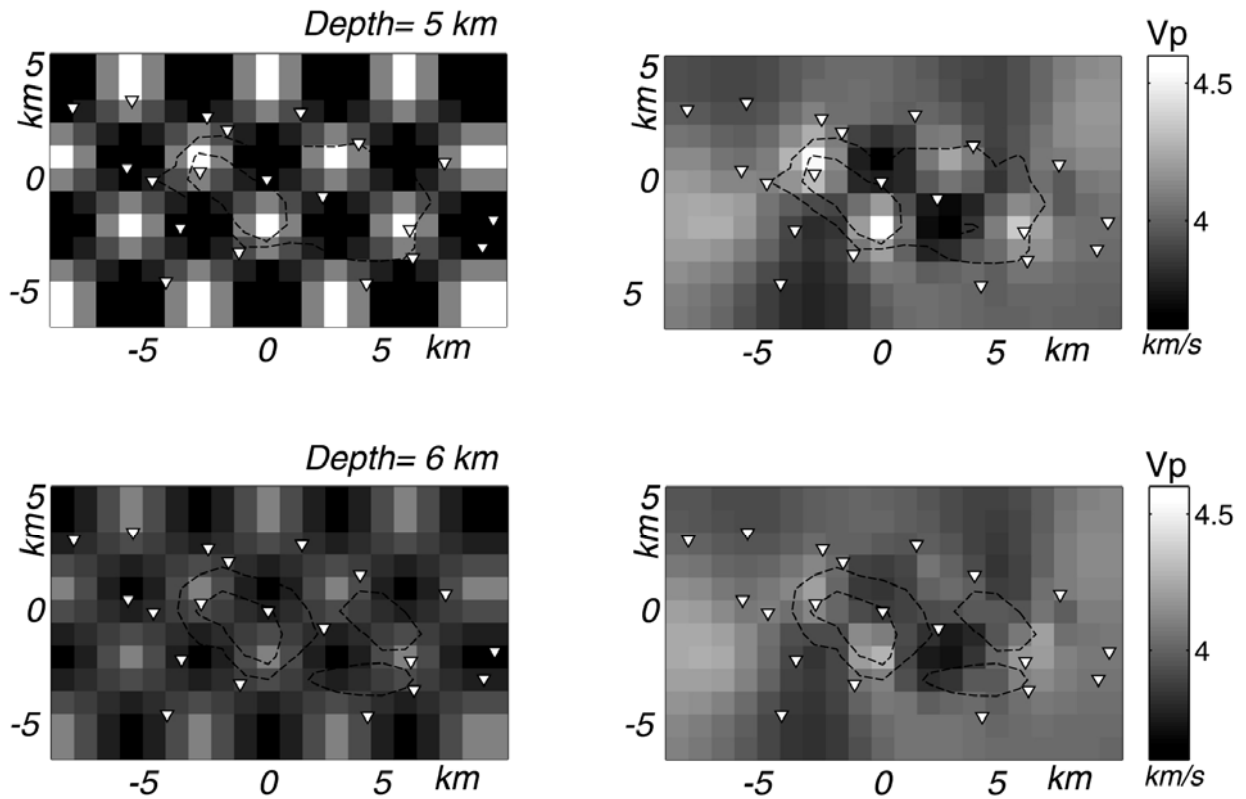
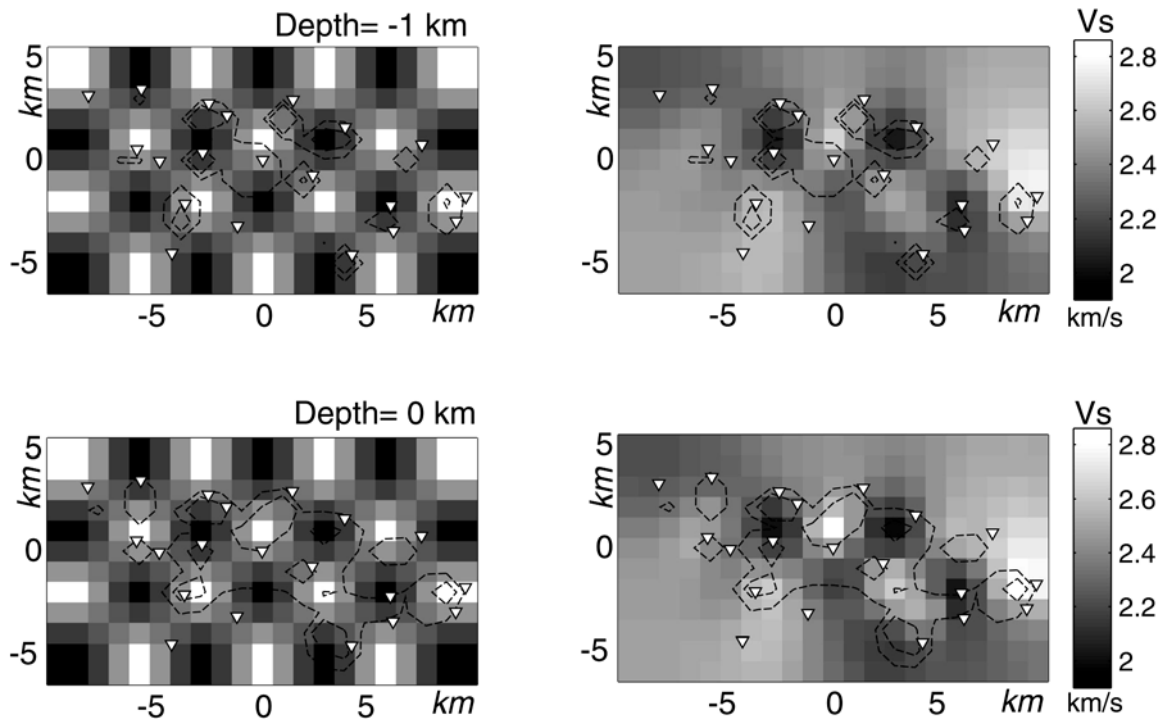


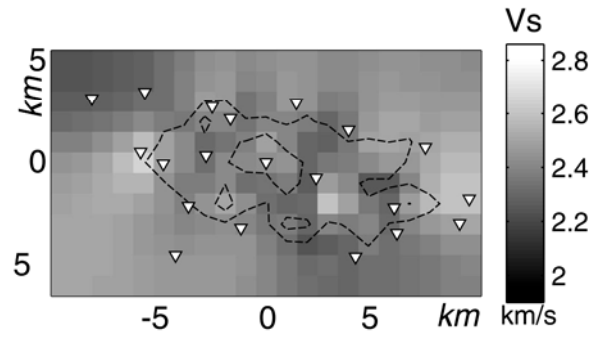
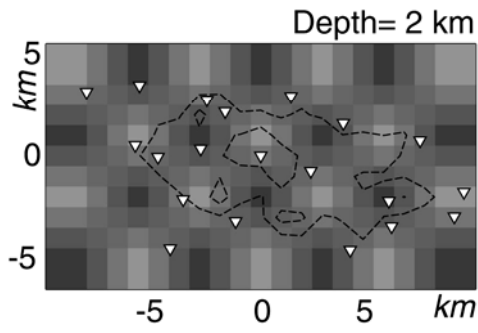
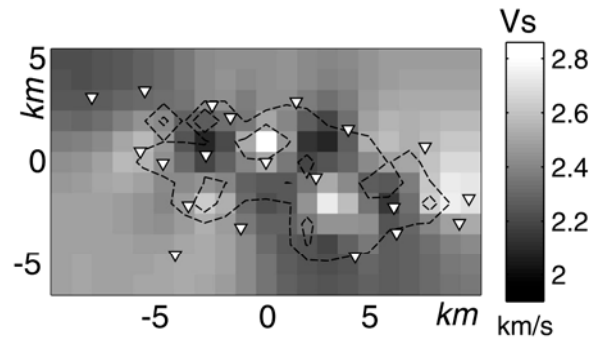
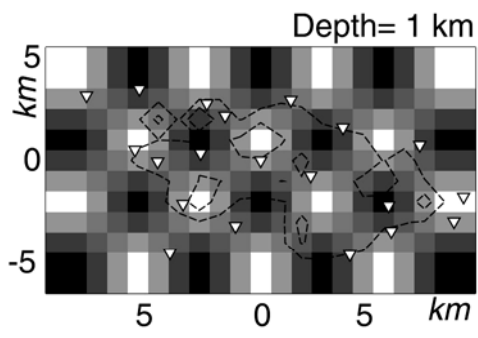
Figure 3.29 Checkerboard test, with synthetic input model (left) and inverted model (right) for P-wave. Map view at 5 and 6 km depth. The contours indicate the total ray path length contained in each $1 \times 1 \times 1$ km cell. Contours are shown for 10 and 40 km total ray length. White triangles are seismic stations.

Analogously, we built a smoothed checkerboard model for S-wave characterized by alternated positive and negative anomalies of $\pm 20\%$ with respect to an initial homogeneous model of 2.4 km/s. The anomaly dimensions were $3 \times 3 \times 4$ km. In this model, we calculated synthetic travel times. A 2.4 km/s homogeneous half-space was used as starting velocity structure for the inversion of the synthetic database.

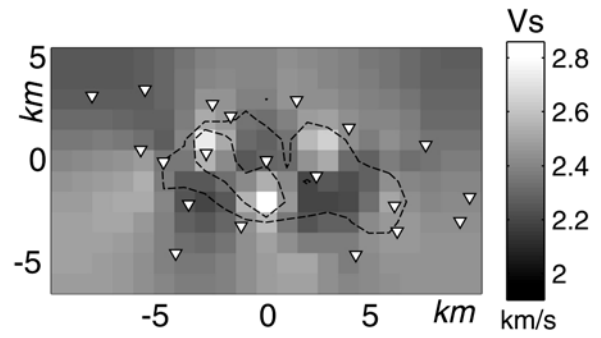
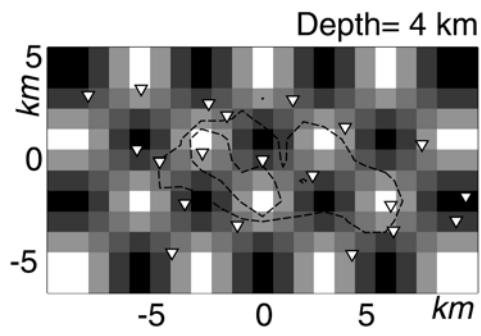
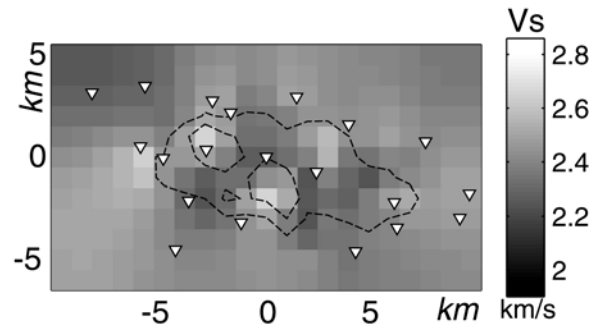
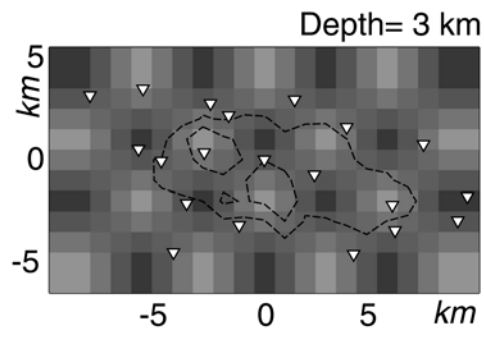
In **Figure 3.30** we show the results of the checkerboard test for horizontal sections every km between -1 and 6 km of depth. The central region, with the highest ray coverage, is better reproduced. The original anomalies are well imaged in this area to a depth of 5-6 km. Also where the anomaly pattern is reproduced, the intensities are generally underestimated.



3 - Central São Miguel



3 - Central São Miguel



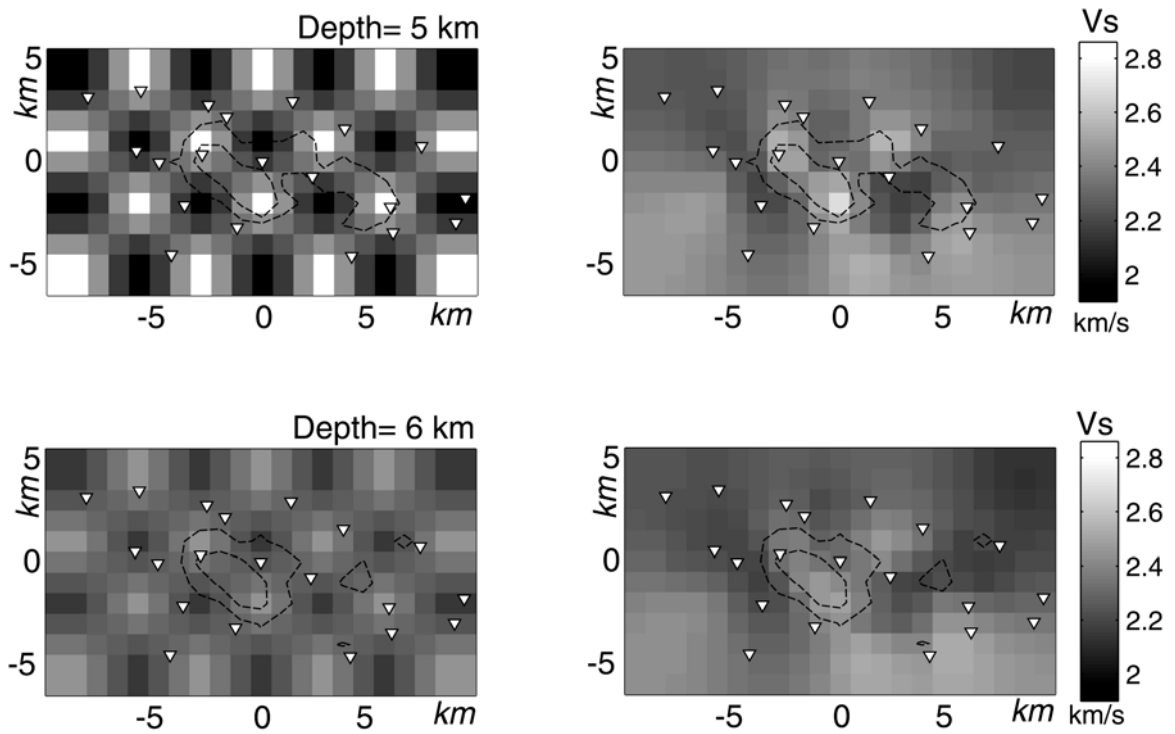


Figure 3.30 Checkerboard test, with synthetic input model (left) and inverted model (right) for *S*-wave. Map view at 5 and 6 km depth. The contours indicate the total ray path length contained in each $1 \times 1 \times 1$ km cell. Contours are shown for 10 and 40 km total ray length. White triangles are seismic stations.

3.7.5.2. Impulse Response Test

In locations where the final model shows the strongest or more interesting anomalies, we introduced spot-like anomalies for synthetic inversion. We choose as surrounding field the same as our 1D initial model, in order to make such a synthetic situation more similar to the true one. For example (**Figure 3.31**), we set up 1 km side cubic spot encircled by

smoothed cells, such as a maximum velocity of 4.3 km/s smoothed through 4.0 km/s cells, in a medium that at this depth has a velocity of 3.83 km/s. The recovered maximum spike has a value of 3.92 km/s and is well located.

This test lets us practically approaching the smearing problem, i.e. the way an anomaly spreads to adjacent nodes (Chapter 2.2.1.4). In the first 3 km of depth the presence of smoothed high velocity spots, from a 10% to 20% with respect to the surrounding field, is almost reconstructed. The smearing mostly affects the closest cells. Deeper than 3 km, more confused boundaries appear. In all tested cases, the anomaly intensities remain clearly below their true values and the amount of recovered anomaly varies depending on damping parameter. This presumably indicates that anomalies in our 3D model are undervalued.

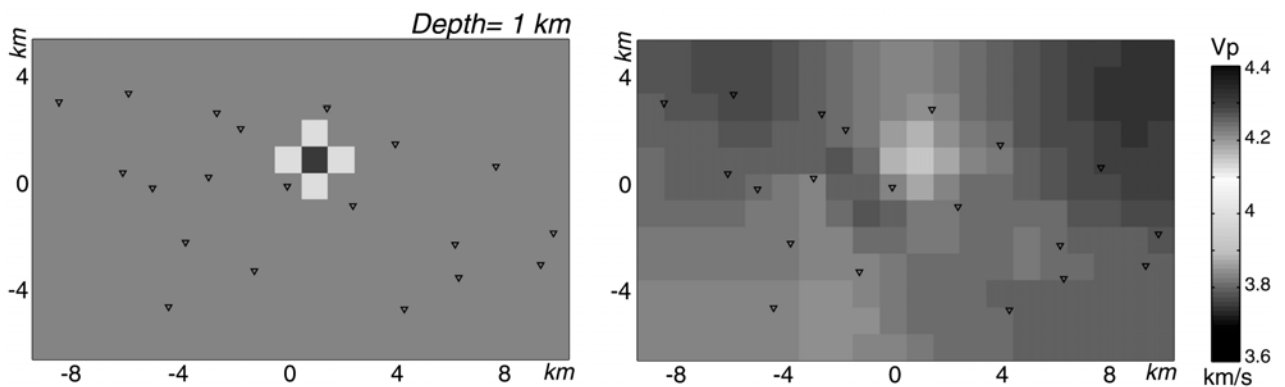


Figure 3.31 Synthetic and reconstructed model for a spot-like high velocity anomaly (contour interval is 0.02 km/s.) White triangles are seismic stations.

3.7.5.3. Reconstruction Test

As final resolution test, we calculated travel times in a velocity model equivalent to the Central São Miguel model. With this analysis we could check how well the inversion performed with anomalies with dimension and position similar to what

we expected to deal with in the real medium. The parameter selection and inversion scheme was the same as in our 3D inversion. We added noise to the synthetic travel times. The noise level was inversely proportional to the quality level assigned to the arrival time picks. To obtain a statistically robust estimate, this procedure was repeated to generate 25 noisy travel time data sets. When inverted, they generated a set of output models that show really slight differences among them. The standard deviations of velocity for each node are quite small, ranging between 0.02 and 0.44 km/s (between 0.0011 and 0.0087 s/km for slowness). We used slowness in spite of velocity because it shows a clearer Gaussian distribution of the final results), with a mean value of 0.1587 km/s (0.0051 s/km for slowness). This can be illustrated in a sample section of the model (**Figure 3.32**). In, we compare the average reconstructed model and our final CSM. We effectively observe that the main features are well recovered.

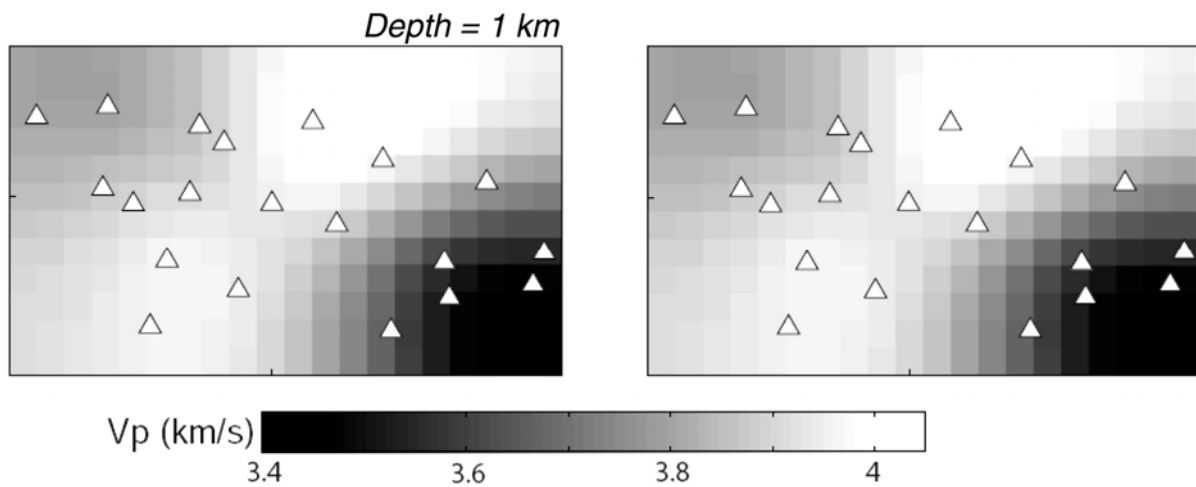


Figure 3.32 *Reconstruction Test.* The comparison is between the P-wave final velocity model (left) and average model from 25 different reconstruction- test inversions (right). White triangles are seismic stations. Horizontal sections at 1 km depth.

3.7.5.4. Starting Models

Finally, we assessed the effects of the starting model and database characteristics. We performed the inversion using different trial structures as initial models. We perturbed the minimum 1D model by $\pm 10\%$ [Barberi et al. 2004], and calculated their final P-wave velocity structures. The results of this test indicate that positions and shapes of the anomalies do not change across the studied volume (**Figure 3.33**).

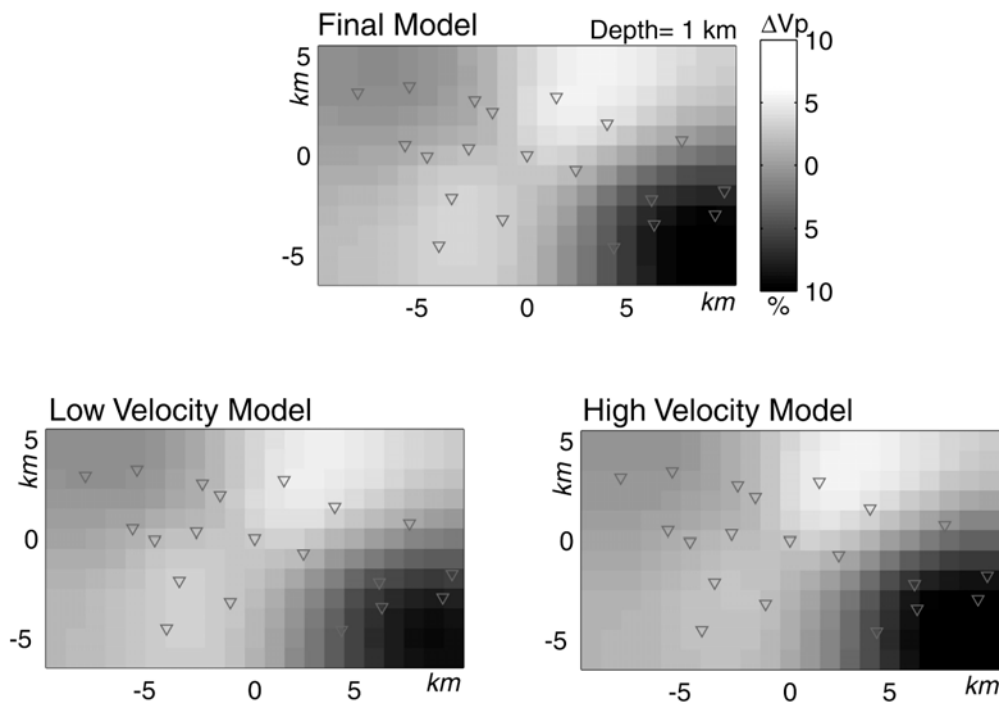


Figure 3.33 Comparison among velocity anomalies at 1 (left side) and 2 km (right side) depth for the final model ('True Model') and these obtained from a low velocity starting model ('Low Velocity Model') and a high velocity starting model ('High Velocity Model'). Contour interval is 1%. Red triangles are seismic stations. Axis are in km.

3.7.5.5. *Jackknife Test*

We then analyzed the control exerted on results by the database selection. We used a variation of the classical jackknife test [Lees and Crosson 1989] .

We performed 25 different inversions, removing a random 10% of the initial dataset, and then examining the variance of the derived models. The standard deviations among these models could be assumed as a measure of the uncertainty in the final model. The standard deviation was calculated for each node slowness among the final models. It ranged from $0.2 \cdot 10^{-3}$ s/km to $2.6 \cdot 10^{-3}$ s/km, with a spatially-averaged value around $1.1 \cdot 10^{-3}$ s/km.

Comparing the average velocity model with the true final model (**Figure 3.34**), we observe that differences are smaller than 2% of the averaged slowness at the same locations. Although the average model slightly smooths the velocity anomalies by presenting higher velocities where the final model presents slow velocity and on the opposite, lower velocities where the final model presents high velocities, the general framework of anomalies is not affected and main perturbations have a robust feature.

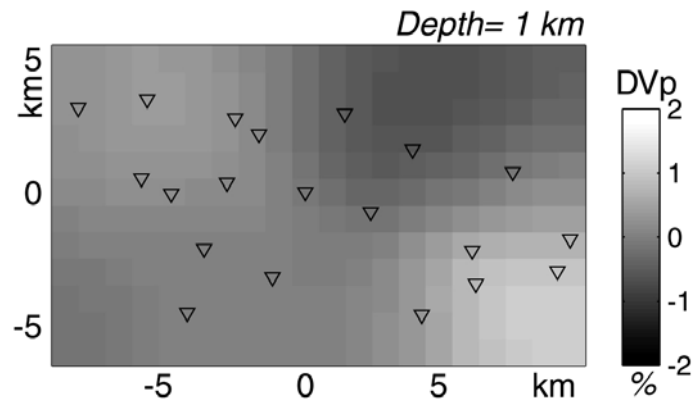


Figure 3.34 *Jackknife Test.* The perturbation of the average jackknife tests with respect to the final model are reported. Contours interval is 0.01 .Triangle are seismic stations.

3.7.6. Results

Travel time data obtained during the 2003 experiment at São Miguel were inverted by using the code by *Benz et al., (1996)*, method extensively described in the Chapter 2.2.3.1. Convergence of the tomographic inversion to a stable solution was obtained after 10 iterations. For P phase arrival times the average residual between observed and calculated values was 0.35 s in the Minimum 1D; in the final 3D model it was reduced to 0.13 s. For the S phase the RMS reduction was from 0.44 s to 0.15 s. This latter value refers to the inversion for the velocity model only.

We observe that 20 earthquakes could not find a new location, mainly depending on inversion volume dimensions because they were located outside the inverted volume. Hypocenter locations moved a mean of 0.77 km (standard deviation 4.037 km) in x direction, 0.23 km (0.719 km) in y direction and 0.26 km (1.018 km) in z direction (**Figure 3.35**). The origin times changed a mean of 0.026 s.

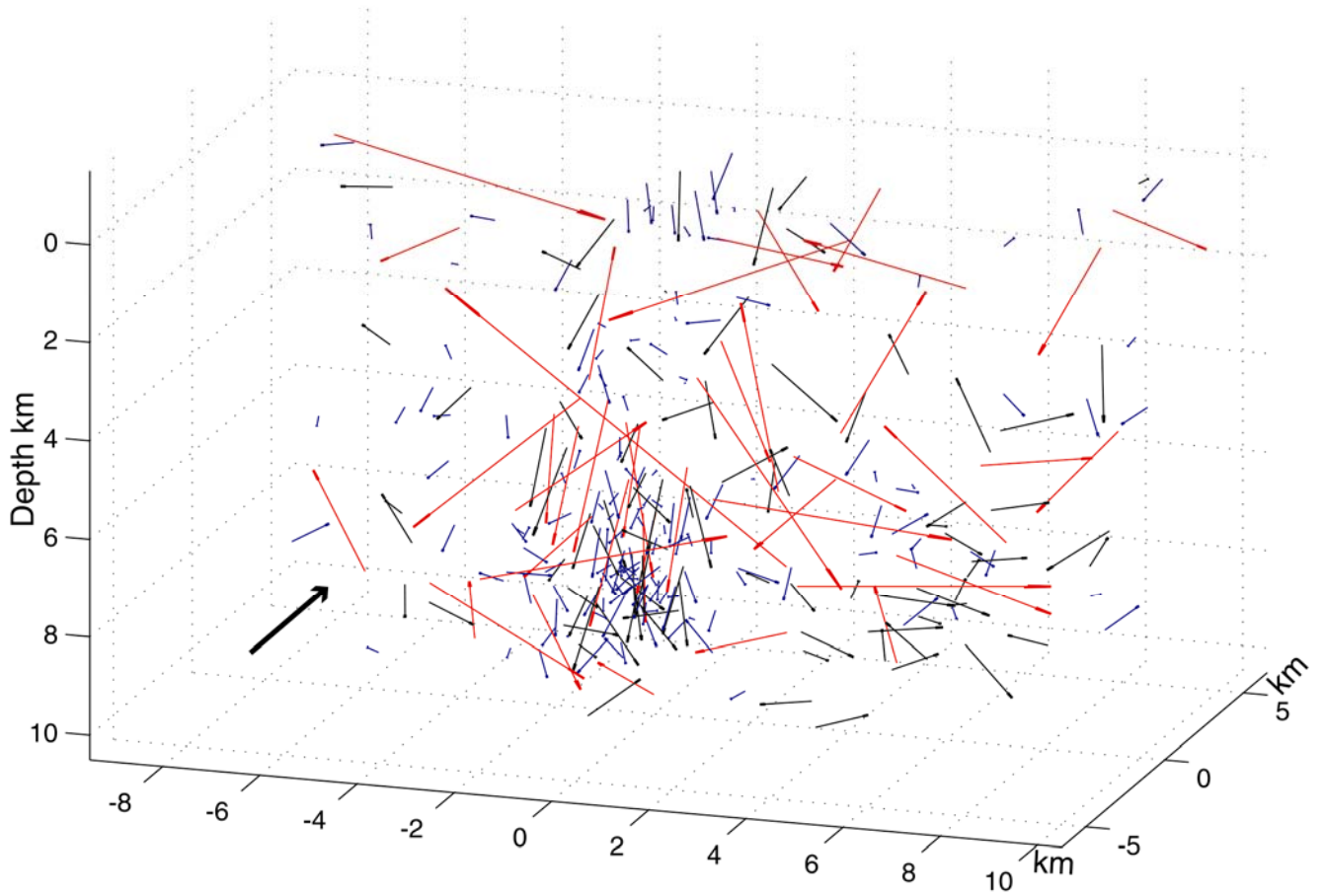


Figure 3.35 Earthquakes location changes from the Minimum 1D to the 3D model. A blue arrow indicates shift < 1 km; black arrow 1-2 km; red arrow > 2 km.

The small perturbations with respect to starting locations indicate that the starting Minimum 1D model was not far from the final 3D model. This means, the true 3D velocity deviations from this model are evenly distributed with zero mean. If we average the values of the 3D model across each layer, we observe that this averaged 1D model stays close to the 1D starting one (**Figure 3.36**). In the Minimum 1D model, the layer velocities approximately equal the average velocity of the

3D structure within the same depth range that has been sampled by the data. If we average the final 3D model for layer velocities considering only these cells which are sampled by ray paths, we still observe a strict similarity.

Moreover, we must note that differences between starting model and averaged final models at not resolved depths are probably artifacts introduced by the code. To reduce them, we slightly changed the Minimum 1D model introduced as starting structure for the 3D inversion by fixing an higher velocity at 9 km depth.

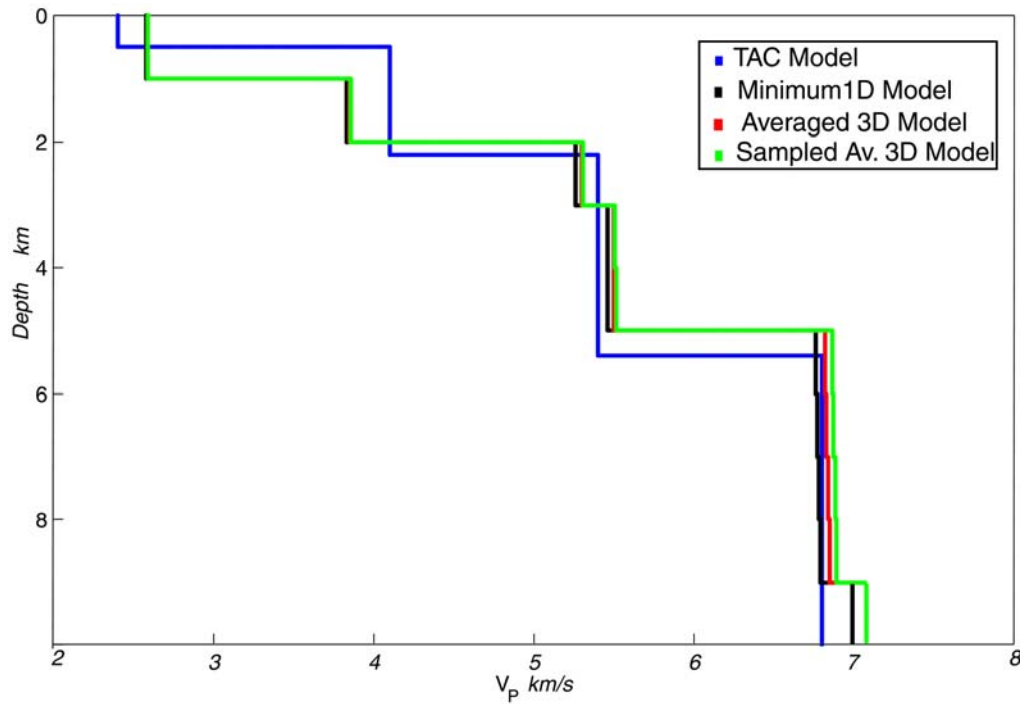


Figure 3.36 Comparison among 1D velocity models for P-wave. They are plotted the TAC model (blue line), Minimum 1 D model (black line), average model derived from the final 3D model (red line) and the average model derived from the sampled cells of the final 3D model.

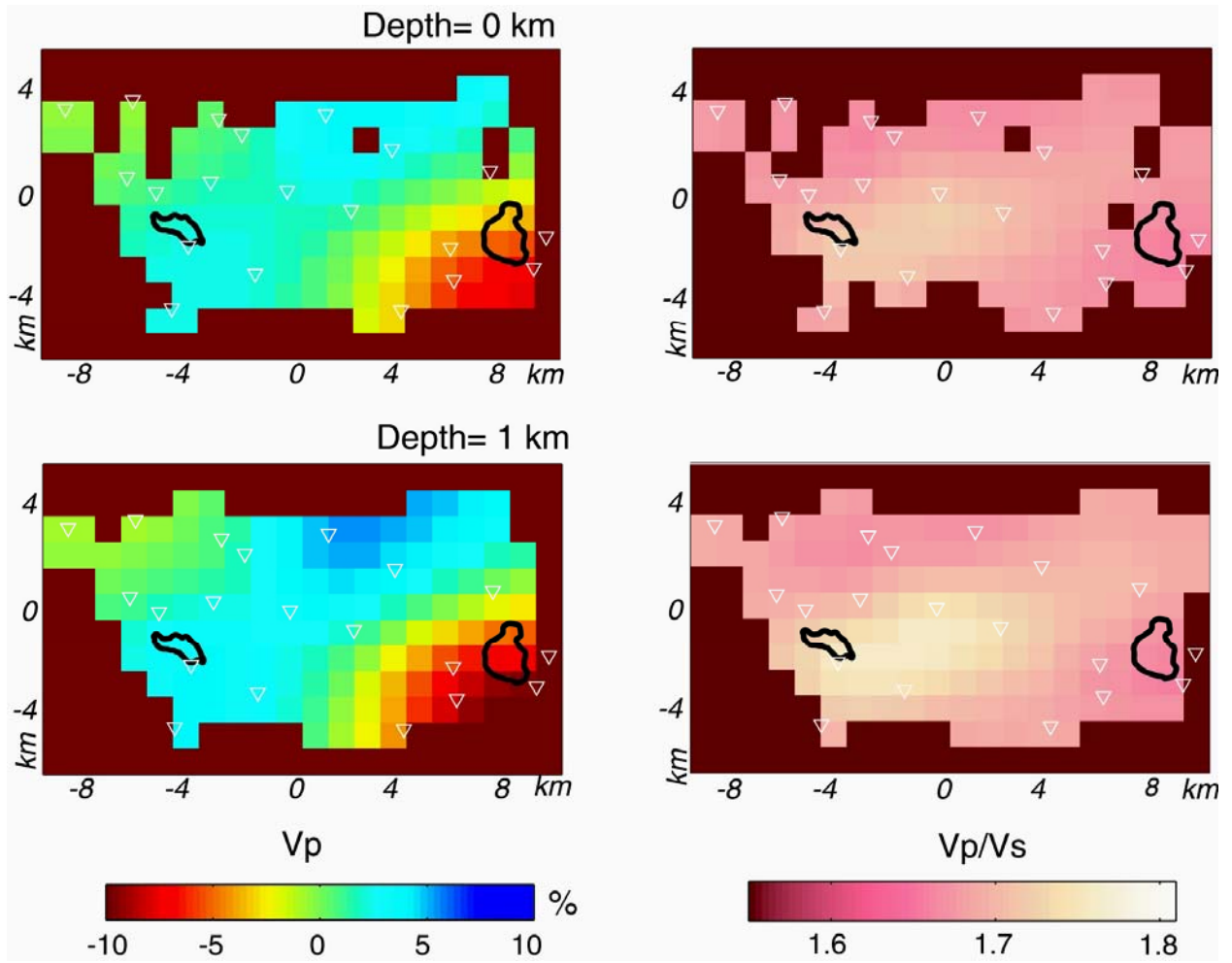
The final model contains several anomalous regions characterized by seismic velocities which strongly differ from their starting values up to 10%. **Figure 3.37** shows the distribution of V_p and V_p/V_s in central São Miguel. Those zones poorly resolved by the inversion, due to no coverage, are shaded. Several remarkable features appear in the seismic structure. We image a low-velocity anomaly in the Furnas zone, highly stable down to 6 km depth. The velocity values are about 10% lower than those of the starting model. Another zone of low velocity is situated in the NW corner of the studied area, between Fogo caldera and the north coast. This negative anomaly is weaker than the SE anomaly, and never surpasses the 2-3% value. Moreover, it stands in a peripheral region of our volume and for this reason it is pointed out by our resolution tests as tentative. This has to be taken into account for the interpretation. On the contrary, the region extending from the south of Fogo to the northwest of Furnas, across Congro area, shows clear positive anomalies, around 10% in their strongest value. It is present in the whole studied depth range, with a dominantly NE-SW trend. These anomalies are actually two main volumes, in the NE and SW extremes, separated by a relatively slow zone (clear at 0-2km depth). This zone has the highest coverage and thus this partition in two sub-regions is probably a real feature of the velocity structure.

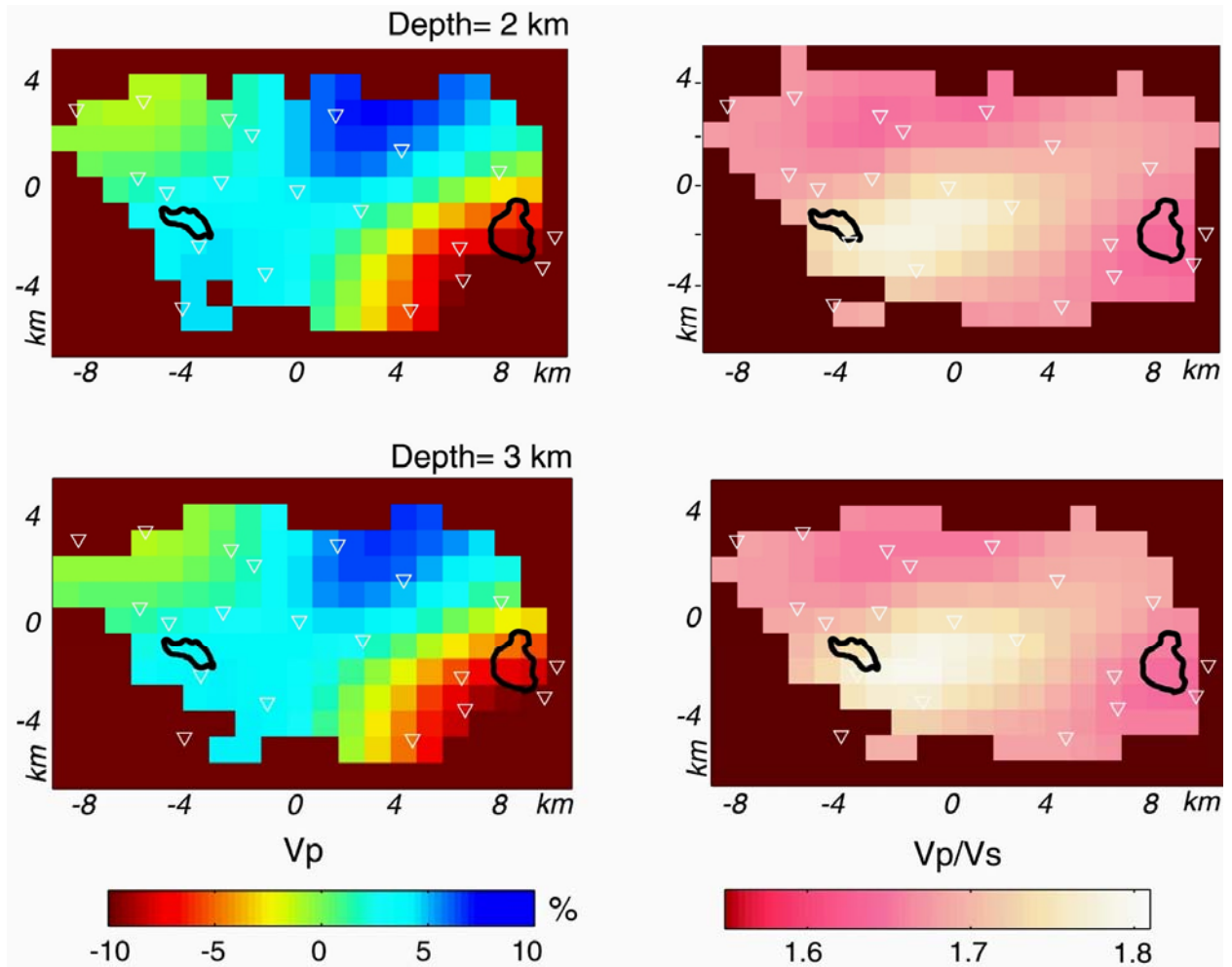
About the vertical distribution of heterogeneity, we observe that the overall position of the model contrasts does not strongly vary with depth. The main anomalies stand in their position, just slightly changing in intensity. This means that whatever mechanisms produce the velocity variations, they extend all the way down to the depth resolved by our inversion. **Figure 3.38** shows interpolated vertical sections along two profiles (see Figure for their positions) across the main anomalies. In this figure, we show the deep, poorly resolved levels as well, in order to understand the likely vertical extent of the anomalies. For example, the Furnas low-velocity anomaly extends in depth from 1 to 5 km, while the Ribeira Grande anomaly appears to be deeper. On the other hand, the north-eastern high-velocity region deepens more than the south-western high-velocity.

With respect to the V_p/V_s ratio of 1.68 previously derived for this area, both higher and lower values are retrieved by our inversion (**Figure 3.37**). A central, high ratio volume stands in the whole depth range. Between 1 and 5 km depth, high values extend eastward, closer to the Furnas area. Slightly high ratios appear between Fogo and the south coast. Low V_p/V_s can be observed in the north-northwest part of our volume and in the Furnas caldera zone. The lowest V_p/V_s ratios in both regions are found at about 2 km depth.

The V_p and V_p/V_s distributions contain features that do not overlap. For example, the SW and NE high velocity anomalies imaged in the V_p structure have completely different behaviour in terms of V_p/V_s . The NE area has low V_p/V_s

ratio, while the SW region has a slightly high value, around 1.7-1.8. This indicates that these two anomalies are not related to the same processes, and underlines the need for Vp/Vs analysis when performing seismic tomography.





3 - Central São Miguel

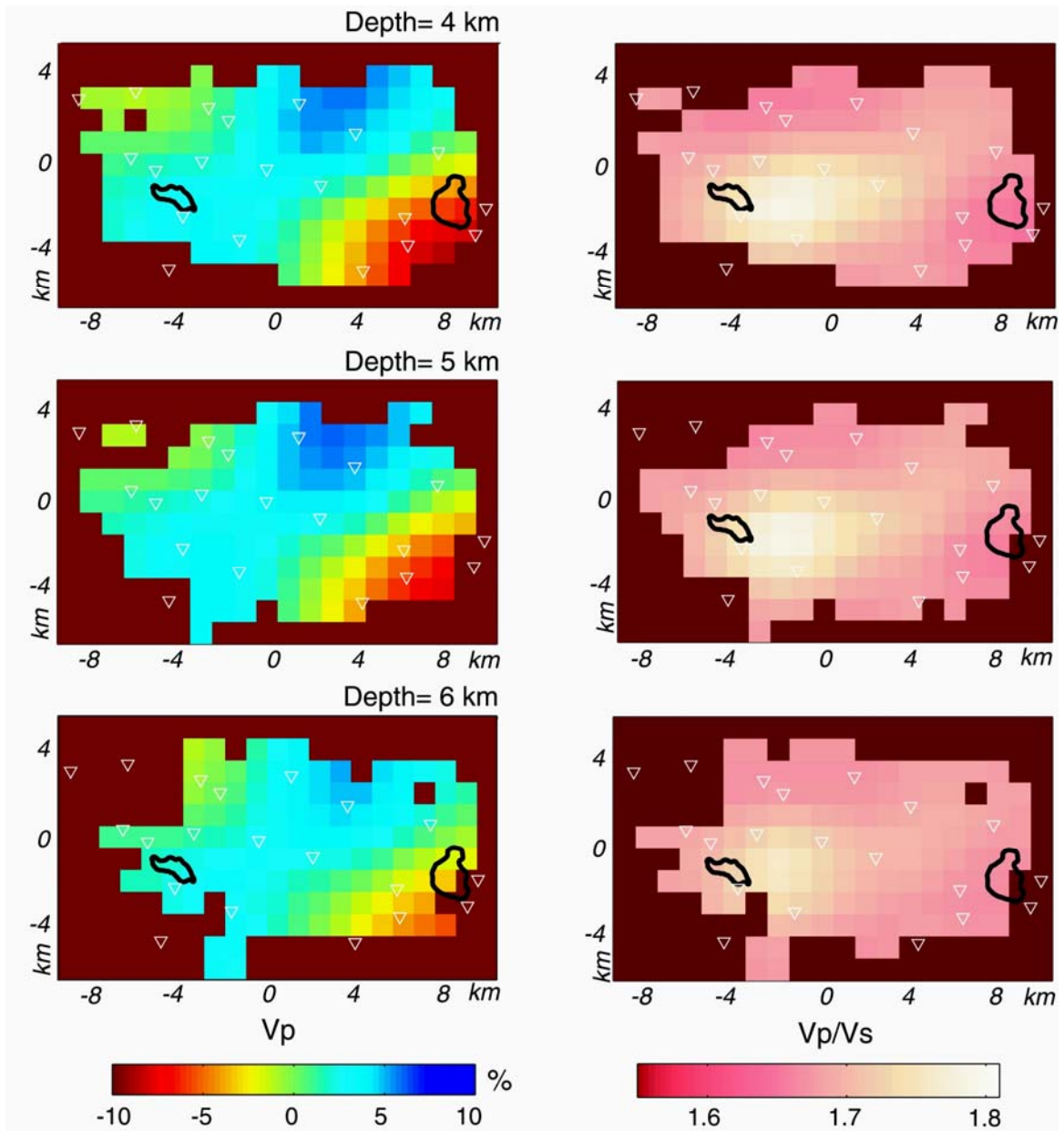


Figure 3.37 -3D Velocity model obtained from the tomographic inversion of P and S travel times. (top) The P-wave model is plotted as perturbations % with respect to the starting model. The S-wave model as V_p/V_s ratio. Triangles represent seismic stations. Fogo and Furnas lakes are marked with a bold line. Depths are also indicated. Unresolved areas are left as blank zones.

3.8. Discussion of Results and Conclusions

As we know (Chapter 1), in seismic tomography applied to volcanic areas, the interpretation of the V_p and V_p/V_s anomalies in terms of rock properties is often not unique. Therefore, any available information proceeding from other geological, geochemical and geophysical studies is necessary to correctly interpret the tomographic results.

In the case of São Miguel Island, we may refer to several works (Chapter 3.3), about the actual knowledge of this volcanic region. Central São Miguel has been the site of several geophysical surveys aimed at the investigation of this volcanic area. Some of them models the internal structure of São Miguel, although there are still several open questions.

From our results, in the central region of São Miguel the shallow velocity structure correlates well with the surface geology and agrees with results from previous geophysical studies, especially of gravimetric type [Camacho et al. 1997; Montesinos et al. 1999] and deformation [Jonsson et al. 1999; Sigmundsson and Tryggvason 1995]. Hence, to understand the nature and meaning of the velocity anomalies depicted in **Figure 3.37**, we combine the information from the V_p and V_p/V_s models, and discuss them in the light of the results of previous studies described above.

In the final results, the V_p distribution displays areas with low and high velocities, related to important lateral heterogeneities across Central São Miguel. We have revealed two low velocity regions around Furnas and northwest of Fogo, as well as two high-velocity regions south of Fogo and northwest of Furnas. These high-velocity anomalies might be linked through a lower velocity region.

Regarding the V_p/V_s distribution, we find two areas of low V_p/V_s ratio around Furnas and north and northeast of Fogo. A region of normal-to-high ratio occupies the center and southwest areas. In average, the V_p/V_s ratio in Central São Miguel tends to be low. This observation agrees with the results of previous studies [Dawson et al. 1985; Saccorotti et al. 2004]. The V_p/V_s ratio observed in active geothermal areas depends on the rock matrix, porosity, pore fluid content, pore pressure, temperature, and pore shape (Chapter 1.2.2). A low V_p/V_s ratio is thought to be caused by abundance of fractures filled with boiling water. Contrarily, melt inclusions reduce S-wave velocity more than P-wave velocity, resulting in high V_p/V_s ratios. For example at Etna volcano a V_p/V_s ratio above 1.82 has been measured [Patane et al. 2006], for zones of

partial melt that map the magma transport pathways. Therefore, the observation of low V_p/V_s values in Central São Miguel suggests that large volumes of partial melt are not present, at least within the shallowest crust.

Moreover, an overall seismic survey for the island [Dawson et al. 1985] gave an average V_p/V_s value of 1.53 to 1.62. It is interesting to note that these values are lower than what we found with our V_p/V_s tomography, as well as in the preliminary work on the *E_RUPTION* experiment data, which retrieved about 1.7 [Saccorotti et al. 2004]. Although the data base and instruments are quite different, we suspect that the reduction of the V_p/V_s ratio can be a real feature. We think that the difference could be attributed to the power plant production. The continuous exploitation of the geothermal system since the 80s could have decreased the steam fraction and/or cooled the system. This could be also the origin of the observed decrease of fumarolic activity [Cruz 2003], and general deflation of the zone [Jonsson et al. 1999].

3.8.1. *Low velocity regions*

The low velocity regions around Furnas caldera and north of Fogo volcano share a set of characteristics. Basically, they are characterized by low P-wave velocities and low V_p/V_s ratios, which decrease with depth until they reach a minimum at 2 km below sea level. Indications of low velocity in Furnas region proceeds also from the seismic profile [Senos and Nunes 1976]. Below Furnas caldera, a perturbation in the 2D velocity distribution indicates lower velocities. Moreover, results from gravity inversions [Camacho et al. 1997; Montesinos et al. 1999] point to the presence of low-density bodies that coincide spatially with our low-velocity regions. Similar low-gravity anomalies have been extensively related with low density products of explosive volcanic activity and collapse processes (Chapter 1.2.4). Taking into account the mainly trachytic, explosive eruptive history of Fogo and Furnas volcanoes, the low-velocity anomalies may be attributed to the presence of pyroclastic products infilling the surrounding areas. These products include pumices, ignimbrite and surge deposits, phreatomagmatic ashes, and dome materials [Guest et al. 1999]. However, while this explanation can be referred to the shallow layers, the continuation of the anomalies in depth may be associated with intensely fractured and/or hydrothermally altered areas as often recognized in calderas (Chapter 1.2.4).

The V_p/V_s ratios are low for both of these areas. The values point to the presence of extensive steam-dominated geothermal fields. The variations of the velocity ratio with depth could be explained by changes in the fluid conditions. In

the shallow part, water seems to dominate the reservoirs, producing a slightly higher V_p/V_s ratio. The existence of thermal springs near Furnas Lake confirms the existence of shallow, mixed-to-liquid-dominated geothermal fields, which are consistent with the higher V_p/V_s ratio observed in the first layers. The deuterium-oxygen isotope signatures indicate that the dominant fluid most likely derives from down-flow meteoric water input [Ferreira and Oskarsson 1999]. At larger depths, the geothermal reservoir would be filled with fluid at supercritical conditions, yielding a lower V_p and V_p/V_s ratio. This decrease in V_p/V_s ratio with depth might suggest that the fluid become steam-dominated at depths around 2 km, closer to the heat sources. The existence of vapour-filled systems at depths of about 4 km has been directly observed in wells at several geothermal fields, for example The Geysers [Moore et al. 2001].

In the Ribeira Grande geothermal system [Carvalho et al. 2006] has identified a fluid differentiated in several levels within 1 km of depth. The fluid in the deeper systems is basically a liquid, while it becomes mixed steam-liquid in the shallower levels. However, our tomographic image does not have enough resolution to describe the V_p/V_s ratio at such small scale. Most likely our results display a weighted average of the combined effect of these different subsystems, leading to a close-to-normal V_p/V_s ratio.

Therefore, a geothermal system embedded in porous, low-density pyroclastic deposits could be the origin of the low V_p , low V_p/V_s , and low density values reported in these areas. Although the similarities point to a common explanation for the velocity anomalies in these areas around Furnas and Fogo, there are also a few differences. For example, the low velocity area north of Fogo is much weaker. The coverage, and therefore the resolution capabilities of the tomography method, are low in this area. This can be at the origin of an underestimate of anomaly intensity.

3.8.2. *High velocity regions*

The high velocity regions in Figure are distributed along a NE-SW trend, from the south of Fogo to the northwest of Furnas. These anomalies could reflect the existence, at various depths, of welded thick pyroclastic deposits, domes and more compacted material. The NE-SW stretch of the anomaly is compatible with the direction of normal faults in the area, either inferred [Carvalho et al. 2006] or detected as electric discontinuities [Gandino et al. 1985]. These faults separate the plains of the north coast from the Fogo volcanic system through structural depressions filled by pyroclastic and lava

products. The gravity survey results [Camacho et al. 1997] evidence an analogous direction for contacts between zones of contrasting densities. In the gravity map, the central high density splits in two arms in its SW extreme. The Fogo zone corresponds to the lower density zone separating the two arms. This gravity minimum, which might be recognized as a low velocity anomaly, stands probably outside our resolvable zone.

The Fogo volcano could stand as a chilled remnant of a magma chamber. The absence of melt under the Fogo edifice is confirmed by the lack of evidence of magmatic activity from geophysical and geochemical surveys [Cruz et al. 2006]. For example the general deflection of the area [Jonsson et al. 1999] and a decrease of the fumarolic system intensity [Cruz 2003] are widely reported. Moreover, the magmatic input of fumarolic system is considered not as strong as to justify a direct connection between hydrothermal and magmatic activity, as reported in the *E_RUPTION* project reports.

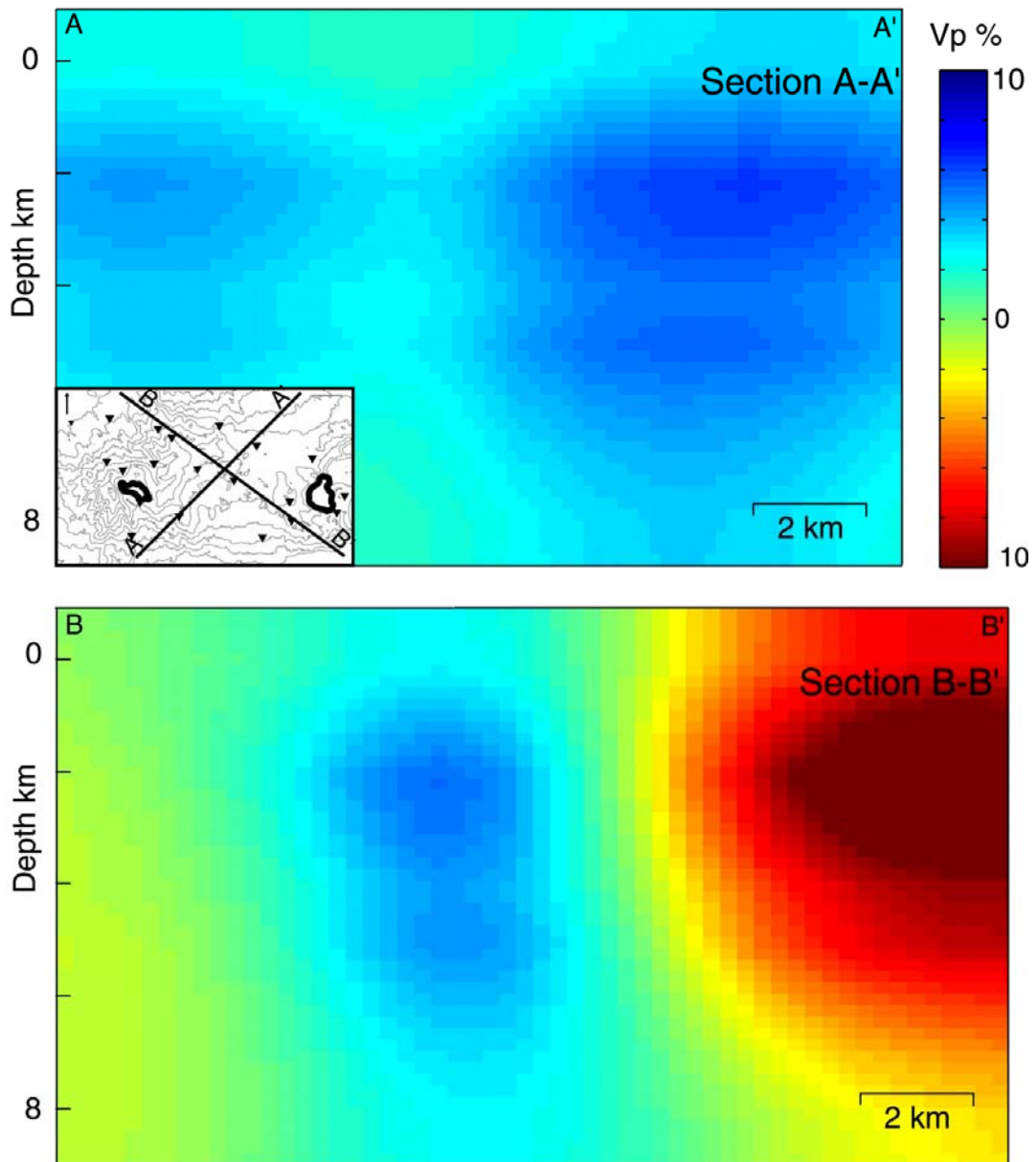
Dawson et al. (1985) image a Vp negative anomaly centered in Fogo volcano. This is contrasting with our observation, but it has to be considered that is inferred from a study of a completely different and probably poor database (seven regional earthquake residuals) and it is interpreted as a hydrothermal reservoir more than a body of partial melt. Otherwise, the sole seismic profiles carried out in the zone [Senos and Nunes 1976], that crosses Fogo volcano, shows a mostly unperturbed velocity distribution.

We observe different Vp/Vs values for the two high velocity regions. Vp/Vs span the whole range between 1.8 (in the SW high Vp anomaly) and as low as 1.65 (in the NE high Vp). They are likely due to different phenomena and constitute an excellent example of the importance of Vp/Vs ratio to interpret information by Vp distribution. The positive Vp anomaly located in Fogo area has high Vp/Vs ratio. This could indicate that this intrusive part is marked by low Vs, i.e. fluids contained in fractures of the medium. From this point of view, we are imaging zones of transport, advection and crystallization of fluids through a solidified intrusive. Given the strong high-Vp anomaly, we think that water could be the fluid involved rather than melt. We assume that this fracture system represents the preferred path for up-welling of water toward the superficial geothermal fields. Something similar has been observed and explained with the presence of melt/water-saturated pathways in several volcanic areas (see Chapter 1.2.4. for examples). On the other hand, the lower Vp/Vs ratio of the northeast high Vp anomaly could be due to volcanic material relatively unaffected by fracturing and geothermal circulation.

An intermediate region divides the two high Vp anomalies. This zone constitutes the main seismogenic region in Central São Miguel. Most of the relocated seismicity clusters here, showing a preferred NW-SE alignment [Bonagura et al. 2004]. Moreover, this direction dominates the tectonics of the zone also in surface geology [Gandino et al. 1985; Guest et

al. 1999]. Although the constituent materials could be the same as in the neighbouring high V_p areas, the high crack density typical of faulted volumes would be at the origin of the observed lower velocity.

Figure 3.38 Vertical cross sections of P-wave model. The velocity model is interpolated. The section positions are reported in the small insert. 



3.9. *Conclusions*

This study represents a first attempt toward delineating the detailed subsurface seismic velocity structure of São Miguel Island. In the zone we are able to resolve, the velocity model depicts a complex picture of heterogeneities in which both the V_p and V_p/V_s have large lateral variations over scale lengths of a few kilometres. Referring to results of our seismic tomography in combination with additional information from studies of seismicity, gravimetry, deformation, but also geochemistry, geology, tectonics, we suggest a model for the distribution of main volcanic structures. Among them, we identify volcanic centres, intrusive bodies, geothermal fields, tectonic features and effects of a heterogeneous surface geology.

Among these factors, these of volcanic origin are by far the most interesting. For example, the coincidence between our velocity structure and the results from several other studies leads us to locate a vigorous geothermal field in Furnas caldera, and not at Fogo volcano. In our interpretation, Furnas has a distribution of low V_p together with low V_p/V_s , that indicates the existence of a water-dominated geothermal field. Fogo area, on the opposite, presents high V_p and high V_p/V_s . Hence, the clearest suggestion of magmatic activity, such as a low V_p with high V_p/V_s , seems to lack. The velocities structure rather images a volume of high V_p . It would be the chilled remnant of a magmatic chamber, which nowadays could constitute only the pathway for magma-related fluids. To these fluids, mostly water of different origin, and not to magma, the high V_p/V_s would be associated.

This picture of volcanic structures is thus expected to improve the knowledge of the past and present volcanic activity of Central São Miguel and the nature of the recorded seismicity. Some evidences recovered by the velocity structure, such as the importance of the regional tectonics on the volcanic evolution of the zone, could be extended to the whole island history. Others, such as the development of geothermal systems in calderic areas, are expected to be found in Sete Cidades and Povoação, among others.

Furthermore, the tomographic image has a risk evaluation feedback. The E_RUPTION project was planned to improve the knowledge of the volcanic activity in the inhabited São Miguel, with a risk evaluation final task. The knowledge of the present state and the insight in the volcanic evolution of the Central area of the island has important implications also for the hazard assessment and management. From our study, the main risk seems to be related to the intense seismic and geothermal activity. There are no seismic evidences of immediate volcanic hazard for the zone. If magma is present, at

shallow crustal levels has its strongest effects in the development of a strong thermal anomaly and several geothermal systems

As natural, more questions arise from the results of this seismic velocity tomography, mostly related with areas of low resolution and scale of resolved anomalies. Imaged structures could be better depicted by a wider database. At this point, long-term data from the permanent seismic network would be desirable. The use of specialized instrumentation could otherwise improve the knowledge of the long period seismic activity, which, on the base of our evidences, is probably intense and widespread.

References

- Almendros, J., Ib, ez, J., s, M., Alguacil, G., and Del Pezzo, E., 1999, Array analysis using circular-wave-front geometry: an application to locate the nearby seismo-volcanic source: *Geophysical Journal International*, v. 136, p. 159-170.
- Barberi, G., Cosentino, M. T., Gervasi, A., Guerra, I., Neri, G., and Orecchio, B., 2004, Crustal seismic tomography in the Calabrian Arc region, south Italy: *Phys. Earth Planet. Int.*
- Beier, C., Haase, K. M., and Hansteen, T. H., 2006, Magma Evolution of the Sete Cidades Volcano, Sao Miguel, Azores: *Journal of Petrology*, v. 47, p. 1375-1411.
- Benz, H. M., Chouet, B. A., Dawson, P. B., Lahr, J. C., Page, R. A., and Hole, J. A., 1996, Three dimensional P and S wave velocity structure of Redoubt Volcano, Alaska: *J. Geophys. Res.*, v. 101, p. 8111-8128.
- Bonagura, M. T., Damiano, N., Saccorotti, G., Ventura, G., Vilardo, G., and Wallenstein, N., 2004, Fault geometries from the space distribution of the earthquakes at Sao Miguel Island (Azores): inference on the active deformation: *Geophys. Res. Abstr.*, v. 6.
- Bufo, E., Udias, A., and Colombas, M. A., 1988, Seismicity, source mechanisms and tectonics of the Azores-Gibraltar plate boundary: *Tectonophysics*, v. 152, p. 89-118.
- Camacho, A. G., Montesinos, F. G., and Vieira, R., 1997, A three-dimensional gravity inversion applied to São Miguel island (Azores): *J. Geophys. Res.*, v. 102, p. 7705-7715.
- Carvalho, M. R., Forjaz, V. H., and Almeida, C., 2006, Chemical composition of deep hydrothermal fluids in the Ribeira Grande geothermal field (Sao Miguel, Azores): *J. Volc. Geotherm. Res.*, v. 156, p. 116-134.
- Cipollini, M., 2002, World Championship: *Gazzetta dello Sport*.
- Cruz, J. V., 2003, Groundwater and volcanoes: examples from the Azores archipelago: *Environmental Geology*, v. 44, p. 343-355.
- Cruz, J. V., Antunes, P., Amaral, C., Franca, Z., and Nunes, J. C., 2006, Volcanic lakes of the Azores archipelago (Portugal): Geological setting and geochemical characterization: *Journal of Volcanology and Geothermal Research*, v. 156, p. 135-157.
- Cruz, J. V., Coutinho, R. M., Carvalho, M. R., Oskarsson, N., and Gislason, S. R., 1999, Chemistry of waters from Furnas volcano, Sao Miguel, Azores: fluxes of volcanic carbon dioxide and leached material: *Journal of Volcanology and Geothermal Research*, v. 92, p. 151-167.
- Chatterjee, S. N., Pitt, A. M., and Iyer, H. M., 1985, Vp/Vs ratio in the Yellowstone National Park Region, Wyoming: *J. Volc. Geotherm. Res.*, v. 26, p. 213-230.
- Chouet, B. A., 2003, Volcano Seismology: *Pure Appl. Geophys.*, v. 160, p. 739-788.
- Dawson, P. B., Rodrigues da Silva, A., Iyer, H. M., and Evans, R., 1985, Seismic study of the Agua de Pau geothermal prospect, São Miguel, Azores: *Geothermal Resources Council Transactions*, v. 9.
- Escuer Tello, M., 2006, Improving seismic Vp and Vs models of the Azores Archipelago, Universidade Dos Acores.
- Fernandes, R. M. S., Bastos, L., Miranda, J. M., Lourenço, N., Ambrosius, B. A. C., Noomen, R., and Simons, W., 2006, Defining the plate boundaries in the Azores region: *Journ. Volc. Geotherm. Res.*

- Ferreira, T., and Oskarsson, N., 1999, Chemistry and isotopic composition of fumarole discharges of Furnas caldera: *J. of Volcanol. And Geotherm. Res.*, v. 92, p. 169-179.
- Forjaz, V. H., 1984, S.Miguel: volcanostratigraphic sketch: *Dep. geociências Universidade dos Açores*.
- Gandino, A., Guidi, M., Merlo, C., Mete, L., Rossi, M., and R., Z., L., 1985, Preliminary model of the Ribeira Grande geothermal field (Azores Islands): *Geothermics*, v. 14, p. 91-105.
- Gente, P., Dymant, J., Maia, M., and Goslin, J., 2003, Interaction between the Mid-Atlantic Ridge and the Azores hot spot during the last 85 Myr: Emplacement and rifting of the hot spot-derived plateaus: *Geochem. Geophys. Geosyst.*
- Goldstein, P., Dodge, D., Firpo, M., and Minner, L., 2003, SAC2000: Signal processing and analysis tools for seismologists and engineers, *in* Lee, W., Kanamori, H., Jennings, P. C., and Kisslinger, C., eds., *The IASPEI International Handbook of Earthquake and Engineering Seismology*, London, Academic Press.
- Gongora, E., Carrilho, F., and Oliveira, C. S., 2004, Calibration of Local Magnitude ML in the Azores Archipelago based on recent digital recordings: *Pure appl. Geophys.*, v. 161, p. 647-659.
- Guest, J. E., Gaspar, J. L., Cole, P. D., Queiroz, G., Duncan, A. M., Wallenstein, N., Ferreira, T., and Pacheco, J. M., 1999, Volcanic geology of Furnas Volcano, Sao Miguel, Azores: *Journal of Volcanology and Geothermal Research*, v. 92, p. 1-29.
- Haase, K. M., and Beier, C., 2003, Tectonic control of ocean island basalt sources on São Miguel, Azores?: *Geophys.Res. Lett.*, v. 30, p. 1856-1859.
- Havskov, J., and Ottemoller, L., 1999, SEISAN: The Earthquake Analysis Software, Norway.
- Havskoz, J., and Alguacil, G., 2004, *Instrumentation in earthquake seismology*: Dordrecht, Springer, 322 p.
- Humpreys, E., and Clayton, R. W., 1988, Adaptation of back projection tomography to seismic travelttime problems.: *J. Geophys. Res.*, v. 93, p. 1073-1085.
- Huttrer, G. W., 1996, The status of world geothermal power production 1990-1994: *Geothermics*, v. 25, p. 165-187.
- Johnson, C. L., Wijbrans, J. R., Constable, C. G., Gee, J., Staudigel, H., Tauxe, L., Forjaz, V. H., and Salgueiro, M., 1998, ⁴⁰Ar/³⁹Ar ages and paleomagnetism of Sao Miguel lavas, Azores: *Earth and Planetary Science Letters*, v. 160, p. 637-649.
- Jonsson, S., Alves, M. M., and Sigmundsson, F., 1999, Low rates of deformation of the Furnas and Fogo Volcanoes, Sao Miguel, Azores, observed with the Global Positioning System, 1993-1997: *J. Volc. Geotherm. Res.*, v. 92, p. 83-94.
- Kissling, E., 1995, *Velest*, Users guide, Internal report, Zurich, Institute of Geophysics.
- Kissling, E., Ellsworth, W. L., Eberhart-Phillips, D., and Kradolfer, U., 1994, Initial reference models in local earthquake tomography: *J. Geophys. Res.*, v. 99, p. 19635-19646.
- Lees, J. M., and Crosson, R. S., 1989, Tomographic inversion for three-dimensional velocity structure at Mount St. Helens using earthquake data: *J. Geophys. Res.*, v. 94, p. 5716-5728.
- Lomax, A. J., Virieux, J., Volant, P., and Berge, C., 2000, Probabilistic earthquake location in 3D and layered models: Introduction of a Metropolis-Gibbs method and comparison with linear locations, *in* Thurber, C. H., and Rabinowitz, N., eds., *Advances in Seismic Event Location*, Amsterdam, Kluwer.
- Lourenço, N., Miranda, J. M., Luis, J. F., Ribeiro, A., Mendes Victor, L. A., Madeira, J., and Needham, H. D., 1998, Morpho-tectonic analysis of the Azores Volcanic Plateau from a new bathymetric compilation of the area: *Mar. Geophys. Res.*, v. 20, p. 141-156.
- Luis, J., 2006, A little insight over the recent Sao Miguel seismic activity, [http://w3.ualg.pt/~sim\\$jluis/SMiguel_seismicity.htm](http://w3.ualg.pt/~sim$jluis/SMiguel_seismicity.htm), Universidade do Algarve.

- Madeira, J., and Ribeiro, A., 1990, Geodynamic models for the Azores triple junction: a contribution from tectonics: *Tectonophysics* v. 184, p. 405-415.
- Miranda, J. M., Mendes Victor, L. A., Simões, J. Z., Luis, J. F., Matias, L., Shimamura, H., Shiobara, H., Nemoto, H., Mochizuki, H., Hirn, A., and Lépin, J. C., 1998, Tectonic setting of the Azores Plateau deduced from a OBS survey *Mar. Geophys. Res.*, v. 20, p. 171-182.
- Montesinos, F. G., Camacho, A. G., and Vieira, R., 1999, Analysis of gravimetric anomalies in Furnas caldera (Sao Miguel, Azores): *J. Volc. Geotherm. Res.*, v. 92, p. 67-81.
- Moore, J. N., Norman, D. I., and Kennedy, B. M., 2001, Fluid inclusion gas compositions from an active magmatic-hydrothermal system: a case study of The Geysers geothermal field, USA: *Chem. Geol.*, v. 173, p. 3-30.
- Moore, R. B., 1990, Volcanic geology and eruption frequency, São Miguel, Azores: *Bull. Volcanol.*, v. 52, p. 602-614.
- Muecke, G. K., Ade-Hall, J. M., Aumento, F., MacDonald, A., Reynolds, P. H., Hyndman, R. D., Quintino, J., Opdyke, N., and Lowrie, W., 1974, Deep drilling in an active geothermal area in the Azores: *Nature*, v. 252, p. 281-284.
- Patane, D., Barberi, G., Cocina, O., De Gori, P., and Chiarabba, C., 2006, Time-Resolved Seismic Tomography Detects Magma Intrusions at Mount Etna: *Science*, v. 313, p. 821-823.
- Ritsema, J., and Allen, M., 2003, The elusive mantle plume: *Earth and Planet. Sci. Lett.*, v. 207, p. 1-12.
- Saccorotti, G., Wallenstein, N., Ibañez, J. M., Bonagura, M. T., Damiano, N., La Rocca, M., Quadrio, A., Silva, R., and Zandomenighi, D., 2004, A seismic field survey at Fogo-Furnas volcanoes, São Miguel, Azores, *Geophys. Res. Abstr.*
- Senos, M. L., and Costa, J., 1978, Estudo da crosta nas ilhas de Sao Miguel e Terceira. Resultados preliminares, Relatório do estágio realizado no Instituto de física do globo de Paris, nos meses de Outubro e Novembro de 1977 e Fevereiro e Março de 1978 pelo geofísico Maria Luisa Conde Senos e pelo observador geofísico analista José Adelino de Costa Nunes, Lisboa, INMG.
- Senos, M. L., and Nunes, J. A. F., 1976, Report do seismic refraction on Ihla Sao Miguel, Lisboa, SMN.
- Sigmundsson, F., and Tryggvason, E., 1995, Slow inflation of the Furnas volcano, Sao Miguel, Azores, suggested from initial leveling and Global Positioning System measurements: *Geophys. Res. Lett.*, v. 22, p. 1681-1684.
- Silva, R., Saccorotti, G., and Wallenstein, N., 2005, Seismic multiplets on São Miguel (Azores). Analysis of source, path and site effects European Geosciences Union General Assembly.
- Silveira, G., Stutzmann, E., Davaille, A., Montagner, J.-P., Mendes-Victor, L., and Sebai, A., 2006, Azores hotspot signature in the upper mantle: *J. Volc. Geotherm. Res.*
- Trota, A., Houli, N., Briole, P., Gaspar, J. L., Sigmundsson, F., and Feigl, K. L., 2006, Deformation studies at Furnas and Sete Cidades Volcanoes (Sao Miguel Island, Azores). Velocities and further investigations: *Geophys. J. Intern.*, v. 166, p. 952-956.
- Widom, E., Farquhar, J., 2003, Oxygen signatures in olivines from Sao Miguel (Azores) basalts: implications for crystal and mantle processes: *Chemical Geology*, v. 193, p. 237-255.
- Zelt, C. A., 1988, Lateral velocity resolution from three dimensional seismic refraction data: *Geophys. J. Int.*, v. 135, p. 1101-1112.
- Zhao, D., Hasegawa, A., and Horiuchi, S., 1992, Tomographic imaging of P and S wave velocity structure beneath northeastern Japan: *J. Geophys. Res.*, v. 97, p. 19909-19928.

4. *Deception Island*

Abstract

Deception Island (62°59' S, 60°41' W) is an active volcano located in Bransfield Strait between the Antarctic Peninsula and the South Shetland Islands. The volcano has a basal diameter of ~30 km and rises ~1500 m from the seafloor to a maximum height of over 500 m above sea level. The 15-km-diameter emerged island is horseshoe-shaped with a flooded inner bay that is accessible to the ocean through a 500-m-wide passage. The island is composed of volcanic rocks which date from <0.75 Ma to historical eruptions (1842, 1967, 1969 and 1970). The volcano origin is poorly understood. The island is situated north of the main axis of the Bransfield Strait, a tensional structure interpreted as an active back-arc basin, but its geochemistry and seismic activity do not fit unequivocally this interpretation and appear to be a further indication of the complexity of Bransfield evolution.

In January 2005 an extensive seismic survey took place in and around the island, with the participation of researchers from Argentina, Germany, Ireland, Italy, Mexico, Spain and the United States. The main objective of the experiment was to collect high quality data to be used for a two- and a three-dimensional P-wave velocity tomography of the volcano. A total of 85 land and 14 ocean bottom seismometers were deployed to record two rounds of shooting, where more than 6600 air gun shots were fired within the caldera and around the island. The initial dataset used for the three-

dimensional seismic tomography comprises more than 70000 P-wave travel times that were determined using both automatic and manual first-arrival picking procedures.

A preliminary three-dimensional P-wave inversion of the travel times resolves the structure down to about 5 km depth. The results of additional tomographic inversions and resolution tests help in the definition of resolved zones and permit the interpretation of only well constrained velocity anomalies.

The tomographic image is characterized by strong velocity contrasts across the whole resolved volume. The most striking feature is the low seismic velocities located beneath the caldera floor. It represents an extensive region of magma that extends below a shallow caldera infilling. Another low velocity zone is present at the east and south-east of Deception Island. This is otherwise interpreted as sedimentary deposits in graben-like structures, crossing the Bransfield, to the Deception Island vicinity. On the opposite, an anomalously high velocity marks the north-western sector of the resolved volume, above the northern portions of Deception Island and between the island and the South Shetland block. This constitutes the seismic evidence of the crystalline basement of the pre-Bransfield continental crust. Other high velocities stand around the southern margins of the caldera and belong to several formations of the ancient Deception Island.

We observe in the tomographic image of Deception Island as prevailing fault systems those NE-SW and NW-SE trend, compatible with the regional tectonics. We suggest that the volcanic evolution of Deception Island is conditioned by the Bransfield geodynamics. In this sense, we support the hypothesis of the fracturing of the Bransfield basin as evolution of continental crust due to the action of the trans-extensional stress field.

Extended Abstract

Introduction

The understanding of Deception Island Volcano is severely limited by the incomplete knowledge of its internal structure. Its evolution and actual state has been extensively studied but, without information on the distribution of melt, the depth of sediments and the location of intrusive bodies and fault zones beneath and around the island, models for the structure and evolution of Deception Island are poorly constrained. It has a complicated tectonic setting and its geochemistry and seismic activity do not fit any unique interpretation in the framework of the regional geodynamics. The main aim of this work is to use seismic tomography to address this problem and to discuss the relationship between obtained images of seismic heterogeneities and other geophysical and geological observations.

Deception Island (62°59' S, 60°41' W) is an active volcano located in the Bransfield Strait between the Antarctic Peninsula and the South Shetland Islands. Located at the western limit of the central of three sub-basins in which the Bransfield Basin can be morphologically divided, the island is a stratovolcano with a horseshoe shape of 15-km diameter and with a flooded inner bay that is accessible to the ocean through a 500-m-wide passage. It is composed of volcanic rocks that date from <0.75 Ma to historical eruptions (1842, 1967, 1969 and 1970). Pyroclastic rocks, agglomerates, tuff and ash form at least 80% of its volume. It has been proposed that the inner bay (Port Foster) probably formed progressively by passive extension along sets of normal faults that cut the island. In fact, structural mapping and seismic reflection studies within Port Foster show that the local tectonics is controlled, among many others, by two major fault systems. A NE-SW striking system, consistent with the regional extensional regime of the Bransfield Strait, controls the alignment of the eruptive centers of 1967 and 1970. The second system strikes NNW-SSE, approximately perpendicular to the first one, is observed in fault orientations and may control the shape of Costa Recta, the eastern coast of Deception Island.

The present volcanic activity of Deception Island is high, and includes vigorous hydrothermal circulation, resurgence of the floor of Port Foster and intense seismicity, that includes volcano-tectonic and long-period signals. These observations, together with gravity and magnetic anomalies and high seismic attenuation, point to the existence of a shallow magma chamber underlying Port Foster, emplaced in a highly fractured medium. The volcano-tectonic activity, which clusters in swarms, as in 1992 and 1995, is attributed to the action of the major fault systems of the island. The source mechanism of the long period activity points to the interaction of thaw water or a shallow aquifer with high-temperature rocks, that is focused along the high-permeability fracture systems.

A three-dimensional seismic P wave tomography survey of Deception Island volcano was conducted as part of the *TOMODEC* project in January, 2005. We describe the seismic experiment, data collection and analysis, the tomographic inversion and its application to our data. We present a preliminary image of seismic velocity structure for Deception Island and its surroundings. Based on these results, we propose a structural and evolution model for Deception Island, in the framework of the regional tectonics.

Seismic Experiment

The seismic experiment was designed to obtain a three-dimensional seismic image of Deception Island and the surrounding region. Airgun shots were fired every minute in a grid pattern inside Port Foster and approximately every two minutes along three concentric rings outside the island. In addition, two long lines of shots that crossed the island were collected, one oriented NNW-SSE and ~90 km long, the other approximately perpendicular to the first and ~55 km long.

Eighty-five land and 14 ocean-bottom seismometers (OBSs) were deployed to record the air gun arrivals. The shooting patterns were repeated and some were relocated between the first and second rounds to increase the ray coverage. The seismic stations were installed at least 0.2 km apart across the island, as autonomous stations and sparse arrays. Also dense seismometer arrays were deployed. The distribution of land stations was constrained by cliffs, glaciers, and lakes. The OBSs were distributed in the inner bay and in a circular configuration around the island. Most of the seismometers were vertical component only, but the OBSs and 20 stations were equipped with 3-component sensors, the OBSs also

included a hydrophone. Nearly 6600 air gun shots were fired using the R/V *Hespérides*, and a total of 120 Gb of data were recorded. In addition to the seismic data, gravity, magnetic and multibeam bathymetry data were acquired along the same ship tracks.

The final dataset consists of travel times for more than 70000 crustal P-wave first arrivals. These were identified, picked, and assigned uncertainties using a combination of manual and automatic picking routines from the Seismic Analysis Code software. Each station recorded an average of ~1500 shots; each shot was picked on more than 15 stations.

The P-wave travel times were inverted for a 3-D velocity model for Deception Island and the surrounding region using the seismic tomography code of Toomey. This method separates the forward problem of travel-time calculation from the inversion for velocity structure. Travel times and approximate ray paths are calculated from every point on a three-dimensional grid to every station using the shortest-path technique. This method is particularly well suited for the Deception Island experiment because it includes topography, bathymetry, and the water-path in the calculation. The inverse problem is solved using an LSQR approach and is regularized by damping and smoothing constraints. The model parameters for velocity structure are defined on a regular three-dimensional grid that is typically sparser than the grid used for ray tracing.

We inverted the data using two grid configurations. The first configuration was a large grid that was centered on Deception Island and extended 53 km and 52 km in the E-W and N-S directions, respectively. The ray-tracing grid had a spacing of 250 m and the perturbational grid 500 m; both grids extended to 12 km depth. For the second configuration, we reduced the grid dimensions to 12 x 14 x 7 km (to the region around Port Foster) and the raytracing and perturbational grid spacing to 100 m and 200 m, respectively.

We conducted three types of tests to evaluate the robustness of the inversion solution. The depth-dependent starting velocity model was obtained from the horizontal average of the two-dimensional tomographic result in the region away from the island. By repeating the inversions using starting models derived from other seismic surveys, we established that the images were not dependent on the starting model. Secondly, we explored a large number of combinations of damping and vertical and horizontal smoothing strengths. The constraints were chosen to simultaneously minimize the data misfit, model roughness, and model variance. For our inversion the final regularization values were 30 for the horizontal and vertical smoothing (20 for the perturbational grid of 200m) and 100 for the damping. Finally, we used checkerboard, impulse-response tests and other hypothesis tests to understand the spatial and amplitude resolution of the tomographic

image. They indicated a high resolution for a central region about 40 x 40 km wide centered in Deception Island between surface and 5 km depth.

Results and Discussion

Convergence of the tomographic inversion to a stable solution was obtained after 6 iterations, when the root-mean-squared (RMS) data misfit was reduced by 80% from 247 ms for the starting model to 52 ms. For the denser grid, the inversion result was also stable after 6 iterations, with a RMS reduction from 260 ms to 34 ms. Results from both grid configurations were used to interpret the velocity structure of Deception Island and surrounding region.

The tomographic image is highly heterogeneous with a lateral variation of > 2 km/s at 1 km depth, and similar contrasts are present between surface and 5 km depth, both at greater and smaller scale. Although P-wave velocities cannot generally be interpreted uniquely, our interpretation of the image is aided by the spatial association of many of the anomalies with known structures. A high-velocity region dominates to the NW of Deception Island at all depths and is separated from the low velocities of the island by a sharp lateral velocity gradient (>0.8 km/s over ~ 2 km) that is linear with its trend parallel to the Bransfield Strait. This boundary is a continuation of the faulted northern margin of the Central Bransfield Basin and likely separates Deception Island and the extended basin from the crystalline basement of the pre-Bransfield continental crust. This anomaly reaches its maximum strength between 1 and 3.5 km depth, and it is not horizontally homogeneous. Two of the three maxima that are superimposed on this high-velocity region appear to disrupt the linearity of the boundary; both the south-western and north-eastern anomalies extend across the boundary and may indicate offset along NW-SE-trending faults. The most pronounced low velocity anomaly lies beneath Port Foster, across the whole resolved depth range. At 1 km, the anomaly is aligned NW-SE and its maximum perturbation exceeds 1 km/s with respect to the starting structure. To about 1.5-2 km of depth this anomaly is due to sediment infilling and it is composed of several maxima coinciding with the location of the 1967 and 1970 eruption centers. However, the amplitude and depth of the anomaly requires high temperatures and partial melt located beneath Port Foster at depths greater than 1.5-2 km. The presence of a magma reservoir beneath Port Foster has been suggested by a number of previous studies.

The low velocity anomaly within Port Foster is partially surrounded by a horseshoe-shaped pattern of high velocities that approximately follows the coast and persists in our image from the surface to ~3 km depth. These high velocities may either correspond to a pre-caldera shield phase of ancient Deception Island, to a previous caldera rim or to frozen, shallow-level intrusions that may have fed earlier eruptions.

Many of the other low- and high-velocity anomalies in the tomographic image can be explained by thicker sedimentary deposits and volcanic features, respectively. The large low-velocity region to the east of Deception Island corresponds to seafloor that is characterized by sediments mainly transported from Deception Island into the Central Bransfield Basin. Its overall shape is strongly irregular although the position of the maximum perturbation at 0.5 km depth corresponds to the location of Costa Recta. The size and position of high-velocity anomaly directly to the south of Deception Island, are similar to that of an isolated Bouguer gravity and magnetization high and may represent a buried intrusion. Another high velocity anomaly is centered on Sail Rock, an eroded andesitic sea stack located to the SW of Deception Island. By contrast, a low-velocity anomaly that is located to the W of Deception Island may be related to a nearby region of extensive seafloor volcanism, and may be the expression of thicker volcanoclastic sediments or an active magmatic system.

Conclusions

A three-dimensional seismic P wave tomographic image of Deception Island volcano shows strong lateral velocity variations that are attributed to a shallow crustal magmatic system beneath Port Foster, as well as frozen intrusive bodies, crystalline basement and sediment thickness variations. A number of these structures have both a NW-SE and a NE-SW trend and can be interpreted in the context of a regional tectonic framework for the Bransfield Basin, that includes extension in the NE-SW direction in addition to the NW-SE extension of the Bransfield Strait, and suggests an influence of NW-SE-oriented transfer zones in the evolution of Deception Island.

4.1. *The Question*

Deception Island is one of few active volcanoes in Antarctica. The history of its volcanic activity goes back to about 0.75 My BP, since when it has been responsible for the production of numerous ash layers dispersed across the whole region, extending to the South Pole area, 3000 km away. It was one of the first destinations for human settlement in Antarctica during the early mid-nineteenth century and object of scientific expeditions and other studies. The scientific interest was momentarily renewed by its historical eruptions (1842, 1967, 1969 and 1970) until 1989, when Spain constructed a new station on the island, from which scientific investigations are supported during each austral summer.

Although the volcano erupted only during few short periods in the twentieth century, it presents clear evidence of continuous volcanic unrest. A complete range of previous studies point to the existence of a magmatic intrusion beneath the caldera, but no seismic tomography has been attempted at Deception Island to resolve this question.

The main scientific goal of the *TOMODEC* seismic experiment hence was the understanding of the magma distribution and its relationships with the recent volcanic activity. Moreover, this investigation was intended to understand the relationships between the volcanic and the tectonic structures and between the faults distribution and ancient and present stress states. Understanding of the evolution of Deception Island in the framework of its tectonic setting was also expected to significantly contribute to the knowledge of the regional geodynamics.

Besides these numerous questions that motivated *TOMODEC* project, we should observe one further purpose. Actually the interest toward Deception Island is not strictly scientific. The island is one of the rare places in the world where scientific and tourist vessels can sail directly into the centre of a restless caldera. More than 10000 people nowadays visit the island in each short austral summer [Smellie 2002]. From this point of view, it is clear that knowledge of the actual volcanic state of Deception Island is also relevant for risk mitigation.

4.2. Tectonic Overview

Deception Island lies in the Bransfield Strait, a NE-SW trending marginal basin 400 km-long 60 km wide, between the South Shetland Islands and the Antarctic Peninsula (**Figure 4.1**).

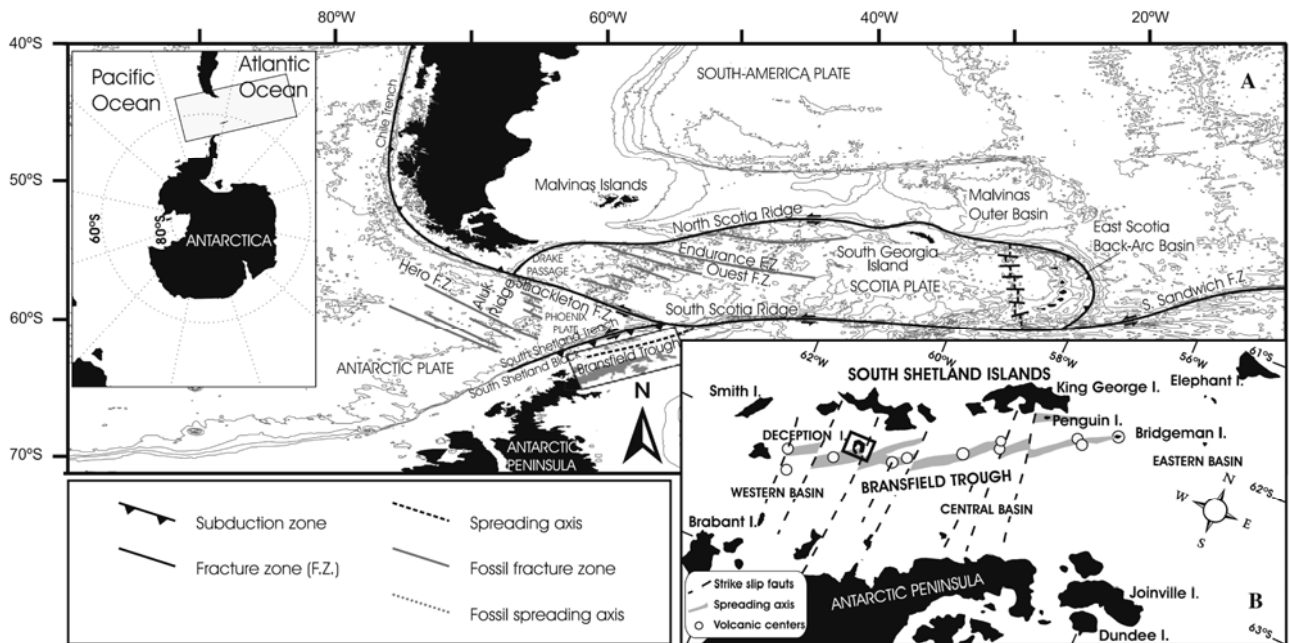


Figure 4.1(A) Regional tectonics of the Antarctic Peninsula and South Shetland Islands region, showing main structures. The key is in the lower left corner of the figure. (B)Close-up of Bransfield Strait. The spreading axis and main volcanic edifices are indicated as a grey bold line and as open circles, respectively. Deception Island is bounded by a square. From Maestro et al. (2007).

The Pacific margin of the Antarctic Peninsula was an active plate boundary during the Mesozoic and Cenozoic, when the oceanic Phoenix Plate was subducting below Antarctic Peninsula, in an ESE direction. When the spreading of the Aluk Ridge NW of South Shetland Islands slowed, at about 4 Ma [Christeson et al. 2003], the subduction rollback process in the descending slab started, leading to an extension regime in Bransfield Strait. The relationship between rollback and extension can explain the NE to SW propagation of non-oceanic rifting described by many authors [Barker and Austin 1998; Christeson et al. 2003; Jin et al. 2002b; Vuan et al. 2005].

Moreover, a major left-lateral strike-slip plate boundary is present between the Antarctic and Scotia plates, along the South Scotia Ridge. Resultant transtension may be competing with slab rollback as the principal driving mechanism for extension at the north-eastern end of the Bransfield Strait [Galindo-Zaldivar et al. 1996; Klepeis and Lawer 1996; Lawver et al. 1996; Maestro et al. 2007; Rey et al. 1995].

Although there is no well defined Wadati-Benioff zone [Pelayo and Wiens 1989], the slow subduction of the former Phoenix plate continues today. The subduction rate has to be similar to the opening rate of the Bransfield Strait, estimated at about 10 mm/yr based on GPS measurements [Robertson et al. 2003]. There are several sources of evidence of this complex geodynamics in the region, mainly pointing to the active extension of the Bransfield:

(1) Seismicity and focal mechanism. Extension through continental rifting is indicated by intermediate depth (5 km), low-magnitude earthquakes and normal faulting mechanism in the Bransfield [Pelayo and Wiens 1989]. Progression of faulting from NE to SW is used to explain the presence of clustered events to the NE of Deception Island and diffuse seismicity to its SW [Robertson et al. 2003]. Other deep earthquakes with mostly strike-slip mechanism below South Shetland suggest active subduction [Guidarelli and Panza 2006; Ibañez et al. 1997; Pelayo and Wiens 1989; Robertson et al. 2003; Vuan et al. 2005]. The mechanism and location of some earthquakes in the region are otherwise related with the lateral motion between South Shetland plate and Antarctic Plate [Robertson et al. 2003].

(2) Volcanism. Since the Quaternary, volcanism has taken place as subaerial activity (Melville Peak and Penguin Island) in the Northern Basin and as a series of submarine volcanoes in the Central Basin (but also Deception Island and Bridgeman Islands. See later for basins classification). Many seamounts show the typical morphology of a cone bisected by a volcanic ridge, which locates the youngest volcanism [Gracia et al. 1996].

(3) Seismic profiles. Several authors recognize oceanic crust [Ashcroft 1972; Gonzalez-Ferrán 1985; Roach 1978] while later studies agree about the existence of faulted and thinned continental crust [Christeson et al. 2003; Grad 1992; Guterch et al. 1985] with normal faults due to its extension.

(4) Multibeam bathymetry [Gracia et al. 1996; Lawver et al. 1996]. Several volcanic edifices and crustal blocks down-faulted coherently with the Bransfield extension are recognized, together with bathymetric steps deepening toward the NE, following a progressive opening from NE to SW of the basin.

(5) High extensional rate of the Bransfield, with spreading velocities ranging from 24 mm/yr [Roach 1978] to 2.5–7.5 mm/yr [González-Ferrán 1991] and 0.83–2 mm/yr [Dietrich et al. 2001; Gracia et al. 1996; Robertson et al. 2003]. Geodetic surveys point to a Bransfield extension directed NW-SE but also to the action of the extensional processes along the Hero fracture [Gonzalez-Ferrán 1985; Ramirez-Rodriguez 2006].

(6) Seismic profiles. Ongoing deformation of the trench sediments and accretionary prism evolution present additional evidence of continuing convergence at the South Shetland Trench [Maldonado et al. 1994].

(7) High heat flow. Several measurements are greater than 220 mW/m² [Nagihara and Lawver 1989]. Such high heat flow values and the large variability of this parameter suggest that active hydrothermal circulation is present in the Bransfield, mostly related to extensional processes, fracturing and continental rifting [Klinkhammer et al. 2001; Schlosser et al. 1988; Somoza et al. 2004].

(8) Magnetic anomalies. Although the West Coast Magnetic Anomaly [Garrett 1990] defines a negative values in the Bransfield region and it is difficult to unambiguously modelling the magnetic profiles, usually too short and with young complex patterns [Gracia et al. 1996], a major positive anomaly in the Bransfield basin is correlated with a large, positive magnetized igneous body associated with the inferred axis of rifting [Ashcroft 1972; González-Ferrán 1991; Keller et al. 2002; Roach 1978].

(9) Gravity anomalies [Garrett 1990; Lawver et al. 1996; Muñoz-Martin et al. 2005]. Both a gravity high over the South Shetland Islands and a steep gradient towards the gravity low of the Bransfield Strait are modelled [Garrett 1990]. The influence of small scale crustal volcanic structures is widely identified with local gravity highs [Lawver et al. 1996] and sharp anomalies on tectonic structures [Muñoz-Martin et al. 2005].

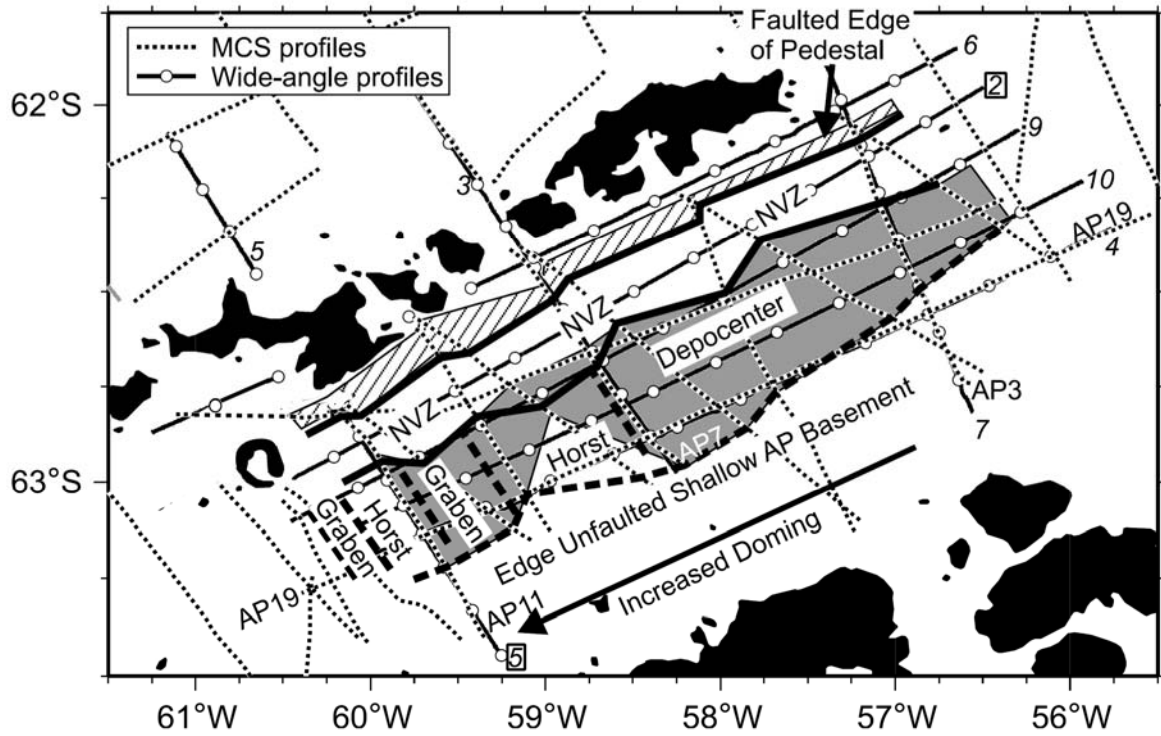
(10) Petrologic constraints. Inter-element plots and associated model calculations suggest that the source regions of all Bransfield Strait volcanics share geochemical features [Weaver et al. 1979] but an unique explication is not given for

their origin. Lavas from these seamounts range from arc-like to resembling enriched MORB in composition, element ratios and isotopic features. Complexities in the source regions and in the processes of magma generation and contamination by slab-derived fluids are detected [Keller et al. 1991], but systematic changes along the central Bransfield basin are not [Keller et al. 2002].

Morphologically, in the Bransfield there are three main sub-basins: the Western, the Central and the Eastern Bransfield basins, respectively separated by Deception Island and Bridgeman Island [Gordon and Nowlin 1978]. The Central Bransfield Basin is 1950 m deep and characterized by submarine volcanoes that delineate the boundaries of flat-floored, thickly sedimented, bathymetric steps deepening toward the NE [Gracia et al. 1996; Prieto et al. 1999]. The seismic multichannel data lead to describe in detail [Barker and Austin 1998; Prieto et al. 1998] the Central Bransfield structural complexity, later simplified [Christeson et al. 2003].

The authors describe the morphology of Central Basin (**Figure 4.2**). Here, South Shetland Islands stay on an eroded basement (pedestal) rifted away from the Pacific margin of Antarctic Peninsula. The basin has a Neovolcanic zone aligned with the basin and located at a 20-25 km cross distance with respect to the basin longitudinal axis, closer to the South Shetland arc. Between the Neovolcanic zone and South Shetland there are closely spaced large offset normal faults, while the gentler margin of Peninsula has low angle faults with collapses and increasing doming toward the SW. To the NW of the Peninsula basement, several faults offset the Neovolcanic zone toward the South Shetland margin and control the extension of several depocenters. Moreover, the Peninsula is marked by horst structures of uplifted basement, possibly filled by sediments (see also their stratigraphy [Prieto et al. 1998]). Geochemistry analyses [Lee et al. 2005] reveal that the sediments derive mostly from intermediate to mafic igneous rocks of the Antarctic Peninsula, South Shetlands Islands and Deception Island, reflecting the nearest source composition. The volcanic ridge aligned along the basin axis forms a topographic barrier among different groups [Prieto et al. 1998]

Figure 4.2 *Geologic structure within Bransfield Strait. NVZ: Neovolcanic zone. The depocenter along the Antarctic Peninsula is indicated by gray shading; the faulted SE margin of South Shetland Islands by diagonal pattern. The NW limit of unfaulted Antarctic Peninsula margin is bounded by thick dashed line. Several tectonic structure as horst and graben are also indicated. The position of OBS line 2 (Figure 4.14) and OBS line 5 (Figure 4.15) are bounded with boxes. Based on multi-channel seismic profiles of Barker and Austin, 1998 and on the interpretation of Christeson et al. (2003). *



4.3. Previous Studies on Deception

The geology and geomorphology of the island are presented following the most up-to-date publication of the British Antarctic Survey, issued by a collaborative venture between British and Spanish geoscientists and the Spanish Antarctic Programme [Smellie 2002].

4.3.1. *Geology and Volcanology*

The island is composed of volcanic rocks which date from <0.75 Ma to historical eruptions (1842, 1967, 1969 and 1970). Traditionally the volcanic rocks of Deception Island are grouped into pre- and post-caldera formations, assuming that a major caldera-forming event took place. This constitutes a question which is still open. [Smellie 2002]. The precaldera period is poorly exposed, and nothing is known about the submarine part of the island. This probably corresponds to the basaltic shield phase typical of the initial growth stage of volcanic islands. However, pyroclastic rocks, agglomerates, tuff and ashes form at least 80 % of the volume of Deception Island [Barker 1975] and are well exposed, except for the extended covers of glaciers or ice-cored moraines (above about 57% of the island) (**Figure 4.3**). The sedimentary structures observed across the deposits of Deception Island indicate that they have been re-distributed and re-worked by geo-morphological agents (volcanic processes, glaciers, streams and lakes). Surface drainage constrains the geomorphology with zones of erosion and flat-floored areas of deposition and is responsible of a high sediment flux into port Foster, especially in January, the ice melting season [Inbar 1995]. This phenomenon is partly responsible of the shallowing rate of the caldera (0.3-0.5 m/y,[Cooper et al. 1999]).



Figure 4.3 Deception Island, in a SE to NW views.

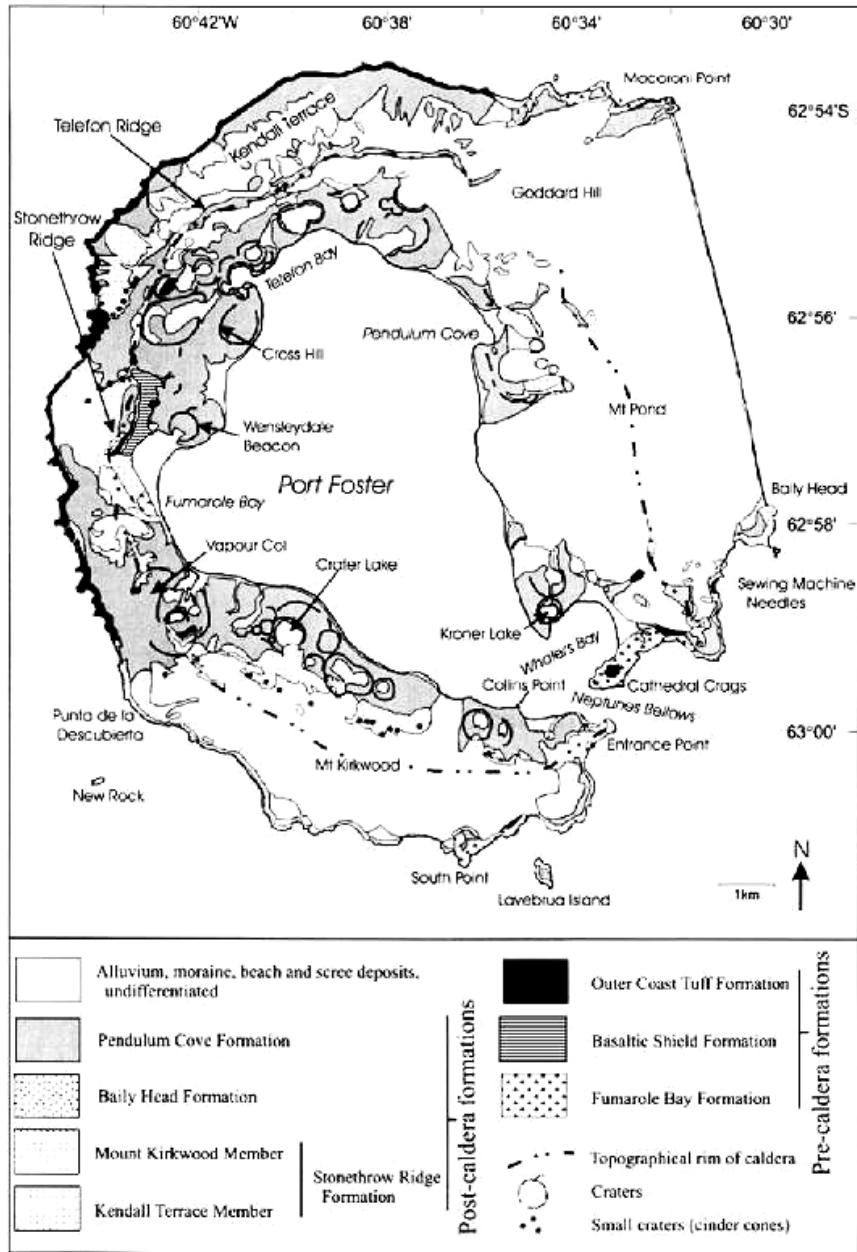
The lithostratigraphy of Deception Island, excluding the more recent deposits of reworked material, is composed by (see table 3.1 [Smellie 2002], and **Figure 4.4**):

(1) Port Foster Group: pre-caldera deposits further divided in Fumarole Bay, Basaltic Shield and outer Coast Tuff formations. Frequently palagonite-altered, they are composed of indurated hyaloclastite breccias, poorly vesicular lava, vitric lapilli-stone and lapilli tuff. They outcrop in wall sections of Stonethrow Ridge, in the Entrance Point, Cathedral Crags, South Point, Vapour Col, Macaroni Point and in the caldera wall west of Cross Hill, almost continuously on the western and northern outer coast cliffs for a distance of 16 km.

(2) Mount Pond Group that dominates the surface geology and includes all the formations belonging to a post-caldera phase. There are three different formations, with the ancient and scarce tuff cones of Baily Head formation, the younger Pendulum Cove and the Stonethrow Ridge variously overlapping the others. The Pendulum Cove Formation is widely distributed. It is present as thin tephra cover on the outer flanks of Deception Island and with tuff cones and maars toward the inner bay. Submarine cones are attributed to this formation. The volcanic edifices are mostly composed by un-lithified stratified lapillistones, lapilli tuffs and ashes. The Stonethrow Ridge Formation crops along the summit ridge and outer coast of Deception Island and in several spot-like outcrops. It includes the products of fissure eruptions of 1839-42 on Mount Kirkwood and of 1969 on Mount Pond. It is composed of red and black coarse scoria and grey mostly blocky lavas

Figure 4.4 *Geologic map of Deception Island and location of main location names. From Smellie (2001).* —————>

4 - Deception Island



4 - Deception Island

In general, Deception Island has been very active during its entire evolution, and ash-falls that are widespread across the region indicate even more periods of activity [Aristarain and Delmas 1998]. Known eruptions took place in 1842, 1967, 1969, 1970 and others are maybe imprecisely dated to 1912 and 1917 [Vila et al. 1992]. Two main eruptive styles [De Rosa et al. 1995] can be recognized in the historical activity of Deception Island: (1) magmatic strombolian explosions (1842, 1969, first phase of 1967 eruption) (2) phreatomagmatic eruptions (1967, 1970) along fault systems of regional affinity (see later for explanation). Historical eruptions are always very small, with limited magma volumes, duration from a few hours to two or three days and moderate in magnitude. The chemical differences observed between products and their location are explained as due to small magma bodies that rise up from a large magma chamber extended across the whole caldera [De Rosa et al. 1995; Ibanez et al. 2003a]. The interaction with water both from ice covering and sea usually leads to surtseyan type eruptions (as in 1967, see **Figure 4.5**), or, if it is more intense, to phreatomagmatic explosion (as in 1970). The magmatic fraction is usually quite small, lower than 40% [Ortiz 1997].



Figure 4.5 Volcanic cone that appeared in Telefon Bay during the 1967 eruption. From Gonzalez-Ferrán, (1995).

Deception Island magma shows a wide range of composition, from basalts to dacite. Even small pyroclastic eruptions, such as those of 1967 and 1970, show such a wide compositional range. On TAS (Total Alkalis-Silica) diagram, Deception Island products are located between the alkaline and sub-alkaline suites, while the series as a whole is distinguished by high $\text{Na}_2\text{O}/\text{K}_2\text{O}$ ratios. Also although the range of alkali ratio is matched only by those in mid-ocean ridge basalts (MORB), other element contents suggest affinities to island arc tholeiites and also back-arc basin basalts. Recently it has been observed [Fretzdorff et al. 2004] that the Bransfield lavas, in general, do not show any trace element or isotopic evidence of any slab-derived component. Thus, Deception Island magmas do not fit in any simple classification and can be considered as a tholeiitic series with quasi-alkaline character caused mainly by enhanced Na_2O contents [Smellie 2002].

The element variations are consistent with low-pressure crystal fractionation and evolution in an open system with external source influence (which could also be crustal material) or periodic replenishment from depth. A genesis model could comprise an upper crustal chamber with mafic magma continuously fractionating and interacting with enclosing crust or influx of small batches of fresh magma, possibly triggered by the regional extensional tectonics, since the end of the pre-caldera period. New magma inputs could also cause thermal perturbation, degassing and the major explosive caldera collapses. An analogous effect could alternatively be caused by an increased scavenging due to fracturing, maybe in the same caldera collapse [Smellie 2001; Smellie 2002].

An important aspect of Deception Island is the presence of several shallow and confined water-saturated layers, as indicated hydrothermal alteration of clasts and chemical composition of gas emissions. The aquifer presence is favoured by the pyroclastic nature of deposits, by the abundance of water from sea and snow [Marti and Baraldo 1990] and by the existence of fractures controlling their circulation (as those NE-SW trending in Fumaroles Bay, [Ortiz 1997]). The chemical composition (Fumaroles Bay), indicates both a magmatic origin (H_2 , 0.2%) and the influence of shallow aquifers (water vapour; H_2S , 0.85%; CO_2 , 98.16%; CH_4 , 0.009%; low SO_2) at an equilibrium temperature of 219 °C at shallow depth, probably 200 m. Such composition changes depending on the state of the aquifers below the fumarolic field. When they are sealed, the gas content from underlying magma (as SO_2 and HCl) is lower and other gases such as CO_2 and H_2S prevail [Caselli et al. 2006]. An increase in SO_2 content and in the chemical deposits of elemental sulphur at the fumaroles vents, noted in occasion of seismic crises (as in 1999 [Caselli et al. 2004]), is related to the emplacement of shallow magma intrusions.

In seismic profiles, submarine hydrothermal vents and mounds are recognized and associated with recent volcanic activity in Port Foster (**Figure 4.6**). Aligned with NW-SE trend, they have formed by hydro-fracturing and fluidisation of boiling pore fluids in gas-charged sediments and used as fluid migration pathways [Somoza et al. 2004].

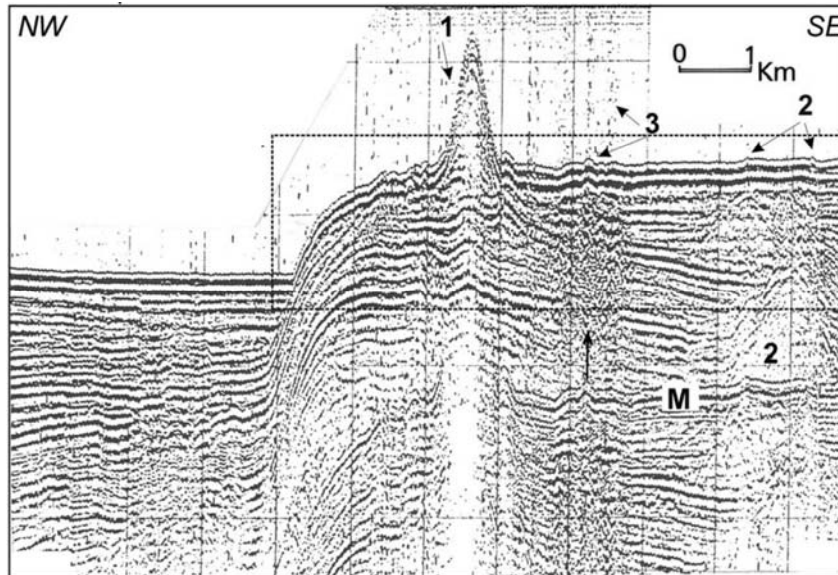


Figure 4.6 Seismic profile across Port Foster showing (1) Stanley Patch, a presumed submarine volcano (2) mound structures and (3) vents associated with subsurface acoustic masking interpreted as fluid-enriched sediments (arrow). M indicates location of the seafloor multiple. From Somoza et al. (2004).

4.3.2. *Structural Geology and Geodynamics*

Although the main volcano-tectonic feature affecting the island is represented by a large central caldera, the whole island shows well defined systems of discontinuity and rectilinear fault scarps. Indication of tectonic lineaments comes primarily from geologic observation and from interpretation of geophysical data. Moreover, recent remote-sensing techniques permit a tectonic study based on a digital elevation model and analysis of satellite data. Many published works present a variety of tectonic interpretations of geological data [Paredes et al. 2006] (**Figure 4.7**).

The main structural directions are *NE-SW* [Baker et al. 1975; De Rosa et al. 1995; Gonzalez-Casado et al. 1999; Rey et al. 2002; Rey et al. 1997] in the north sector of Deception Island, steeply dipping and parallel to the Bransfield Strait, to the 1968 and 1970 eruption centres, and to the fumarolic activity; *NW-SE* [De Rosa et al. 1995; Gonzalez-Casado et al. 1999; Paredes et al. 2006] as in the 1842 eruption centres alignment; *E-W* [Gonzalez-Casado et al. 1999; Paredes et al. 2006]; *N-S* [De Rosa et al. 1995; Paredes et al. 2006] as in the 1969 eruption centres alignment ; *ENE-WSW* [Paredes et al. 2006]; *NNW-SSE* [Rey et al. 2002; Rey et al. 1997] as in the Costa Recta direction and alignment of volcanic cones on the sea bed of Port Foster.

Six main systems of faults have been recently recognized [Maestro et al. 2007]. The N50-60 trend (in the north of Deception Island) is still active with synthetic Riedel NE-SW (north of Port Foster), conjugate antithetic NNW-SSE (Costa Recta), and synthetic P-shears ENE-WSW (western Mount Pond). In addition, they find also N-S, NNE-SSW, WNW-ESE faults, that are related to an older stress regime that is different with respect from the present stress field. This fault system could represent a Riedel shear fracture system in a first stage of island development, before a likely counter-clockwise rotation of Deception Island.

4 - Deception Island

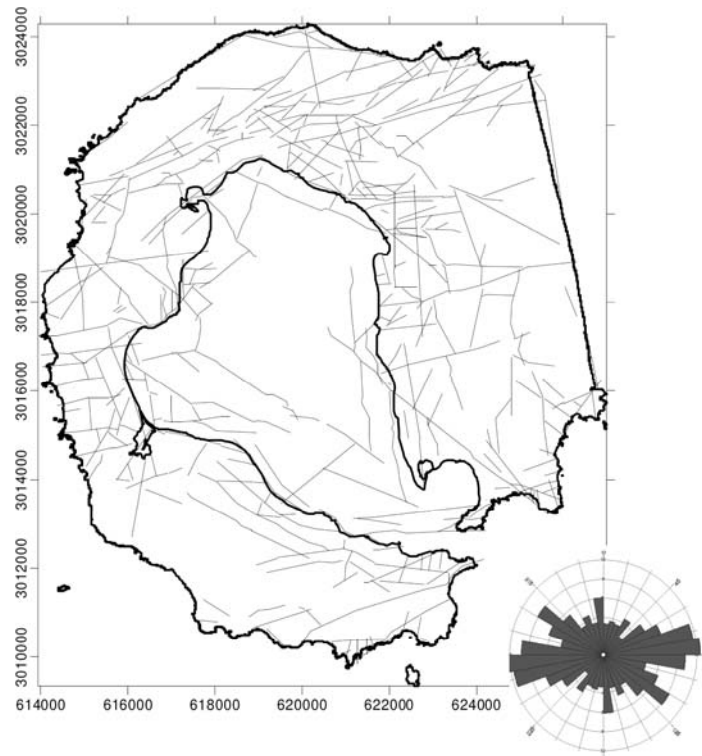


Figure 4.7 Synthetic map of tectonic lineaments at Deception Island, based on bibliographic data as collected and unified by Paredes et al. (2006).

The contemporaneous influence of regional tectonic processes and of the local volcanic evolution on the development of these structural lineaments is therefore widely recognized.

The deformation which is not accommodated by fracturing processes is studied mostly by means of Global Positioning System, and by establishing precise geodetic control points for references purposes [Dietrich et al. 2001]. If the tectonic trend, dependent on the regional deformation, is separated from the volcanic, local deformation, hence variable

behaviour is observed for Deception Island deformation during last few years [Ramirez-Rodriguez 2006]. On a regional scale, the action of Bransfield extensional processes is widely confirmed.[Dietrich et al. 2001; Robertson et al. 2003].

However, locally, Deception Island displacements respond to the activation of fractures parallel to the Bransfield Strait spreading axis, rapidly interchanging with extensive processes along the Hero Fracture Zone.

Port Foster shows a vertical deformation which is controlled by the uplift of the seafloor in its northern sector, at a mean rate of 0.07 m/y [Cooper et al. 1999]. This phenomenon is related to the input of sediments from near deposits, to the volcano-tectonic development of a large scale NE-verging monoclinial antiform associated with a WNW-ESE normal fault [Smellie 2002], and, above all, to the tectono-magmatic development of a shallow magma chamber. In fact, the northern basin coincides with an elongated zone of low mass density, low magnetic intensity and high seismic attenuation of dyke-like structure with lower velocity (25%) than adjacent rocks [Vila et al. 1995]. These observations could be explained by a hot magmatic intrusion, at least 200 m wide, in this region.

4.3.3. *Gravimetry and Magnetics*

Land and marine gravimetric data, combined, offer indications about several levels of correlated signals [Navarro et al. 2002]. The most remarkable features are: (1) From the systematic component, related to the regional tectonics, an increase SE-to-NW trend with maxima in the NW, compatible with the existence of two different geotectonic units to the north-west and south-east of Deception Island respectively (2) From the first prediction component, related to more local tectonic structures, two minima at 5 km E of Costa Recta and at the same distance at the WSW of Deception Island. (3) Two maxima one located across Deception Island (with a NNW-SSE trend and maximum to the south of Neptune Bellows) and the other far away in the NE of Deception Island. They are attributed to ancient volcanic deposits (4) From the second prediction component, and interpreted in terms of recent volcanic structures, a minimum in the north of Port Foster, with a NE-SW trend. It is referred to by the authors as a magmatic body at shallow depth.

Later [Muñoz-Martin et al. 2005] several gravity anomalies have been recognized, organized along two main directions: NE-SW, parallel to the South Shetland archipelago and Bransfield Strait, and NW-SE (**Figure 4.8**).

4 - Deception Island

(1) A NE-SW alignment of maxima considered to be the SW prolongation of Livingstone Island. The southern limit is a high gradient area, and is interpreted as a fracture separating two types of crust. The maxima axis is interrupted in the NNE of Deception Island by a high gradient area trending NW-SE that presents an apparent dextral displacement of 10 km. (2) A SW-NE axis of positive anomaly 10 km long, South of Deception Island interrupted by a possible fracture zone with NW-SE trend (C-C' in figure [Muñoz-Martin et al. 2005]). (3) A local maximum, south of Deception Island, related to high-density submarine volcanic domes and/or as an uplifted high density-block that is limited by two NW-SE and NE-SW-oriented fracture systems. (4) A minimum outside Deception Island, NW-SE trending, going toward the Peninsula (5) A strong minimum inside Port Foster with NW-SE trend.

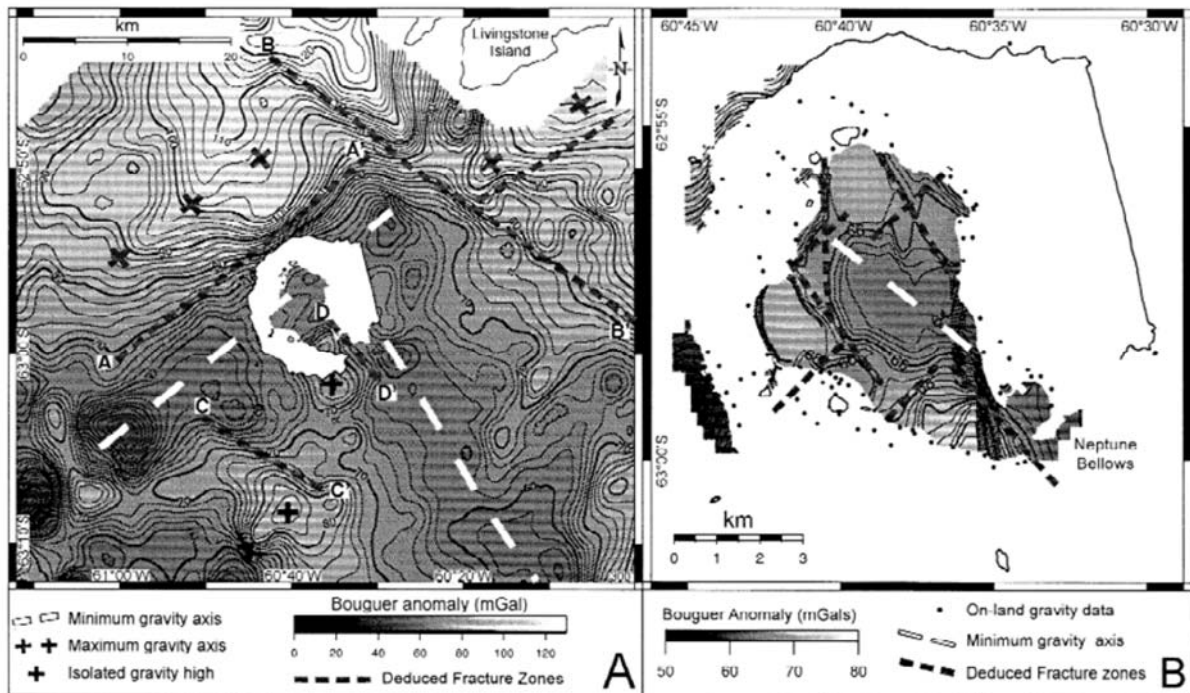


Figure 4.8 (a) Bouguer gravity anomaly map in the Deception Island area and (b) in the inner bay. Main deduced fracture zones are also indicated (see explanation boxes below maps). From Muñoz-Martin et al. (2005).

After a work [Ortiz et al. 1992] where a NNW-SSE direction was observed for a large minimum magnetic anomaly, >3000 nT strong, and coincident with the most recent eruptions vents, the main discontinuities [Muñoz-Martin et al. 2005] are described (**Figure 4.9**) (1) A NE-SW maximum across the northern coast of Deception Island. It correlates with the gravity minimum axis and could correspond to the line of volcanic edifices of the Central Bransfield, if shifted about 15 km by the NW-SE fault described for the gravity maxima of Livingstone (2) A NW-SE trending minimum in the NE of Port Foster, corresponding to the location of the latest eruptive episodes (1967, 1970) and of some intense thermal anomalies. This minimum is attributed to a high temperature body of andesitic magma at 2 km depth, that is responsible for a reduction in thermo-remanent magnetization. As a secondary effect the magnetic properties are degraded by the presence of shallow aquifers. This minimum is part of a dipole structure (with the SW maximum) which shows a strong gradient compatible with a NW-SE direction, probably related to the submarine volcanic axes.

Moreover, the volcano-magnetic signal shows variations which can be correlated with seismic activity changes. During the seismic crisis of 1991-1992, a sharp decrease in the magnetic intensity (the difference between the daily mean at Deception Island and at the Polish Geomagnetic Observatory in King George Island) was observed, followed by a general increase, until 1994. This increase is explained by the thermo-magnetic effect of the emplacement of a body at high temperature [García et al. 1997]. This injection into the local shallow fracture system (about 1 km of depth for the top) took place quickly at the start of 1999 but magma froze slowly during the 2 years that followed [Catalan et al. 2006].

The VT activity at Deception Island has been monitored only seasonally since 1986 [Ortiz 1997], but its level seems to be characterized by a highly variable distribution, with the occurrence of small volcano-tectonic events clustered both in space and time [Vila et al. 1992]. Interestingly, they are distributed along the main fractures of the island; they mostly have normal mechanism and fault-planes that are nearly vertical [Vila et al. 1995]. In 1992, 1995 and 1999 intense swarms took place along alignments which are approximately parallel to the major fault systems of the island, including the NE-SW (**Figure 4.10**). In both cases they were accompanied by changes in the fumarole gas composition, deformation and gravity variations [Ibañez et al. 2000; Ortiz 1997].

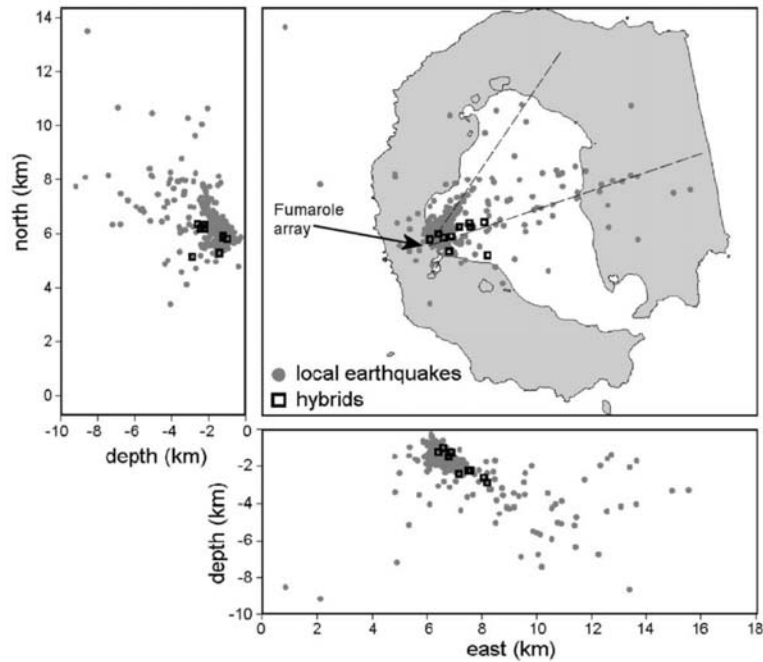


Figure 4.10 Hypocentral locations of the VT earthquakes (dots) and hybrid events (squares) recorded during the 1998-1999 crises. From Ibañez et al. (2003)

An analysis of the temporal occurrence of the entire VT seismicity of the island gives an average inter-event time of the order of 130 minutes, too short to be due to tectonic activity [Correig et al. 1997]. This instead points to a different mechanism, such as the vaporization of ground water at depths of 2-3 km (the estimated focal depths of events). Water is mainly ice and sea water, and the presence of fractured medium and shallow aquifers facilitate the whole process.

By using seismic antennas, intense long period activity has also been recorded, and differentiated into three different groups [Alguacil et al. 1999]: (1) long period events (LP) with a quasi-monochromatic spectral content (1-3 Hz peak frequency, **Figure 4.11**) and variable duration, until greater than 50 s. Often they occur in swarms, from several minutes to some days of duration (2) volcanic tremor with spectral shapes similar to those of LP but lasting several minutes (3) hybrid events with high-frequency initial phases followed by low frequency phases similar to LP. The high frequency phase show presence of P waves and it is resolved also in some LP and tremor.

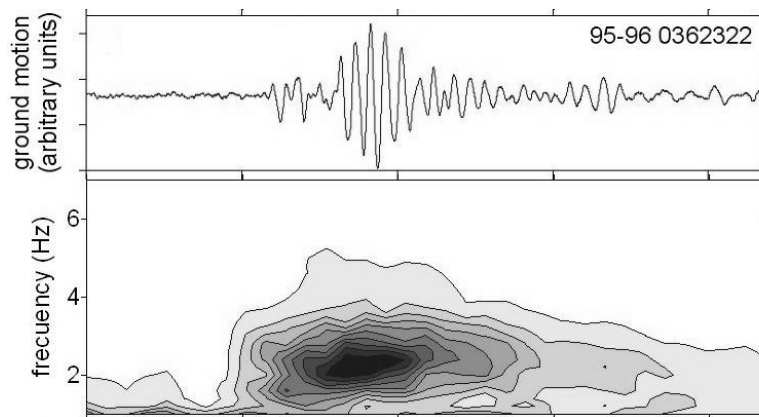


Figure 4.11 Example of vertical-component velocity seismogram and spectrogram for LP event recorded at Deception Island, with a frequency content centered at 2.5 Hz. The horizontal axis interval is 5 s.

The common origin of long period events is attributed to the presence of a shallow aquifer in contact with high temperature rocks. The mechanism could be the crack resonance [Chouet 2003] excited by exploding or imploding bubbles of steam. In this sense the tremor would be a superposition of hybrid events, each produced by an explosion in the aquifer. The hybrids with the same location of VT are considered to be produced by the resonances of cracks filled with fluid (probably water) and that also causes the lubrication of faults and hence VT activity [Almendros et al. 1997]. A relationship with geothermal noise that originates in the uppermost vents of the fumarole system is suggested [Vila et al. 1992] on the base of the local geology.

Unfortunately, the study of seismicity has been limited by the uncertainties in the velocity structure of the island, which is likely to be highly heterogeneous. Differences of the apparent velocities for regional earthquakes at two arrays [Saccorotti et al. 2001] indicate structural heterogeneity for the first 200 m beneath two sites. In Fumarolas Bay the velocity model is compatible with the regional crustal structure ($V_p=2.3$ km/s), apart from the shallowmost 40 m thick, slower ($V_p=0.9$ km/s) sedimentary layer. The array located in the Obsidiana Beach detects a much slower structure (0.5-0.65 km/s) in the first 150 m, probably due to a structural depression successively filled by volcanoclastic deposits. A sharp lateral velocity contrast bends rays impinging at the northernmost array downward, as **Figure 4.12** indicates. The inferred velocity discontinuity is associated with a fracture system bordering the caldera with NNE-SSW trend.

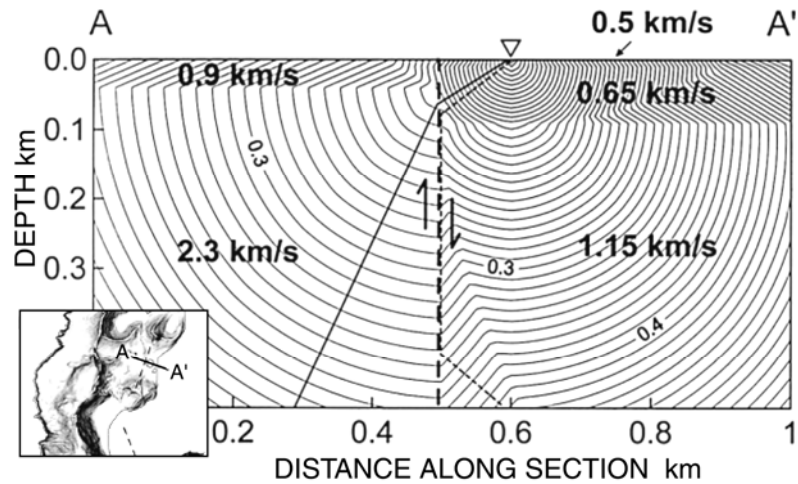


Figure 4.12 Cross section along the profile indicated in the smaller box. The triangle indicates the array position. Contour lines are wave fronts for a source located at the hub of the array (0.01 s contour interval). P-wave velocities are indicated by different shading and bold numbers. The bold black line represents a seismic ray impinging at the discontinuity. Modified from Saccorotti et al. (2001).

Low velocities due to a deep anomalous body are suggested by the study of traveltimes residuals [Vila et al. 1992]. These data point to the existence of a dike structure with a velocity 25% lower than rocks in the surrounding area and a characteristic length of the order of 450 m. A similar body is suggested by the abnormally low Q value for local seismic attenuation [Vila et al. 1995]. Other low Q values, abnormally high frequency dependence, as well as large dispersion, are due to the geologic setting, fracturing, and hydrothermal alteration.

4.3.5. Seismic Structure

In order to give some more insights about Deception Island structure, a number of seismic experiments have been conducted at the island. Unfortunately, they have been limited to shallow seismic reflection experiments [Rey et al. 2002] or have not focused on the island itself, instead belonging to larger-scale experiment across the Bransfield Strait [Agudo-Bravo 2003; Ashcroft 1972; Christeson et al. 2003; Grad 1992; Grad et al. 1997; Jin et al. 2002a; Sroda 2002; TEAM 1990].

In a seismic survey carried out inside Port Foster, low velocities (between 1.80 and 3.96 km/s, [Ashcroft 1972]; 1.9-2.3 km/s,[Grad 1992]) of the shallowmost layer have been attributed to ash and assorted volcanic debris in various degrees of compaction above more consolidated volcanic rocks (4.1-4.3 km/s ,[Grad 1992]). For Ashcroft (1972), to 2 km of depth no faulting is evident and for this reason the author assumes that the middle of the caldera has subsided *en-bloc*. Other authors indicate low but variable velocities inside Port Foster. For example Grad et al. (1992), in the profile from Pendulum Cove to Neptune Bellows model the 4.2 m/s boundary at 1.4 km depth to the southern end of the line and at 0.6 km depth to the north (**Figure 4.13**). A fault, located between them, could cause this contrast, possibly defining blocks of caldera collapse. Others [Agudo-Bravo 2003] assume the existence of a fault with NNE-SSW trend, in the middle of Port Foster, of normal mechanism and with a displacement of 700 m of the shallower crust. Again, this indicates the presence of several vertically-displaced blocks up and down, controlled by the primary tectonic directions.

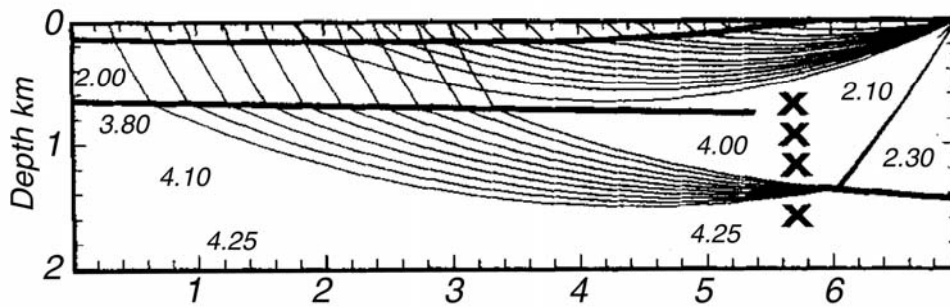


Figure 4.13 Ray diagram for the seismic profile from Telephone Bay (0 on x-axis) toward Neptune Bellows, with a N160 trend. Distances are in km, From Grad et al. (1992).

Seismic lines to the NW, connecting Deception Island with Livingstone, show the presence of a low velocity crustal layer (6.2 km/s), between 4 and 8 km of depth, and of a fault along the SE coast of Livingstone [Ashcroft 1972]. This fault is modelled as a strongly inclined layer in the same 6.1 km/s of acid crystalline continental basement [Grad 1992]. At the E and SE of Deception Island purely continental structure with extensional horst-graben character has been identified [Christeson et al. 2003; TEAM 1990] with volcanic edifices at greater distance [Jin et al. 2002a; TEAM 1990] that do not perturb the stratigraphy close to the island ([Christeson et al. 2003] **Figure 4.14**). The crustal structure shows no signs of seafloor spreading, it is rather a rifted basin with a sediment infill about 700 m thick [TEAM 1990] or more (2-4 km, [Grad 1992] 5 km, [Sroda 2002]). The seafloor velocities are about 1.7-2.0 km/s [Christeson et al. 2003], while the uppermost sediments have velocities of 3-4.0 km/s and cover acid crystalline bedrock with velocities of 5.5-5.7 to 6.4-6.7 km/s at 2-4 and 5-6 km of depth [Grad 1992]. To the SW of Deception Island the upper crust is shallower (top at 1 km of depth, [Grad 1992]) and no volcanic structures are evident. Only large scale normal faulting in the basement is seen [Jin et al. 2002b]

On the *whole*, in along-axis sections of the Bransfield, seafloor velocities are 1.7-2.1 km/s [Christeson et al. 2003]. Velocities of 1.9-2.2 km/s (1.8-2.8 km/s [Agudo-Bravo 2003]) indicate sedimentary cover, with considerable tuff deposits.

Sediments may also constitute the underlying layer, with 4.0-5.7 km/s, if they are more consolidated or have intercalated volcanic sequences, between 1 and 5 km. At greater depth, to 12-17 km, the upper crust has acid crystalline rocks with velocities of 5.5-5.7 km/s, or basic rocks with values of 6.4-6.9 km/s [Agudo-Bravo 2003; Grad et al. 1997]. The top of the upper crust is otherwise identified [Christeson et al. 2003], with the 4.0 km/s contour (or 4.5 km/s [Agudo-Bravo 2003]). It is shallow in the Peninsula margin (0.1-0.9 km) and South Shetland shelf (< 0.5 km), and deepens in the Neovolcanic zone (1.5 km) and depocenter region (2.6 km) (**Figure 4.15**).

A high velocity body with V_p greater than 7.4 km/s is found at 12-16 km depth in lower crust rocks while the mantle is at 28-32 km [Grad et al. 2002; Grad et al. 1997; Sroda 2002]. Christeson et al., (2003) interpreted the 7.4 km/s as upper mantle, which does not require the contrast at 32 km but is justified by partial melt along the Bransfield axis. For these authors, the Moho is shallowest in the NE of Neovolcanic zone (<15 km) and generally deepens from NE to SW. It reaches a depth of 21-26 km along the South Shetland shelf and at the same distance toward the Peninsula it is around 18-23 km. It continues to deepen to the SE, possibly to 40 km depth

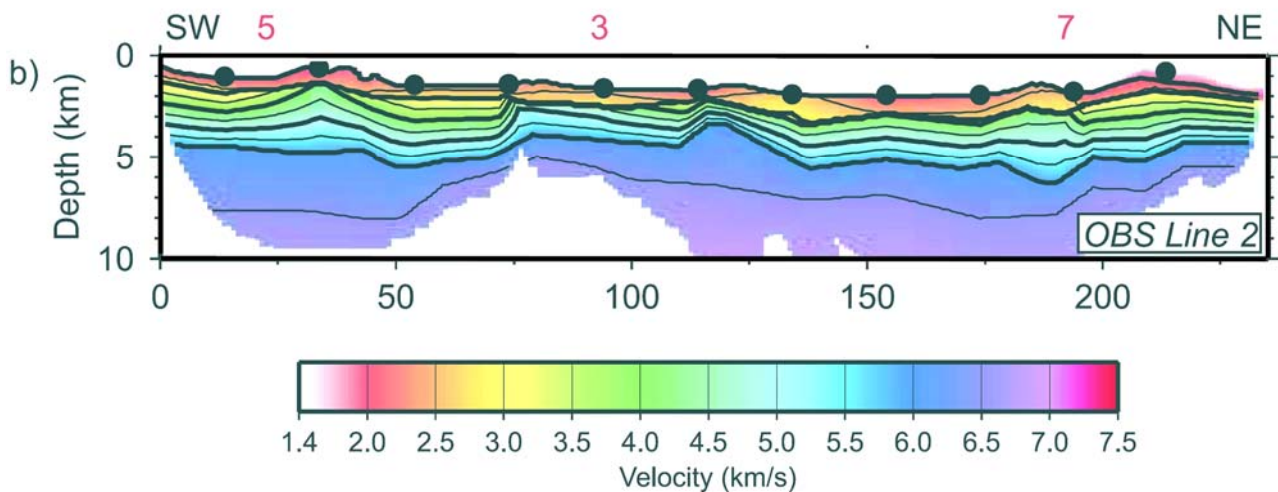


Figure 4.14 Velocity model for strike profile OBS line 2 (see **Figure 4.2** for location). Contours are plotted every 0.5 km/s. Solid circles mark positions of OBS receivers. Red number mark intersections with the three dip profiles. From Christeson et al. (2003).

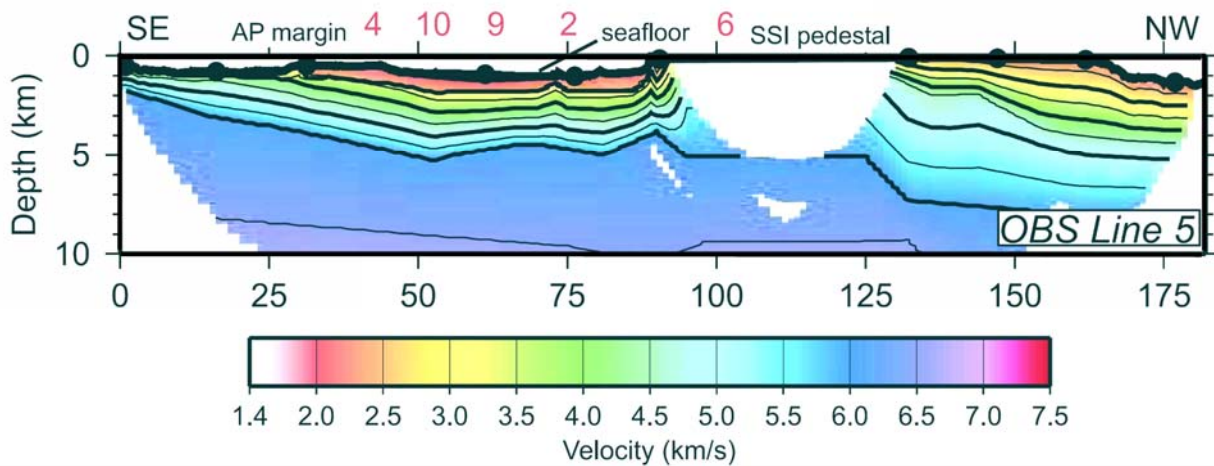


Figure 4.15 Velocity model for dip profile OBS line 5 (see **Figure 4.2**) for location. Contours are plotted every 0.5 km/s. Solid circles mark positions of OBS receivers. Red number mark intersections with the three along-strike profiles. From Christeson et al. (2003).

4.3.6. Resuming the 'State of the Art'

Numerous investigations have been conducted in the island. Here we have reviewed only a part of the geophysical, geological and geochemical studies, with particular interest in the structure of Deception Island, whose knowledge is the main aim of our work. Broadly summarising, the main conclusions from all these studies are that at the present, Deception Island activity includes hydrothermal circulation [Caselli et al. 2004; Marti and Baraldo 1990], resurgence of the floor of Port Foster [Cooper et al. 1999] and intense seismicity [Alguacil et al. 1999] both of volcano-tectonic [Ibanez et al. 2003b] and long-period type [Almendros et al. 1997]. These observations, together with gravity and magnetic anomalies [Muñoz-

Martin et al. 2005] and high seismic attenuation [Vila et al. 1995], point to the existence of a shallow magma chamber underlying Port Foster.

4.4. Seismic Experiment

4.4.1. Objectives

There are several open questions about Deception Island volcano. Many seismic experiments have been conducted in the region until now but, unfortunately, due to Deception Island position respect to their location [Ashcroft 1972; Christeson et al. 2003; Grad 1992; Grad et al. 1997; Jin et al. 2002a; Sroda 2002; TEAM 1990] and the resolution [Rey et al. 2002], they have not improved our knowledge about the deep structure of the island. At the same time, it is evident that the full understanding of Deception Island state and evolution is severely limited by an incomplete knowledge of its internal structure. Without such information, the size, location of the supposed magma body and its evolution relative to the state of regional stress only can remain on a speculative plane.

These are the main reasons that motivated the *TOMODEC* project and the seismic experiment held in January 2005. A primary goal of *TOMODEC* was to perform a 3D seismic tomography of Deception Island and surroundings using P-wave first arrival times.

After a short presentation of the field work carried out during the experiment, in this work we describe that part of the *TOMODEC* project directed towards the creation of a 3D tomographic velocity model for the study region

In addition, the determination of 2D tomographic images along two orthogonal profiles across Deception Island, based on the same dataset, was planned for a contemporary study [Ben-Zvi et al. 2007]. Multibeam bathymetry data were acquired as well, to perform a detailed study of geomorphology and tectonic structures of the seafloor [Barclay et al. 2007], and will be compared to the obtained seismic velocity model.

4.4.2. *Institutions*

The experiment at Deception Island took place with the collaboration of several research institutions. For the field work and data collection there was the active participation of (with number of researchers and provided instruments): CENAPRED, Mexico (1); LAMONT DOHERTY EARTH OBSERVATORY, Columbia University, USA (4, 14 OBS); INGV-CATANIA, Italy (1, 4 land stations of M24 type); INGV-OSSERVATORIO VESUVIANO, Italy (1, 7 land stations of Marslite type); INSTITUTO ANDALUZ DE GEOFÍSICA, Spain (12, 10 land stations of maliAG type); UNIVERSIDAD DE CÁDIZ, Spain (2); UNIVERSIDAD DE COLIMA, Mexico (1); UNIVERSITY COLLEGE, Ireland (1); UNIVERSIDAD COMPLUTENSE DE MADRID, Spain (1); UNIVERSIDAD DE LA PLATA, Argentina (1); UNIVERSITY OF SEATTLE, USA (3); USGS, VOLCANIC HAZARD TEAM, USA (2).

4.4.3. *Experiment Design*

The seismic experiment was designed to obtain a three-dimensional seismic image of Deception Island and surrounding region. A total of 85 land and 14 ocean bottom seismometers were deployed within a 54 x 80 km² area approximately centered on Deception Island to record seismic signals from nearly 6600 explosive sources. The airgun shots were fired along pre-established patterns both inside Port Foster and outside the island. The shooting patterns were repeated once and some stations were relocated between the first and second rounds. In addition to the seismic data, gravity, magnetic and multibeam bathymetry data were acquired along the same ship tracks.

The experiment consisted of three parts: (1) field work, during the austral summer 2003-2004, for campaign preparation. We surveyed the entire island and established the location of seismic stations and camps. We elaborated a handbook to be used during the 2004-2005 summer deployment with precise locations (by portable GPS) and routes to hike

across the island (2) a field phase of data collection during the austral summer 2004-2005. This took place in the period 4 to 20 of January 2005 and included the deployment of seismic stations and the data collection (3) a laboratory phase of data gathering, organization and analysis.

During the early days of the geophysical survey (phase 2), a total of 4 camp tents with their furniture and mountaineering equipment was installed. Almost immediately, 11 autonomous seismic stations and 10 arrays of maximum 12 channels each were deployed. This work included the recognition of pre-established location sites for stations, their installation and a check of their working status. For autonomous stations the installation consisted of a true plug-and-play and a real-time check in the field (**Figure 4.16**). The array installation implied the deployment of sensors connected to the acquisition system through 50-to-200-m-long cables. Their data could be checked in a quasi-real time after their conversion to readable format (see Chapter 4.4.5.1). At the same time 11 OBS outside the island and 3 inside were placed on the seafloor. This procedure included on-deck instrument assembly, deployment on the seafloor and verification of their status using acoustic communication tests (**Figure 4.16**). During the days 8 to 11 the first round of shots was fired, both inside and outside the bay.

At the end of this phase, researchers again worked on land to change station positions while the vessel personnel shifted ocean stations in a new configuration. New shots were fired during days 16 to 18 of January.

Most of seismic stations were recovered at the end of the survey. Only 4 land stations of M24 type (see 4.4.4.2) and 12 OBS were left in their final position. All this equipment was left until middle of February, in order to record data of the natural seismicity in and around Deception Island.

The analysis of data involved an initial phase of data gathering from instruments of different types, their organization in a database, their conversion to a common format and, finally, their introduction as traveltimes input into the tomography code. Considerable part of the laboratory work as been developed in conjunction with the School of Oceanography of Washington University (Seattle, USA).

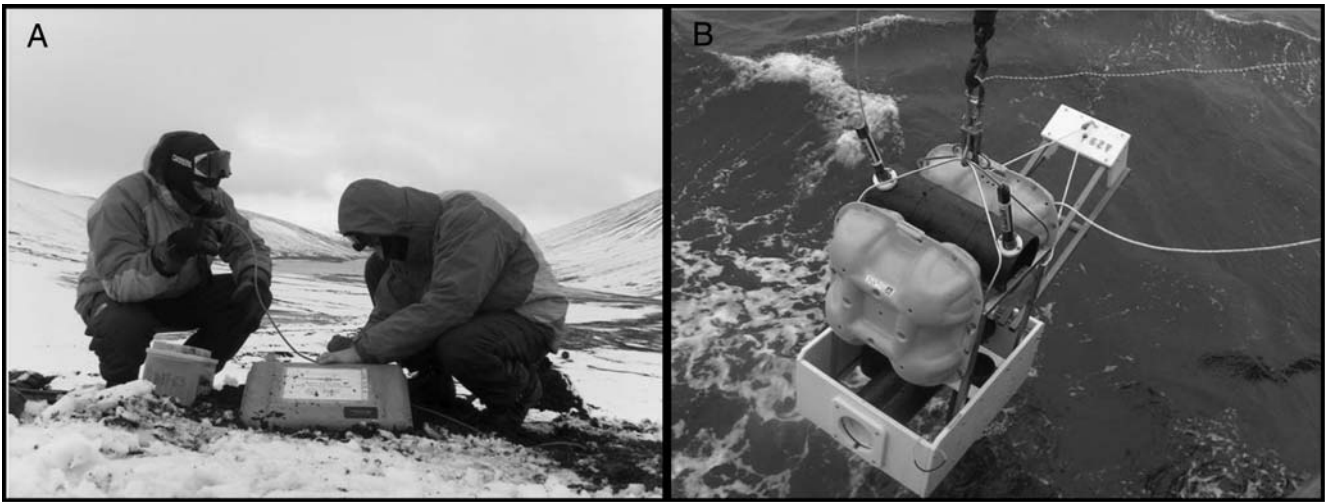


Figure 4.16 Seismic station deployment: (A) field work and installation of a Marlite station and (B) drop of an OBS (Ocean Bottom Seismometer).

4.4.3.1. Air-gun Shooting Configuration

The explosive sources for the seismic experiment were airguns, fired using the *R/V Hespérides* in a pre-established arrangement. The airgun shot configuration was designed to provide a dense coverage inside and around the island. In the interior of Port Foster, the tracks followed a dense grid of perpendicular lines with shots spacing of 120 m on a 0.5 km grid (**Figure 4.17**). A safety distance from the coast of less than 500 m was respected. Outside the island shots were fired at a spacing of 170-340 m in three main trajectories (**Figure 4.18**): (1) two straight tracks, one 92-km-long and NNW-SSE oriented and the other 55-km-long in a WSW-ENE direction, for refraction profiles (2) concentric lines around the island (out to 20 km from the center of the island) (3) lines in a 'star' configuration, in order to further improve data coverage. The theoretical tracks were planned on the base of the station distribution, with the aim of sampling known tectonic structures with an optimum source and receiver configuration. For example, the seismic line oriented NNW-SSE was designed to

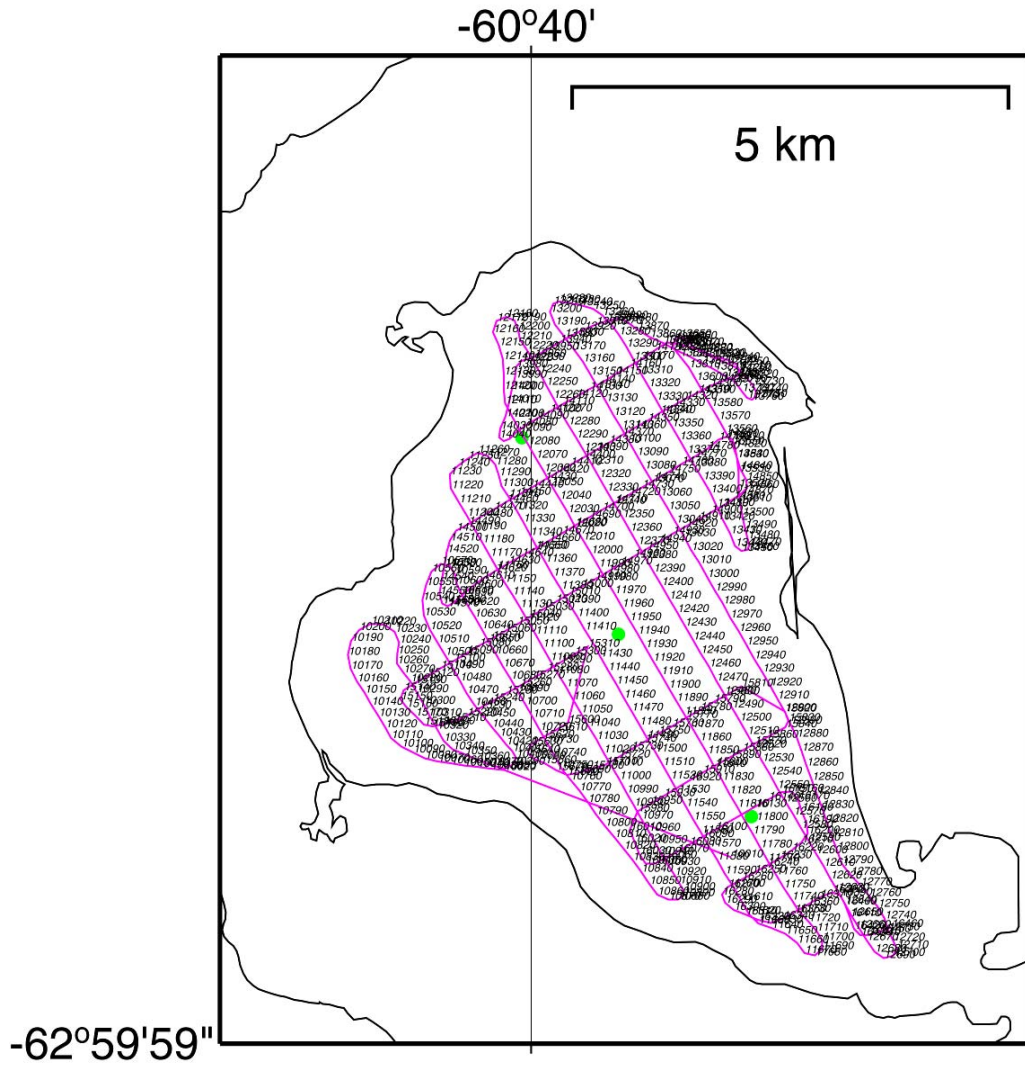
4 - Deception Island

obtain a 2D section of the expected velocity contrast NW of Deception Island (see for example 4.3.3). In reality, the true pattern was partially influenced by the navigational constraints. Avoiding inshore shoals sea ice often resulted in an erratic ship track. Approximately 320 miles of airgun shooting was collected. This configuration plus the operation capability of the airguns allowed the recording of high-energy P-wave signals at distance as great as 40 km.

The data set consists of 6630 useful shots, fired at a 1-minute interval along the tracks inside the island and a 2-minute interval for shots around the island. For the longer lines, the shot frequency was also 1 shot/minute.

Figure 4.17 First round shots distribution inside Port Foster (coast line in black). Each number identifies a located shot. Also three OBS positions (green circles) are indicated. For logistic reasons, the second round was repeated with different instrument location but very similar shot configuration. 

4 - Deception Island



4 - Deception Island

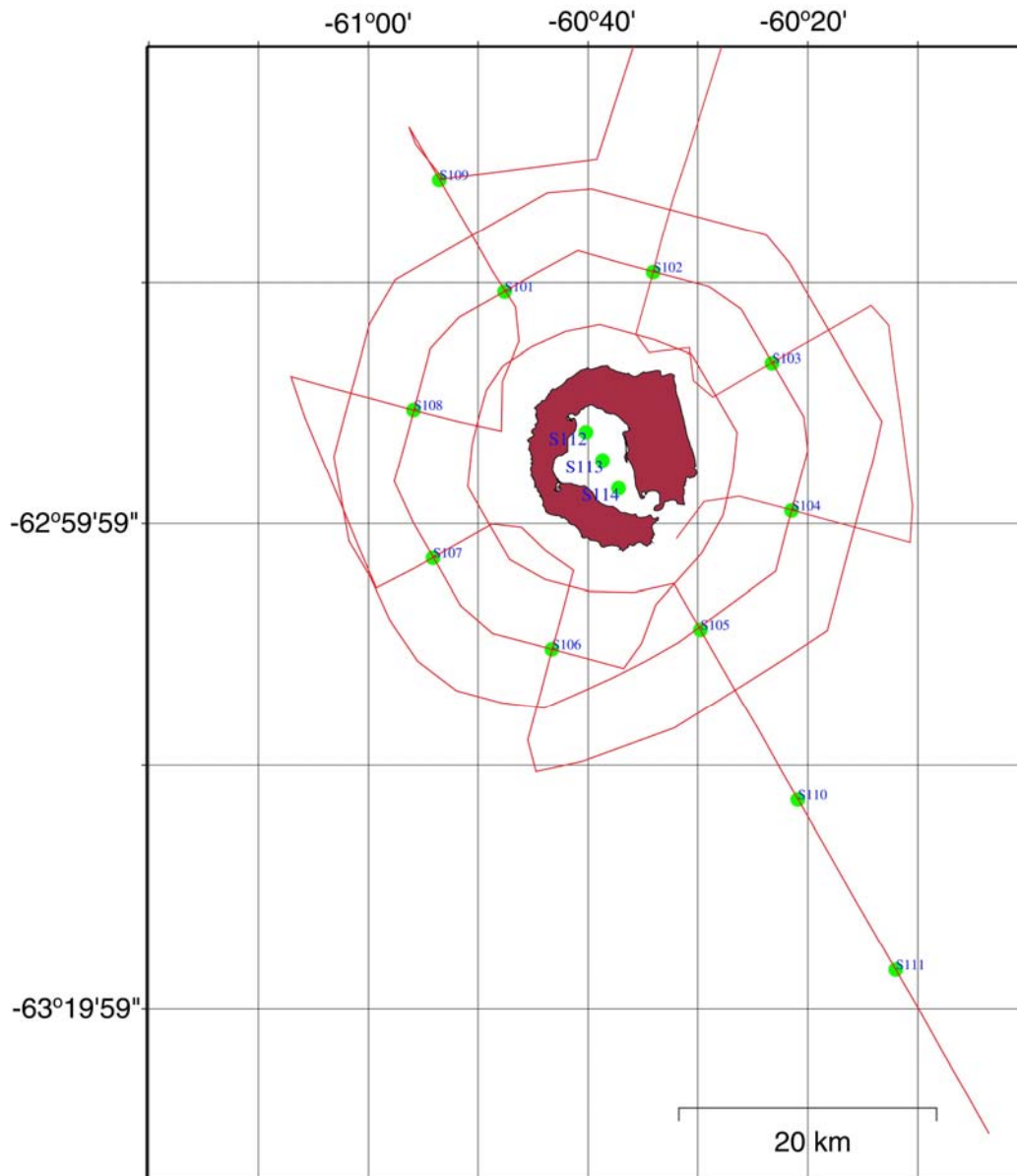


Figure 4.18 First round shots distribution (brown line) outside Deception Island (shaded brown area). OBS positions and names are also indicated (with green circles and names). For logistical reasons, the second round was repeated with different instrument location but very similar shot configuration.

4.4.3.2. Source Generation

The airgun array and signal generation during the seismic survey were planned on the base of the previous experience of the scientific vessel in analogous seismic experiments. Six BOLT 1500LL airguns were used in a 12-m-long configuration, with 2.5 m separation and 0.8 m between pairs (**Figure 4.19**). In the first round of shots in the bay only 4 guns (500, 500, 255, 265 cu. in., a total of 1520 cu. in.), while outside all airguns were used (3520 cu.in.). In the second round, inside the bay, the total capacity was increased to 2020 cu. in., by replacing a 500 cu. in. with a 1000 cu. in. gun.

The airgun modelling is performed by the Gundalf engine. It takes into account of all air-gun interactions including interactions between sub-arrays. It can predict peak-to-peak and primary to bubble parameters across a very wide range of operating conditions. The modelled signals can be directly used in deconvolution procedures.

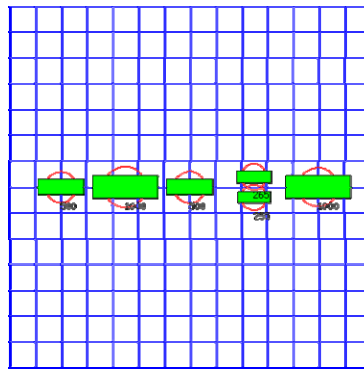


Figure 4.19 Geometry of air guns used as the source in TOMODEC experiment. Air guns are indicated as green rectangles with the corresponding volumetric capacity in cubic inches The grid has 1 m spaced lines (UTM,2005)..

4 - Deception Island

The air guns are controlled by a Hydra Minipulse system, which synchronizes the guns and gives them the shot signal. Using the information proceeding from a sensor located in each gun, the system can correct the fire instant in order to synchronize perfectly (less than 1 millisecond of difference) the shot (aiming point). The shot command is initially supplied by the GPS Seapath to the KONMAP navigation system (fix point) with a delay of 1 ms. Then this information is sent to the gun control system within 60 ms. Summing up all these time intervals, the real shot time has a delay of 61 ms with respect to the time written in the telegram supplied for every shot. This telegram contains information about the fix point, such as latitude, longitude, date, direction of vessel, speed, depth, name of the line of shots and number of the fix point. The location information actually applies to a position acquired 60 ms earlier (after correction for the distance between GPS and guns). After the shots another message is reported to these data by the Minipulse system: number of working airguns, total capacity and delay of each gun with respect to the aiming point. All these data are supplied for every shot and are recorded by a PC as text format. The whole telegram is made up of two parts: a first part (starting with the \$HYDRA sequence) with data supplied by the Minipulse system and a second part which comes from the navigation system (\$HESSIS sequence). Due to the huge amount of data, the output files are filtered in order to make them more manageable: 6 fields with shot number, latitude, longitude, date, hour, fix. The first field is extracted from the shot telegram, the others from the navigation telegram. Moreover, a log file is supplied about failure of systems and errors. As a result of this organization of data, it is possible to present them in a final 'shot-file' format of this type:

```
10060 30 -62.97158 -060.67955 2005 008 02 40 22.061 8 277 54 -62.97172 -060.67710 617756 3015435
10070 31 -62.97142 -060.68247 2005 008 02 41 22.061 9 276 59 -62.97154 -060.68002 617609 3015460
10080 32 -62.97102 -060.68532 2005 008 02 42 22.061 10 287 64 -62.97135 -060.68296 617460 3015487
```

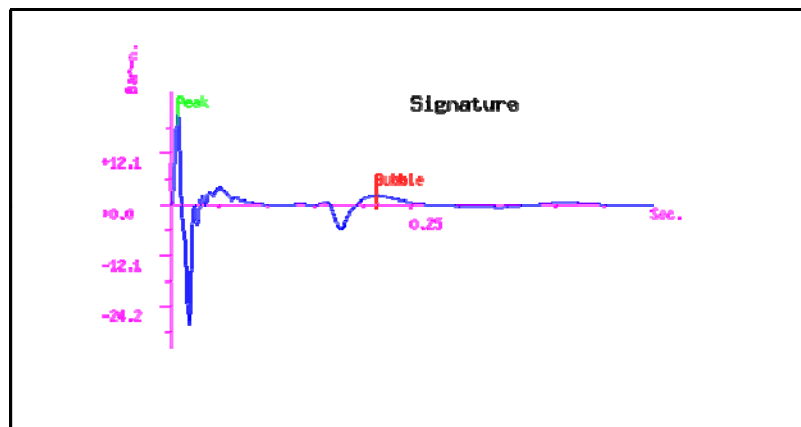
where the fields are: 1. revised shot number, 2. original shot number, 3. ship GPS latitude (deg N), 4. ship GPS longitude (deg E), 5. year, 6. julian day, 7. hour, 8. minute, 9. second, 10. navfix, 11. ship heading, 12. water depth (m), 13. gun latitude (deg N), 14. gun longitude (deg E), 15. gun X (UTM) , 16. gun Y (UTM).

The gun positions are assumed to be 125 m eastern and 5 m to port of GPS antenna, with a constant depth of 9 m. In the UTM conversion to geographical coordinates, the UTM region is 20E.

During these corrections, a constant delay, exactly 1s long, of the ship timing system with respect to the recording station timing was found and verified using the expected time of water-wave arrivals to OBSs and stations around Port Foster. We think it has not been noted in other seismic surveys due to the self-consistent timing base used in multichannel seismic reflection profile. This delay is obviously corrected in the final shot file.

4.4.3.3. *Signal Characteristics*

The airgun signals recorded at stations presented waveforms which strongly vary at different seismometer locations. Their characteristics at the source are instead pre-established and little variable. In the time domain, the signal shows a maximum peak in the first 0.05 s, with a peak to peak amplitude of 50.4 bar-m. This pulse is followed, about 0.20 s later, by the bubble signal. In the frequency domain (**Figure 4.20**), the maximum amplitude belongs to low frequencies, with the maximum spectral ripple (db, relative to 1 microPa per Hz at 1 m), in the 10-50 Hz interval, at 6.62 Hz.



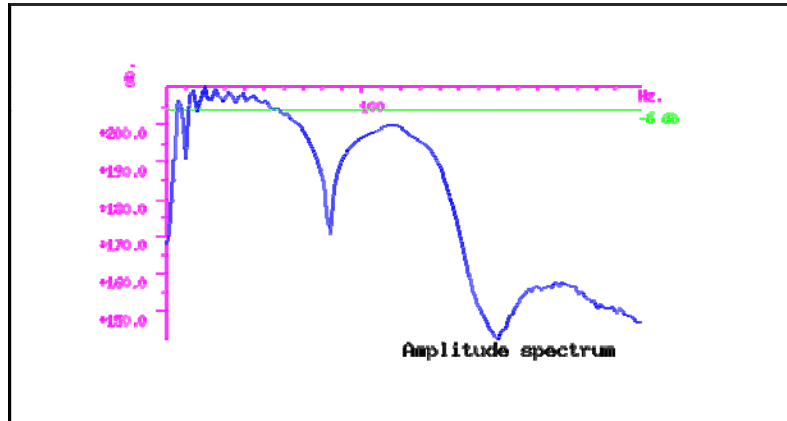


Figure 4.20 Signal characteristics at the source, in time domain.(Filter: 6.0/18.0 – 128.0/72.0) (above) and in frequency domain. (UTM, 2005).

4.4.4. Station Types

Land seismic stations belong to different institutions and are of different types and technical characteristics. In the *TOMODEC* survey 85 land seismometers have been used. They included 7 Lennartz Marslite seismic stations (covering 14 positions), 4 M24 (covering 7 positions) and 10 malIAG hub (with 74 sensors, gathering a total of 85 different positions), all of them working in continuous recording mode. Moreover, 14 OBS were deployed

4.4.4.1. *Lennartz Marslite*

The Marslite seismic stations are data acquisition systems of 20 bits of dynamical range working with three channels. They have one separate ADC for each channel, with a sampling rate of 125 Hz. The preamplifiers work on all three inputs simultaneously and can be set up by the user. There is a preamplifier with four 12 dB steps. Since digitisation always takes place at a fixed sampling rate of 4 kHz, the digital data stream need to be decimated to the final sampling interval, after the signal has been digitally low-pass filtered by a FIR (Finite Impulse Response) filter. The system is completed with a GPSlite time signal receiver. The recording is on rewriteable magneto-optical disks of 540 Mb, in binary format. The acquisition systems were programmed to record in continuous mode. The power supply was provided from an external 12 V DC supply, later stabilized and changed to the required voltages by the system. They were equipped with Lennartz LE-3Dlite MkII seismometers with 1 s natural frequency.

4.4.4.2. *Lennartz M24*

Lennartz M24 Compact/LP are portable seismic stations of 24-bits of dynamic range working with three built-in channels. There is one separate oversampled A/D converter per input channel, that digitizes the signal coming from the preamplifier at very high frequency (20 kHz) and the data stream is then decimated down to the user's desired sampling rate: in our case, a sampling frequency of 100 Hz was chosen. One single chip works as a general-purpose CPU (Central Processing Unit) and as a DSP (Digital Signal Processor). The latter functionality is required to achieve the high-speed, high-precision digital filtering commonly associated with oversampled ADCs. The operating system managing the station is a Pentium-class UNIX powered server that uses a TCP/IP connection procedure. GPS timing is performed by a built -in receiver combined with an exterior antenna connected trough a cable. The selected data format was of binary type, and recording was on a removable 2.5" IDE hard disk of 20 GB. For the power supply it accepts external 12 V DC power (in our case, a 100 A/h battery supplemented by a solar panel of 47 W +/- 10%) and converts to all internally required voltages.

The acquisition system was equipped with a Lennartz LE-3D (20s) seismometer, which has a corner frequency of 0.05 Hz, an output voltage of 1000 V/m/s and damping of 0.707.

4.4.4.3. *mallAG*

The mallAG modules are high resolution (24 nominal bits) with an acquisition system that can work with a maximum of 12 sensors, in array configuration. The sample frequency was configured to 100 s/s and the ganancy to 1. Data acquisition is performed by 4 SEISAD18 plates, each of them managing 3 analog channels. The plates are synchronized thanks to a PLL plate, whose time pulse is supplied by a GPS (Garmin 35-HVS) connected with a serial port. Digital data from 4 plates are passed to a commercial PC (Lippert Cool Roadrunner II) with low energy consumption, and are finally stored on a 30 GB USB hard. In addition the system has a hard disk of 10 GB for the operating system and the temporary storing of a data buffer that is transferred to the external hard disk every 6 hours.

The mallAG modules were approximately the same of those used during the Azores experiment in 2003, but were slightly improved in their characteristics in order to work under extreme weather conditions such as those in Antarctica. This means that the electronic part remained substantially unchanged, with modifications in the hardware quality, protection and security.

To avoid the timing problems revealed by their use in the Azores experiment, the software configuration was slightly changed. The central control of the process, achieved by means of a low power industrial PC, works under MSDOS and no longer Windows 98. The acquisition software generates files in binary .ARR format, which embeds timing information in the data stream each second.

Physically, the mallAG systems are composed of a plastic suitcase which contains the acquisition system and which has to be connected through military connectors to an antenna for the reception of the GPS signal and to a 'knot' where cables from several channels can be handed without any danger for the acquisition system. The same case is connected to 12 V batteries for the power supply.

The array modules used as antennas were supplied with vertical L-28B Mark Products sensors, with preamplifier and a natural frequency of 4.5 Hz. Electronic extension allowed all the sensors to achieve a flat response curve in the 1-50 Hz frequency interval. In this manner, their response is almost identical to other 1Hz commercial sensors, at much lower cost. Some of them were equipped with three-component L-4C Mark Products sensors, without preamplifier.

4.4.4.4. *OBS*

The Lamont instruments are very low power, have recording capacities exceeding 18 GB, employ 24 bit digitizers, and are equipped with broadband three component seismometers with noise levels below 10^{-16} (m/s²)²/ Hz in the band from 0.01 to 50 Hz. A broadband hydrophone provides an additional seismo-acoustic channel. The pressure sensor is used primarily to provide a redundant channel (looking very much like vertical velocity) in case the seismic sensor fails. The pressure sensor is considered to provide good Rayleigh and body wave records, as well as good active source and microearthquake data at shorter periods. The instruments sample continuously at 125 Hz (they can work at user selectable rates including, moreover, 10, 20, 40, 100 Hz), and are easily converted to standard PASSCAL sampling rates. These “broadband” seismometers are actually short period sensors (1 Hz geophones) coupled to efficient and very low noise amplifiers [Webb 1998]. The large sensor sphere hangs from a simple arm during deployment. The recording and recovery electronics are contained within two cylindrical aluminium pressure cases carried within a polyethylene plastic frame. Glass floats provide flotation to bring the instrument back to the surface for recovery. Cylindrical, 34 kg anchor weights are carried in two plastic cylinders under the flotation. Burnwire releases drop these weights for recovery under control from two redundant acoustic releases. After the instrument has settled on the bottom the sensor sphere drops off the arm (burn wire release on a timer) to settle on the bottom about 1 m from the main frame. Separating the sensor package from the main recording package even this short distance substantially improves coupling and reduces the noise from ocean currents. The geophones are mounted in motor driven gimbals to provide a full 360° of levelling to insure levelling in any terrain. The amplifiers, levelling electronics and tiltmeter are mounted with the geophones inside a glass pressure housing and inside a plastic hard hat, above an anchor plate. The weight of the sensor is only about 8 kg in water, which affords good

coupling on soft mud. Time keeping is maintained by a QTech Co. temperature compensated clock that provides a timing accuracy of better than 30ms over 1 yr after correcting for average drift.

4.4.5. *Data Processing*

4.4.5.1. *Data Formats and Software*

Data from the four types of stations (M24, Marslite, maliAG, OBS) had different formats and we needed different programs to handle them. The original format of M24 and Marslite seismic stations was of binary type, but the data were stored as SAC files [Goldstein et al. 2003] as soon as they were recovered from the station. Because the digitalizer of the M24 stations introduces a delay in the conversion from analog to digital signals, the start time of these data is always - 0.2288 s before the nominal starting time of the file (and this has to be taken in account during the conversion of data to SAC format). Data from the maliAG instruments were in .ARR format, easily converted and managed with the common seismic software *SEISAN*, at least to visualize records and plot some spectral analyses. The OBS systems stored raw data in binary format organized in file of 8192 records. Each record, of 1 Mb, has data following a 28-bytes header information. The header contains information about the instrument, timing and sample rate. The data were easily converted to SEGY format [Barry et al. 1975] after retrieval.

Hence, we opted to convert our database to two user-friendly main formats, i.e. SAC and SEGY. The selection of the first one was due to the wide spectrum of analysis possibilities associated with this format, especially in the frequency domain (i.e. spectrograms) and of waveforms (i.e. cross-correlation and automatic picking of the first arrival). The SEGY format was selected because it permits the gathering of traces in time windows after each shot and the display of record section. This facilitates the comparison (and identification) of the waveforms. Moreover, because in this format only 2 minutes of data are stored, it results in efficient manipulation and display of the data (**Figure 4.22**).

4.4.5.2. *Data Quality*

The quality of data recorded during the seismic experiment was generally good, with low noise recorded both by land and ocean bottom seismometers. Due to the nature of the emplacement site, cultural noise was completely absent. The record quality only got worse in land stations because of strong winds shaking the island coasts, wave action and in OBS records due to sea currents and probably other source of noise, including whale song (Barclay, personal communication). The clearest signals in seismic traces were those produced by shots (**Figure 4.21**), although the records likely also included a variety of seismic signals that could be classified according to their shape, magnitude and frequency content. For example, possible natural signals included ice-quakes, local and regional earthquakes, and tremor/long-period events.

The air-gun signals have P-wave arrivals recognized out to 40 km range. We clearly recognized crustal phases (Pg), except when they were masked by water-wave phases (easily identified due to their traveltimes, considering a velocity of about 1.5 km/s and a known shot-receiver distance, and to their larger amplitudes, **Figure 4.22**). At greater distances, depending on the crust thickness, first arrivals belonged to mantle refraction phases (Pn). Interestingly, waveforms of crustal phases with similar ray paths showed strong variability in their shapes, which were probably due to closely-spaced attenuating heterogeneities in the medium (**Figure 4.22**). Other observable phases belonged to reflected waves. In principle, they could be used to image discontinuities at their origin, such as (PmP) for the Moho discontinuity. There were also a number of disturbance waves that could be referred, as in similar OBS experiments, to a bubble effect in the water (as phases with 0.2-0.4 s of delay after the water-wave first arrival) at the source or a reverberation effect near either the source or the receiver (visible, for a 15-20 km distance, as 1 s delay phases). The observed wavefield was also complicated by converted phases (of P and S combinations). The Pg data provided three-dimensional ray coverage down to depths of 5 km below the seafloor, as predicted from our raytracing in a reasonable 1-D velocity model (**Figure 4.32**).

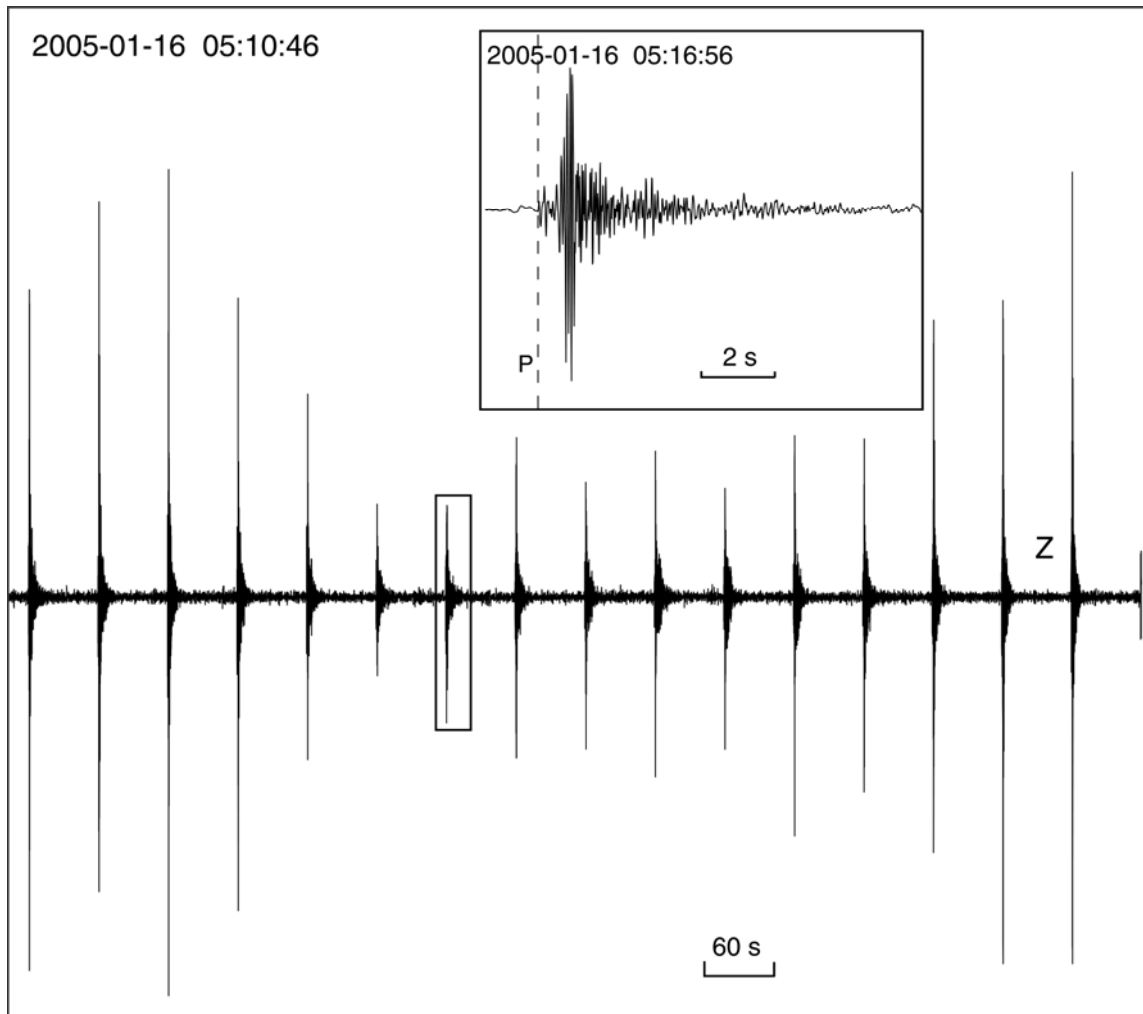


Figure 4.21 Example of velocity seismogram of the vertical component of a land station for the air gun signals. Enlarged window is of one arrival, showing the P-wave arrival time. Vertical axis indicates ground motion in arbitrary units, horizontal axis is time in seconds.

4 - Deception Island

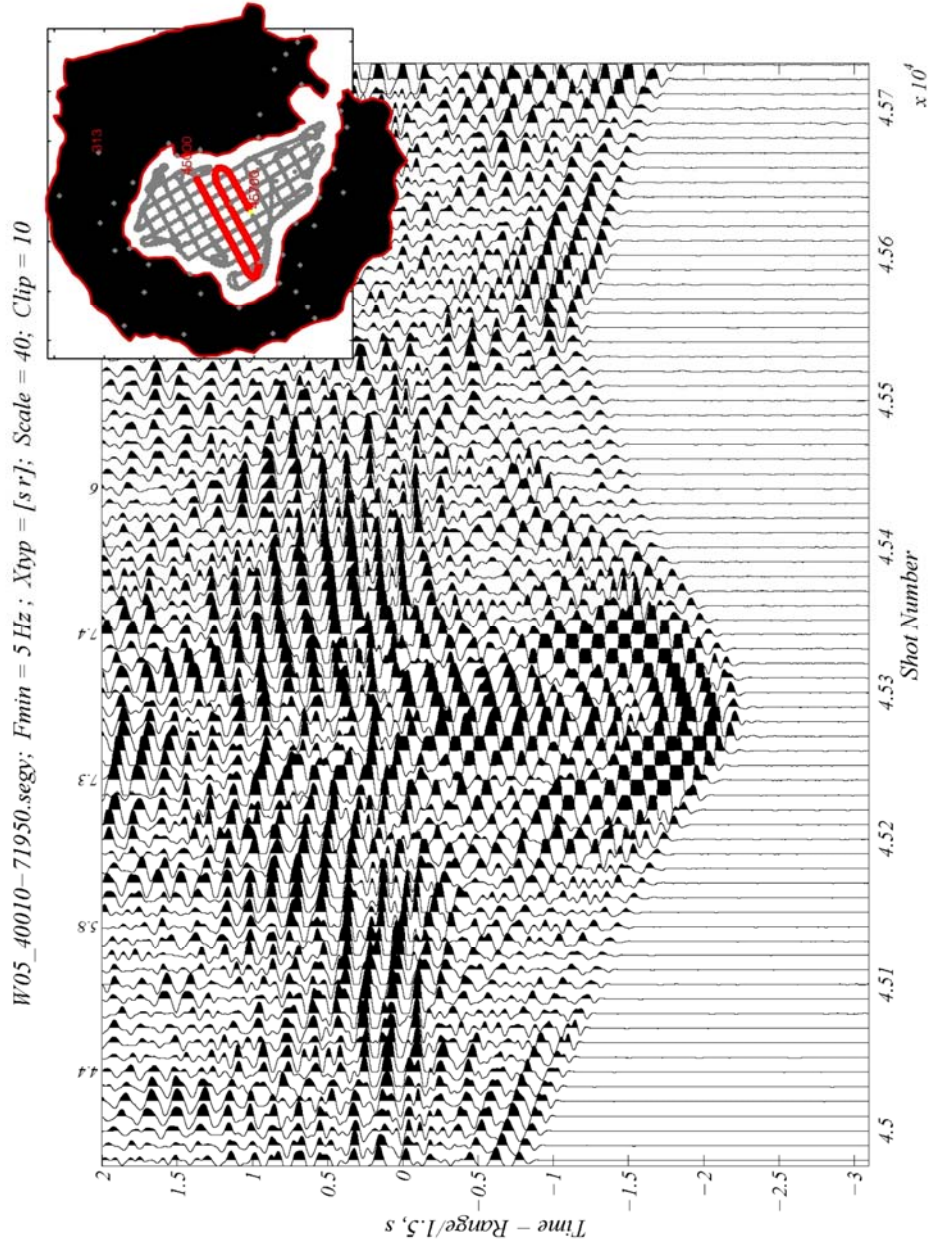


Figure 4.22 Seismic record section from the vertical component of station W05 for several shots (SEG Y data format, UPICKER software, see later). The position of station and shots is indicated (red numbers/circles) in the map in the corner. The velocity is reduced (see vertical axis, in km/s). The shot number is indicated in the horizontal axis. The signal is filtered (high-pass filter at 5 Hz). The positive (up) swings in each seismogram have been shaded.

4.4.5.3. P Arrival Time Determination

The huge amount of data recorded during the survey required the use of an automatic picking algorithm in order to detect the first-arriving of P-wave for each shot at each station. Comparing traces of adjacent shots for the same station, we recognized an extreme variability in their waveforms and we assumed that a cross-correlation technique could not perform well in our case. Other methods had to be preferred, such as these based upon abrupt changes in the ratio of a short term and long term running average of the signal [Allen 1978].

In particular, we used the SAC routine called *APK*. With this algorithm, the detection of a pick is based upon abrupt changes in the ratio of a short term and long term running average of the signal. Once detected, the pick is subjected to an optional validation phase which attempts to distinguish a true event from cultural noise. Once validated, the pick is further evaluated to determine other characteristics of the event. Currently this is limited to its duration. Other features such as maximum amplitude, period, and decay rate may be added as required.

We only changed the values of two parameters. We increased C7 parameter (to 1e8) in order to consider as many data as possible. In fact, a station is assumed to be dead when the absolute value of the characteristic function is greater than C7. At the same time, in order not to introduce low quality data, we increased the value of C5 (to 6), the parameter that refers to the ratio between the short term and long term average of the characteristic function. By this way, the thresholds to declare an event becomes more severe and results are therefore more robust. Moreover, we used the shot times to constrain the algorithm to work only on the time windows when arrivals were likely.

To assess about the performance of the *APK* routine, we compared the automatically obtained picks with the real traces. Usually we observed that the results for detected traces differed by an average of 0.02 s (standard deviation 0.26 s) with respect to the hand-picked arrivals [Zandomenighi et al. 2005]. This can be considered an acceptable performance of

the automatic routine but, in order to be sure not to introduce any 'falsely triggered' arrival and to take in account as many phase arrivals as possible phase arrivals, we visually checked the automatic algorithm result.

For this task, we used the *UPICKER* software. This program permits trace gather plotting, starting 2 s before shot time and during 20 s. This choice depended on the known interval between following shots, which was 2 minutes. The plot can be adapted to filter traces as done in the *SAC* picking routine, i.e. with a high pass filter at 5 Hz. We checked the error introduced by filtering the traces in *SAC* and we found out that it is usually below 1 sample, although sometimes could sometimes be as big as 2-3 samples, i.e. 0.02 s. Unfortunately, the filter was necessary in order to detect first arrivals. Although, eventual errors introduced by the filters could not be avoided they were, in any case, the same for the whole database and hence self-consistent.

The final database includes delay times from more than 70000 (70411 precisely) crustal P-waves arrivals (**Figure 4.23**), automatically picked and manually checked. On average each station, that we used, recorded almost 1500 shots, while each shot was constrained by something more than 15 observations (for the sparse grid, see later). In the dense grid, we reduced the dimensions of the studied area, and therefore the number of stations and shots, and we used more than 20700 (20754) traveltimes, with a mean of 610 arrivals per station.

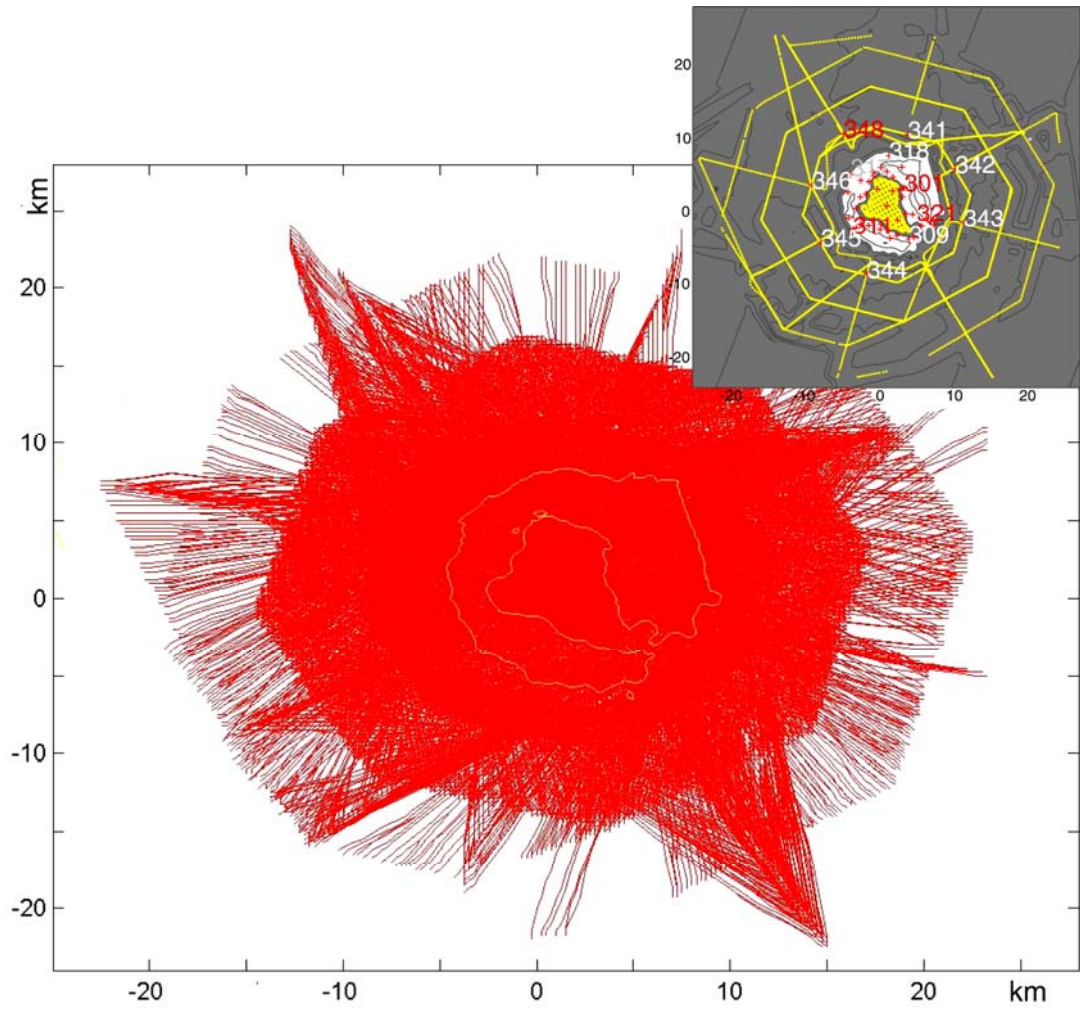


Figure 4.23 Coverage of seismic rays used in this work. The yellow contour outlines the coast. The reported data, are only those of stations indicated in the small map (with the numbers corresponding to the station names and yellow points as shots positions).

4.4.5.4. *Input Format*

The tomographic inversion technique we used is based on first arrival input data, and is easily converted to traveltimes values for controlled-source experiments. For each shot, given its location and origin time, a travel time value is calculated for each station. Stations without any recorded arrival phase are fixed with a null traveltimes value. Errors are associated to travel times and supplied to the inversion code. As example of input file for 10 stations (named 301 to 310) is:

```
10010 5 1 8 214 57.061 -62 58.880 -60 36.880 0.01
301 302 303 304 305 306 307 308 309 310
0 0 0 0 0 0 0 0 0 0
0.2 3.3 0.2 3.3 3.3 3.3 3.3 3.3 3.3 0.1
1.450 0.000 1.678 0.000 0.000 0.000 0.000 0.000 0.000 1.989
```

where in the first line contains the shot identification number, time and location, the second line has the station names, the fourth line the error for each arrival time (with 3.3 as a flag to discard the traveltimes) and finally in the fifth line the travel times in seconds.

4.4.6. *Other Results from the Experiment*

During the *TOMODEC* survey, together with seismic signals, gravity, magnetics and swath bathymetry data were acquired along the same cruise tracks.

4.4.6.1. *Gravimetry*

Gravity data were obtained during the *TOMODEC* experiment with a Bell Aerospace TEXTRON BGM-3 (Lockheed Martin Federal Systems) marine gravimeter. The system has a sensor mounted on a stabilized platform. Data are managed, filtered and scaled with the software BGM, which stores them in a hard disk memory and also send them by Ethernet to the comprehensive acquisition system. The gravimeter had been recalibrated using a portable gravimeter Worden mod. MASTER on 12/29/2004 at Ushuaia AeroNaval Base [UTM 2005].

4.4.6.2. *Magnetics*

The magnetic survey was carried out only during the first phase of the seismic experiment. The SeaSPY (Marine Magnetics) magnetometer worked with an omni-directional Overhauser sensor, synchronized to 1 ppm with the GPS signal. The system was temperature-stabilized, in order to perform the same functionality both in cold and warm water. Due to its design, it is considered almost exempt from heading problems. The magnetometer works with a resolution of 0.001 nT and a precision of 0.2 nT, at a sample rate of 4 to 0.1 Hz. [UTM 2005]

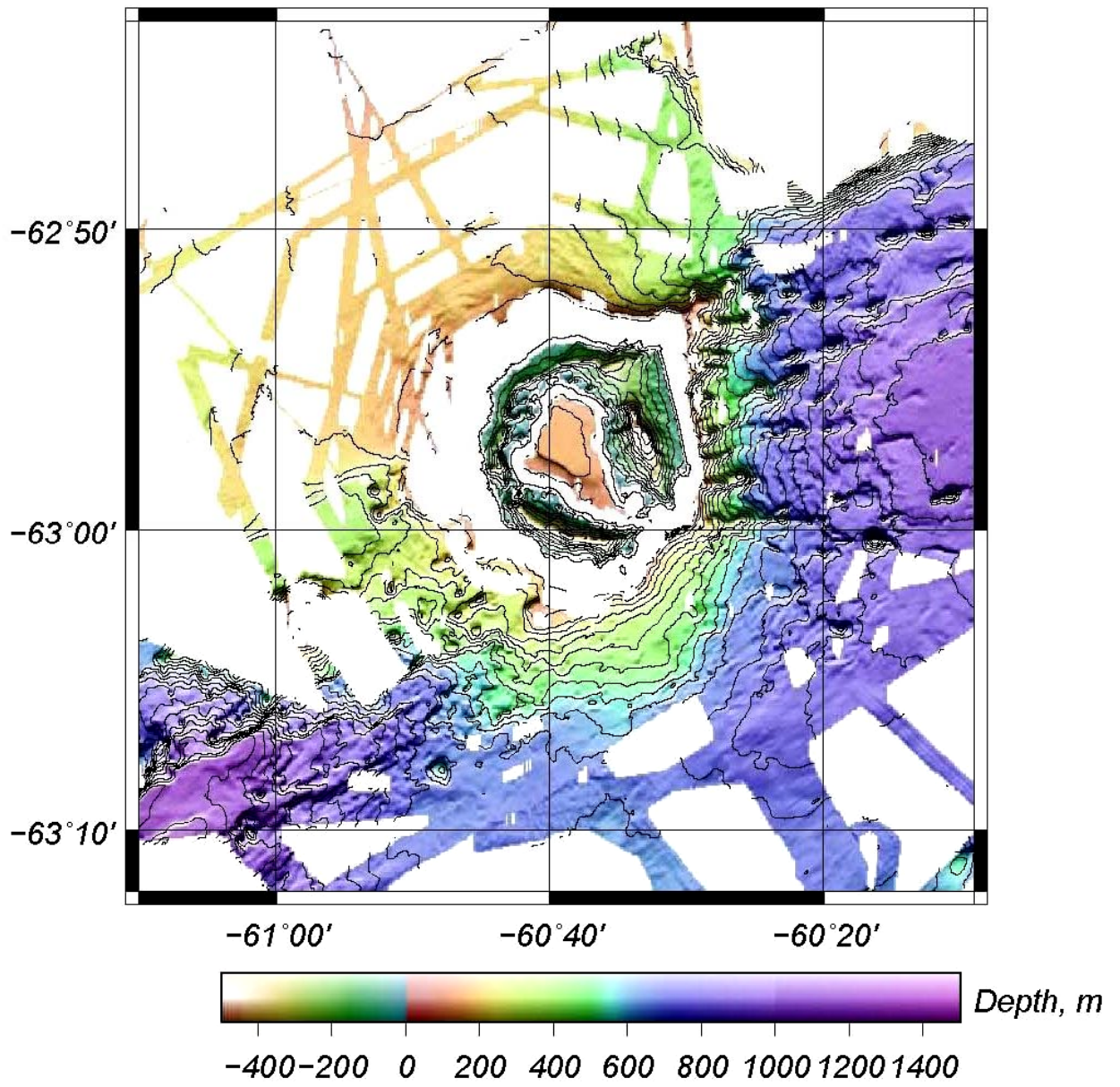
4.4.6.3. *Bathymetry*

Bathymetric data were collected along all the ship tracks. A multi-beam SIMRAD EM 120 system (2kHz sample rate, estimated vertical resolution between 10 and 40 cm), for sea floor deeper than 700 m, and a multi-beam EM-1002 (9 kHz of frequency, resolution in the order of 10 cm or 0.2% of the depth) for depths between 2 and 700 m were used [UTM 2005]. Bathymetry data are object of a contemporary work [Barclay et al. 2007]. In order to elaborate a high resolution

bathymetric model, the data from this survey are matched with those of pre-existent database. Then, the area is divided in regions and main tectonic features are delineated (**Figure 4.24**).

Figure 4.24 Preliminary bathymetric map of Deception Island area, from the TOMODEC survey and previous campaigns. From Barclay et al. (2007). 

4 - Deception Island



4.4.6.4. *Water Measurements*

In order to obtain accurate sound velocities, water-temperature profiles were also collected. The SIPPICAN MK-21 bathy-thermo-graphic system was connected to several sensors: for temperature data (sensor XBT), sound velocity (XSV), conductivity and salinity (XCTD). The system acquires information in a quasi-real time. The nominal resolution of the system is about 2% of water depth or ± 0.15 °C.[UTM 2005].

As recognized by others surveys [Lawver et al. 1996] water temperature difference at depths between 100 and 400 m result in velocities difference of up to 10 m per second. With standard corrections, bathymetric data collected at normal-incidence angle give good relative depth results, while for low angles of incidence there is a strong dependence on temperature variations in the stratified water column. With the simultaneous thermo-bathymetric survey, an appropriate model of sound velocities was used to recalculate the multibeam bathymetry.

4.5. 3D Tomography

4.5.1. Method

We employed the method presented by Toomey [Toomey et al. 1994] and later improved [Barclay and Solomon 1998] to invert the P-wave travel times for a three-dimensional velocity structure (Chapter 2.2.3.2.). This method, up to date, has been mostly applied to study smaller regions. These experiments have been mostly offshore (East Pacific Rise, [Dunn et al. 2001; Tian et al. 2000; Toomey et al. 1998; Toomey et al. 2007; Toomey et al. 1994]; Mid Atlantic Ridge, [Barclay and Solomon 1998; Magde et al. 2000]) This method is extremely precise in the ray path tracing, and permits the calculation of a detailed travel time field for each station also in presence of the water layer. Moreover, the method has been successfully applied in regions, such as those along mid-ocean ridges, which present sharp velocity contrasts at small scales (up to 50% in 5 km [Barclay and Solomon 1998]), which the code easily handles. From the previous knowledge about Deception Island, we expected to find velocity anomalies as strong as those described for mid-ocean ridges and at similar distance scales. As the method can manage sharp velocity contrasts and realistic seafloor topography, it was particularly appropriate for inverting the data of our air gun source experiment.

4.5.2. *Input*

4.5.2.1. *Grids Definition and Parameters Selection*

4.5.2.1.1. *Grid Selection*

The tomography method requires, among other input parameters, the definition of a grid of perturbational nodes and a denser grid of velocity nodes for traveltime calculation. For the three-dimensional tomography of Deception Island, we opted for a two-step approach and we built two grid configurations. Firstly, we applied the method to the study of a larger region, encompassing Deception Island and surroundings. In this case the volume, geometrically represented in an x-y-z Cartesian system, is 53 x 52 x 12 km wide and centered in the middle of Port Foster (latitude $-62^{\circ}58'$ and longitude $-60^{\circ}40'$). It is parameterized by a 0.25 km grid-node spacing for the ray tracing and 0.5 km grid-node spacing for the velocity perturbations. We called this configuration the 'Sparse' grid (**Figure 4.25**). Here, the total number of perturbational parameters (280875) is significantly lower than that used for ray tracing (2181333) (see Chapter 2.2.3.2).

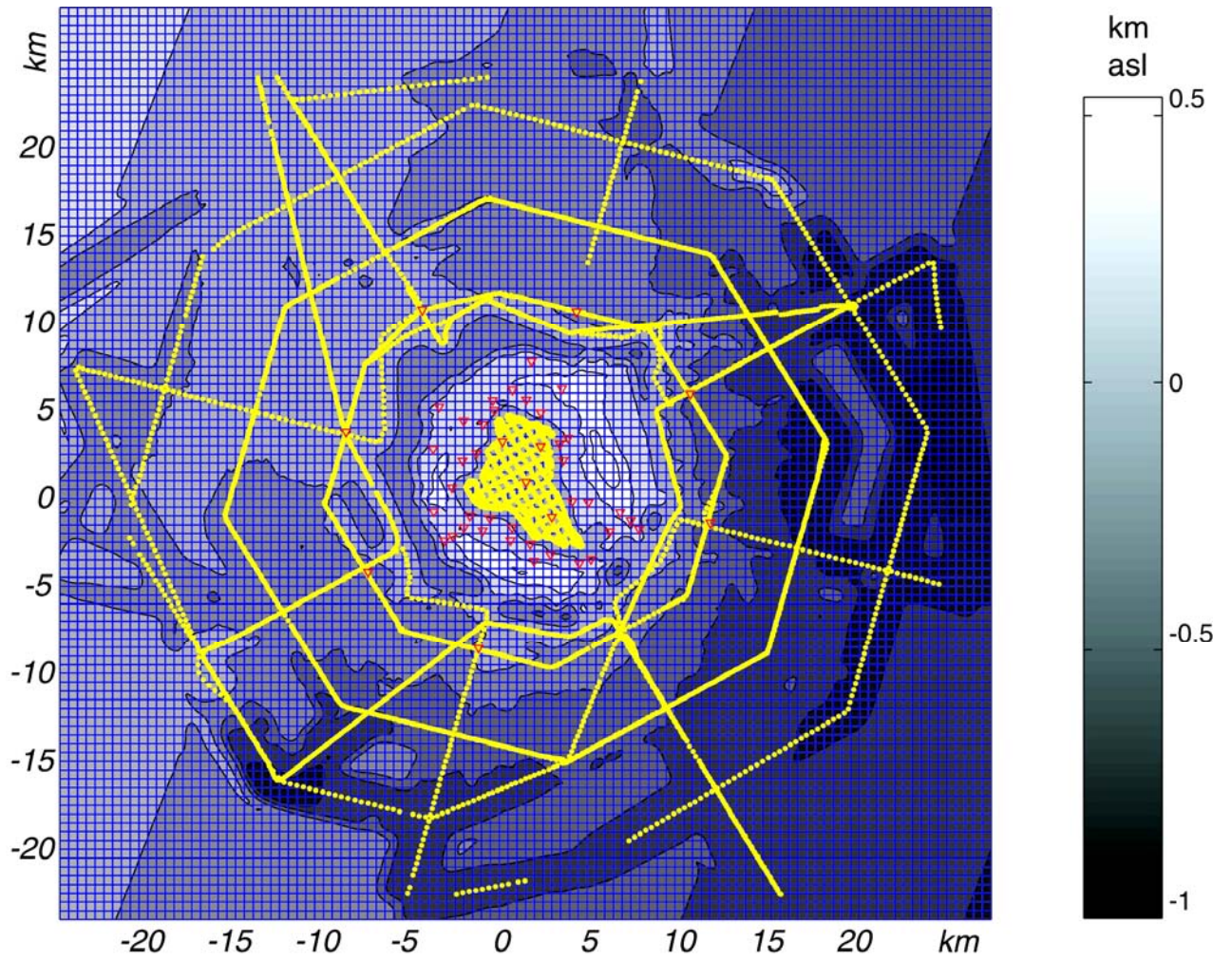


Figure 4.25 Sparse inversion parameterization. Shaded gray: topography model used in the inversion (see scale on the right). The yellow dots are air gun shot positions used for the study. The red triangles are seismic station names. The blue grid is the perturbational grid of the velocity model (0.5 km spacing).

4 - Deception Island

In a second case, we focused on Port Foster and we reduced the studied area to a sub-region 12 x 14 x 7 km, centered in the middle of the bay (latitude $-62^{\circ}57.2'$ and longitude $-60^{\circ}37.2'$). We increased the density of nodes in the parameterization grids, by using a 0.1 km grid for the ray path tracing and 0.2 km for the velocity perturbation. We called this configuration the 'Dense' grid (**Figure 4.26**). In this case, the total number of perturbational parameters (155916) was significantly lower than that used for ray tracing (1211331).

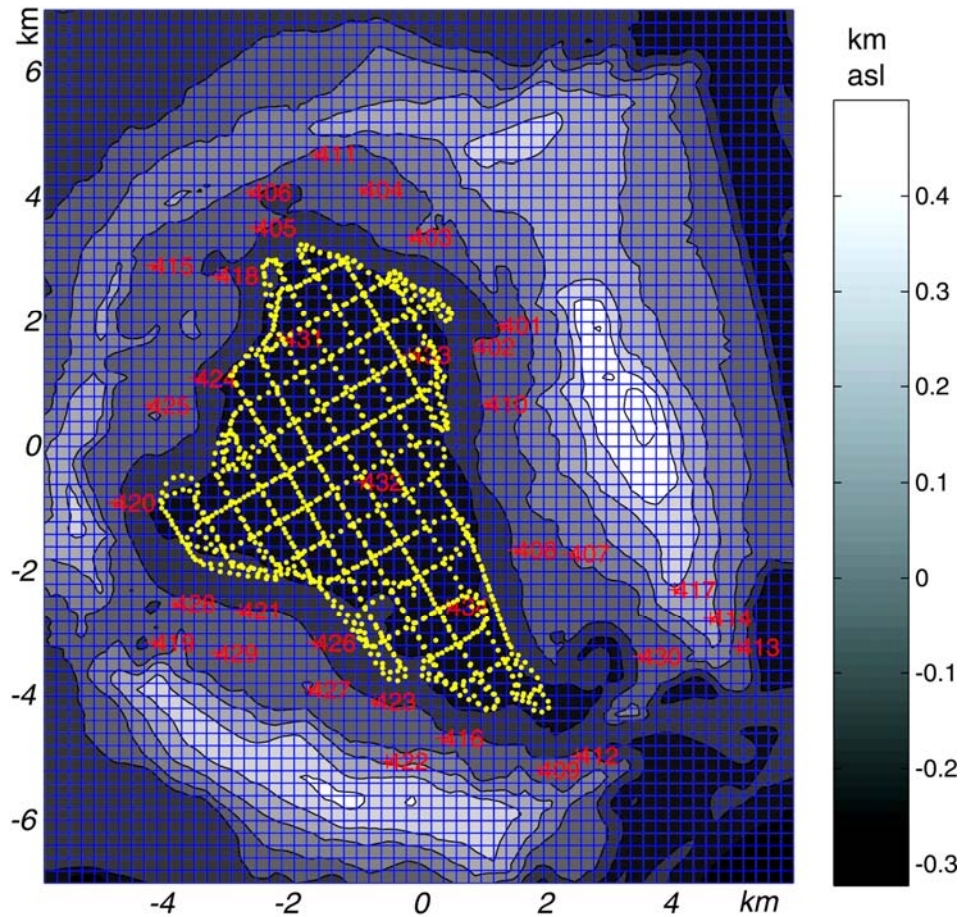


Figure 4.26 Dense inversion parameterization. Shaded gray: topography (see colour scale on the right). The yellow dots are air gun shot positions used for the study. The red numbers are seismic stations names. The blue grid is the perturbational grid of the velocity model (0.2 km spacing).

4.5.2.1.2. Reference Ellipsoid

The grid handling was performed by the code on a rotated Cartesian grid. As all the input coordinates were instead of geographical, they had to be converted to kilometres distances from the center of the volume. Coordinate conversion from geographical values (in degrees) to kilometres was performed by introducing a conversion factor which depends on the latitude zone of the studied area. The reference ellipsoid is the GRS80 (which is the same of WGS84) and the distances are converted with the *setorg.f* routine, where two different conversion factors are set up, for latitude and longitude, respectively. For both of them, great and minor circles crossing the point are considered as circular.

4.5.2.1.3. Parameters

Several input parameters for the code govern the regularization of the matrix inversion. The equation expressing the inversion problem needs to be constrained by damping and smoothing values for the model covariance matrix and by a linear length to apply as a smoothing decay parameter for the perturbation at each inversion node.

In order to evaluate the best parameters to be used, we investigated the RMS variation due to different choices of regularization values. At the same time, we qualitatively checked the final image, because in a trial approach for tomographic inversion (Chapter 2.2.3.2.), visual inspection can indicate wrong choices. For example, an under-damped inversion can lead to a small RMS but the final image may instead indicate that we are introducing artefacts by modelling noise. In any case, we note that the major features in the final images are almost insensitive to different choices of these parameters, and any variations appear mostly at small scales.

For parameter selection, we used a coarser parameterization (i.e., 1 km spacing instead of 0.5 km) for the perturbational model. The coarser grid is more efficient computationally and, on the basis of the final images, both grid spacings lead to similar results. The values of variable regularization parameters are hence determined by conducting approximately 20 different inversions using a 1 km perturbation grid. The final, selected parameters are also applied to the entire set of synthetic tests (see 4.5.4). In this way, we further verified the appropriateness of the selected parameters. The final regularization values were: half length for smoothing $\tau_x = \tau_y = \tau_z = 1.1$ (for the sparse inversion) and 0.8 (for the dense grid); damping $\lambda_p = 100$; horizontal and vertical smoothing $\sqrt{\lambda_s} = h\lambda_s = 30$ (for the sparse inversion) and 20 (for the dense).

4.5.2.2. *Data Selection*

For the sparse inversion almost all shots and stations data are used (see **Figure 4.25**). We excluded shots at the extremities of the long NNW-SSE line as well as the data recorded by two most distant OBS (S110 and S221), which were otherwise included in the 2D seismic lines [Ben-Zvi et al. 2007]. We decided not to include them in order to limit the inversion volume and the number of unknowns, which increases with the cube of the increase in any one dimension.

For the dense inversion we selected data from only these OBS which were deployed in the inner bay and land stations that were installed close to the inner coast (see **Figure 4.26**). The shot data were restricted to the sources fired inside Port Foster. In this, the used traveltimes represent a sub-dataset of those used for the sparse grid.

4.5.2.3. *Initial Model*

The starting model for the inversion consists of several layers: offshore, there is a water layer with a velocity of 1.5 km/sec underlain by parallel crustal layers each of constant velocity and variable gradients among them. Obviously,

modelling the land velocities implies the same crustal layers but no water. In the 3D inversion, this 1D model is re-sampled and interpolated with the grid configuration and spacing used for the 3D ray tracing.

One of the major advantages of the method is that seafloor topography is explicitly included in the model and the calculations. So, in addition to velocity data, a high-resolution earth surface model was also supplied to the program, in order to better calculate ray paths connecting shots to stations. The bathymetry grid, combined with the island's topography, was used as one of the interfaces (between water layer and the sea bed crustal layer) with a node spacing of 50 or 25 m for the sparse and dense grid respectively. The code incorporates topography by shearing the columns of nodes vertically to follow the land surface and the local seafloor relief [Toomey et al. 1994].

4.5.2.4. Bathymetry

The topographic interface has to be supplied to the code, in order to create a velocity model that is as close as possible to the real earth, and to calculate the most accurate traveltimes. Because of the strong velocity contrast at the seafloor, this is particularly important for the ray tracing in the water layer and at the ray entry point at the seabed.

A surface map was built up using a combination of *GMT* [Wessels and Smith 1995] and *Matlab* gridding and plotting tools. Once the data were collected and the area of interest defined, the bathymetry and topography data combined and the small gaps in the data were interpolated to produce a seamless map. The bathymetry grid was later sub-sampled to produce smaller scale maps that were used as interface topography for the ray-tracing.

The main steps we followed were (1) we started with the sub-sampling of the ASCII topography file (x, y, z values for each node) and we created a *GMT* bathymetry .grd file, that included the (previous) topography and (recently-collected) bathymetry data for the whole region of interest (2) we used a *Matlab* script (*bathy_fix.m*) to define the bathymetry grid we wanted to use for the inversion and to write the coordinates of each node out in a final ASCII file (*matlab_asc.out*). In detail, this *Matlab* script first defines the geographic limits of the region, the degree equivalent of Cartesian distances (for example $xlnkm = 0.8425$ km/minute, of longitude; $xltk = 1.8532$ km/minute, of latitude at Deception Island) and creates a grid of desired coordinates, converted from Cartesian to geographical values and stored in an ASCII (*tracksin_tmp*). (3)

GMT was then used to extract the depth or height data from the starting bathymetry .grd file for each node point and write it into a binary file (bathym.bin) (4) this file was again read by *Matlab* to reshape the data into a matrix where depths were ordered in W-E rows, starting at the NW point of the box (written as ASCII file matlab_asc.out).. Finally, a header was added with information about the corner position in kilometers, grid spacing and number of bathymetry points to be later used by the ray tracing code (5) A *FORTRAN* program (*readtest.f*) then created a binary file (bathout.bin) from the ASCII file (matlab_asc.out). This step was necessary because the code reads the bathymetry data as a machine-specific *FORTRAN* binary file (6) finally, because bathymetry points were read by the ray tracing algorithm, they had to be introduced in the code. In particular, it was necessary to edit two entries, *knrow_cb* and *kncol_cb*, in the *Params.f* program (which includes parameters for array declarations).

For our larger inversion, the bathymetry-topography interface was discretized through a 50 m grid which was considered enough for the calculation of traveltime in a ray paths grid of 0.250 km spacing (**Figure 4.27**).

4 - Deception Island

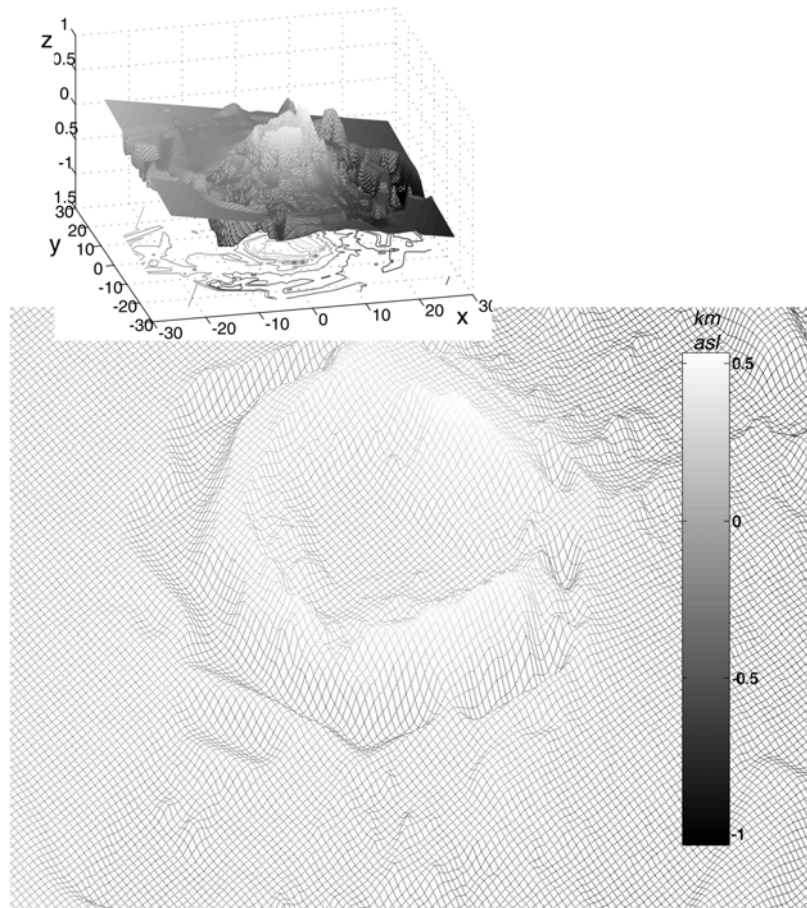


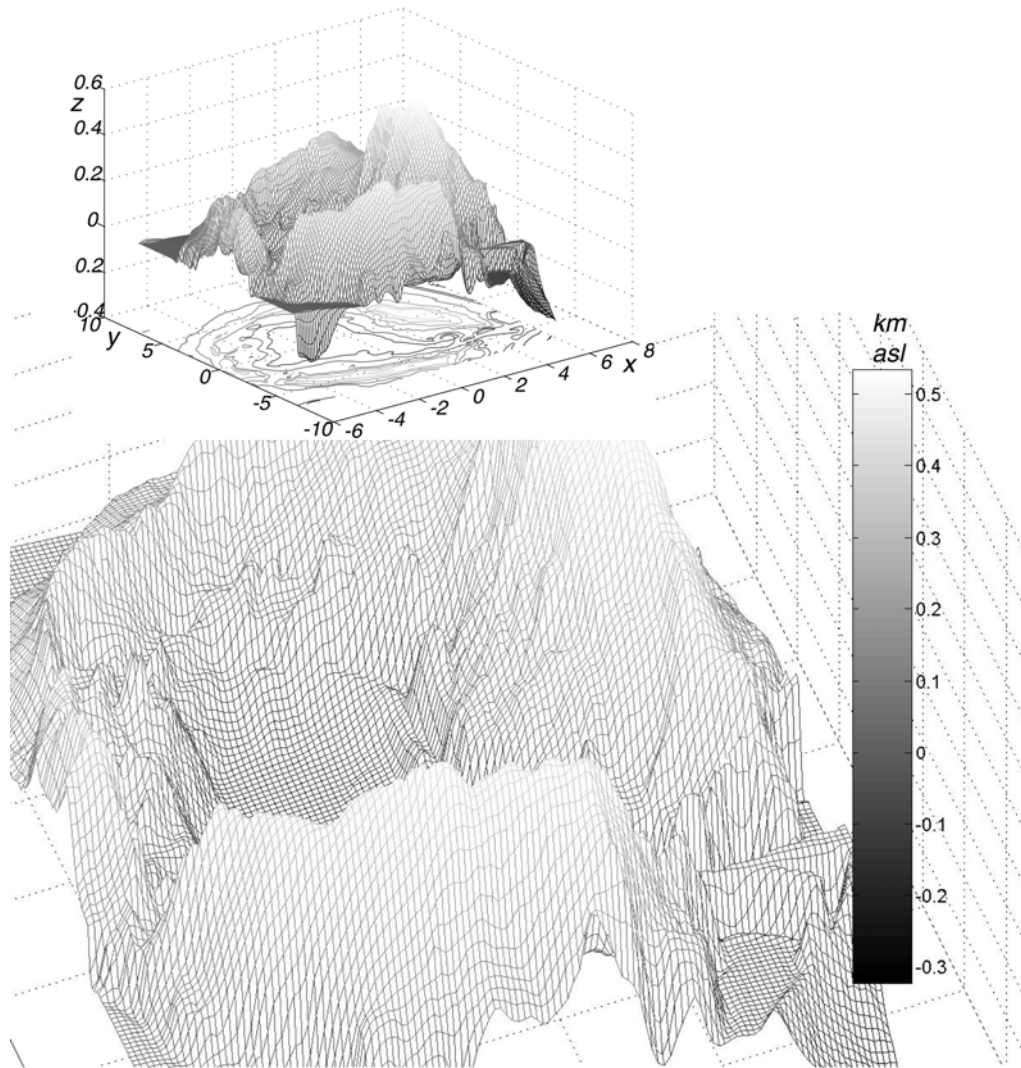
Figure 4.27 Topography grid used by the code for the ray path tracing (for sparse grid, 0.25 km spacing). The grid orientation is shown in the small box at the top of the figure.

For the dense inversion that focused on Port Foster, we used a denser grid for both the perturbation and traveltime calculations. Therefore, also the topography grid had to be denser, in order to calculate precise traveltimes. The same steps described above were repeated for a final bathymetry interface which was then used by the ray path tracing by a 0.1 km spacing (**Figure 4.28**).

A major difficulty in this phase was the definition of the starting bathymetry.grd file where there was no data coverage. These regions included the seafloor off the inner and outer coasts of Deception Island where the ship could not operate and data gaps between ship tracklines. Because the bathymetry file read by the tomography code required real values everywhere, these gaps had to be filled by spline interpolation between known values. This was especially inconvenient in the case of the dense grid due to the relative weight of the error introduced by the interpolation process with respect to the grid spacing (see later 4.5.3). We therefore produced a densely sampled and complete bathymetry grid (25 m spacing) for the whole area, including topography and bathymetry, using the *GMT surface* program.

Figure 4.28 Topography grid used by the code for the ray path tracing (for dense grid, 0.1 km spacing). The grid orientation is shown in the small box at the top of the figure. 

4 - Deception Island



4.5.3. Error Definition

As explained above, the basic idea in a tomography study is to best fit a trial velocity model to data. With this aim, it is vital to know how much of the data variance can be attributed to stochastic processes, as opposed to unknown seismic structure [Barclay and Solomon 1998].

The main sources of error for calculated travel times are summarized in the **Table 1** : they are due both to position and time uncertainties. The instruments and source location errors were converted in uncertainties in time by assuming velocities of 2.5 km/s at stations [Christeson et al. 2003], 1.5 km/s at sources and a horizontal ray parameter of 0.28 s/km at the sea bed (i.e. an incidence angle of 45°). In general, the change in travel time due to a small shift in position can be quantified as $\delta t = \delta x \cdot \cos(\beta) / V$, where β is the angle between ray path and x_i axis and V is the velocity. For uncertainties in the in-water location, we considered the same value of incidence angle (it could be slightly more vertical, as in deep waters, and then the error would be smaller). So, we can describe them as in the following points:

- 1) Shot location. The position of the shots was recorded in the telegram produced by the GPS Seapath 200. Actually, what we knew was the position of the GPS receiver, and from this, we obtained the shot position by considering it to be 125 m behind and 5 m to port of the ship's GPS receiver. We considered that the GPS position is subject to a maximum error of 1.5 m, and added it to the error due to the ship's movement during the 61 ms of delay between impulse generation/location definition and shot. This amounted, for a speed of 10 knots (about 19 km/h), to approximately 0.3 m. So a total horizontal error of 2 m meant less than 1 ms as time, which is insignificant. The source depth was controlled by floating the airguns and so the error in this measure was also assumed to be negligible, as it was probably only affected by wave movement. A nominal depth of 9 m +/- 5 m is a very conservative estimate. Note that if the air guns weren't floated, then the depth would depend on the speed of the ship.
- 2) Station location (land and ocean bottom). This uncertainty was defined as a vertical/depth and a horizontal error. A depth error was estimated as the average of the absolute difference between relocated depth for each OBS and the depth picked from the bathymetry (and in a similar way, between the GPS elevation of stations and the topography for land

stations). Its value was less than 2 m (smaller for land stations, about 1 m, with respect to OBS, 11 m) for the sparse grid and less than 3 m for the dense grid. In order to be conservative we considered 3 m to be the bathymetry error.

Moreover, to explore the effects introduced by the OBS depth errors, we performed additional tomographic inversions while changing the OBS location. In other words, we compared results of the inversion for which the OBS depths were the same as the local bathymetry with inversion where the OBS depths were determined from shot and/or acoustic transponder travel time. We observed a difference in RMS misfit between the results of the two inversions after the first iteration (which was smaller when the calculated OBS depth was equal to bathymetry), but this difference reduced as the inversion progressed reaching zero after the 6th inversion, when the final images were the same. We concluded from this test that any effects due to uncertainties in OBS depths are managed and reduced by inversion and are not significant and modelled.

The horizontal uncertainties in land stations position were due to the GPS locations and included applied corrections and technical characteristics of the instruments (we used handheld Magellan GPS), and to the quality of the fix.. Based on experience gained from repetitive measurements from previous campaigns at Deception Island, the average error is never greater than 20 m. For the OBSs, the GPS location of drop point was improved with a relocation analysis (Ben-Zvi, personal communication). Water-wave arrivals from the shots (picked on the hydrophone channel) and two-way traveltimes from acoustic ranging were used [Creager and Dorman 1982] to invert for the OBS positions. The GPS drop positions were used as starting values for the inversion, which was necessary because of drift as the instrument falls. The source depth was fixed to 9 meters as indicated in the ship technical report and the velocity structure in the water column was derived from the bathythermograph log taken during the experiment [UTM 2005]. The final RMS for the travel time of the water wave was 10 ms after relocation of the OBS. This value could not be directly translated to position uncertainty, as it can be also due to other difficulties, such as water velocity uncertainty, or limitations of the inversion algorithm. In any case, it could be considered as a conservative indication of the expected error due to OBS mislocation. The land station horizontal error of maximum 20 m was translated in a timing uncertainty of 6 ms. We therefore assumed the uncertainty of 10 ms (from OBS mislocation) as due to the uncertainty both for land and OBS positions.

3) Bathymetry. The traveltime uncertainty due to bathymetry inaccuracy can be quantified as $\Delta u \cdot \Delta z$, with Δu as the slowness contrast across the seafloor and Δz the error in the depth. If we assume [Barclay and Solomon 1998] Δu of 1.0 s/km (which would correspond to a seafloor velocity of approximately 2.5 km/s, [Christeson et al. 2003]) and we find a Δz ,

we can estimate the effect of bathymetry uncertainty where the rays enter the seafloor. The sounding equipment was based on a SIMRAD EM120 and a SIMRAD EM1002 system, depending on the depth. The nominal resolution for these instruments is at worst 0.6 m, with the largest source of error being the water velocity structure, because any other sources are centimetres. The bathymetry data were corrected for tides, ship heave (up-and-down), ship roll, pitch, and navigation errors. In Barclay's experience (personal communication) the errors are less than a *few meters*, based on the agreement in depth and swath intersections. The errors were probably greater for the outermost beams, but because most of the outer beams were removed and because the seafloor ray-entry point moves closer to the ship as the water depth increases, errors in water sound speed were minimized. Within Port Foster, assuming a correct velocity profile, derived from crossing tracks was *less than 1 m*.

Another possible source of error was the effect of averaging the bathymetry, which is likely to be small. The seafloor, well-sedimented, is probably not very rough on scales of ~ 50 m, the spacing of the larger bathymetry grid used in the sparse inversion. For a typical water wave at 10 Hz, the wavelength is 150 m and the seafloor Fresnel zone (the reflecting zone at the interface where the seismic ray incises, [Spetzleer and Snieder 2004; Yilmaz 1988]) is a quarter of that, so a bathymetry dataset that is laterally averaged over ~ 50 m is probably fine.

In order to assess about uncertainty in bathymetry we plotted the bathymetry data used by the code to calculate the ray paths. This represents what the code 'thinks' is x , y , and z as defined on the ray tracing grid and can be compared against the shot and receiver locations by contouring them up (**Figure 4.29**). Actually this test is somewhat circular, it provides an useful verification of many of the spatial-referenced data are read into the inversion code

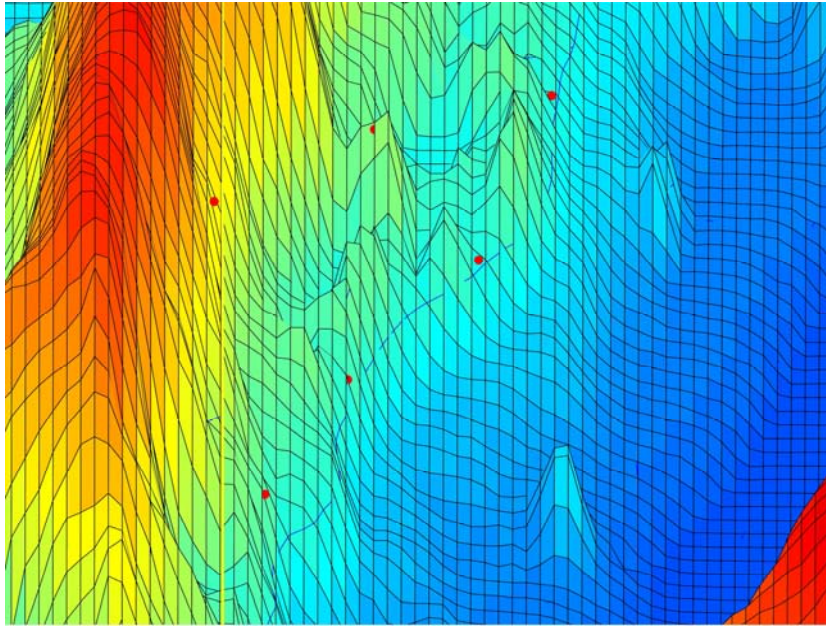


Figure 4.29 Comparison between topography/bathymetry (gridded surface) and seismic stations (red dots) for the denser grid. Only a sector of the Port Foster coast is represented. The grid has a 0.25 km spacing. The blue horizontal line marks the coast line. The surface/seafloor colour-scale depends on level asl (between approximately 450 m, in red, and 300 m, in blue).

The average difference between the stations and surface for the two different topography grids was 1.6 m for the 50 m and 2.9 m for the 25 m grid (at the same stations). We would expect a smaller difference for the more precise topography grid, but these differences were both so small that they indicate that the results were essentially independent of the grid spacing.

Finally, we concluded that any error in the multibeam bathymetry depths is about 5 m, which is equivalent to a 2 ms travel time uncertainty.

- 4) Clock drift. It was assumed to be *negligible*.

5) Picking. While this probably represents the main source of uncertainty its magnitude can be estimated. We determine an average picking error of *11 ms*, where uncertainties are referred to positive/negative difference between picking time (manually marked and again checked) and arrival time. Smallest error was 7 ms, and the largest 226 ms. The standard deviation was 4 ms.

6) Shot origin time. this uncertainty was the timing error indicated in the GUNDALF array modelling suite report, and was 1 ms. It is guaranteed by the Minipulse system, which applies corrections in order to have as *1 ms* as maximum error with respect to the aiming point (Gundalf array modelling suite-array report [UTM 2005])

7) Ray tracing calculation. This can be an important source of error. For the coarse inversion, the velocity structure was defined by a 3-D grid with a horizontal and vertical node spacing of 0.25 km. Ray paths and travel times were calculated on this grid. Perturbations to the slowness values were instead applied to a grid with a horizontal and vertical node spacing of 0.5 km, which is in turn re-sampled to the traveltimes grid spacing in order to repeat the forward calculation in subsequent iterations. The same philosophy was followed with the dense grid, with the difference that the raytracing grid was 0.1 km and the perturbation grid 0.2 km.

In order to assess the effect of grid spacing on the accuracy of the travel time calculation, we performed an analytical calculation of traveltimes in a synthetic velocity model with constant gradient. We compared this result with traveltimes calculated by the code, for the same velocity model. The calculation was performed for a station ideally located in the center of the model space, in a constant gradient velocity model and with no bathymetry/topography (i.e. flat surface) because the analytical solution cannot manage the irregular surface of the water layer. Both the station and the shot were located at 0 m elevation. The synthetic starting model was calculated with a first layer with velocity of 2.5 km/s, and a gradient of 1.5. The traveltimes were calculated analytically [Dix 1955]. Comparing the results of these two techniques, we observe a systematic difference (**Figure 4.30**), that is mostly dependent on the distance of the point from the station, i.e. the length of the ray path. As can be seen in the figure, the difference at a given distance is greater where the path crosses the grid diagonally.

By comparing travel times calculated for a linear velocity gradient with analytical results, we estimated a mean difference of 0.033 s, with a standard deviation of 0.010 and maximum of 0.134. The magnitude of this error would constitute a large proportion of the total error. Fortunately, because the error is always positive (analytical ray paths are faster), we expected that much of the error is mapped into the depth-dependent component of the velocity model (starting

with the 1D model) and his effect on the lateral velocity variations at any one depth is reduced. The average error is approximately 15 ms among rays at similar ranges, and regions with the highest error are outside the well-sampled, resolved, regions (see later 4.5.4).

We have to consider that our ray tracing algorithm has its strength in the calculation of the entry point of the seismic ray on the surface. This means that this synthetic example does not correspond to any real direct problem solution. Hence, this error calculation was not indicative of the true error introduced by the code in the ray tracing phase and could represent only a really conservative estimate. The comparison between our results with those of the analytical calculation had to take into account that with the second approach we could never manage the topography information or the sharp three dimensional velocity perturbations. Moreover, the code routine *initializeSP.f* actually considers the real position of the station and it accurately ponders that the station doesn't sit exactly on the node of the ray tracing grid.

The use of a denser grid would provide more accurate ray tracing, but the computational cost for the entire region encompassing Deception Island would be prohibitive. From previous experience (Barclay, personal communication) the final velocity model is less sensitive to the grid spacing for the ray tracing that might be suggested by **Figure 4.30**. This contention is supported by comparison of the tomographic images for the sparse grid within Port Foster and the dense grid solution, in which the primary features are common to both.

For all these reasons and the real difficulty to establish the effect of the travelttime calculation uncertainty, we decided not to consider it in the overall expected uncertainty except for the synthetic tests, when this effect will be included by slightly increasing the noise added to the synthetic data (Chapter 4.5.4).

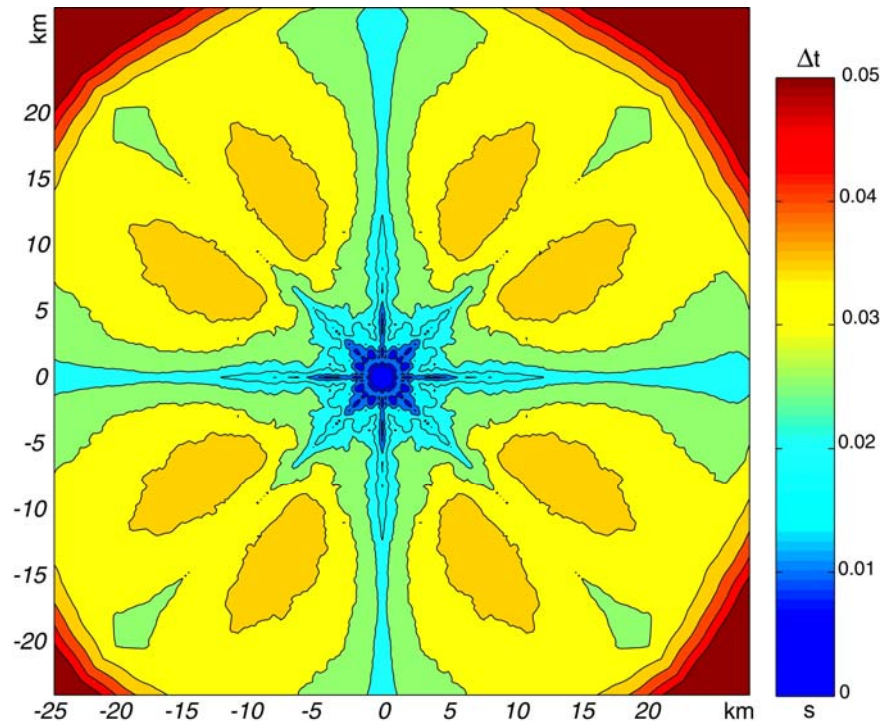


Figure 4.30 Traveltime calculation difference between analytical solution and values as calculated by the ray tracing code. The comparison is for a central station, flat topography and constant gradient velocity variation. Contour interval is 0.005 s

The final predicted uncertainty is the sum of the variances of the individual error sources. As expected, this turns out to be dominated by the picking uncertainty, which for our data is around 11 ms (**Table 1**).

4 - Deception Island

| Source of error | Location error, m | Timing error, ms |
|------------------|-------------------|------------------|
| Shot Location | 1 | <1 |
| Shot depth | 5 | 3 |
| Station Location | -- | 10 |
| Station Depth | 3 | <1 |
| Bathymetry | 5 | 2 |
| Clock Drift | -- | <1 |
| Picking | -- | 11 |
| Shot Origin Time | -- | 1 |
| Ray Tracing | -- | -- |
| TOTAL | | 15 |

Table 1 Main sources of uncertainty. Times are in ms and distances in m.

4.5.4. Resolution Analysis

Resolution is generally defined as the ability to distinguish separate features. This is measured by the minimum distance between two features so that they can be detected separately rather than as only one. Obviously, both the vertical and horizontal distribution of this parameter needs to be investigated in a three-dimensional tomography.

In the following section, we refer to Resolution Analysis as the study of the resolution capability of the inversion and also how it changes across the model in the horizontal and vertical directions, out to zero resolution in the peripheral zones of the model.

In order to test for the reliability of the velocity features in the crustal layers, empirical methods were applied. Among them, the examination of the ray distribution across the model and the results of synthetic inversion for known structures (see chapter 2.2.1.4).

The Derivative Weigh Sum is a weighted measure of the ray distribution across the model. In our model it reaches the maximum value around 1 km depth, indicating potentially high resolution at these depths. We tested the code/data resolution by applying several synthetic tests. All of them consist in creating a synthetic model, and calculating traveltimes for this model. Later, noise proportional to the previously calculated uncertainty is added. Finally, these traveltimes are used as input data for an inversion which has the same configuration and parameters of the true inversion. On the base of the results of these tests, we, on the whole, observe that the resolution, as expected, is high in the centre of the model, in the area included by the shots/stations distribution. The maximum resolved depth instead varies depending on the type of anomaly, and it's hence hard to quantify. We resolve structures from surface to a depth which fluctuates between less than 4 km (Checkerboard Test 4.5.4.2) to more than 7 km (Spike-High Velocity 4.5.4.3.3). So, we comprehensively assume a resolution depth for our model of 5 km, taking into account that at these depth only major anomalies can be plausibly imagined.

We then studied the effects of the choice of the 1D starting model on the final 3D result. We tested several structures available from previous seismic experiments, and we concluded that main anomalies are stable independently

from the initial velocity model. We assume as best starting 1D model that derived by the seismic profile of Christeson et al. (2003) inverted to a 2D seismic profile and then averaged to a 1D model.

4.5.4.1. *DWS Definition*

We analyzed the distribution of the Derivative Weight Sum (DWS) in order to evaluate the ray path coverage. The partial derivative of a travel time with respect to a model parameter (slowness perturbation at a node) is the length of the path influenced by that parameter. If for each parameter at a node the summation over all possible seismic ray paths is weighted by linear interpolation depending on the distance, we obtain the value of DWS as weighted sum for that parameter. This weighting function provides a measure of the seismic ray distribution which is superior to a simple un-weighted count of total length of rays in each cell, as traditional values of coverage provide. Its advantage is that it is sensitive to the spatial separation between ray path and node [Toomey et al. 1994] and it also reflects the smoothing constraints.

By plotting the DWS distribution in the shallowest layers (**Figure 4.31**), we observe that ray paths penetrate the upper crust at near-vertical angles, and hence the DWS is low, far from stations and shots and high directly beneath the stations. This is especially evident for the region outside the island, where higher DWS coincides with OBS positions. At greater depths, from 0.5 km depth to 1 km, the DWS values increase with the maximum DWS values around 1 km depth, where many of the rays turn and travel horizontally for a significant distance (**Figure 4.32**). The maximum values of DWS, close to 350 km (for the 0.5 km perturbational grid), mark the inner bay, between 0.5 and 1 km of depth. Inside the bay, as revealed by the small inversion with denser grid, the DWS distribution again indicates the highest values below the seafloor. As expected, the absolute value of DWS, which is roughly proportional to the number of rays crossing close a node, is lower in dense grid. In this case the maximum value is approximately 40 (compared to 350 of the sparse grid)

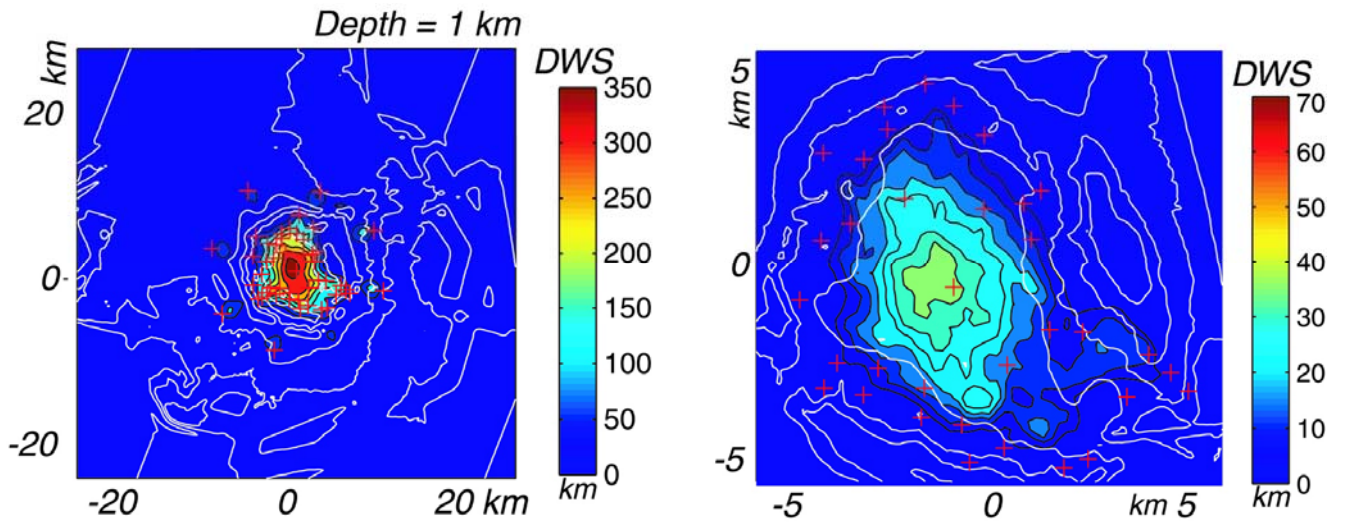


Figure 4.31 Map view of the Derivative Weight Sum (DWS) for the 0.5 (left) and 0.2 km (right) spacing perturbation grid (contour interval 50 km left, 5 km right). Red crosses are seismic stations, white line the bathymetry (contour interval 400 m right; 100 m left)

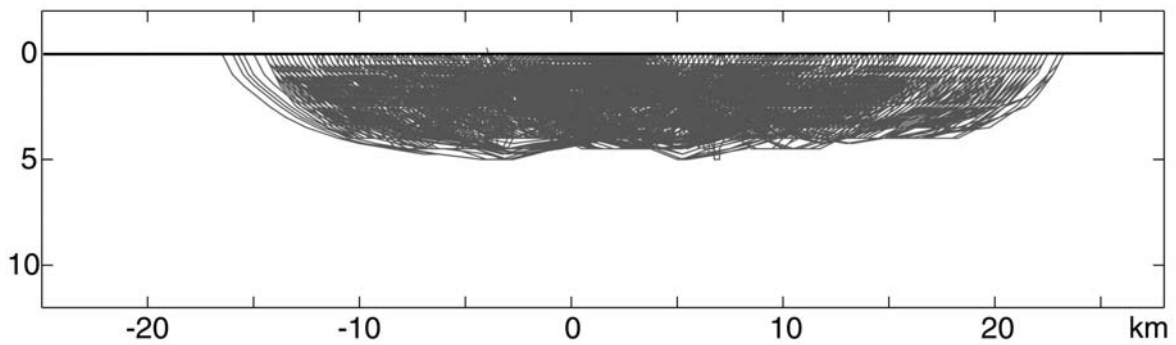


Figure 4.32 Seismic rays distribution in depth for three stations, indicated with red colour in **Figure 4.23**

On the basis of these observations, we used the indication proceeding from DWS to represent the velocity model only where the DWS is greater than 0.1. We chose this threshold value in order to show only the regions that are sampled by seismic rays. Although this is a minimal threshold, it effectively masks the regions with no ray coverage but where false perturbations may be generated by the noise modelling by the code or interpolation used by the plotting software

The weight of a 0.1 threshold can easily understood by a comparison of the model result for several different DWS values (**Figure 4.33**). For the purposes of interpretation, there is not practical difference between choosing a threshold DWS value of 0.1, 0.01 or even, 1.0. We considered 0.1 to be a reasonable value

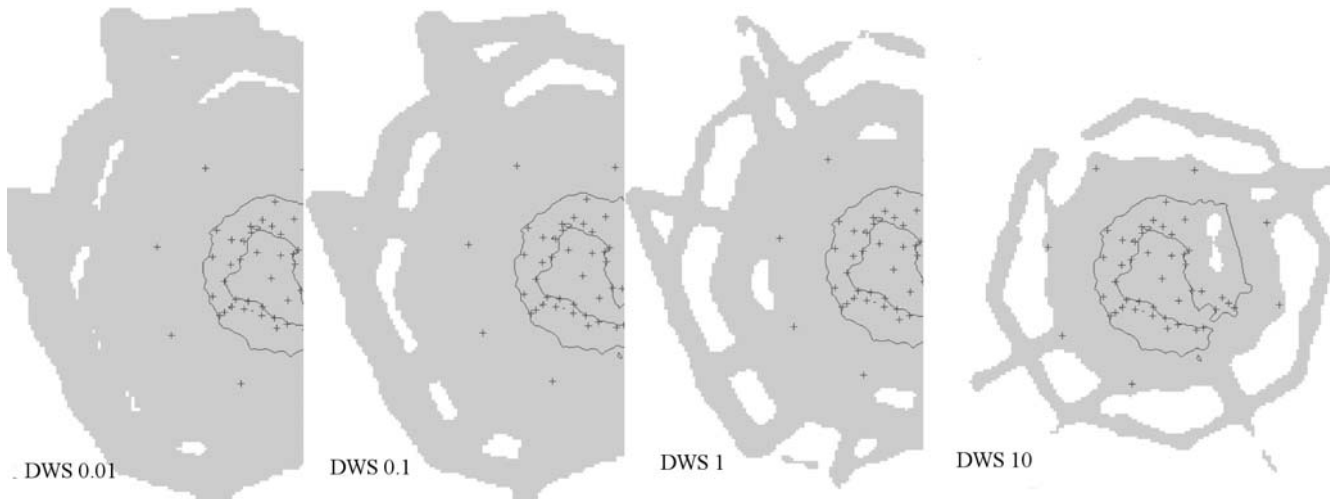


Figure 4.33 Comparison of the final model resolved area for different values of threshold DWS at 1 km depth.

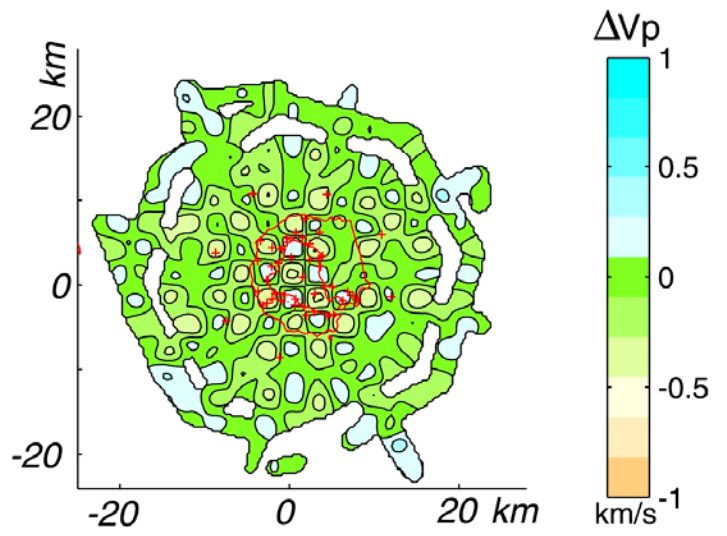
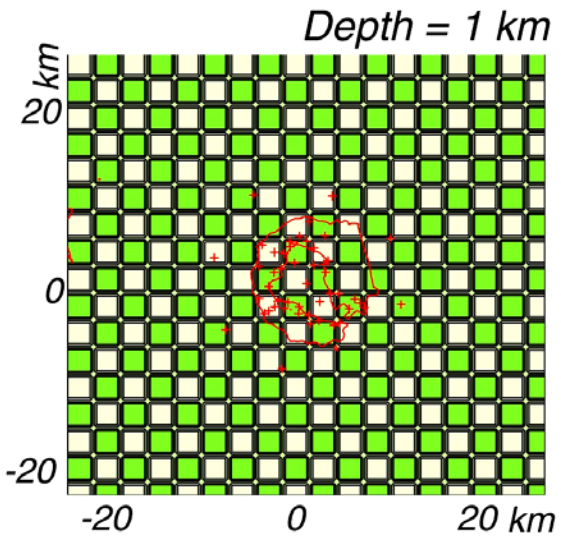
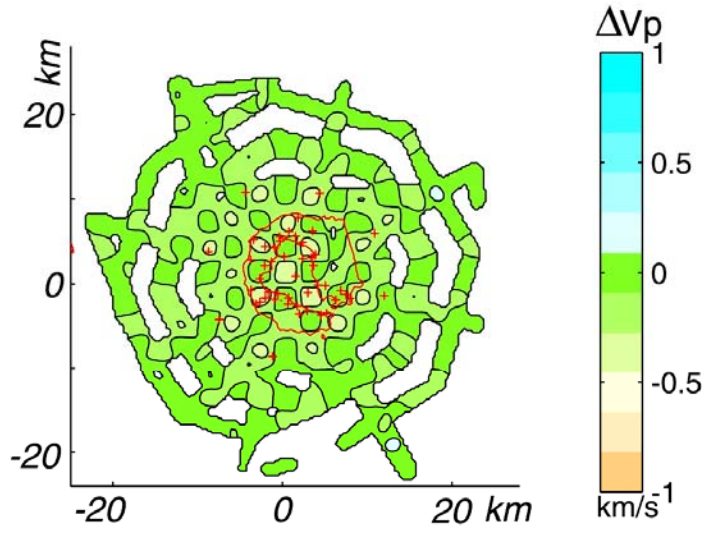
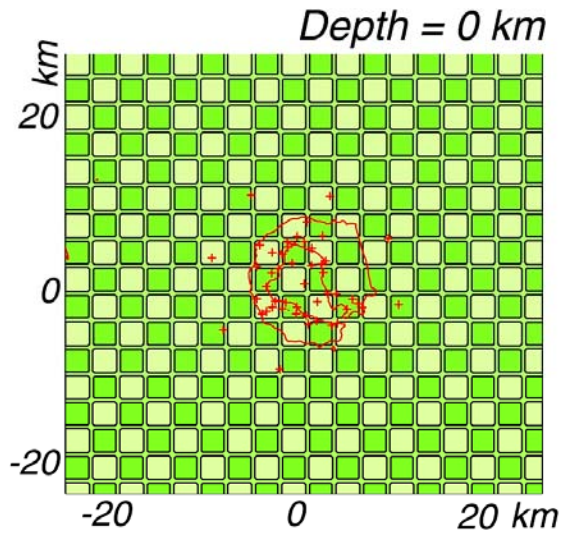
4.5.4.2. Checkerboard Test

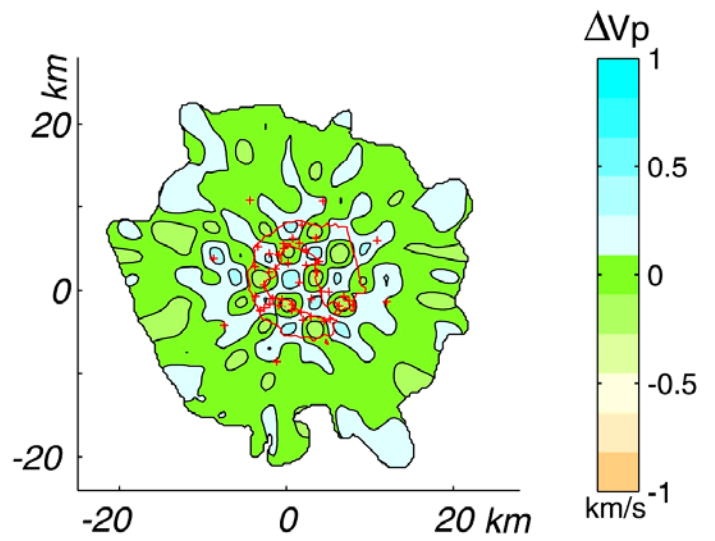
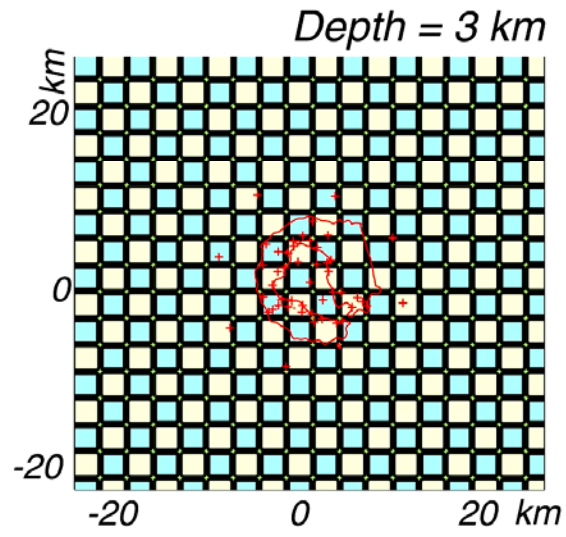
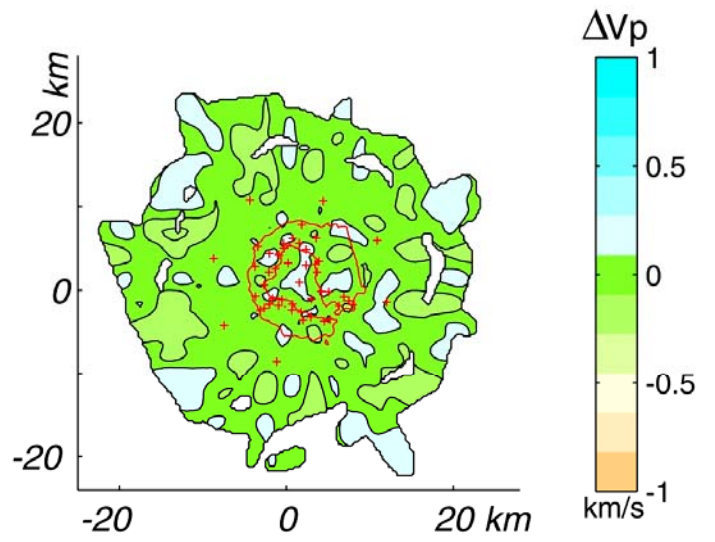
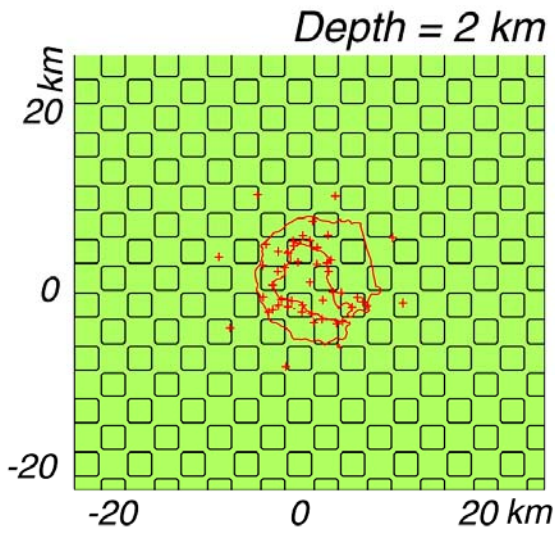
4.5.4.2.1. Sparse Inversion

Among synthetic tests based on the reconstruction of known pattern of anomalies, the checkerboard test supplies crucial information about inversion resolution. Cuboids of 10% velocity perturbation with horizontal length 3 x 3 km in and 2 km thickness were added to the initial 1D model. These anomalies were changed to slowness values and so smoothed along three dimensions, with a box filter as the convolution kernel (the algorithm 'SMOOTH BOX N' makes the average of N adjacent channels and divides the number of channels by N). Our experience indicates that with smoothed boundaries between anomalies this method performs better during the ray tracing phase because it does not need to manage critical regions (as very sharp contrasts or caustics within short distances). The 10% variation we chose is large enough to provide a perturbation greater than that expected from a noise level equivalent to the final RMS but also small enough to minimize the deviation of ray paths from those in the final model. [Evangelidis et al. 2004]. Travel times calculated in this synthetic velocity model and with the same shot-receiver geometry of the real inversion, were then added with a random distribution of noise. The noise was proportional to the previously calculated total error, i.e. 15 ms, but we increased the amount of added noise by another 50% to 22 ms, in order to partially take into account the ray tracing error we were not able to quantify (see 4.5.3 item 7). The new travel times were then used as starting data for an inversion identical to that of the real dataset, also in terms of parameters and number of iterations. The starting model was the same as for the true inversion and equal to that model we have overlapped anomalies to.

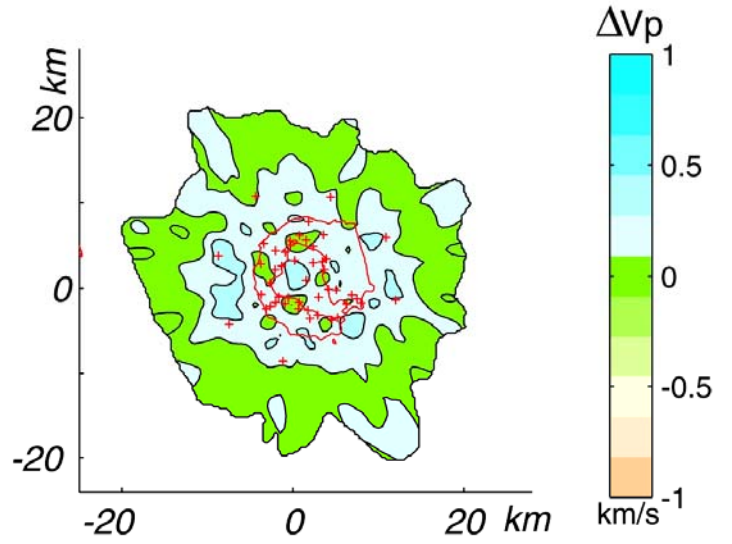
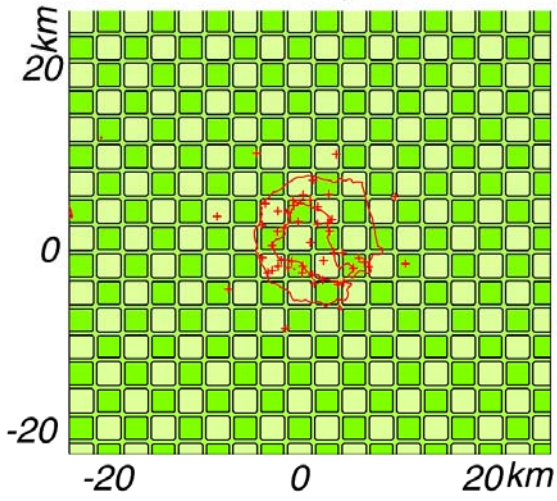
A comparison between the resulting model and the known synthetic can indicate the resolution capabilities and the robustness of the result (**Figure 4.34**). The first striking observation concerns the good spatial recovery of the anomalies. About their distribution, we can observe that in depth they are recognized until 4 km from the surface. Their horizontal distribution is well reconstructed until 15-20 km from the centre of the model, at least in the first 3 km. Until 3 km of depth their shapes and location are similar to the original and contacts among anomalies are quite sharp, with little to none deformation of contouring lines between neighbour blocks. This seems to indicate that really small smearing is affecting close nodes in the model. At about 2 km of depth the checkerboard pattern is lost because also in the synthetic model we

are approaching the depth where positive smoothly change to negative anomalies. The anomaly intensities are recovered as well. The amount of recovered anomaly (recovery rate) can be described by the ratio between starting synthetic and reconstructed model values at each node. It is mostly close to 1, always between 0.74 and 1.46, with mean of 1.022 and standard deviation of 0.0866 (**Figure 4.35**). The average difference between velocity values at nodes is 0.38 km/s with a standard deviation of 0.2397, a maximum difference of 1.25 km/s.





Depth = 4 km



Depth = 5 km

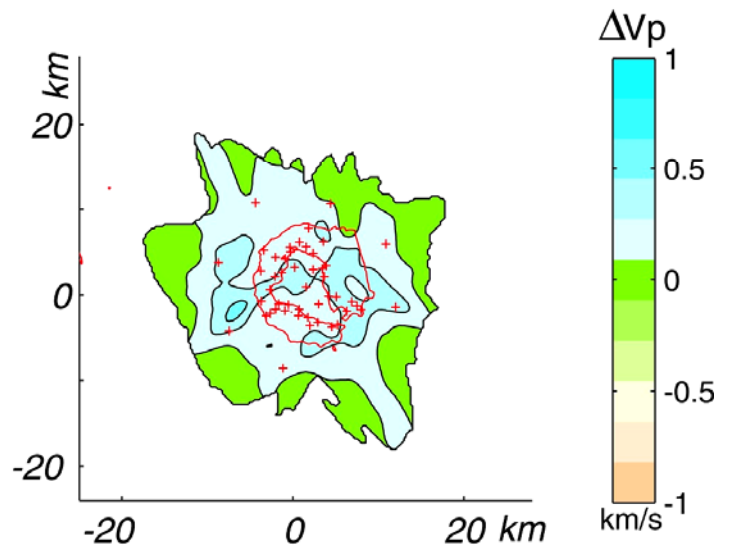
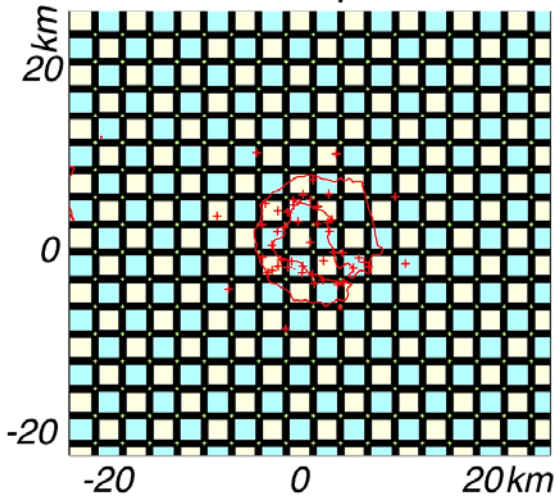


Figure 4.34 Checkerboard test for the sparse inversion (0.5 km spaced of perturbational grid). The map view of the starting synthetic model (left) and reconstructed model (right) shows the best resolved depths. Contour interval is 0.2 km/s. The red line represents the coast; the red crosses are seismic stations.

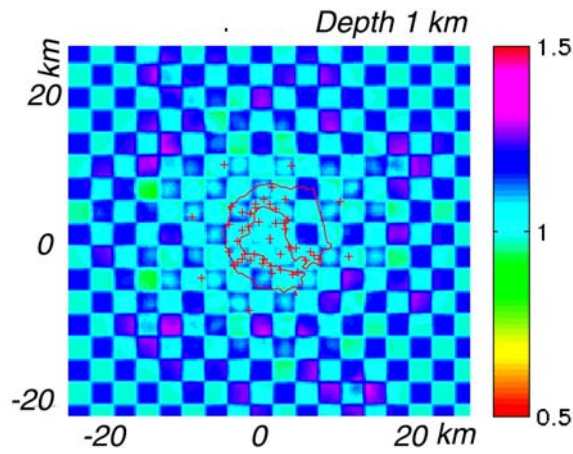


Figure 4.35 Checkerboard recovery rate for the sparse inversion (0.5 km spacing of perturbational grid). The map view is at 1 km depth and represents the ratio between the final recovered model and the starting synthetic model. The red line is the coast; the red crosses are seismic stations.

4.5.4.2.2. Dense Inversion

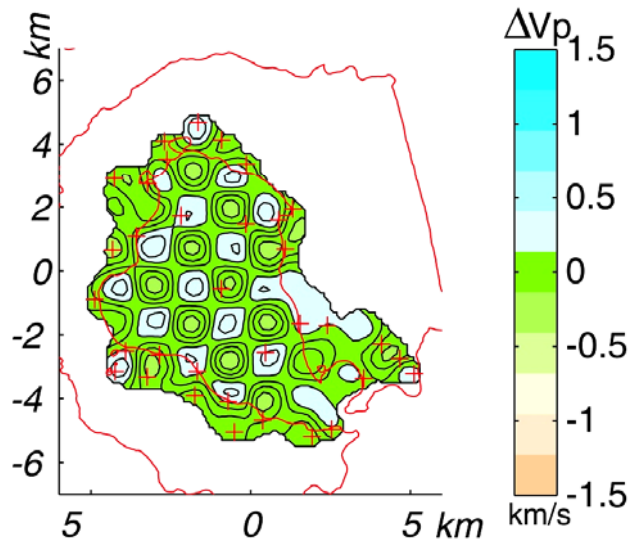
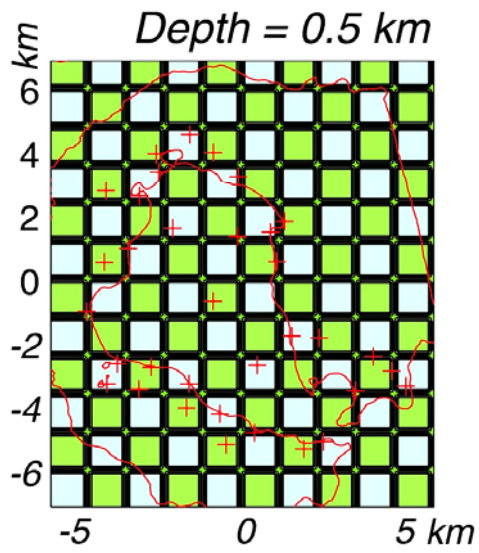
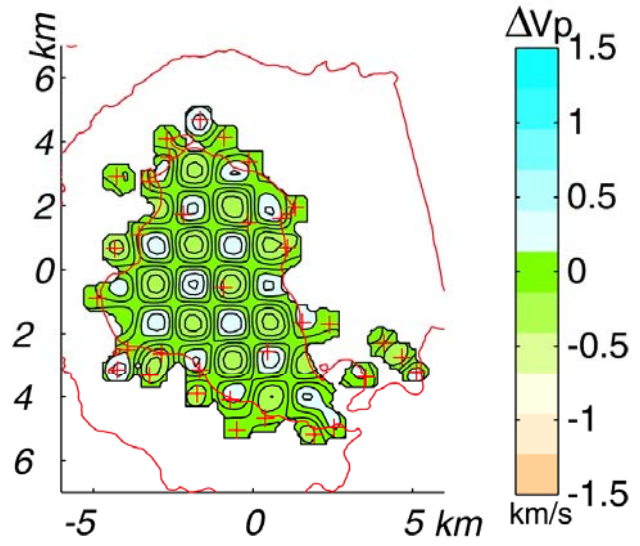
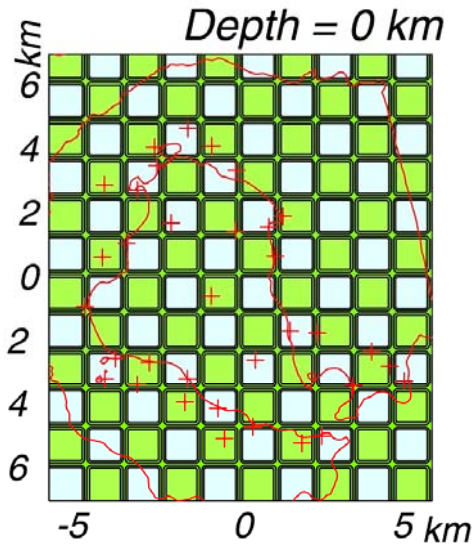
The checkerboard test was used to evaluate the resolution of the dense inversion, which included the vicinity of Port Foster. This was necessary in order to understand the resolution for the small-scale structures that the dense inversion produced. We produced a synthetic model with 1 x 1 x 1 km smoothed anomalies, that were 10% faster and slower with respect to the starting model.

Firstly, we observe very good recovery for the checkerboard pattern for layers shallower than 1 km (the first layer of perturbation nodes) (**Figure 4.36**). As expected, at this depth only anomalies in the bay or close to coast stations are well resolved. The strength of the recovered anomalies is well reconstructed, almost perfectly for the centre of the cuboids. If we plot the recovery rate as ratio between recovered model and original model, we observe that it is mostly close to 1, always between 0.83 and 1.24, with mean of 1.0153 and standard deviation of 0.0783 (**Figure 4.37**). As for the sparse inversion, the highest similarity between recovered and expected model occurs within the central region.

In order to test what is the relationship between the recovery of anomalies and their polarity, we performed an additional checkerboard test that was identical to the previous except that the sense of the anomalies was flipped (**Figure 4.38**). In this way we can explore the performance of the code at different locations and how it manages anomalies of opposite sign. Our results show that the resolution does depend on the sign of the anomaly. We explain this different behaviour as the tendency of the ray tracer (which is directly based on Fermat's principle of shortest time) to force ray paths to enter high velocities and avoid low velocity regions and thus changing the recovery ability. In any case, we conclude from this result that this kind of synthetic test can just give us an idea of resolution, which remains in any case, sign, shape and position-dependent.

We also observe that the code returns anomalies to 1-1.5 km depth, that are strongly smeared in the SE of the bay, where anomalies show a systematic NW-SE elongation.

4 - Deception Island



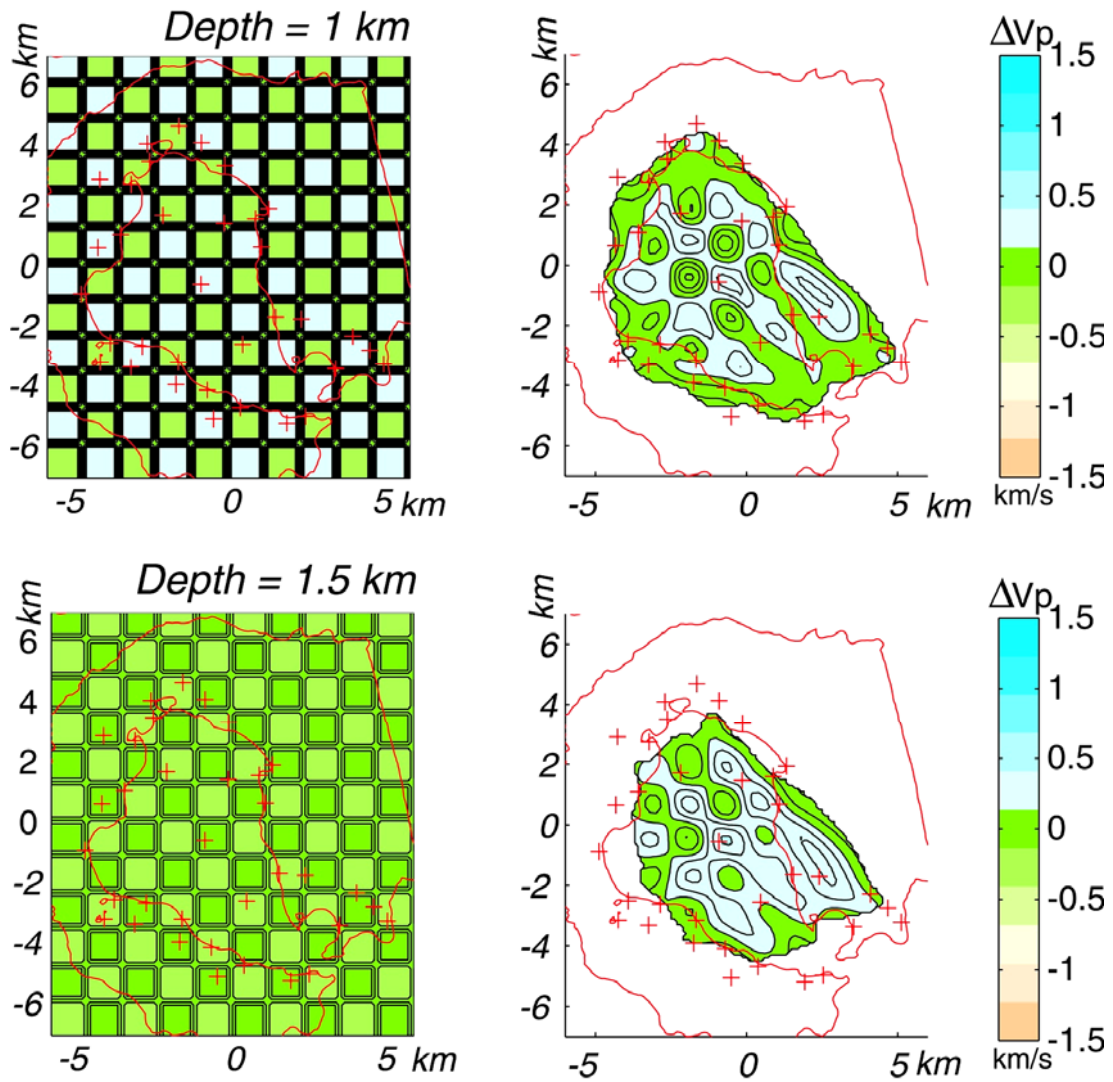


Figure 4.36 Checkerboard test for the dense inversion (0.2 km perturbational grid). The map view of the starting synthetic model (left) and of the reconstructed model (right) shows the best resolved depths. Contour interval is 0.1 km/s. The red line is the coast; the red crosses are seismic stations.

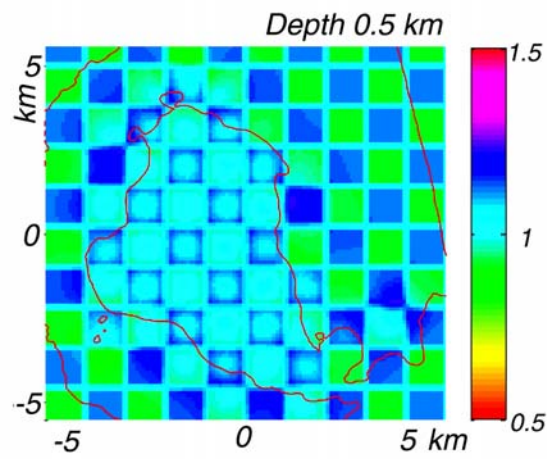
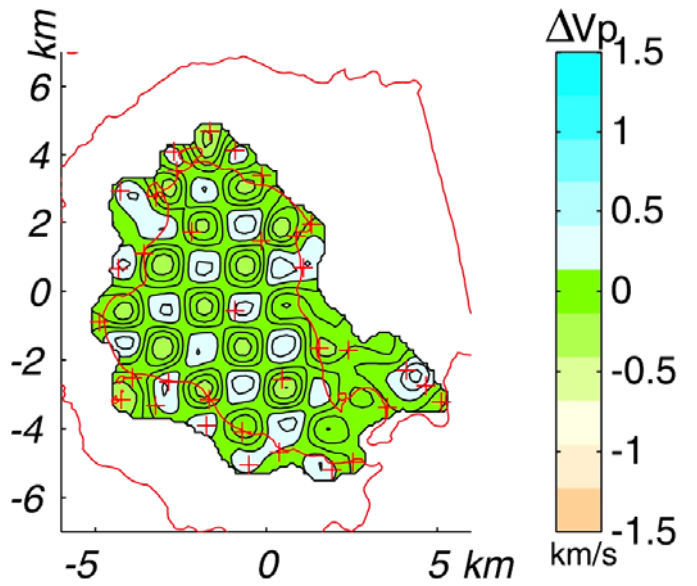
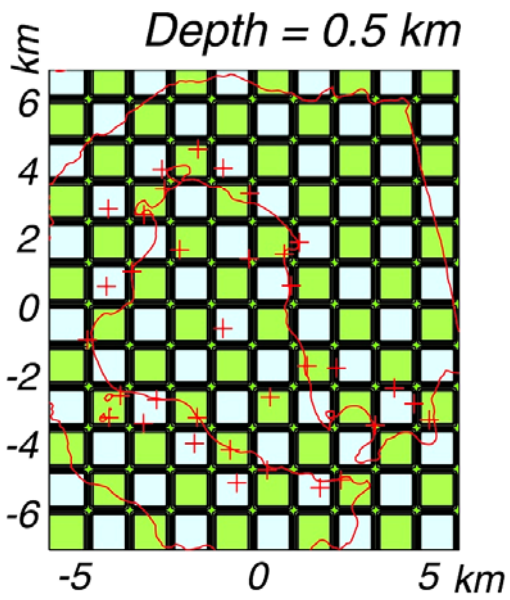
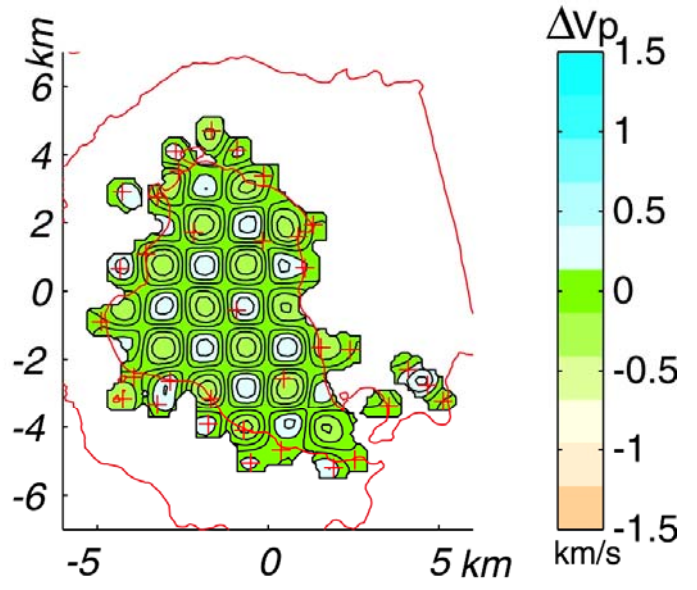
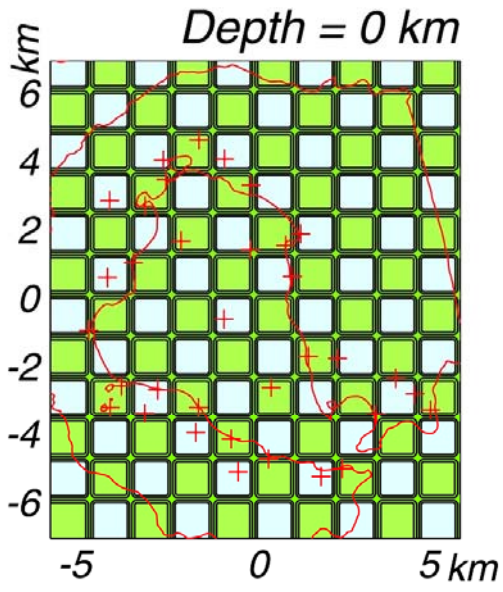


Figure 4.37 Checkerboard Recovery rate for the dense inversion (0.2 km perturbational grid). The map view is at 0.5 km depth and represents the ratio between the final recovered model and the starting synthetic model. The anomaly pattern is equal to that of **Figure 4.36**. The red line represents the coast.



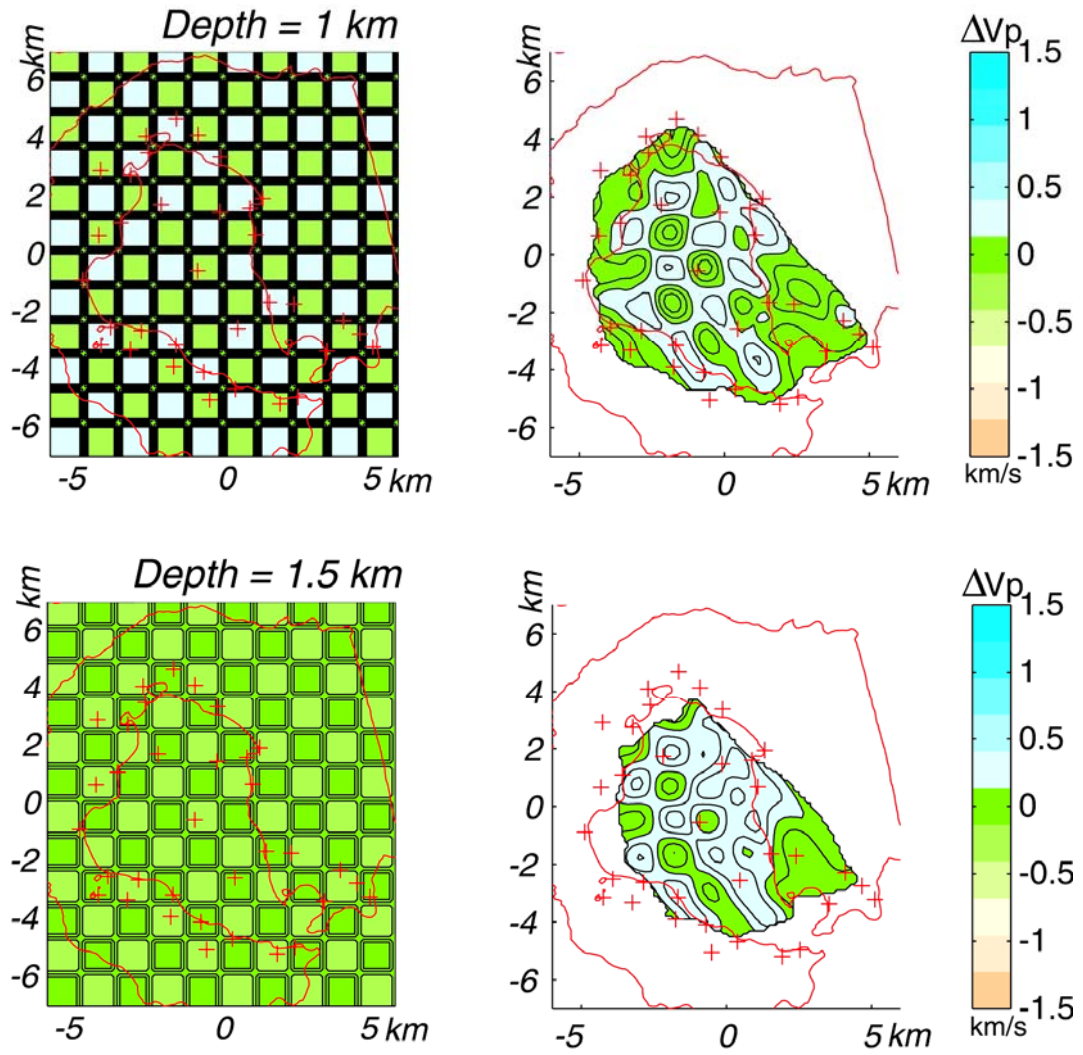


Figure 4.38 Checkerboard test for the dense inversion (0.2 km perturbational grid) with inverted scheme with respect to **Figure 4.36** (see text for explanation). The map view of the starting synthetic model (left) and of the reconstructed model (right) shows the best resolved depths. Contour interval is 0.1 km/s. The red line represents the coast; the red crosses are seismic stations

4.5.4.3. *Impulse Response Test*

In order to focus on the inversion code's resolving capability for specific locations inside the studied volume, where the main anomalies are, we performed the impulse response synthetic test. We introduced anomalies into a synthetic velocity model at the locations where we wanted to study the resolution and we calculated synthetic traveltimes which were then used as input data. We applied this approach to three main anomalies, which, as presented in the final discussion, are especially interesting for the tomography interpretation. In particular, we considered a low velocity in the middle of Port Foster, a high velocity in the NW sector of the island and a high velocity to the SW of Neptune Bellows.

4.5.4.3.1. *Spike-Low Velocity in Port Foster*

The first synthetic model has a smoothed, low-velocity anomaly (70% of the starting value) located in the middle of the bay, extending 4 x 4 km in the horizontal plane and across the whole volume in depth. We calculated synthetic traveltimes for the same configuration of shots and stations as was used in the true inversion. We added to these synthetic traveltimes a random noise that was proportional to the inversion error and we inverted these synthetic data. We used the same starting model, parameters and number of iterations as for the real inversion. The first observation from the inversion result concerns the lateral resolution of the inversion (**Figure 4.39**). In the shallower layers (the top 2 km), we observe that the anomaly is perfectly reconstructed in terms of position and limits, with an intensity that is close to the original value (approximately 5% faster than the original). Between 2 km and 4.5 km, the recovered anomaly is still present with intensity that is weaker than its original value, while the surrounding perturbations appear to dominate. By contrast, the vertical reconstruction of the anomaly is not complete. It stops at a depth shallower than 5 km, while the original spike extends deeper. This observation is important because, if it is not due to limits of the test itself, it demonstrates that our

code/data can not resolve low velocity anomaly at depth greater than, conservatively, 4.5 km. For this reason we probably are not able resolve the deeper levels of a low velocity anomaly located in the middle of the bay.

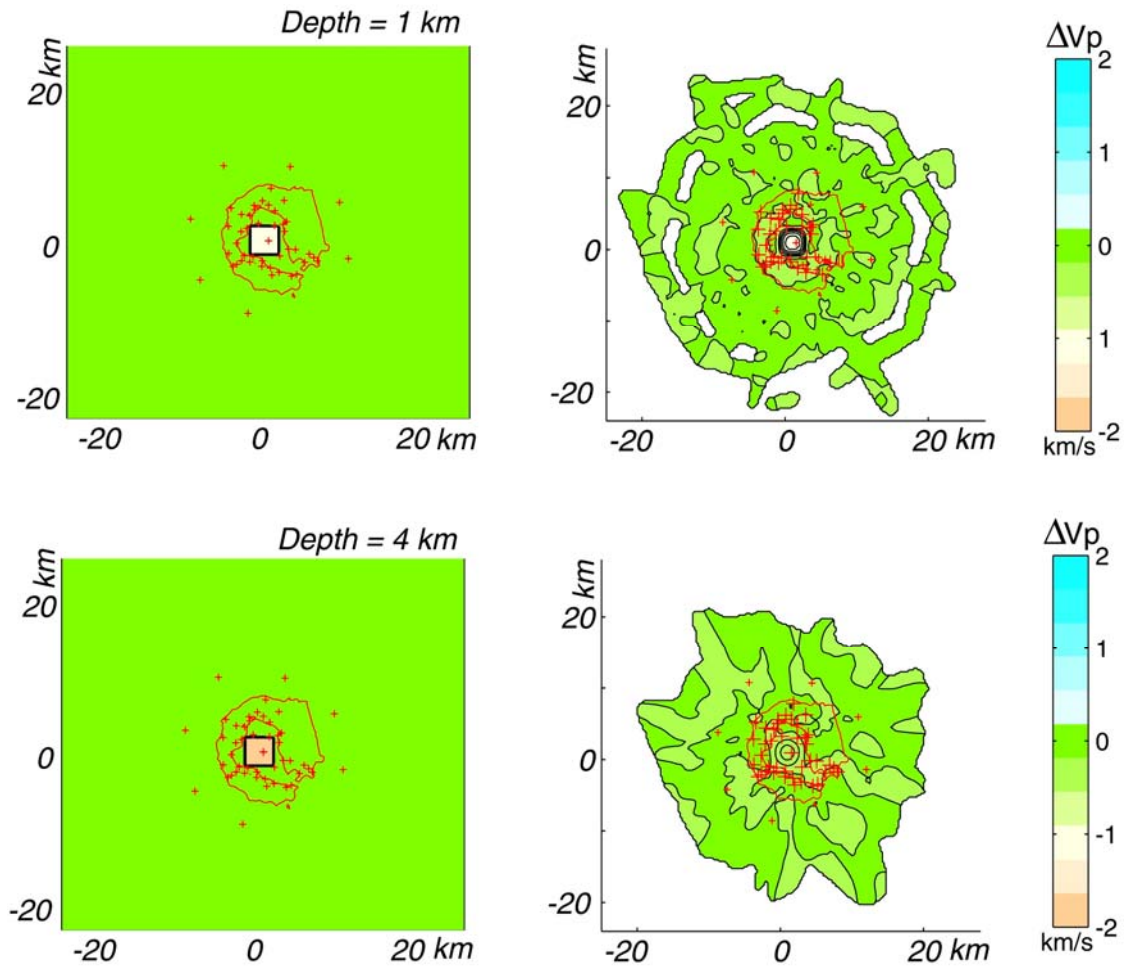


Figure 4.39 Impulse Response test for the sparse inversion (0.5 km perturbational grid). The map view of the starting synthetic model (left) and of the reconstructed model (right) shows a well resolved depth and the depth at resolution limit. Contour interval is 0.2 km/s. The red line represents the coast; the red crosses are seismic stations.

4.5.4.3.2. *Spike-High Velocity in the NW*

We performed a similar test for a high velocity anomaly in the NW corner of the studied volume. Synthetic traveltimes were calculated in an artificial model that had a strong positive anomaly in its NW corner, and smoothed edges, and was superimposed on the usual starting model.

The results indicate that the lateral contrasts are fully recovered and there is very little smearing of the limits of the high velocity anomaly (**Figure 4.40**). The intensity of this high velocity is well reconstructed, at least for the central portion. About the resolution in depth, we observe that the high velocity corner (originally crossing the entire depth range) is returned by the code with a sharp boundary to a depth greater than 5 km. This observation suggests that a similar anomaly observed at a similar depth in the true tomographic image would likely be real. We also see perturbations within the reconstructed high velocity region that were not in the original input model. These perturbations are artefacts and some of them (those aligned parallel to the contact) are probably introduced by the code, as result of its inability to recover sharp limits.

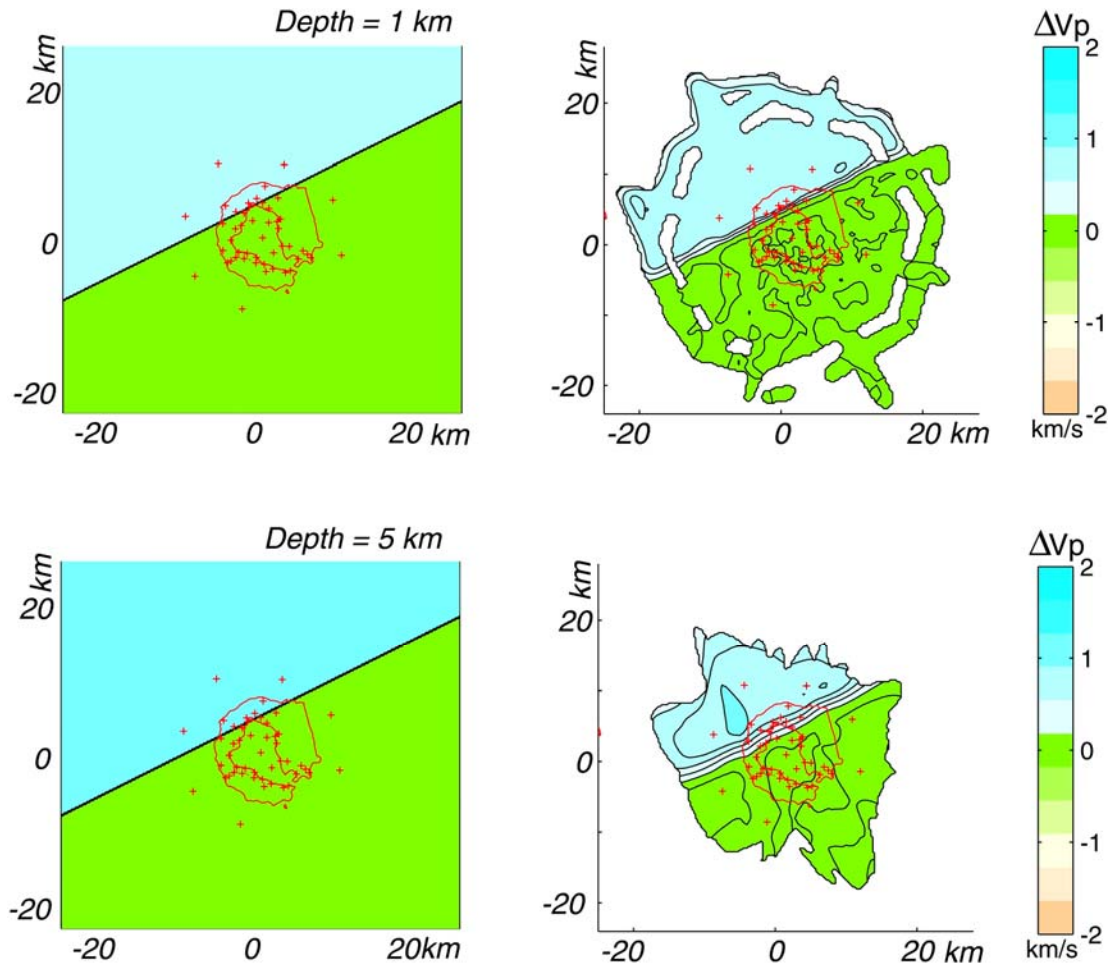


Figure 4.40 Impulse Response Test for the sparse inversion (0.5 km perturbational grid). The high velocity anomaly stands at the NW of Deception Island. The map view of the starting synthetic model (left) and of the reconstructed model (right) represents a well resolved depth and the depth at resolution limit. Contour interval is 0.2 km/s. The red line represents the coast; the red crosses are seismic stations.

4.5.4.3.3. *Spike-High Velocity at Neptune Bellows*

We also tested an isolated high velocity anomaly located SE of Neptune Bellows (**Figure 4.41**). We calculated synthetic traveltimes for a model with a spot like anomaly of +15%, 5 x 5 km wide and present at all depths. We inverted the travel times using similar parameters as before and we compared the reconstructed model with the synthetic one. The shape of the anomaly is perfectly reconstructed in the horizontal plane to 5 km depth, where it becomes more rounded (but still persists to 7.5 km depth). For amplitude, the recovery ratio between the reconstructed model and the synthetic model (not reported) is essentially stable at approximately 1 from 0 to 4.5 km depth, below which the recovered amplitude is reduced.

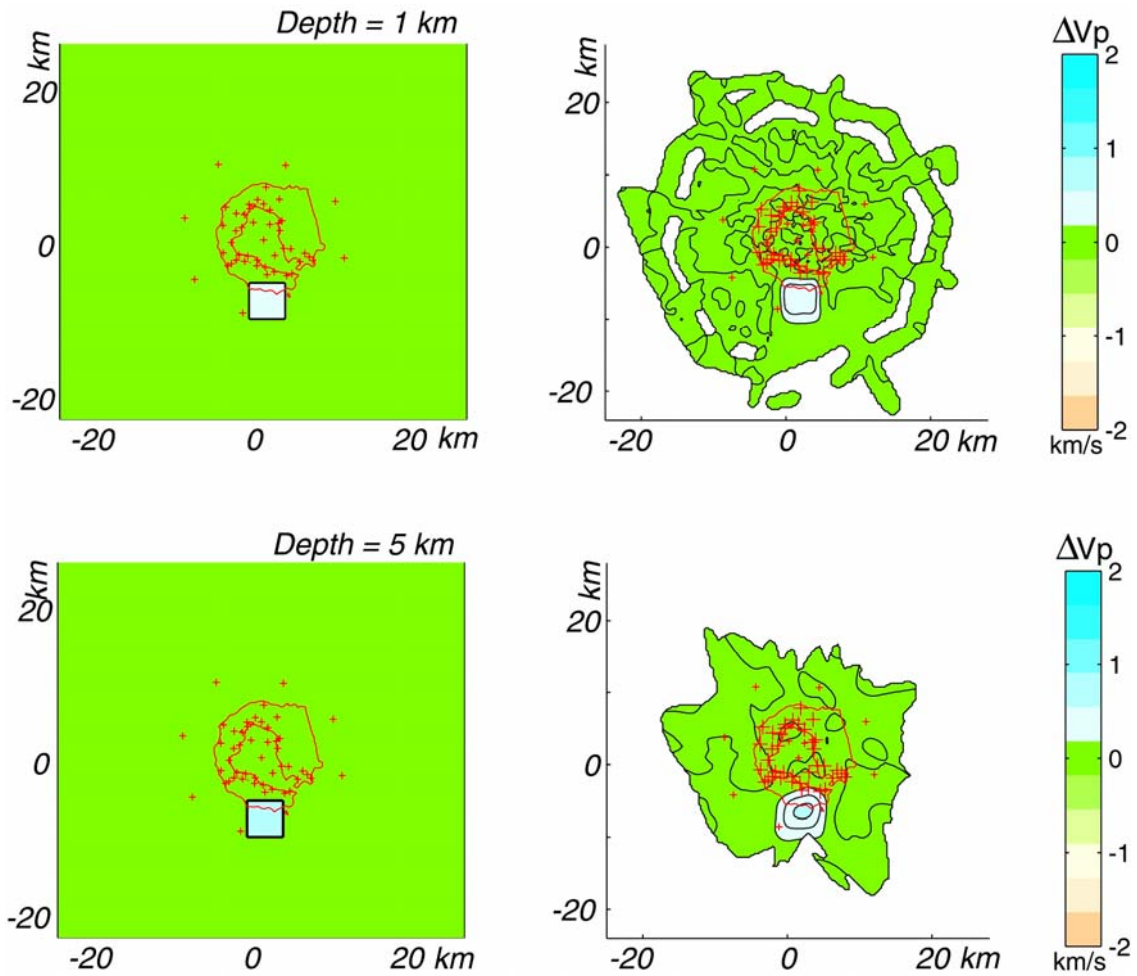


Figure 4.41 Impulse Response test for the sparse inversion (0.5 km perturbational grid). The high velocity anomaly is located close to Neptune Bellows. The map view of the starting synthetic model (left) and of the reconstructed model (right) represents a well resolved depth and the depth at resolution limit. Contour interval is 0.2 km/s. The red line represents the coast; the red crosses are seismic stations.

4.5.4.4. *Reconstruction Test*

This test explores the ability of the database and code to image a realistic seismic structure. In this case, we considered as synthetics the same seismic anomalies as those of the true model, which are at the origin of the observed-calculated traveltimes misfits. We ‘traced’ ray paths through the final three dimensional model, for the same configuration of stations and shots as we used in the true inversion. Then we added random noise to the travel times. In a second step these traveltimes were used as input data for the inversion which used the same starting model, parameters and number of iterations as the true inversion. As a result (**Figure 4.42**), we observe that the main anomalies are similar to these of the known velocity structure, in sign, intensity, position and shape. The maximum resolved depth depends on the anomaly. In particular we recognize the low velocity in the inner bay, which is recovered until 4.5 km depth, albeit with decreased intensity. The high velocity NW corner is also well recovered, at all depths, as are the main heterogeneities within it. Other low velocity perturbations are retrieved with somewhat less fidelity.

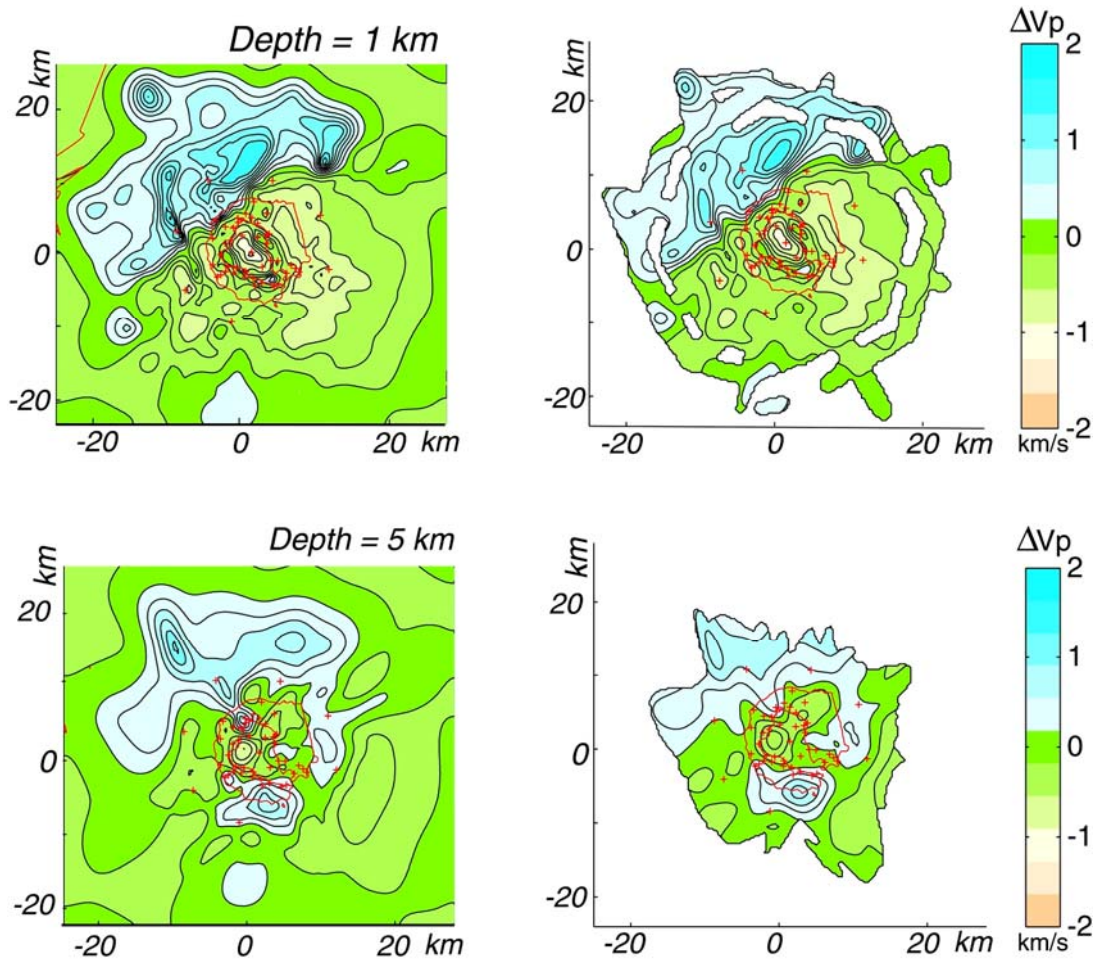


Figure 4.42 Reconstruction test for the sparse inversion (0.5 km perturbational grid). The synthetic model is equal to the true final model. The map view of the starting synthetic model (left) and of the reconstructed model (right) shows a well resolved depth and the depth at resolution limit. Contour interval is 0.2 km/s. The red line represents the coast; the red crosses are seismic stations.

4.5.4.5. *Spike on Reconstructed Image*

We assumed that the best approach for understanding the resolution of the inversion method is to use the final model as synthetic model instead of any artificial structure, which may be unrealistically far from reality (4.5.4.4). Another interesting test, in this philosophy, was performed by introducing spot-like anomalies into the final 3D model. We wanted to use a realistic structure in order to observe how the code reproduces specific anomalies using ray paths that are as close as possible to those used for the real data. For example, to check the performance of the code for the low-velocity region within the inner bay, we superimposed on the final model, the same perturbation as we used in the spike test. We then ray traced to produce the synthetic traveltimes dataset. We used these data (with noise added) to observe the ability of the code to retrieve the anomaly. The position of the anomaly (**Figure 4.43**) is well resolved and moreover the amplitudes are better resolved in this test than in the comparable spike test superimposed on the starting model. In depth, we also observe that the code can recover the spot to nearly 5 km depth, which is significantly better than the simple spike test. Our only concern regards the shape which is still rounded and smoothed by the inversion. In any case, this test clearly indicates that the anomaly is better resolved over a greater depth range when the ray paths appropriate for the real model are used. But the true vertical extension of the anomaly is still not recovered in its whole depth range.

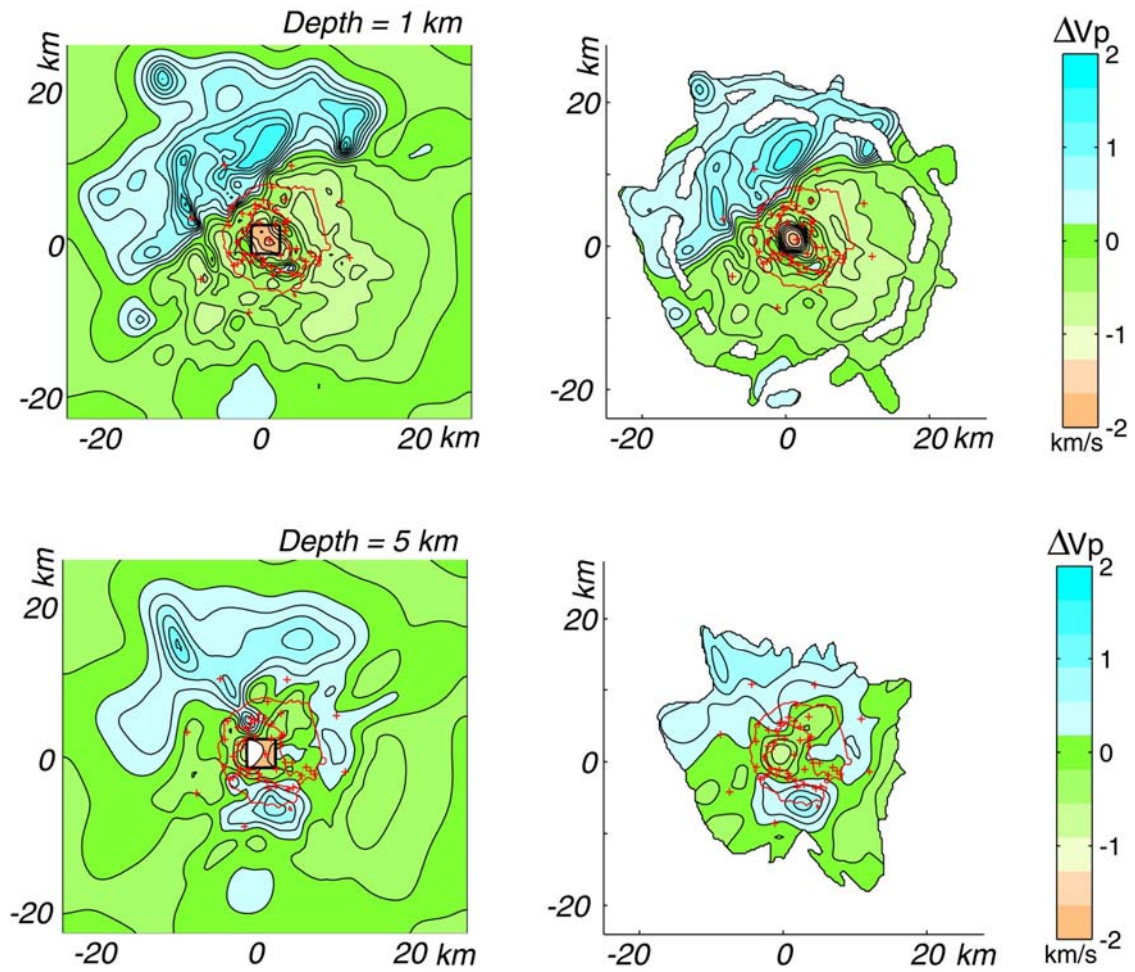
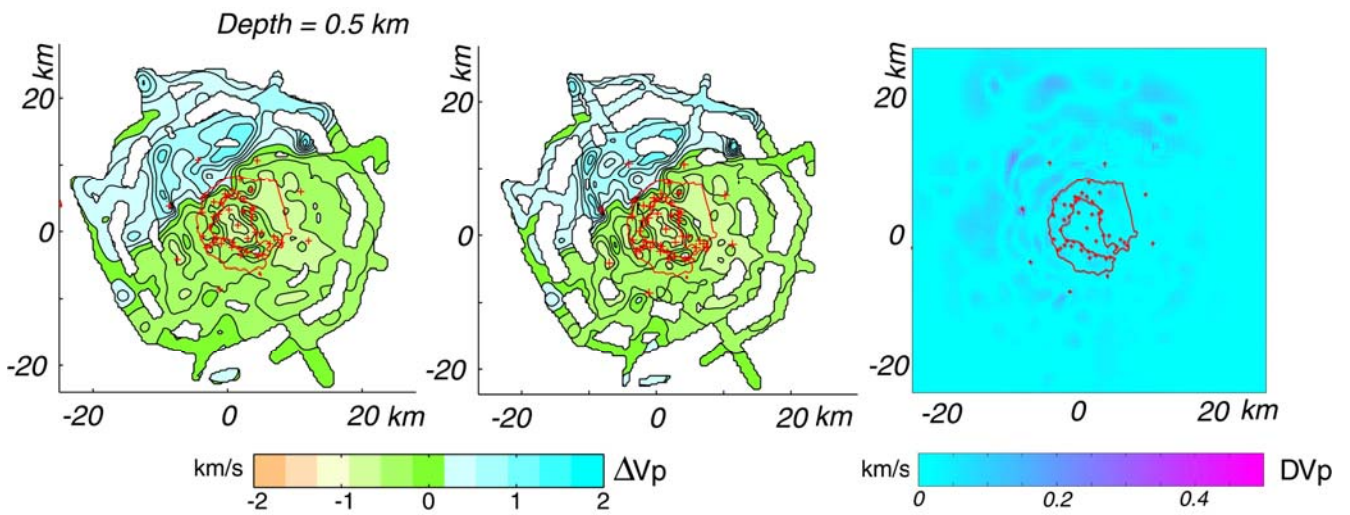


Figure 4.43 Spike on Reconstructed test for the sparse inversion (0.5 km perturbational grid). The synthetic model is equal to the true final model with a low velocity spike in the center of Port Foster. The map view of the starting synthetic model (left) and of the reconstructed model (right) shows a well resolved depth and the depth at resolution limit. Contour interval is 0.2 km/s. The red line represents the coast; the red crosses are seismic stations.

4.5.4.6. *Shifted Grid Test*

As an additional test to check the influence of the grid parameterization on tomographic image, we shifted the grids (of perturbations and also of traveltimes calculation) laterally in both directions by repositioning each node by one-half node spacing in both x and y directions. In a qualitative comparison of the final tomographic images, we observe slight changes only in the shapes of smallest anomalies in the sparse grid (**Figure 4.44**, above, left and center). Otherwise the dense inversion does not show any change (**Figure 4.44**, below, left and center). Moreover, we must note an interesting feature of the shape of the low velocity anomaly on the west coast of Deception Island. At 0 and 0.5 km depth it coincides with the Costa Recta in the shifted grid inversion. If we interpolate the un-shifted final model at a cell grid used for the shifted one, we can plot the difference between the final interpolated model and the shifted model, as absolute differences in velocity (**Figure 4.44**, right). We confirm that the overall difference is low.



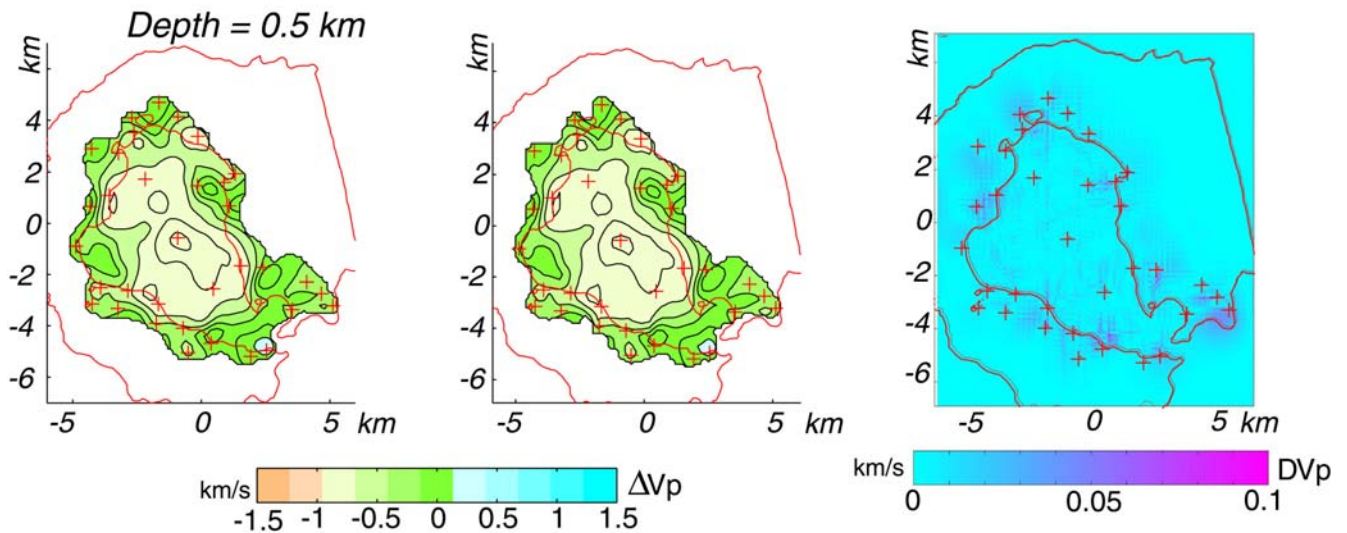


Figure 4.44 Shifted Grid test for the sparse inversion (above) and for the dense inversion (below). Map view shows at 0.5 km depth the true final model (left, contour interval 0.2) and the model resulting from a shifted grid inversion (center, contour interval 0.1). In both cases the right-hand figure shows the difference between shifted and un-shifted models at the same depth.

We conclude from this test that the grid parameterization does have an effect on the final result, but the grid spacing is more important than the grid position. For the 0.25 km perturbation grid, the uncertainty due to this effect is negligible; for the 0.5 km perturbation grid it is more important. In any case, if the scale of the interpreted anomalies is significantly greater than the grid spacing, this effect can be neglected for both the sparse and dense grid.

4.5.5. Starting Model

The choice of the initial model is an important step in any linearized inversion study (Chapter 2.2.2.) since an inappropriate starting model may not allow the algorithm to converge on the best solution. The starting model is often the

result of a previous one dimensional inversion of the same dataset. The same code can be used to obtain a 1D model, by modifying the perturbational grid from 3D to the 1D performance. In our case, due to the distribution of seismic ray paths, only the shallowest kilometres were sampled. As we could obtain a 1D model only for these shallowest layers, we used another approach.

Deception Island lacks any measured ‘a-priori’ velocity model at regional scale, and only velocity structures obtained from previous geophysical campaigns were available. These were derived from seismic profiles, and sometimes integrated with gravimetric and magnetic data. Because none of them corresponded exactly to our zone, we decided to test several of them and to demonstrate insensitivity of the inversion to the starting model by ensuring that they converged to similar results. With this intention, we averaged or ‘sampled’ published 2D profile to obtain a 1D model or we directly introduced the 1D profiles when possible. We then performed a 3D inversion and we depth-averaged its result. We chose the 1D starting model that was closest to the averaged final-1D model, and which gave the best fit (lowest RMS) in the 3D inversion.

From seismic models (4.3.5), we considered:

- (1) The result of the regional (1997) and local (1992) seismic refraction investigations of Grad (as ‘Grad’). Following this author, we simplified the local velocity 2D velocity model along the south-to-north profile that crossed the island (the POP-LIV seismic line) for the shallowest layers and we integrated it with results of the regional profile (DSS-20) of 1997 paper, which passes close to the island.
- (2) The model derived from the Christeson et al., (2003) averaged 1D velocity structure from the OBS line 2 (as ‘Chris1D’). We compared it with the 2D result from the same line, which overlaps our region at its SW end.
- (3) Four 1D profiles extracted from 2D models of Ashcroft (1972). Among them, ‘Ash17’ is a 1D model derived from the Ashcroft seismic line 17 (extending between Deception Island and Livingstone island, 65 km long). Similarly, ‘Ash16’ is taken from seismic line 16 that extends to the SW from Deception Island (65 km long). ‘Ash22’ refers to seismic line 22, which extends 20 km to the southwest of Deception Island. Finally, ‘Ash30’ is derived from a seismic 2D model for the interior of Port Foster, to 2 km depth, and integrated with profile 17 for deeper layers.
- (4) A starting model derived from the Christeson 1D model but modified: it was used as starting model for a 2D inversion with the same code and a subset of the *TOMODEC* data along an EW seismic profile (Ben-Zvi, personal communication). This result was averaged to obtain a new 1D model that we call ‘ChrisTa’.

The 3D results of the inversion of these starting models show almost the same positions and shapes for the major anomalies (**Figure 4.45**). Instead, depending on the starting model, absolute velocity intensities changes from model to model. To quantify such differences, we extracted a 1D model from the 3D result, as average of the cells with higher DWS (with an averaged value higher than 100). We then compared starting and 'final' models for these samples (**Figure 4.46**). Especially for three cases ('Ash17', 'Ash30', 'Grad'), in the final 1D model appear unrealistic velocity inversions, at 1.5 and 2.5 km depth. Although there may be local velocity inversions beneath Deception Island, regional inversions are not likely. We suspected that these velocities are so far from the real data that the inversion finds it easiest to compensate by introducing an inversion at shallower depths. We decided that this can constitute a good reason not to accept these three models (Ashcroft 17, Ashcroft 30, and Grad) as starting ones.

For the Ashcroft 22 model, a great difference of the starting 1D with respect to the real data can be at the origin of the incapability of the code to adjust traveltimes and, so, of the big final RMS for the inversion that uses this starting model. What we observe is that substantially the initial model is slightly changed by the inversion.

The remaining three models (Chris1D, ChrisTa and Ash16) show good performing. And actually the final velocity perturbations are similar each other. So, we decided to select one of them on the base of the final RMS and the speed the inversion can converge toward the minimum of these values. Moreover, the Ashcroft16 result has a bit more instable behaviour, with slight tendency to introduce velocity inversions. Our final selection supported the Christeson model, as averaged by a 2D inversion.

4 - Deception Island

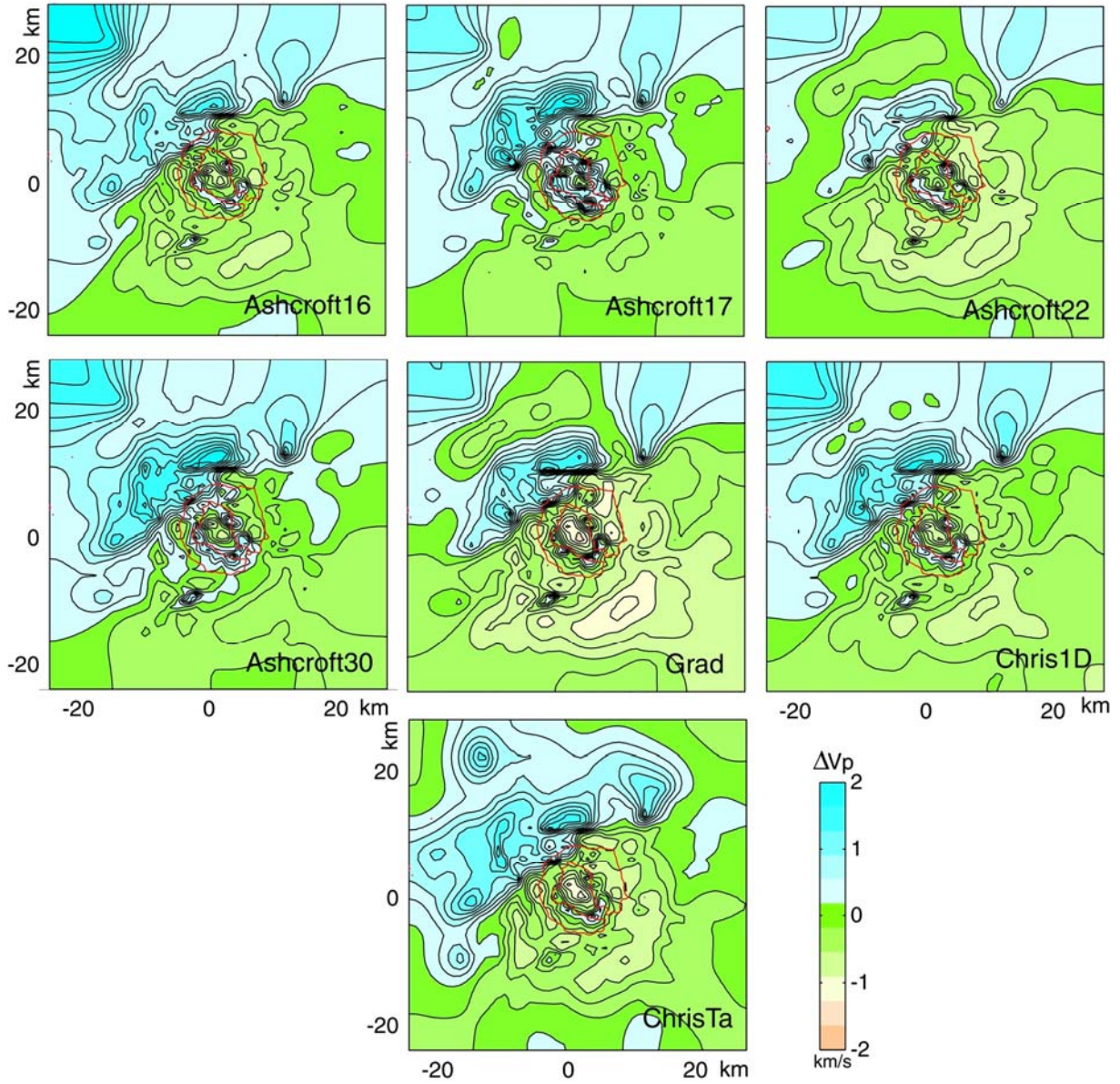


Figure 4.45 Starting velocity model selection. The result of the 3D inversion for each tested model is presented as section at 1 km depth. Contour interval is 0.2 km/s. The red line represents the coast

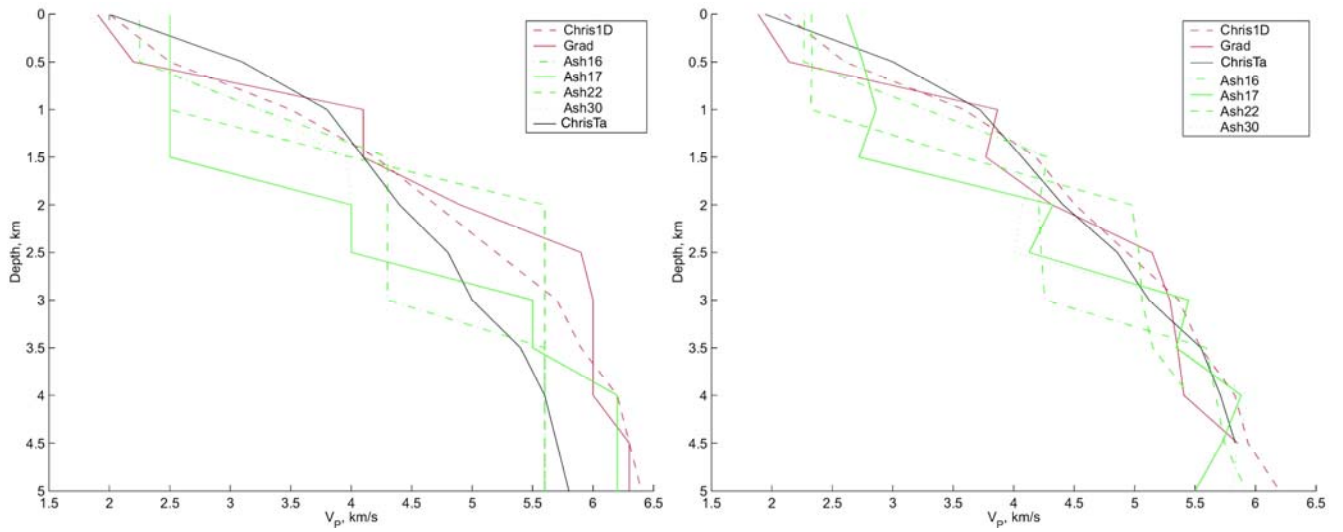


Figure 4.46 Starting velocity model selection. Initial 1D models (left) are compared to the 1D average (no weighted for coverage values) of their 3D inversion result (right).

4.6. Results

4.6.1. Description of Results

Traveltime data obtained during the 2005 seismic survey at Deception Island were inverted using the code developed by Toomey [Toomey et al. 1994] (Chapter 2). As discussed above, the code has been applied with two different grids, in order to study the entire region around Deception Island using a relatively sparse grid and to focus on the inner bay (Port Foster) using a more accurate dense grid.

Convergence of the tomographic inversion to a stable solution was obtained after 6 iterations, when the root-mean-squared (RMS) data misfit was reduced by 80% from 247 ms for the starting model to 52 ms. For the denser grid, the inversion result was also stable after 6 iterations, with a RMS reduction from 260 ms to 34 ms. Results from both grid configurations were used to imagine the overall velocity structure of Deception Island and surrounding region

The final velocity model strongly differs from the starting 1D structure, somewhere more than 50% in isolated positions. Although the velocity perturbations are strong, if we average the values of velocities across each layer, we observe that the horizontally-averaged 3D model has a distribution of velocities with depth that is comparable to that of the starting model (**Figure 4.47**). This indicates that the chosen starting model was a reasonable choice, but also that the real structure is highly heterogeneous and cannot be well modelled using a 1D velocity structure.

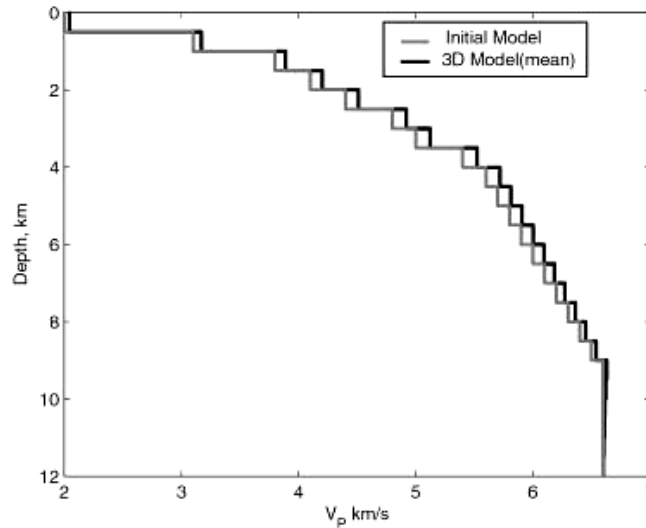


Figure 4.47 : Comparison of the initial 1D velocity model (grey line) and the averaged (for each 0.5 thick layer) of the final 3D velocity model (black line).

Several remarkable anomalies are present in the seismic structure, both at greater and smaller scale, beside zones not resolved which are left blank in **Figure 4.48**. The tomographic image is highly heterogeneous with a lateral variation of > 2 km/s between the surface and 5 km depth, for both grid configurations.

We observe a wide high velocity region that dominates to the NW of Deception Island (A1), and which is in sharp contact with low velocity zones. Other smaller high velocity anomalies are recognizable in the model, including the anomaly directly to the south of Deception Island (A2); the anomaly with a horseshoe shape which approximately follows the south coast of Deception Island (A3) and, finally, the anomaly to the west of the island that is centered on Sail Rock (A4). Low velocities are also present. The most pronounced is the anomaly which lies beneath Port Foster (B1), but low velocities also appear to the E and SE of the island (B2), and, finally, to its SW (B3). In the vertical direction, the overall appearance of the image (as defined primarily by the distribution of the major features) is mostly unchanged with depth. Although the positions of the main anomalies are relatively constant with depth, they do change in dimension and intensity. A detailed description of the main features of the image is as follows:

A1) This high velocity anomaly covers the NW corner of the resolved area, and is stable between surface and 5.5 km of depth. It is characterized by a sharp limit with a SW-NE direction, that appears linear until 2.5 km depth. The perturbation reaches its maximum strength between 1 and 3.5 km, and it is not horizontally homogeneous. There are at least three maxima, and two of them deform the rectilinear border by extending across boundary toward the SE.

A2) This spot-like anomaly appears at 1 km below the surface and widens in depth until losing its circular shape at 4 km, where it merges with the surrounding. Its amplitude remains stable to 2 km depth.

A3) This horseshoe shaped anomaly encircles the SE margin of Port Foster where it broadly matches the inner coast. Present from the surface to resolution limit depth, it merges with the A2 anomaly below 3-4 km depth. The strength is relatively stable from 0.5 km to greater depth.

A4) The location of this spot-like anomaly coincides with that of Sail Rock, from surface to the maximum resolved depth. It has a stable shape and dimension, with its highest value at 1 km of depth.

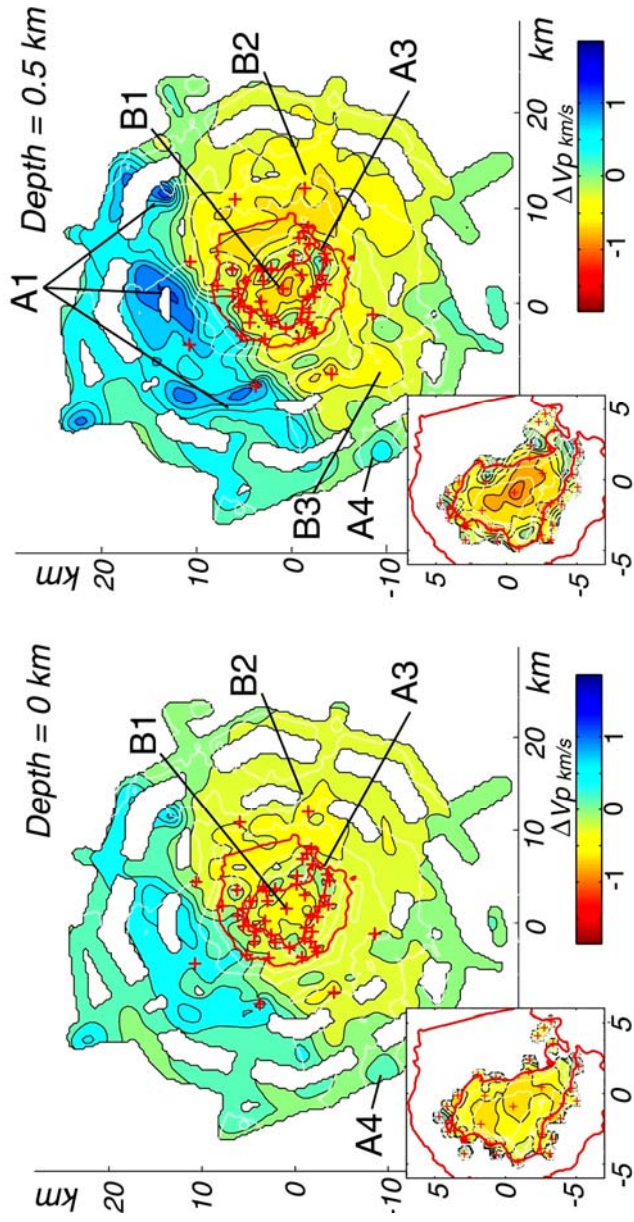
B1) This low velocity anomaly is located in the inner bay from the surface to 5.5 km of depth, i.e. throughout the entire resolved volume. Its maximum strength is reached at 1 km depth and maintained until at least 3.5 km, below which it seems to decrease. We use the solution for the denser grid inversion to image this anomaly in more detail between the surface and 1.5 km depth. At 0-0.5 km depth the anomaly is composed of several spots of higher intensity, located beneath the 1967 and 1970 eruption craters, and, inside Port Foster, in front of Black Glacier, of the Spanish Base and of Fumarolas Bay. At greater depths, these spots are organized in a single anomaly with an overall NW-SE elongation. Its shape is defined by high gradients and has relatively linear boundaries. In particular we note, among them, the NNW-SSE trending contours along the anomaly's eastern and western sides that are deflected in front of Pendulum Cove in a NE-SW direction and in Whalers Bay by a linear N-S contact.

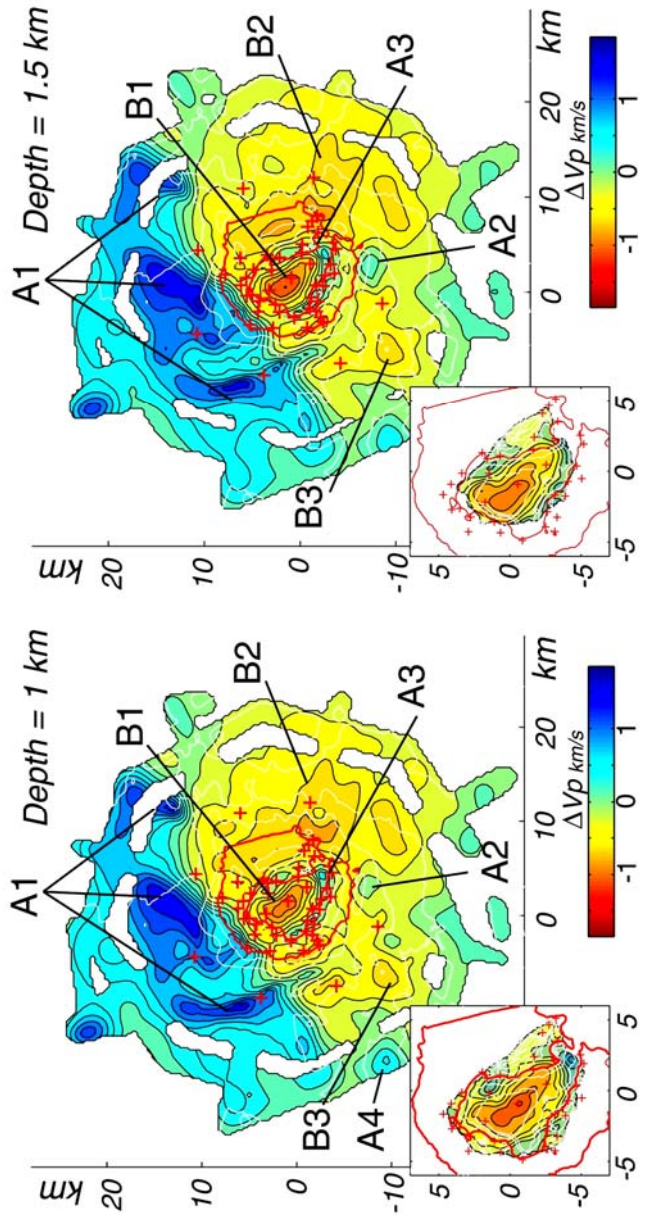
B2) This low velocity anomaly encompasses the eastern arm of Deception Island and extends offshore into the Central Bransfield Basin. Below 2.5 km depth it breaks into two main parts, one of them still below the island (and which disappears at 4 km of depth) and the other one located towards the SW corner of the resolved area. Maxima of intensity are reached close to Deception Island, between 1 and 3 km depth. The overall shape is strongly irregular but there is a slight correspondence with the shape of Costa Recta at 0.5 km depth.

4 - Deception Island

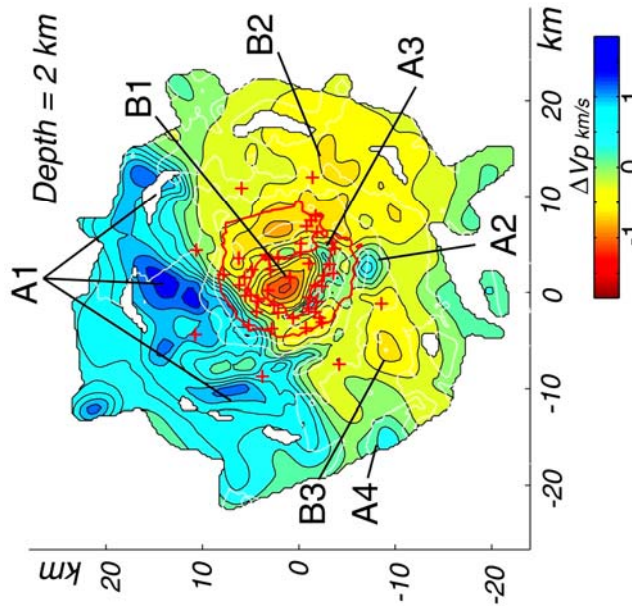
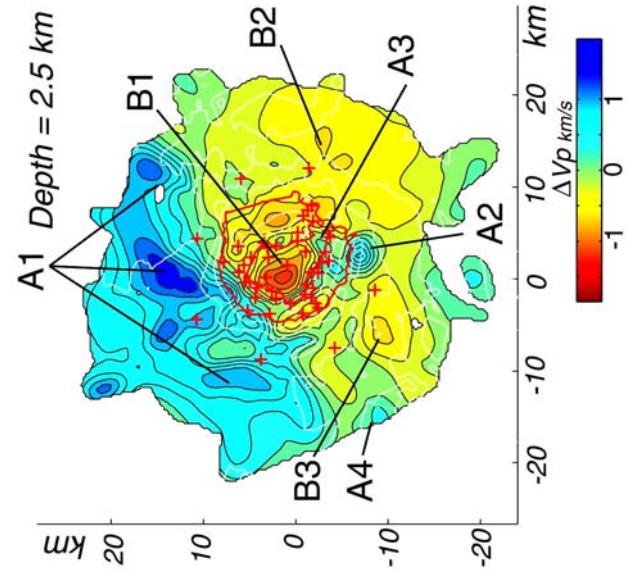
B3) This negative velocity perturbation extends to the SW of Deception Island extends from the surface (where its partly unresolved) to more than 4 km depth. The irregular shape near the surface changes to a cylinder-like body from 1 km to 2-2.5 km, where the maximum amplitude is reached.

4 - Deception Island

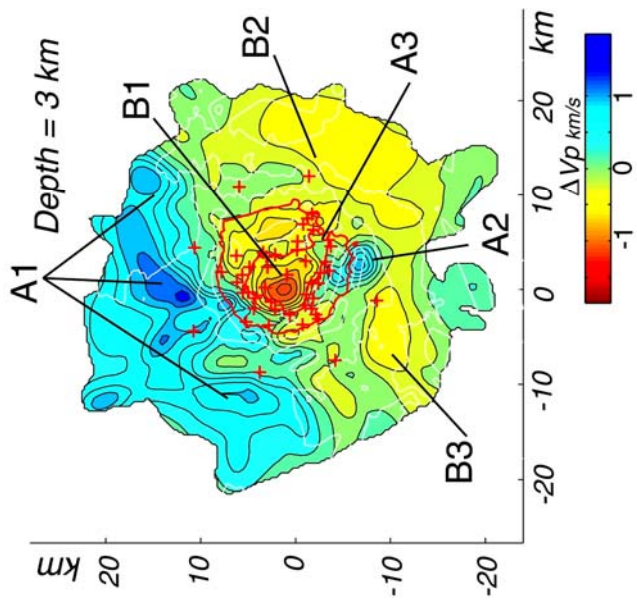
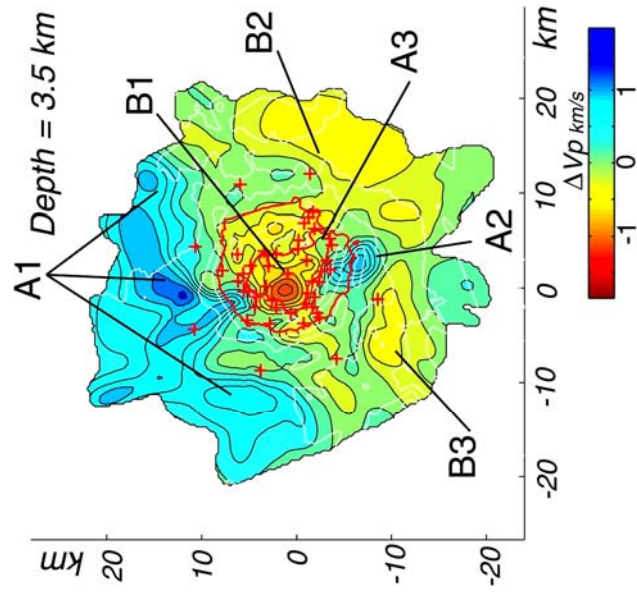




4 - Deception Island



4 - Deception Island



4 - Deception Island

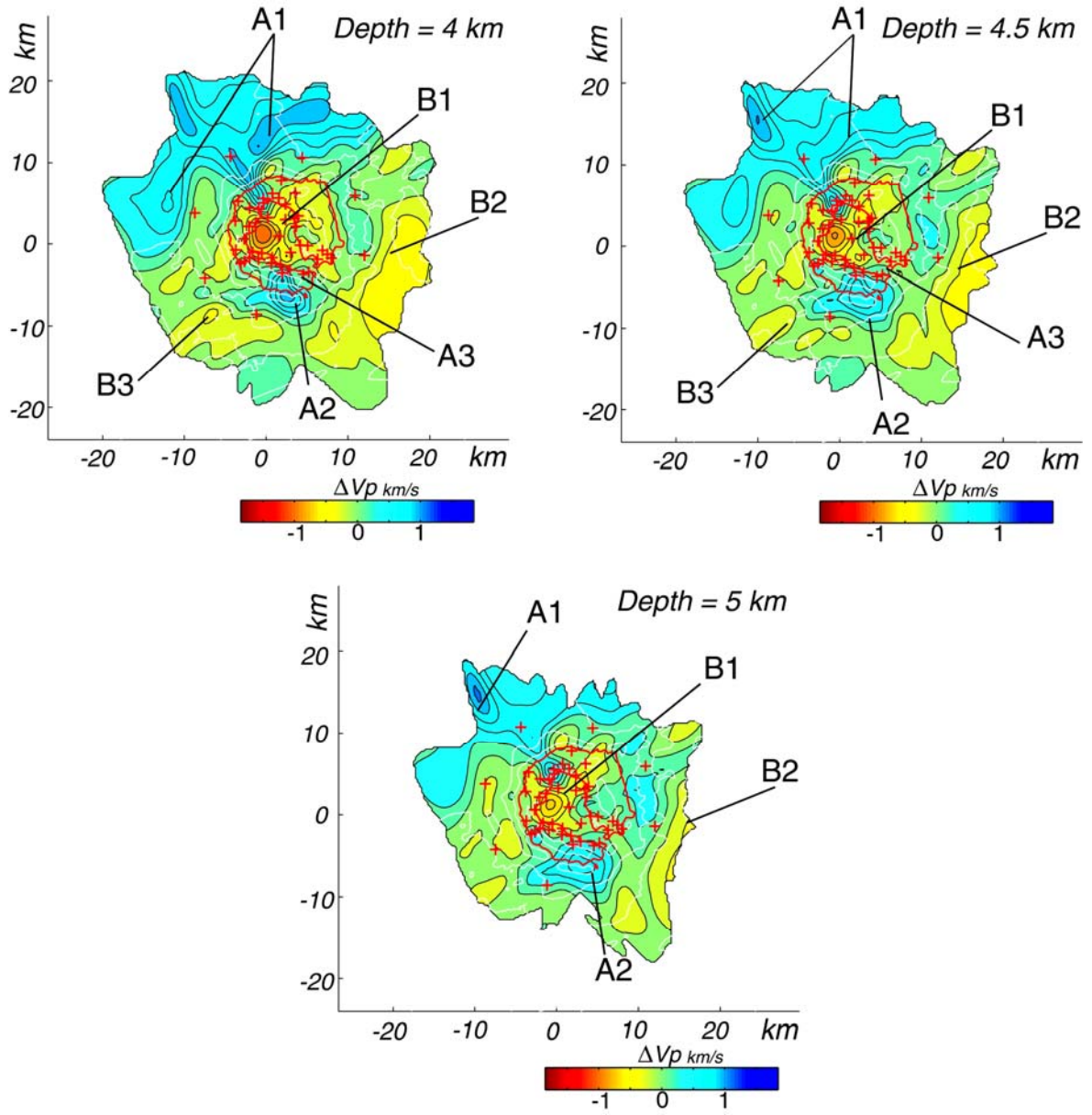


Figure 4.48 *P-wave velocity perturbations at several depths (indicated in figure). The coastline is outlined in red; crosses are positions of receivers. Contour interval is 0.2 km/s. The main figure and inset show results for sparse and dense grids, respectively.*

4.6.2. More about the Result Quality

4.6.2.1. 2D Profiles

The quality of the tomography results is mainly evaluated through the application of synthetic tests, as explained in Chapter 4.5.4. This is a common approach for establishing the stability of tomographic results and for separating true anomalies from artefacts. In the case of Deception Island the *TOMODEC* experiment data have been used for two other contemporary studies. At the moment, a 2D seismic tomography [Ben-Zvi et al. 2007] and a high resolution bathymetric survey [Barclay et al. 2007].are available. By comparison with these results we can further assess the resolution and quality of our 3D velocity image.

The 2D seismic profiles were collected along a NW-SE 92-km-long line and a NE-SW 55-km-long line, and both of them cross our study volume. However, because they also include data from the most distant air-gun shots and OBSs, their modelled ray paths sample deeper crustal levels. As a result, the maximum resolved depth is about 9 km beneath the center of the NW-SE profile and this permits us to constrain deepest features of our model which are poorly resolved. The main features observable in the NW-SE 2D profile (**Figure 4.49**), also confirmed in the NE-SW profile (**Figure 4.50**), are (1) a low velocity anomaly (as strong as -0.7 km/s at 3.5 km depth in the NW-SE profile, and -1 km/s at 2.6 km depth in the NE-SW profile) below the caldera. (2) a large high velocity perturbation (about 1.5 km/s) toward the northern end of the NW-SE section and in sharp contact with the low velocity of anomaly 1 (3) narrow high velocity anomalies that partially underlie the low velocities of the caldera and bounding it at the SE, in the NW-SE profile, and at the NE, in the

4 - Deception Island

NE-SW profile (4) a large low velocity feature beneath the south-eastern coast of Deception Island and offshore.(5) a pronounced high velocity region approximately 50 km to the SE of Deception Island.

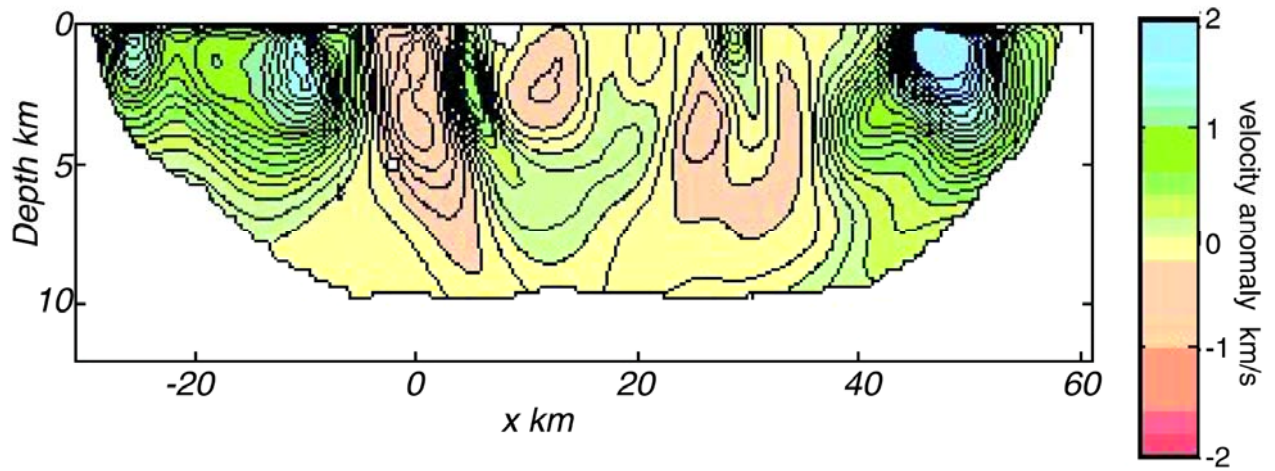


Figure 4.49 Two-dimensional perturbational model along NW-SE seismic profile. From Ben-Zvi et al.(2007)

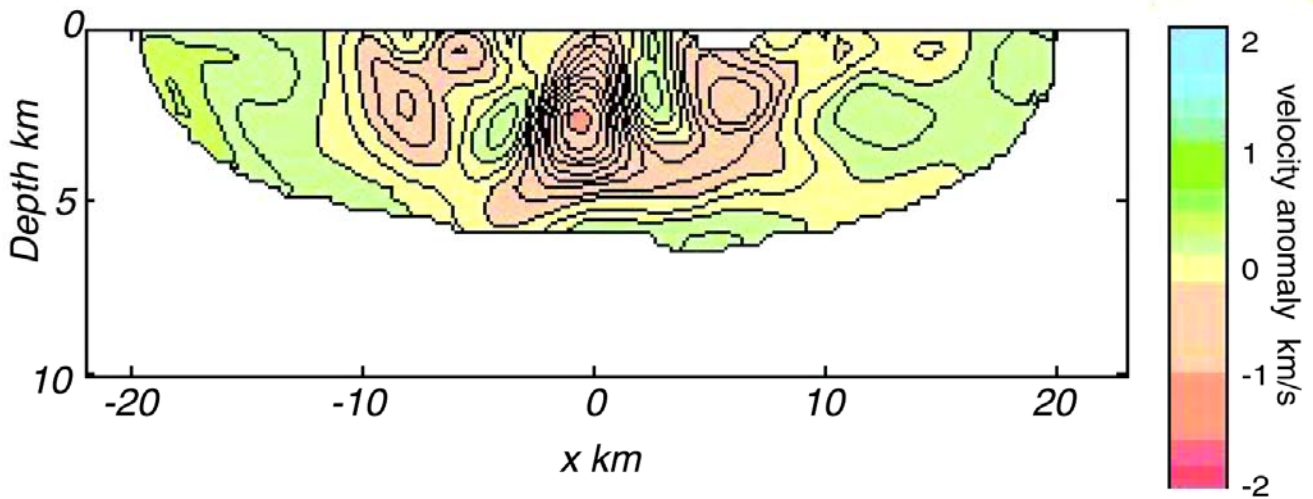


Figure 4.50 Two-dimensional velocity model along NE-SW seismic profile. From Ben-Zvi et al.(2007)

We note the striking correspondence of these results with our modelled anomalies, based on their position, shape and strength (**Table 2**).

| | | | | |
|---------------|------------------|---------|---------------------------|---------------------------|
| 2D PROFILES | (1) | (2) | (3) | (4) |
| | RL | 7-8 | RL | 7-8 |
| | (NW-SE NE-SW) | (NW-SE) | (NW-SE) 3-4 (NE-SW) | (NW-SE) 4-5 (NE-SW) |
| 3D TOMOGRAPHY | B1 | A1 | A3 | B2 |

Table 2 Correspondence of anomalies between our results (3D TOMOGRAPHY) and those obtained by a 2D seismic profile inversion (2D PROFILE) by Ben-Zvi et al. (2007) with number of the anomaly, corresponding maximum depth in km. (RL. indicates un- constrained depths) and resolving profile.

This correspondence indicates that the common features in the 3D and 2D images are most likely real. Although both studies have used data from the same experiment and the same tomography code, the picking, grid spacing (0.2 km in the 2D ray tracing) and choice of parameters were independent. For the 3D result the most significant conclusion is that the common anomalies are probably real. An additional consequence of the strong agreement between the 3D and 2D results is that we may confidently include the 2D results in the interpretation of anomalies that extend deeper than our maximum resolved depth.

4.6.2.2. Bathymetry

The bathymetry of Deception Island and its surroundings was surveyed as part of the *TOMODEC* experiment to study, using high resolution swath bathymetry, the superficial expression of the major tectonic and geomorphologic features affecting the seafloor. This analysis was intended to provide insight into the current structural state and the processes active during the evolution of the Bransfield Basin. When combined with our tomographic results, it can potentially supply further details about those structures which presumably have both a seismic signature and a physical effect on the seafloor. The similarity between tomographic and topographic results has to be severely considered, however. As systematic miscalculations or errors in correcting for the water ray path can introduce artefacts into the tomographic image, they would most likely be manifest as a correlation between perturbations and bathymetry. The best way to identify any such problems is by directly comparing the bathymetric model and velocity structure from the 3D inversion. We qualitatively observe that the two models do not systematically correlate and hence we conclude that they are independent of each other (**Figure 4.51**). At the same time, however, several anomalies do correspond to structures that are clearly observable in the bathymetry and whose existence is revealed independently by the tomographic inversion. For example, the SW margin of A1 coincides with an abrupt bathymetric margin, while anomaly B2 corresponds to a zone of rough seafloor where depositional structures clearly dominate.

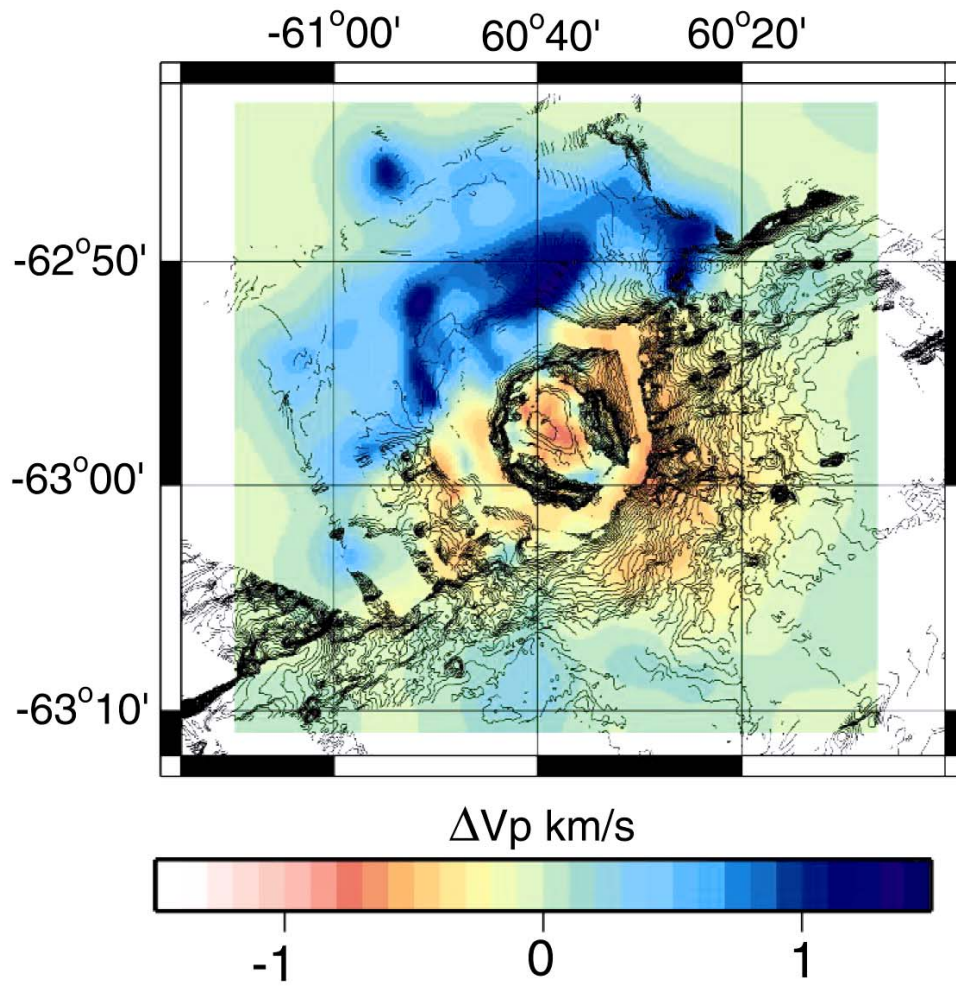


Figure 4.51 Comparison between topography and velocity model (at 0.5 km depth). The contour interval for the bathymetry is 20 m, for the velocity perturbation is 0.1 km/s

4.6.3. Discussion of Results

The velocity structure of Deception Island is characterized by several P-wave velocity contrasts. As we know, interpreting their meaning is difficult and hardly unique. Moreover the absence of Vs data and hence of seismic Vp/Vs ratio information, makes a single interpretation of these anomalies even more difficult, in terms of volcanic and sedimentary structures and the presence of fluid. This problem can be mitigated by incorporating into our interpretation existing information about Deception Island from other studies. Fortunately, there is a considerable number of these, including different fields, from geology to geochemistry and geophysics.

Moreover, our velocity structure is imaged with very high resolution and therefore can be compared with information from small scale studies, such as tectonics and geology from field surveys, or seismo-tectonics from precise source mechanism studies. For example several well defined velocity contrasts, fully confirmed by resolution tests, coincide with the location of known faults.

4.6.3.1. A1

This high velocity anomaly is probably the seismic image of the crystalline basement of the pre-Bransfield continental crust. It coincides in position and absolute velocity value (between 4.0 km/s,[Christeson et al. 2003], and 5.5 km/s, [Grad et al. 1997] **Figure 4.53**) with the crystalline basement of the South Shetland Islands, that is known to be close to the surface [Christeson et al. 2003]. In agreement with the south-western high gradient boundary of A1, large normal faults have been described as along the whole South Shetland south margin, broadly parallel to the Bransfield Strait [Barker and Austin 1994; Christeson et al. 2003; Lawver et al. 1996]. In addition, the systematic component of the gravity anomaly [Navarro et al. 2002] is compatible with the existence of two different geotectonic units at either side of Deception Island, respectively to the NW and SE of the island. The second prediction component confirms the existence of a high density zone in the NW sector of Deception Island, although this is close to the limit of the resolved area for that study. Muñoz-

Martin et al. (2005) map the Bouguer gravity anomaly in the area and recognize an alignment of maxima in strict correspondence with the A1 anomaly. Maxima of magnetic anomalies, marking the limit between two different crust types are recognized with a comparable trend across the island itself [Muñoz-Martin et al. 2005].

The SE limit of A1 crosses the northern portion of Deception Island. Geological studies on land reveal a distribution of fault directions that are compatible with the A1 boundary trend. Close this boundary, at Pendulum and Fumarole Bay, several authors [De Rosa et al. 1995; Gonzalez-Casado et al. 1999; Maestro et al. 2007] have recognized steeply-dipping normal faults with a prevailing orientation N40-N60. Moreover, several submarine fractures in this region have NE-SW direction [Rey et al. 2002] and may be organized in graben-like structures across the bay [Rey et al. 1997]. The volcano-tectonic seismic activity described Vila et al (1992) is distributed along fracture plains with NE-SW orientation and normal mechanism. Ibañez et al. (2003) located VT activity mostly to the NNE and NE of Fumarole Bay. The seismic long-period activity located around Port Foster also indicates the presence of analogous fault systems, where abundant hydrothermal fluids can circulate [Almendros et al. 1997]. Moreover, the A1 velocity boundaries are in close spatial correspondence with an alignment of eruption centers (1967 and 1970 eruptions) and with the highest concentrations of As, Rb, Ba [Somoza et al. 2004].

The Bransfield Strait is crossed by several NW-SE oriented faults that offset the western sector of the axis of the Neovolcanic zone toward the South Shetland margin [Christeson et al. 2003]. According to the GRAPE TEAM [TEAM 1990] the whole continental upper crust of the Bransfield Basin is characterized by extensional horst-graben structures. These are formed by NW-SE trending fault systems, approximately normal to the Bransfield Strait axis, and are related to the southward propagation of the Hero Fracture Zone [Rey et al. 1995]. A recent study of data from a local geodetic network [Ramirez-Rodriguez 2006] indicates simultaneous activity of the Hero Fracture Zone and of the fracture system parallel to the Bransfield Strait. The velocity anomaly A1 has some maxima whose shapes are probably the result of offset along such NW-SE faults. For example the maximum in the NE of A1 is displaced with a dextral offset, with respect to the rest of A1. An analogous pattern is imaged in the same location by the Bouguer gravity anomaly of Muñoz-Martin et al. (2005), where an alignment of gravity maxima is interrupted presumably by the dextral strike slip fault which is displacing the Livingstone Island basement toward the SE. In addition Ashcroft (1972) notes in seismic profiles the presence of a fault across the SE coast of Livingstone, while Grad et al.(1992) model a strongly-inclined basement reflector in the same location.

Therefore, the A1 anomaly is likely the seismic image of the crystalline basement of the pre-Bransfield continental crust. Its SW margin is the continuation of the faulted northern margin of the Central Bransfield Basin and crosses Deception Island along several known faults. In the island history these faults have acted as preferred pathways for upwelling magma at least in the 1967 and 1970 eruptions, and are a significant component of extensional tectonics of Port Foster. The effect of this crustal interaction may also be responsible also for the mixed nature of the magmatic products. The presence of different magmas has been recognized and attributed to the regional extensional tectonics with scavenging of fractures [Smellie 2002].

4.6.3.2. A2

This anomaly likely represents the remnant of a buried intrusion. By analogy with other volcanic islands (for example Strombolicchio, close to Stromboli volcano, Italy) the structure of Deception Island may include a volcanic neck, as the relict conduit of a previous volcanic edifice at ancient Deception Island. The presence of a high density body is indicated by the first component of gravity anomaly [Navarro et al. 2002] and related to the oldest Deception Island formations (Entrance Formation of the Foster Group, Chapter 4.3.1) or three parasitic cones of the early pre-caldera phase. Muñoz-Martin et al. (2005) also describe a local gravity maximum in this position and attribute it to the presence of a high density submarine dome. Another interpretation is also possible, however. According to the GRAPE TEAM (1990) the entire continental crust of the Bransfield Basin is marked by extensional horst-graben structures. If Port Foster is limited to the north by extensional faults (see 4.6.3.1), we may expect analogous tectonics at its southern margin. The A2 high velocity could therefore represents the foot wall of a graben structure that is centered in the inner bay of Deception Island.

4.6.3.3. A3

This conjunction of anomalies which surrounds Port Foster may either correspond to a pre-caldera shield phase of ancient Deception Island, to a previous caldera or to frozen, shallow level intrusions that may have fed earlier eruptions. In

fact, pre-caldera formations are mostly composed of indurated hyaloclastite breccias and poorly vesicular lavas that outcrop in the Entrance Point, Cathedral Crag, south of Point Collins (Smellie, 2002) The 1842 eruption, located coincident with the western sectors of these anomalies, produced dense fissural lava flows The presence of high density material is indicated in the southern part of the island by the second prediction component of gravity anomaly [Navarro et al. 2002].

4.6.3.4. *A4*

This anomaly possibly constitutes the seismic image of Sail Rock, an eroded andesitic sea stack located to the SW of Deception Island. The presence of a high density body, in addition to bathymetric evidences, is confirmed by the gravity data [Navarro et al. 2002].

4.6.3.5. *B1*

This pronounced low velocity anomaly lies beneath Port Foster and is the result of two major overlapping sources of anomaly, depending on the anomaly depth. The shallow level of this anomaly is possibly the image of pyroclastic deposits infilling Port Foster. Fragmental deposits have been formed throughout the entire volcanic history of the island [Smellie 2002] and have been deposited in Port Foster by streams, ice an mass wasting [Inbar 1995]. At 0-0.5 km depth the anomaly is composed of several maxima and some coincide with the location of the 1967 and 1970 eruption centers. The analysis of Saccorotti et al. (2001) indicates the presence of a slower medium at shallower levels that is explained as sediments infilling a structural depression that is limited by NNE-SSW-trending faults. Seismic profiles [Ashcroft 1972; Grad 1992] indicate the presence of ash and assorted volcanic debris. Previous 2D profiles [Grad 1992] and those of *TOMODEC* dataset [Ben-Zvi et al. 2007] show that Port Foster is filled with at least 1.2 km of sediments. The occurrence of similar material and at similar depths is confirmed by our absolute velocity beneath Port Foster, which is approximately 3 km/s from the surface to ~1.5 km depth (**Figure 4.53**). This value is consistent with ash deposits at various levels of

compaction [Ashcroft 1972; Grad 1992], that host a vigorous geothermal system, that is inferred to exist beneath Port Foster from geochemical and geophysical observations [Caselli et al. 2004; Marti and Baraldo 1990].

The amplitude and depth of the anomaly cannot be explained by thicker sediments alone and also requires high temperatures and partial melt to be located beneath Port Foster at depths greater than about 2 km. The presence of a magma reservoir is supported by a number of previous studies. The deformation which inflated the northern sub-basin of Port Foster is attributed to a high sedimentation rate and also to magma influx at depth [Cooper et al. 1999]. Magnetic anomalies show a large minimum with a NNW-SSE trend [Ortiz et al. 1992], that may be explained as the thermo-remnant magnetization of a magma body, combined with the degradational effects on magnetic properties by shallow aquifers circulation. Geochemically [Caselli et al. 2004] the changes in fumaroles composition, such as those observed during 1999, are consistent with the emplacement of shallow magma in the Fumaroles Bay area. The origin of the LP seismic activity is related to the presence of a shallow aquifer in contact with high temperature rocks and, at depth, magmatic fluids [Almendros et al. 1997]. The VT activity of 1998-1999 also indicates [Ibanez et al. 2003b] stress modification due to a deep magmatic injection. The study of traveltimes residuals for preliminary locations [Vila et al. 1995] reports the existence of a dyke structure with a velocity of 25% lower than surrounding rocks, while abnormally low values of seismic Q inside Port Foster also indicate the existence of a hot magmatic intrusion [Vila et al. 1995]. In addition, VT activity is described in the northern sector of Deception Island but not within the inner part of Port Foster [Alguacil et al. 1999]: this may be due to the inability of a partially-molten body to sustain brittle fracturing. Similarly, seismic profiles of Port Foster indicate the absence of faulting at depth in the middle of the bay [Ashcroft 1972; Grad 1992]. Taken together these final two observations point to possible ductile behaviour of the material below shallower sedimentary levels.

Two different origins for the low velocity region at shallow and deep levels is further supported by the dense inversion results. Anomaly B1 owes its superficial low velocities to sedimentary cover, both on land and on the seafloor. This explains the irregular shape of the shallow levels of B1 and its correspondence with the eruption center of 1967 and 1970. At greater depth, at levels where the magma chamber is finally sampled, B1 elongates in a NW-SE direction, to 3 km depth, where (near the limit of resolution) it becomes more circular.

4.6.3.6. B2

This large low velocity region to the east of Deception Island corresponds to a seafloor that is characterized by sediment transport structures (gullies, ridges and debris flows, [Barclay et al. 2007]) from Deception Island into the Central Bransfield Basin [Lee et al. 2005]. The entire Bransfield Strait is deformed by horst-graben-like structures of uplifted basement, possibly filled by sediments [Christeson et al. 2003; Jin et al. 2002a; TEAM 1990]. The low velocities we see may therefore correspond to the infilling of these tectonic structures. Moreover, the origin of the sediments near Neptune Bellows can be related to the presence of pyroclasts by eruptive centers located in that zone (Caselli, personal communication). The presence of a low density anomaly with a NNW-SSE elongation is indicated by the first component of gravity anomaly [Navarro et al. 2002] and by the alignment of Bouguer gravity anomaly minima [Muñoz-Martin et al. 2005], which together define a larger-negative anomaly extending towards the Antarctic Peninsula. The results of seismic profiles [Grad et al. 1997] point to low velocities at shallow depths to the E of Deception Island.

The overall shape of this anomaly is strongly irregular although the position of the maximum perturbation at 0.5 km depth corresponds to the location of Costa Recta [Fernandez-Ibanez et al. 2005]. Several previous studies have suggested that NNW-SSE is a major structural direction in the island's evolution, both on local [Gonzalez-Casado et al. 1999; Maestro et al. 2007] and regional [Christeson et al. 2003; Jin et al. 2002a; TEAM 1990] scales. No seismic activity with this alignment has been identified and therefore these structures can be probably considered as actually inactive. The lack of seismic evidence at shallower depths in our results and its absence in the bathymetry data [Barclay et al. 2007] suggest that if a major structure related to Costa Recta exists, it is hidden and possibly buried by sediments.

4.6.3.7. B3

This low velocity anomaly coincides with a region of extensive seafloor volcanism located to the west of Deception Island. It may be the expression of thicker volcanoclastic sediments, thermal anomalies, or active magmatic

systems. The bathymetric seamount edifices [Barclay et al. 2007] roughly correspond to the gravity minimum pointed out in the first prediction component [Navarro et al. 2002].

4.7. Conclusions

The three-dimensional seismic P-wave tomographic image of Deception Island volcano shows strong velocity variations (**Figure 4.52**). The high resolution tomography allows us to obtain an accurate image of Deception Island and to combine it with the result of other studies. Among the major anomalies characterizing the region, there is a large high velocity zone to the NW of Deception Island (A1). This feature represents a block of the continental crystalline basement produced by fracturing of the ancient Antarctic Plate, before it fragmented into the South Shetland platform and the Antarctic Peninsula [Christeson et al. 2003]. We are hence observing in our tomographic image the results of the intense fracturing of such continental crust that affects the entire region in two main directions: NE-SW, which is the main trend of the Bransfield Strait, and the normal direction of NW-SE.

A number of other seismic structures can be interpreted in the context of this regional tectonic framework. At a smaller scale, the influence of the regional tectonics is evident in the break-up of Deception Island crust into smaller blocks that are compatible with this stress field [Maestro et al. 2007]. The main structural lineaments of Deception Island are those with NE-SW and NW-SE trends, as pointed out by several field works [Paredes et al. 2006]. Their presence is also supported by seismic evidence in our tomographic image, including, for example, the elongation of anomaly B1, the similarity of anomaly B2 and Costa Recta, the NW-SE alignment of A3 velocity maxima or the SE boundary of anomaly A1.

Volcanic activity has occurred along some of these tectonic discontinuities, as shown by the location of historical eruptions (and B1 shallow minima NE-SW alignment), and also by the seismic imprint of ancient volcanic episodes (e.g. the alignment of the western maxima of anomaly A3).

This means that the evolution of Deception Island, its structural development and volcanic history, are closely related to the regional tectonics and the present magmatic state of Deception Island can be interpreted in this framework. The central bay of Deception Island hosts a magma chamber extending from approximately 1.5 km depth and is resolved throughout our resolved volume, 5 km depth, and probably more [Ben-Zvi et al. 2007]. The inferred reservoir has a NW-

SE-oriented elongation axis, while towards the surface the B1 anomaly deforms the northern sector along a NE-SW trend. In the context of the wider tectonics, the NW-SE fault system could act as a preferred pathway for the magma upwelling at depth, while the NE-SW system would constitute normal faults of an extensional regime, that controls the emplacement of the shallow batches of magma and its supply for short-lived eruptions, such as those of 1967 and 1970. By contrast, the 1969 fissure-style eruption, which took place along the NW-SE fault system, had a less evolved magma [De Rosa et al. 1995], and could have been fed directly by the deeper system.

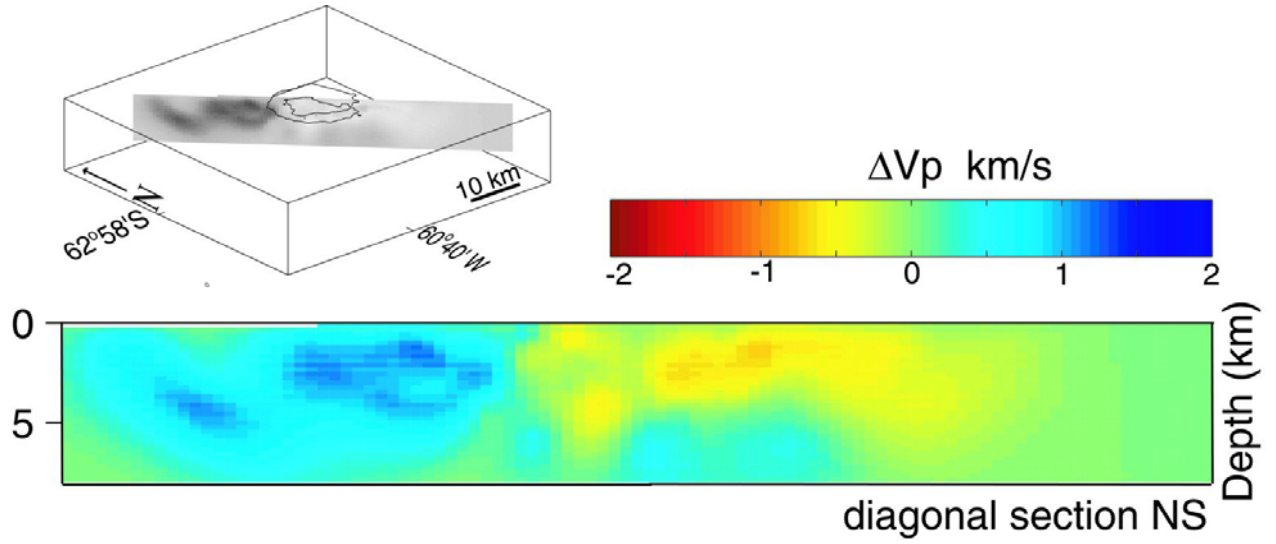
It is difficult to assess the chronological order in which the main fault systems were active or indeed if they are contemporary affecting the island's volcanism. The timing, trend and location of volcanic eruptions and the actual magma chamber model presented above probably indicate the contemporary action of both systems. This conclusion supports the recent geodetic measurements [Ramirez-Rodriguez 2006], in which the observed displacements respond to a annual-scale periodicity of deformation that alternates between fractures parallel to and perpendicular to the Bransfield Strait.

In conclusion, the main seismic features of Deception Island and the surrounding region are outlined in this work. A complex picture of velocity contrasts emerges in the high resolution P-wave tomographic image. The interpretation of these anomalies is a challenging task and poses several questions about their origin and significance in a wider tectonic context. We suggest that the seismic structure of Deception Island itself has a complicated relationship with the regional tectonics of the South Shetland-Antarctic Peninsula complex.

These preliminary results evidence the complexity of the seismic structure and the need for further research. To better constrain the Deception Island volcanic structure and fluid-related processes, the V_p/V_s seismic ratio could help to reduce the unavoidable ambiguity of the P-wave velocities. This would require a study of the natural seismicity inside and around Deception Island. The use of earthquakes data may also help to illuminate the deep structure of Deception Island, which is not well-resolved in our analysis. A teleseismic or regional seismic experiment in particular could be used to address the deep crust and mantle structure beneath the island. At the opposite scale, data from dense array could help in the definition of the very shallow seismic structure. Precise location of both VT and LP activity, improved by our seismic model, could provide crucial information on actively deforming regions and focal mechanisms could provide constraints on the stress field. The inclusion of earthquake data would also help in the definition of the anisotropic properties of the crust and likely reflect its primary structural directions that affect the entire evolution of the island. Similarly, the strongly

4 - Deception Island

heterogeneous nature of the structure could be evidenced by a comprehensive attenuation study, especially when it is constrained by the results of this study.



4 - Deception Island

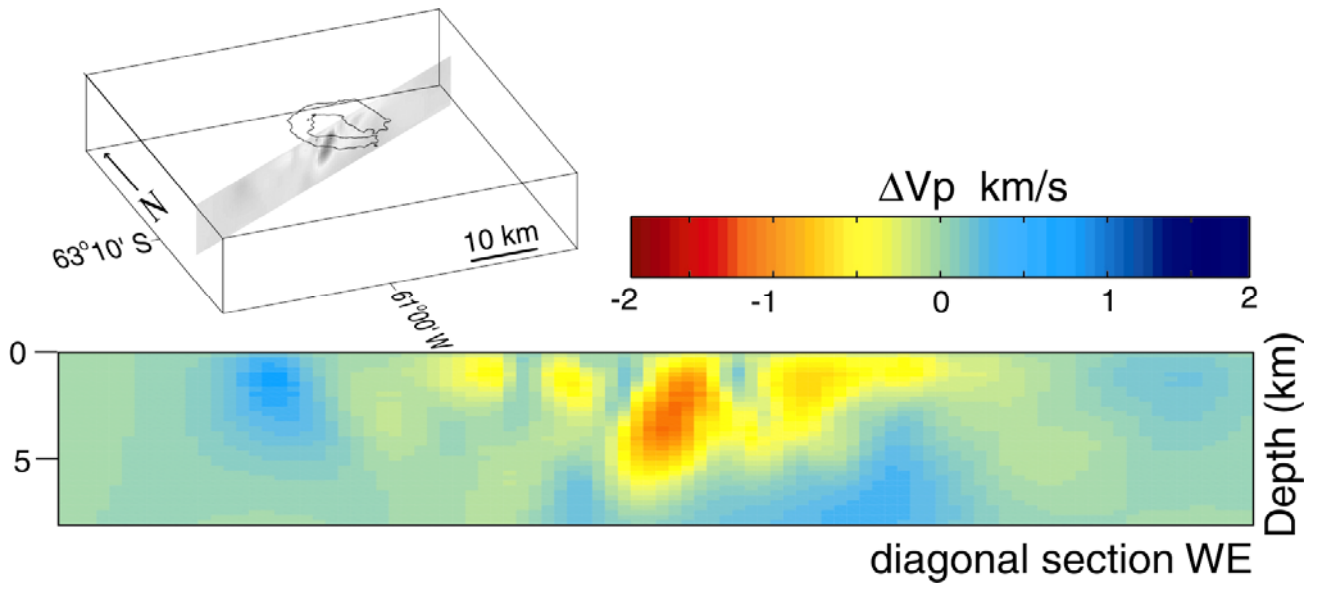


Figure 4.52 P-wave velocity perturbations across the 3D model (NS above, EW below). The small insets indicate section position, Deception Island coastline and coordinates of the centre of the model

4 - Deception Island

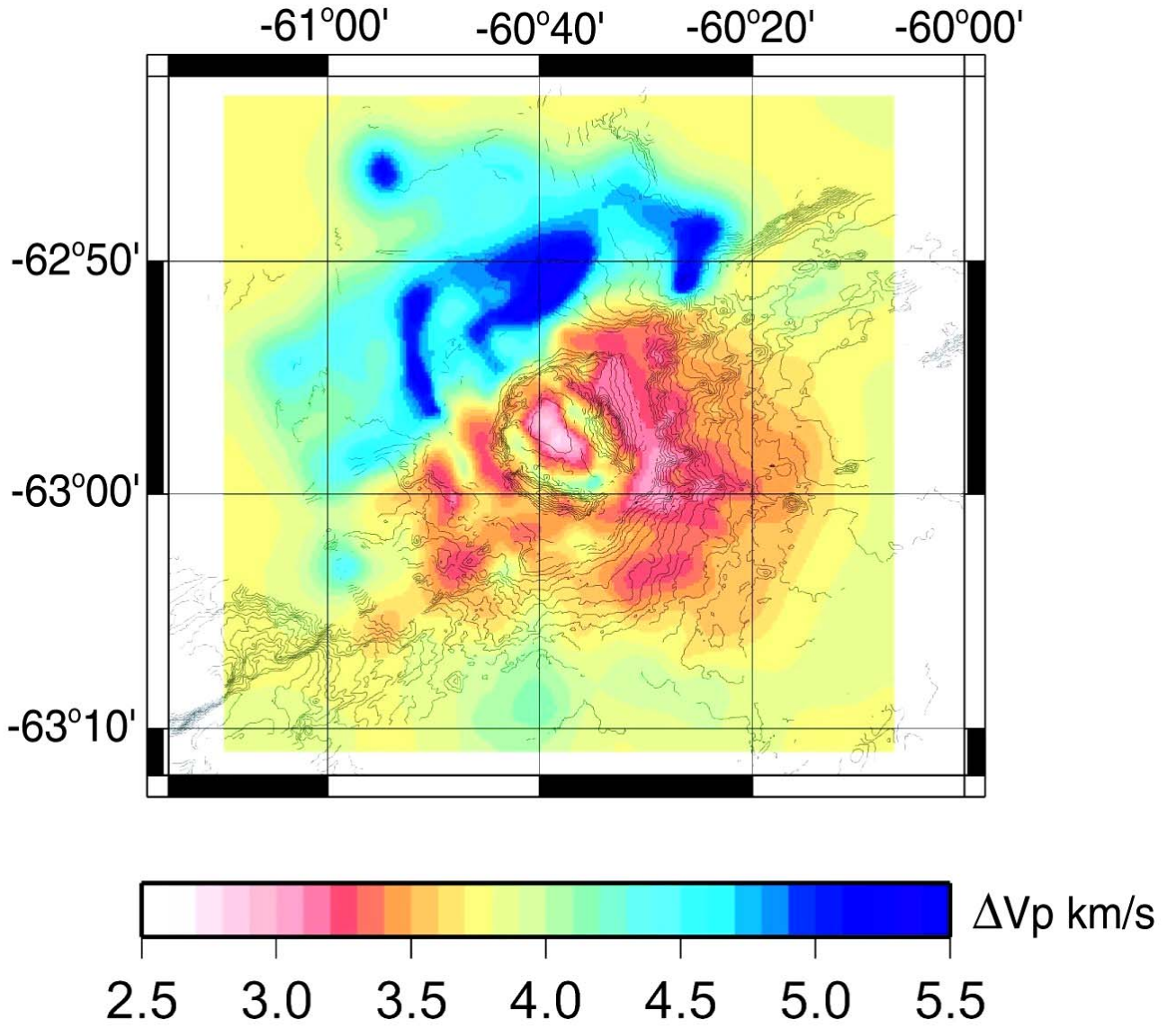


Figure 4.53 *P*-wave absolute velocity at 1 km depth. The contour interval for topography is interval is 50 m, for the velocity model is 0.1 km/s.

References

- Agudo-Bravo, L. M., 2003, Estudio Sismico de la Isla Decepcion (Antartida): Unpub. Trabajo de investigacion de Tercer Ciclo thesis, Universidad Complutense.
- Alguacil, G., Almendros, J., Del Pezzo, E., García, A., Ibanez, J. M., La Rocca, M., Morales, J., and Ortiz, R., 1999, Observations of volcanic earthquakes and tremor at Deception Island, Antarctica: *Annali di Geofísica*, v. 42, p. 417-436.
- Almendros, j., Ibañez, J. M., Alguacil, G., Del Pezzo, E., and Ortiz, R., 1997, Array tracking of the volcanic tremor source at Deception island, Antarctica: *Geophys. Res.Lett.*, v. 24, p. 3069-3072.
- Allen, R., 1978, Automatic earthquake recognition and timing from single traces: *Bull. Seis. Soc. Am.*, v. 68, p. 1521-1532.
- Aristarain, A. J., and Delmas, R. J., 1998, Ice record of a large eruption of Deception Island volcano (Antarctica) in the XVIIth century,: *Journ. Volcan. Geotherm. Res.*, v. 80, p. 17-25.
- Ashcroft, W. A., 1972, Crustal structure of the South Shetland Islands and Bransfield Strait: London, British Antarctic Survey ;, [1], 43 p., 1 fold. leaf p.
- Baker, P. E., McReath, I., Harvey, M. R., Roobol, M. J., and Davies, T. G., 1975, The geology of the South Shetland Islands: volcanic evolution of Deception Island, Scientific Reports, British Antarctic Survey.
- Barclay, A. H., and Solomon, S., 1998, Seismic Structure and crustal magmatism at the Mid-Atlantic Ridge, 35N: *Journ. Geophys. Res.*, v. 103, p. 17827-17844.
- Barclay, A. H., Wilcock, W. S. D., and Ibañez, J. M., 2007, Tectonic and volcanic influences at Deception Island, South Shetland Islands: submitted.
- Barker, D. H. N., and Austin, J. A., 1994, Crustal diapirism in Bransfield Strait, West Antarctica: Evidence for distributed extension in marginal-basin formation: *Geology*, v. 22, p. 657-660.
- , 1998, Rift propagation, detachment faulting, and associated magmatism in Bransfield Strait, Antarctic Peninsula: *Journ.Geophys. Res.*, v. 103 p. 24017-24043.
- Barker, P. E., McReath,I., Harvey,M.R., Roobol,M.J.,Davies,T.G, 1975, The geology of the South Shetland Islands: volcanic evolution of Deception Island, Scientific Reports, British Antarctic Survey.
- Barry, K. M., Cavers, D. A., and Kneale, C. W., 1975, Report on recommended standards for digital tape formats: *Geophysics*, v. 40, p. 344-352.
- Ben-Zvi, T., Wilcock, W. S. D., Barclay, A. H., Zandomeneghi, D., Ibañez, J. M., Almendros, J., and Group, T. W., 2007, The P-wave velocity structure of Deception Island, Antarctica, from two-dimensional seismic tomography: ISAES.

- Caselli, A. T., Bengoa, C. L., Agosto, M. R., Badi, G., and Ibañez, J. M., 2006, Analisis comparativo de la geoquímica de gases y la actividad sísmica de la Isla Decepcion, Antártida: posible efecto sello sobre acuífero: VII Simposio Español de Estudios Polares.
- Caselli, A. T., Santos-Afonso, M., and Agosto, M. R., 2004, Gases fumarólicos de la isla Decepcion (Shetland del Sur, Antártida): variaciones químicas y depósitos vinculados a la crisis sísmica de 1999: *Rev.As. Geol.Arg.*, v. 59, p. 291-302.
- Catalan, M., Agudo, L. M., and Muñoz-Martin, A., 2006, Geomagnetic secular variation of Bransfield Strait (Western Antarctica) from analysis of marine crossover data: *Geophys. J. Int.*, v. 165, p. 73-86.
- Cooper, A. P. R., Smellie, J. L., and Maylin, J., 1999 Evidence for shallowing and uplift from bathymetric records of Deception Island, Antarctica.: *Antarctic Science*, v. 10, p. 455-461.
- Correig, A. M., Urquizu, M., Vila, J., and Martí, J., 1997, Analysis of the Temporal Occurrence of Seismicity at Deception Island (Antarctica). A Nonlinear Approach: *Pure Appl.Geophys.*, v. 149, p. 553-574.
- Creager, K. C., and Dorman, L. M., 1982, Location of instruments on the seafloor by joint adjustment of instruments and ship positions: *J.Geophys.Res.*, v. 87, p. 8379-8388.
- Chouet, B. A., 2003, Volcano Seismology: *Pure Appl. Geophys.*, v. 160, p. 739-788.
- Christeson, G. L., Barker, D. H. N., Jr., J. A. A., and Dalziel, I. W. D., 2003, Deep crustal structure of Bransfield Strait: Initiation of a back arc basin by rift reactivation and propagation: *J. Geophys. Res.*
- De Rosa, R., Mazzuoli, R., Omarini, R. H., Ventura, G., and Viramonte, J. G., 1995, a volcanological model for the historical eruptions at Deception Island (Bransfield Strait, Antarctica): *Terra Antarctica* v. 2, p. 95-101.
- Dietrich, R., Dach, R., Engelhardt, G., Ihde, J., Korth, W., and Kutterer, H.-J., 2001, ITRF coordinates and plate velocities from repeated GPS campaigns in Antarctica--an analysis based on different individual solutions: *Journal of Geodesy*, v. 74, p. 756-766.
- Dix, C. H., 1955, Seismic velocities from surface measurements: *Geophysics*, v. 20, p. 68-86.
- Dunn, R. A., Toomey, D. R., Detrick, R., and Wilcock, W. S. D., 2001, Continuous Mantle Melt Supply Beneath an Overlapping Spreading Center on the East Pacific Rise: *Science*, v. 291, p. 1955-1958.
- Evangelidis, C. P., Minshull, T. A., and Henstock, T. J., 2004, Three-dimensional crustal structure of Ascension Island from active source seismic tomography.: *Geophys. J. Int.*, v. 159, p. 311-325.
- Fernandez-Ibanez, F., Perez-Lopez, R., Martinez-Diaz, J. J., Paredes, C., Giner-Robles, J. L., Caselli, A. T., and Ibañez, J. M., 2005, Costa Recta beach, Deception Island, West Antarctica: a retreated scarp of a submarine fault?: *Antarctic Science*, v. 17, p. 418-426.
- Fretzdorff, S., Worthington, T. J., Haase, K. M., Hekinian, R., Franz, L., Keller, R. A., and Stoffers, P., 2004, Magmatism in the Bransfield Basin: rifting of the South Shetland Arc?: *Journ. Geophys.Res.*, v. 109.
- Galindo-Zaldivar, J., Jabaloy, A., Maldonado, A., and de Galdeano, C. S., 1996, Continental fragmentation along the South Scotia Ridge transcurrent plate boundary (NE Antarctic Peninsula): *Tectonophysics*, v. 258, p. 275-301.
- García, A., Blanco, I., Torta, J. M., Astiz, M. M., Ibañez, J. M., and Ortiz, R., 1997, A search for the volcanomagnetic signal at Deception volcano (South Shetland I., Antarctica): *Annali di Geofisica*, v. 40, p. 319-327.
- Garrett, S. W., 1990, Interpretation of reconnaissance gravity and aeromagnetic surveys of the Antarctic Peninsula: *Journ.Geophys.Res.*, v. 95, p. 6759-6777.

- Goldstein, P., Dodge, D., Firpo, M., and Minner, L., 2003, Signal processing and analysis tools for seismologists and engineers, *in* Lee, W., Kanamori, H., Jennings, P. C., and Kisslinger, C., eds., *The IASPEI International Handbook of Earthquake and Engineering Seismology*, London, Academic Press.
- Gonzalez-Casado, J. M., Lopez-Martinez, J., Giner, J., Duran, J. J., and Gumiel, P., 1999, Analisis de la microfracturación en la Isla Decepcion, *Antartida Occidental: Geogaceta*, v. 26, p. 27-30.
- Gonzalez-Ferrán, O., 1985, Volcanic and tectonic evolution of the Northern Antarctic peninsula –Late Cenozoic to recent: *Tectonophysics*, v. 114, p. 389-409.
- González-Ferrán, O., 1991, The Bransfield rift and its active volcanism, *in* Thomson, M. R. A., ed., *Geological evolution of Antarctica*, Cambridge, UK, Cambridge University Press, p. 505-509.
- Gordon, A. L., and Nowlin, W. D., 1978, Basin waters of Bransfield Strait: *J. Phys. Ocean.*, v. 8, p. 258-264.
- Gracia, E., Canals, M., Farran, M. L., Prieto, M. J., and Sorribas, J., 1996, Morphostructure and Evolution of the Central and Eastern Bransfield Basins (NW Antarctic Peninsula): *Marine Geophys. Res.*, v. 18, p. 429-448.
- Grad, M., Guterch, A., Janik, T., and Sroda, P., 2002, Seismic characteristic of the crust in the transition zone from the Pacific Ocean to the northern Antarctic Peninsula, West Antarctica., *in* Bulletin, R. S. o. t. N. Z., ed., *Antarctica at the close of the millennium.*, p. 493-498.
- Grad, M., Guterch, A., Sroda, P., 1992, Upper crustal structure of Deception Island area, Bransfield Strait, West Antarctica: *Antarctic Science*, v. 4, p. 469-476.
- Grad, M., Shiobara, H., Janik, T., Guterch, A., and Shimamura, H., 1997, Crustal model of Bransfield Rift, West Antarctica, from detailed OBS refraction experiments: *Geophys. J. Int.*, v. 130, p. 506-518.
- Guidarelli, M., and Panza, G. F., 2006, Determination of the seismic moment tensor for local events in the South Shetland Islands and Bransfield Strait: *Geophysical Journal International*, v. 167, p. 684-692.
- Guterch, A., Grad, M., Janik, T., Perchuc, E., and Pajchel, J., 1985, Seismic studies of the crustal structure in West Antarctica 1979-1980-Preliminary Results: *Tectonophysics*, v. 114, p. 411-429.
- Ibanez, J. M., Almendros, J., Carmona, E., Martinez-Arevalo, C., and Abril, M., 2003a, The recent seismo-volcanic activity at Deception Island volcano: *Deep Sea Research Part II: Topical Studies in Oceanography*, v. 50, p. 1611-1629.
- Ibanez, J. M., Carmona, E., Almendros, J., Saccorotti, G., Del Pezzo, E., Abril, M., and Ortiz, R., 2003b, The 1998-1999 seismic series at Deception Island volcano, Antarctica: *Journal of Volcanology and Geothermal Research*, v. 128, p. 65-88.
- Ibañez, J., Morales, P., Alguacil, G., Almendros, J., Ortiz, R., Del Pezzo, E., La Rocca, M., E., and Garcia, A., 2000, Seismovolcanic signals at Deception Island volcano, Antarctica: wave field analysis and source modelling: *J. Geophys. Res.*, v. 135, p. 13905-13931.
- Ibañez, J. M., Morales, J., Alguacil, G., Almendros, J., Ortiz, R., and Del Pezzo, E., 1997, Intermediate-focus earthquakes under South Shetland Island (Antarctica): *Geophys. Res. Lett.*, v. 24, p. 531-534.
- Inbar, M., 1995, Fluvial morphology and streamflow on Deception Island, Antarctica: *Geogr. Ann.*, v. 77, p. 221-230.
- Jin, Y., Kim, Y., Nam, S. H., and Kim, K. J., 2002a, Seismic structure of the western Bransfield Strait, Antarctic Peninsula: rift propagation from northeast to southwest, Antarctica at the close of the millennium, *Royal Society of the New Zealand Bulletin*, p. 499-506.
- Jin, Y. K., Larter, R. D., Kim, Y., Nam, S. H., and Kim, K. J., 2002b, Post-subduction margin structures along Boyd Strait, Antarctic Peninsula: *Tectonophysics*, v. 346, p. 187-200.

- Keller, R. A., Fisk, M. R., Smellie, J. L., Strelin, A., and Lawer, L. A., 1991, Geochemistry of back arc basin volcanism in Bransfield Strait, Antarctica: subducted contributions and along-axis variations: *J. Geophys. Res.*, v. 107.
- Keller, R. A., Fisk, M. R., Smellie, J. L., Strelin, J. A., and Lawver, L. A., 2002, Geochemistry of back arc basin volcanism in Bransfield Strait, Antarctica: Subducted contributions and along-axis variations: *J. Geophys. Res.*, v. 107 p. 2171.
- Klepeis, K. A., and Lawer, L. A., 1996, Tectonics of the Antarcti -Scotia plate boundary near Elephant and Clarence Islands, West Antarctica.: *J. Geophys. Res.*, v. 101, p. 20211-20231.
- Klinkhammer, G. P., Chin, C. S., Keller, R. A., Dahlmann, A., Sahling, H., Sarthou, G., Petersen, S., Smith, F., and Wilson, C., 2001, Discovery of new hydrothermal vent sites in Bransfield Strait, Antarctica: *Earth Planet. Sci. Lett.*, v. 193, p. 395-407.
- Lawver, L. A., Sloan, B. J., Barker, D. H. N., Ghidella, M., Von Herzen, R. P., Keller, R. A., Klinkhammer, G. P., and Chin, C. S., 1996, Distributed, Active Extension in Bransfield Basin, Antarctic Peninsula: Evidence from Multibeam Bathymetry: *GSA Today*, v. 6, p. 1-6.
- Lee, J. I., Park, B. K., Jwa, Y. J., Ho Il, Y., Kyu Chul, Y., and Kim, Y., 2005, Geochemical characteristics and the provenance of sediments in the Bransfield Strait, West Antarctica: *Marine Geology*, v. 219, p. 81-98.
- Maestro, A., Somoza, L., Rey, J., Martinez-Frias, J., and Lopez-Martinez, J., 2007, Active tectonics, fault patterns, and stress field of Deception Island: A response to oblique convergence between the Pacific and Antarctic plates: *Journal of South American Earth Sciences*, v. 23, p. 256-268.
- Magde, L. S., Barclay, A. H., Toomey, D. R., Detrick, R. S., and Collins, J. A., 2000, Crustal magma plumbing within a segment of the Mid-Atlantic Ridge, 35°N *Earth Planet. Sci. Lett.*, v. 175, p. 55-67
- Maldonado, A., Larter, R. D., and Aldaya, F., 1994, Forearc tectonic evolution of the South Shetland Margin, Antarctic Peninsula: *Tectonics*, v. 13, p. 1345-1370.
- Marti, J., and Baraldo, A., 1990, Pre-caldera pyroclastic deposits of Deception Island (South Shetland Islands) *Antarctic Science*, v. 2, p. 345-352.
- Muñoz-Martin, A., Catalan, M., Martin, J., and Carbo, A., 2005, Upper crustal structure of Deception Island area (Bransfield Strait, Antarctica) from gravity and magnetic modelling: *Antarctic Science*, v. 17, p. 213-224.
- Nagihara, S., and Lawer, L. A., 1989, Heat flow measurements in the King George Basin, Bransfield Basin: *Ant. J. Sci.*, v. 23, p. 123-125.
- Navarro, F. J., Velez, E. J., Camacho, A. G., and Vieira, R., 2002, A gravity survey of Dception Island (South Shetland Islands, Antarctica), *Antarctica at the close of a millennium: Royal Society of New Zealand Bulletin*, p. 515-523.
- Ortiz, R., 1997, Monitoring of the volcanic activity of Deception Island, South Shetland Islands, Antarctica (1986-1995), *Antarctic Region: geological Evolution and Processes*, p. 1071-1076.
- Ortiz, R., Vila, J., Garcia, A., Camacho, A. G., Diez-Gil, J. L., Aparicio, A., Soto, R., and Viramonte, J. G., 1992, Geophysical features of Deception, *in* Yoshida, Y., Kaminuma, K., and Shiraishi, K., eds., *Recent progress in Antarctic earth sciences*, Tokyo, Terra Scientific Publishing Company, p. 443-448.
- Paredes, C., Perez-Lopez, R., Giner-Robles, J. L., de la Vega, R., Garcia-Garcia, A., and Gumiel, P., 2006, Distribucion espacial y zonificacion tectonica de los morfolinemanetos en la Isla Decepcion (Shetland del Sur, Antartida): *Geogaceta*, v. 39, p. 75-78.
- Pelayo, A. M., and Wiens, D. A., 1989, Seismotectonic and relative plate motions in the Scotia Sea Region: *J. Geophys. Res.*, v. 94, p. 7293-7320.

- Prieto, M. J., Canals, M., Ercilla, G., and de Batist, M., 1998, Structure and geodynamic evolution of the Central Bransfield Basin (NW Antarctica) from seismic reflection data: *Marine Geology*, v. 149, p. 17-38.
- Prieto, M. J., Ercilla, G., Canals, M., and de Batist, M., 1999, Seismic stratigraphy of the Central Bransfield Basin (NW Antarctic Peninsula): interpretation of deposits and sedimentary processes in a glacio-marine environment: *Marine Geology*, v. 157, p. 47-68.
- Ramirez-Rodriguez, M. E., 2006, Modelización de la deformación superficial en áreas volcánicas mediante la teoría de wavelets. Aplicación al volcán Decepción, Universidad de Cádiz 264 p.
- Rey, J., Maestro, A., Somoza, L., and Smellie, J. L., 2002, Submarine morphology and seismic stratigraphy of Port Foster, *in* Smellie, J. L., and López-Martínez, J., eds., *Geology and geomorphology of Deception Island*, Cambridge, British Antarctic Survey, p. 40-46.
- Rey, J., Somoza, L., Martínez-Frías, Benoto, R., and Martín-Alfageme, S., 1997, Deception Island (Antarctica): a new target for exploitation of Fe-Mn mineralization?, *in* Nicholson, K., Hein, J. R., Nuhn, B., and Dasgupta, S., eds., *Manganese Mineralization: geochemistry and mineralogy of terrestrial and marine deposits*: Geological Society Special Publication, p. 239-251.
- Rey, J., Somoza, L., and Martínez-Frías, J., 1995, Tectonic, volcanic and hydrothermal event sequence on Deception Island (Antarctica): *Geo-Marine Lett.*, v. 15, p. 1-8.
- Roach, P. J., 1978, The nature of back-arc extension in Bransfield Strait: *Geophys. J. R. Astron. Soc.*, v. 53, p. 165.
- Robertson, S. D., Wiens, D. A., Shore, P. J., Vera, E., and M. Dorman, L. M., 2003, Seismicity and tectonics of the South Shetland Islands and Bransfield Strait from a regional broadband seismograph deployment: *J. Geophys. Res.*, v. 108.
- Saccorotti, G., Almendros, J., Carmona, E., Ibañez, J. M., and Del Pezzo, E., 2001, Slowness Anomalies from Two Dense Seismic Arrays at Deception Island Volcano, Antarctica: *Bull. Seism. Soc. Am.*, v. 91, p. 561-571.
- Schlosser, P., Suess, E., Bayer, R., and Rhein, M., 1988, ³He in the Bransfield Strait waters: indication for local injection from back arc rifting: *Deep-Sea Research*, v. 35, p. 1919-1935.
- Smellie, J. L., 2001, Lithostratigraphy and volcanic evolution of Deception Island, South Shetland Islands: *Antarctic Science* v. 13 p. 188-209.
- , 2002, *Geology and geomorphology of Deception Island*: Cambridge, United Kingdom, British Antarctic Survey.
- Somoza, L., Martínez-Frías, J., Smellie, J. L., Rey, J., and Maestro, A., 2004, Evidence for hydrothermal venting and sediment volcanism discharged after recent short-lived volcanic eruptions at Deception Island, Bransfield Strait, Antarctica: *Marine Geology*, v. 203, p. 119-140.
- Spetzler, J., and Snieder, R., 2004, the Fresnel volume and transmitted waves: *Geophysics*, v. 69, p. 653-663.
- Sroda, P., 2002, Three dimensional seismic modelling of the crustal structure between the South Pacific and the Antarctic Peninsula: *Royal Society of the New Zealand Bulletin*, v. 35, p. 555-561.
- TEAM, G., 1990, Preliminary results of seismic reflection investigations and associated geophysical studies in the area of the Antarctic Peninsula: *Antarctic Science*, v. 2, p. 223-234.
- Tian, T., Wilcock, S. D., Toomey, D. R., and Detrick, R. S., 2000, Seismic heterogeneity in the upper crust near the 1991 eruption site on the East Pacific Rise, 9 50' N: *Geophys. Res. Lett.*, v. 27, p. 2369-2372.

- Toomey, D. R., Wilcock, W. S. D., Solomon, S. C., Hammond, W. C., and Orcutt, J. A., 1998, Mantle Seismic Structure Beneath the MELT Region of the East Pacific Rise from P and S Wave Tomography: *Science*, v. 280, p. 1224-1227.
- Toomey, D. R., Joussetin, D., Dunn, R. A., Wilcock, W. S. D., and Detrick, R. S., 2007, Skew of mantle upwelling beneath the East Pacific Rise governs segmentation: *Nature*, v. 446, p. 409-414.
- Toomey, D. R., Solomon, S. C., and Purdy, G. M., 1994, Tomographic imaging of the shallow crustal structure of the East Pacific Rise at 9 30' N: *J. Geophys. Res.*, v. 99, p. 24135-24157.
- UTM, 2005, HE102, Informe Técnico Campaña Tomodec, Barcelona, UTM.
- Vila, J., Correig, A. M., and Marti, J., 1995, Attenuation and source parameters at Deception Island (South Shetland Islands, Antarctica): *PAGEOPH*, v. 144, p. 229-250.
- Vila, J., Marti, J., Ortiz, R., Garcia, A., and Correig, A. M., 1992, Volcanic tremors at Deception Island (South Shetland Islands, Antarctica): *J. Volc. Geoth. Res.*, v. 53, p. 89-102.
- Vuan, A., Robertson Maurice, S. D., Wiens, D. A., and Panza, G. F., 2005, Crustal and upper mantle S-wave velocity structure beneath the Bransfield Strait (West Antarctica) from regional surface: *Tectonophysics*, v. 397, p. 241-259.
- Weaver, S. D., Saunders, A. D., Pankhurst, R. J., and Tarney, J., 1979, A geochemical Study of magmatism associated with the initial stages of back-arc spreading. The Quaternary volcanics of Bransfield Strait, from South Shetland Islands: *Contrib.Mineral.Petrol.*, v. 68, p. 151-169.
- Webb, S. C., 1998, Broad seismology and noise under the ocean: *Rev. of Geophysics*, v. 36, p. 105-142.
- Wessels, P., and Smith, W. H. F., 1995, New version of generic mapping tools released: *EOS*, v. 76, p. 329.
- Yilmaz, O., 1988, *Seismic data processing*, Tulsa, Society of Exploration Geophysicists, p. 526.
- Zandomenighi, D., Barclay, A. H., Ben Zvi, T., Wilcock, W., Ibáñez, J. M., and Almendros, J., 2005, Preliminary seismic tomography of Deception Island Volcano, South Shetland Island (Antarctica): AGU-Fall Meeting.

5. *Conclusions*

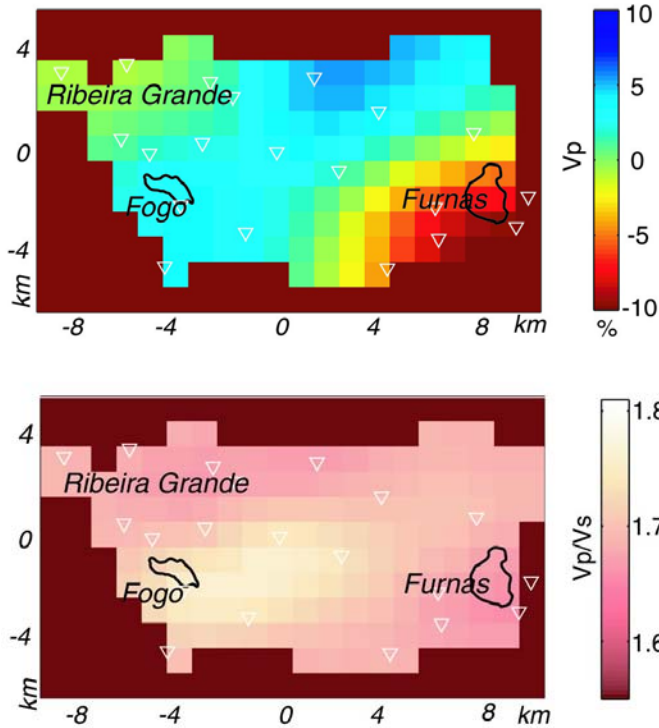
Volcanic edifices are commonly located in regions that are strongly heterogeneous in the distribution of their geophysical properties. The geodynamical setting that host them are often very complex, with numerous tectonic processes that act on different scales. Moreover, these areas have commonly a history of variable volcanic activity and present a composite geology. They can be related to transient (short living) phenomena such as geothermal activity, eruptions, and landslides, and/or they are connected to greater scale and stable structures, as in mantle feeding processes and tectonic plate interactions. This complex evolution finds physical evidences in the extreme variety of phenomena: among other, of the gravity and magnetic field, geodetic regime, and seismic attributes of volcanic regions.

In this work, we particularly focused on the heterogeneity of the seismic structure, which can be quantitatively evidenced and interpreted via seismic tomography. The seismic parameters distribution can be ultimately explained by variation of elastic proprieties, composition, fluid distribution, temperature and pressure, among others. From them, the determination of the internal structure of a volcano is finally possible. This is a fundamental step to understand active magmatic systems and determine the extent of source regions of magmatic energy (Chouet, 2002). Moreover, such knowledge is critical for any evaluation about the eruptive evolution and the hazardous impacts.

We considered two volcanic islands, as São Miguel (Azores) and Deception Island, which, besides their genesis and volcano-tectonic difference, are similarly characterized by intense seismic and volcanic activity and incomplete knowledge of their seismic structure. We imaged the interiors of these volcanoes through the application of two different tomographic techniques, passive and active experiments for São Miguel and Deception Island respectively. We suggested an interpretation in order to relate the structure with their present activity and with any other geophysical observation proceeding from different studies.

5 - Conclusions

For Central São Miguel we determined the three-dimensional distribution of P- and S-wave velocities by tomographic inversion of local earthquake arrival times. We used P- and S-phases from 289 earthquakes recorded by a network of 20 seismic stations. We observed several velocity anomalies, with good resolution in the shallowest 5-6 km, and we interpreted them as pyroclastic deposits, intrusive bodies, geothermal fields, or the effects of tectonic activity. Specifically, a low V_p zone marks the caldera of Furnas and evidences the accumulation of volcano-clastic sediments and geothermally altered deposits. Another low V_p zone extends in correspondence of the highly fractured area of Ribeira Grande, between Fogo and the north coast. Conversely, strong positive anomalies are found south of Fogo and northwest of Furnas. They were interpreted in terms of high-density deposits and remnants of a plutonic intrusion. These high velocities are separated by a region which presents slightly lower V_p and which corresponds to a faulted zone, matching the regional tectonics.

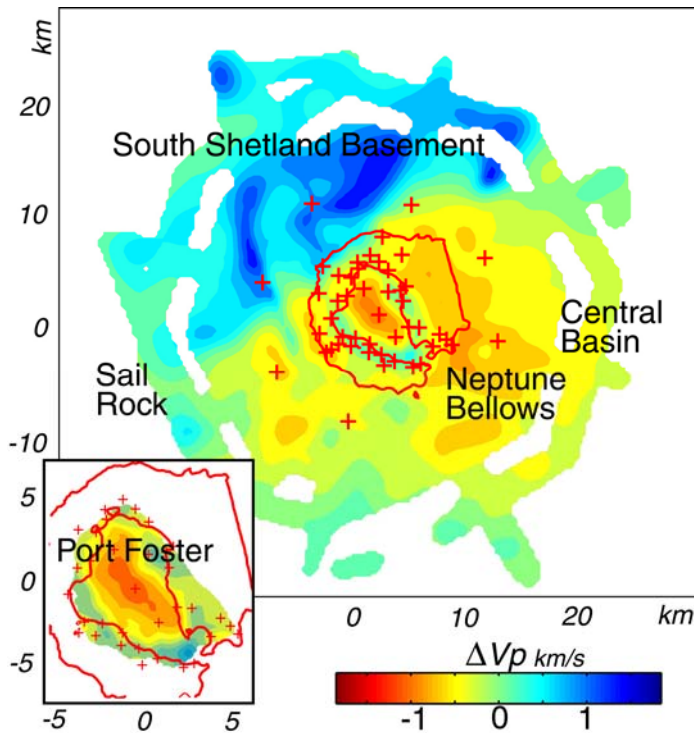


These interpretations were further detailed throughout the study of the V_p/V_s spatial distribution. This ratio reveals as a powerful tool to understand the nature of fluids involved in the actual volcanic state of the region. Hence, the low V_p and low V_p/V_s of Furnas can be definitely associated with the development of an intense vapour-dominated geothermal field in pyroclastic caldera-infilling. No evidences of magma are observed. On the opposite, the geothermal plant in Ribeira Grande, between Fogo and the north coast of the island, is mainly fed by liquid-dominated fluids, as consistent with our results. The chilled remnant of the Fogo magma chamber does not show nowadays any indication of volcanic activity. Otherwise, the only fluids involved are probably water as liquid phase.

Deception Island structure was studied by inverting P-wave travel times from active sources. More than 6600 air gun shots were fired and a total of 85 land and 10 ocean bottom seismometers were deployed for a total of 119 recording positions. The three-dimensional inversion resolves strong velocity contrasts down to 5.5 km depth. The most striking feature is the low seismic velocity beneath the Port Foster caldera floor which represents an extensive region of magma.

5 - Conclusions

The shallower levels of this anomaly are otherwise due to the presence of pyroclastic caldera-infilling deposits. Low velocities at the east of Deception Island correspond to a seafloor that is characterized by sediment transport structures (gullies, ridges and debris flows) into the Central Basin. Pyroclastic deposits from ancient small volcanic cones can be responsible of the low velocities to the SW of Neptune Bellows. The low velocity zone to the west of Deception Island constitutes the seismic evidences of volcanic edifices or ridges and may be the expression of thicker volcanoclastic sediments, thermal anomalies, or active magmatic systems.



High velocities are present as well. The widest anomaly dominates the north-western sector of the region and is composed by several maxima. It denotes the presence of the crystalline basement of continental crust in correspondence of the South Shetland block. The sharp contact with lower velocities at the SW has a well-defined NE-SW trend, compatible with the regional tectonics of the Bransfield extension. Other high velocities mark, in the Neptune Bellows zone, the location of the ancient basement of Deception Island, probably dated back to the shield past of the volcano. A high velocity anomaly is observable also in the south of the island and it probably constitutes the seismic image of an ancient volcanic dome or of the neck of the previous feeding system. On the west of the island a high velocity anomaly possibly constitutes the seismic

image of Sail Rock, an eroded andesitic edifice.

As seen, the velocity models of these volcanic regions represent the first attempt to image the inner structure of two active volcanic zones that have been intensively studied by other techniques without supplying, until now, a comprehensive picture of their nature. In this sense, our velocity models tries to finally establish a base to interpret previous observations and so respond to the numerous questions posed by a pure scientific curiosity.

Remarkably, part of these new structural indications can be related to the regional tectonic framework, and hence can have a key importance for geodynamical interpretations. In the case of São Miguel, for example, it is evident the role played by the regional NW-SE fault systems, which hence can be considered still active across the area. The magmatic supplying of the volcanic edifices of São Miguel, if nowadays present, only can be associated to deep, great scale magmatic feeding systems. Similarly the seismic structure of Deception Island evidences the relationship between the evolution of the island and the regional tectonics. Main features point to the action of two dominant fault systems, NE-SW and NW-SE, which have been widely recognized at greater scale. They have been conditioning the volcanic history of Deception Island, its past eruptions, the emplacement and evolution of the caldera and the actual distribution of seismicity.

Many more considerations could be done about the relationship between our imaged seismic structures and the regional tectonic setting, but this obviously goes beyond the main purposes of this work. Nevertheless, there are some more aspects to be shortly reminded.

A deeper knowledge of our volcanic regions has several practical implications. The São Miguel situation perfectly clarifies the importance of the volcano understanding for technological objectives. Since years, the island supplies a remarkable fraction of energy demand by means of geothermal power plants. On the base of our result, we obviously confirm the existence of the geothermal field of Ribeira Grande, already exploited in the North of the Island. Interestingly, we suggest the presence of a high temperature geothermal field in the Furnas zone, for which the fluids at supercritical conditions could be of economic interest (to our knowledge, only recently it has been planned the study of the area with economic interest). On the opposite, the region of Fogo volcano does not result appealing to the geothermal prospecting. Similarly, the strong thermal anomaly evidenced in Deception Island, centered in Port Foster, and the well know abundance of circulating water both point to the presence of a geothermal resource which have been completely under-estimated (a part for tourist soaks!) and which could be considered for the development of a no-impact self-sustaining Antarctic base. But this also goes beyond the limitations of the Antarctic Treat and the purposes of this thesis.

The knowledge of the present state and the insight in the volcanic evolution of these islands has important implications also for the hazard assessment and management. We cannot forget that São Miguel is densely inhabited and Deception Island is yearly visited by several researchers and thousands of tourists. We infer from our study that, apart the risk related to the intense seismic and geothermal activity, the superficial crustal structure of Central São Miguel does not suggest any immediate high volcanic hazard for the zone. For Deception Island, obviously, the presence of an extensive volume of magma melt at shallow depths has to be taken carefully into account.

The comparison between the applied tomographic techniques, the obtained velocity models and their structural significance, lets us generalize the results of our surveys with some more considerations about merits and weaknesses of passive contra active tomographic experiments. Many differences we have observed between the two approaches belong at the same time to the input data and to the output results.

From a quantitative point of view, active experiment permit the collection of a huge amount of data in a short interval time, while passive techniques often necessitate a collection of data of several-months/years-long observations. This is not always the case, because, for example, the occurrence of seismic swarms is quite common in volcanic areas. But in this situation, the seismic sources are almost clustered and, as we have seen, of scarce utility for our tomographic purposes.

And this lets us introduce the main problems related to the quality of data proceeding from tomographic experiments, i.e. the poor coverage by seismic sources. In the case of natural activity, the seismic sources are often clustered and not well distributed across the studied area, and with respect to the station positions. This unfortunately means that ray paths have sub-parallel paths which do not add much more information (clusters) or cannot cross the whole volume we want to image (no appropriate distribution). Hence, the lateral extension of the resolved area can be strongly reduced by an unappropriated distribution of ray paths. The capability of data to distinguish close objects, i.e. the proper resolution, is reduced by such seismic rays. The scale of imaged structures also depends on the wave length, which strongly varies for each event, but usually is longer for natural sources with respect to air gun shots. There is another difficulty which is increased by a poor database in passive experiments, and it is of a more mathematical nature. It relates with the increased non-linearity of the inversion scheme when the problem of earthquakes location is added. Obviously, few traveltimes make this problem strongly under-determined.

For São Miguel experiment we faced with the difficulties of a small database from a seismic survey three months long, where many earthquakes were too far from our studied region, or too close each other in small clusters or, finally, recorded by few stations. A poor database forced us to continuously check its quality with respect to the uncertainties it could

introduce. Often the best strategy has been to further reduce it, in order not to include additional systematic error. This justifies the 'endless' data preparation phase we performed, and the continuous selection and control of the results through several tests, along with the first inversion steps. The final uncertainty in the resolved velocity structure is hardly separated from the error due to imprecise earthquakes location. Considering all these factors, and in particular the final amount and distribution of data, only it was permitted the imaging through 1 km wide cells. Hence, this dimension became the scale length of the smallest structure we could recognize and interpret.

The experiment of Deception Island, on the opposite, supplies in a two-week-long survey a great quantity of shots data, perfectly distributed around the target region and with respect to the recording positions. The lateral resolution of data is high and makes possible the imaging of small features, as wide as few tens of meters. The only selection data need is due to the eventual noise they present in the seismograms. In particular, the waveforms are strongly affected by the water wave arrival, which are obviously stronger in oceanic source-receiver distributions. As the source location is known, also the direct problem of ray tracing is considerably easier and can reach a higher level of accuracy. In this case, at least in the case of marine air guns sources, the calculation of their path is only complicated by, after the path across the water layer, the location of the entry point in an irregular sea bed surface.

However, the passive approach presents noticeable advantages as well. In fact, several 'useful' seismic phases are recognized and modeled. For example, extraordinary information proceeds from the V_p/V_s ratio, which is easily retrieved from data of natural sources. In the São Miguel experiment, we have been able to figure out the distribution of V_s , together with V_p . This reveals as basic information in the interpretation of seismic anomalies and internal fluids distribution. Moreover, the occurrence of deep hypocenters can extend in depth the resolved volume dimensions. With shots experiment, the seismic sources are shallow and ray paths only cross shallow structures. So, proportionally to the areal extension of the experiments, São Miguel tomography could model deeper structures with respect to those of Deception Island, whose deep roots setting remains still unclear.

Finally, last but not least, an active sources survey often follows a long phase of logistics preparation, a delicate field phase and a considerable economic impact. In the Deception Island experiment we had a strict timetable to follow, in order to deploy as many seismic stations as possible contemporaneously with signal generation. Obviously, this implied the joined effort of several researchers.

Hence, as main methodological conclusion, we insist that it is not possible to definitely prefer a tomographic technique with respect to the other. Their selection strongly depends on the specific conditions and aim of the study. Different

5 - Conclusions

advantages and problems distinguish the preparation and the execution of the campaigns, the final data recover and the conclusive analysis. Obviously, the best- and more difficult- approach is that of their integration, and also, if possible, with more techniques. For these reasons, is highly desirable an improvement of the knowledge of the seismic structure of the whole São Miguel. The organization of an active experiment and the deployment of seismic arrays could reveal the overall structure of the island with greater detail. The use of dense arrays would be a unique tool to study the long period seismic activity that, as seen, is a lacking piece of the picture. For Deception Island, on the other side, the past of seismic records could be considered to study the seismic structure by means of the P and S wave information. This could clarify the internal distribution of fluids and the deeper structures. The magma chamber could be easily detailed, together with zones of geothermal activity and fluid circulation. In a detailed velocity structures, also the previously studied seismicity, both of volcano tectonic and long period, could find a precise location and source explication. If a considerable amount of data would be available, the study could be also focused to illuminate historical changes in the seismic structure of the island during its last evolution (to a 4D seismic tomography).

A Final Consideration

In this work a seismic evidence has been presented that, going on over the seismic tomography, needs to be carefully considered: the relationship between the regional tectonics and the volcanic evolution of Deception Island. Until now we have outlined this relationship on a general plane, through the observation of structural elements that point to a volcanic activity broadly compatible with the geodynamical setting. The tomographic image represents an instantaneous picture of the present state of the island; nevertheless it is crucial to temporally relate volcanism and tectonics.

If we are able to give insights on the relationship existing between volcanic activity and tectonics, we can understand the mechanism that controls the volcanism itself. It is obvious that such a modeling of the volcano behavior has strong consequences on risk assessment and management.

The main difficulty in the study of Deception Island is the lack of knowledge about the volcanic history and style due to its geographic remoteness. Past eruptions are poorly or not documented also in historical times and nowadays the volcanic island is only seasonally monitored. Hence, our knowledge of the volcanic activity is only partial. The record of the seismic activity is also poor and carried out by few seismic stations, far and inadequately located respect to the area. Usually only large events are located [Ibañez et al. 1997; Pelayo and Wiens 1989; Robertson Maurice et al. 2003; Simkin et al. 1981; Talandier and Okal 1987], while the smallest events only are recognized and studied during seasonal campaigns.

As we know, three main eruptions have been reported: in Deception Island: in 1967, 1969 and finally in 1970. From the study of lake sediments in the Antarctic Peninsula a large eruption of Deception Island is dated 1641 ± 3 [Aristarain and Delmas 1998]. Probably other eruptions took place also in 1842 (at Mount Kirkwood) and between 1912 and 1917 (at Kronen Lake) [Baker et al. 1975].

Our knowledge of the biggest eruptions is mostly due to descriptions of researchers at the Scientific Bases and by few old Argentinean seismograms: (1) before the onset of the 1967 eruption (4 December 1967) earthquakes were recorded at the British Antarctic Survey station on Deception Island, since late April 1967. (2) on 21 of February 1969 the scientists of the scientific stations were shaken by what they reported as a 'particularly strong earthquake' which was briefly followed

by the eruption. (3) The 1970 eruption had not direct testimony, but the seismograph at the British Antarctic survey station in Rey George recorded an earthquake located near Deception Island.

In seismic catalogs the period between 1967 and 1970 is characterized by intense seismic activity [Pelayo and Wiens 1989]. The location of a group of earthquakes during 1970 indicates their clustering around Deception Island, occurring on dates of the reported volcanic eruption.

Other events in 1974 were aligned along a seismogenetic zone extended SW-NE between Deception Island and Livingstone Island. Two major events, not followed by eruptions, on 8 February 1971 (magnitude $m_b = 6.3$) and on 13 December 1982 ($m_b = 5.8$) took place SW of Deception Island, with the same alignment.

From these observations, we suggest that volcanic eruptions and regional earthquakes can be related. Known eruptions have been always preceded by strong seismic activity with an intensity or a timing gap which is hardly referred as consequence of the eruptive process itself. The location of main events indicates that the fault system acting is that represented by the sharp, extended in depth, velocity contrast we imaged in the NW of Deception Island. The SW limit of the South Shetland Island is represented by an arrangement of normal faults which are extending the continental crust and which are responsible of major earthquakes. This fracture system interacts with the volcanic edifice in depth and creates a stress field favorable to the magma upwelling. The occurrence of earthquakes in the more competent crustal regions, with brittle behavior and high seismic velocity, is by far accepted [Lees and Malin 1990; Zhao and Kanamori 1993]. Hence, the NW high velocity reasonably is the most important seismogenetic zone in Deception Island.

The events of 1971 and 1982 were not followed by any eruptive phase at Deception Island. This could be due to a situation unfavorably to triggered eruptions: a great distance between magmatic source and hypocenter location, or an un-recharged magmatic system, among others.

Moreover, the interaction between major earthquakes and volcanic eruptions has been widely observed [Linde and Sacks 1998]. Earthquakes occurred close to volcanic regions have coincided with changes in the eruptive behaviour at nearby magmatic [Walter et al. 2007] and mud [Manga 2007; Mellors et al. 2007] volcanoes. The onset of eruptions is considered as one of several possible subsurface responses to earthquakes. Different types of other changes are possible, such as the increase of volcano tectonic seismicity and degassing [Linde and Sacks 1998], hydrothermal activity enhances and geyser eruptions [Manga and Brodsky 2006]. The mechanism by which volcanoes are triggered or influenced by permanent stress changes (static displacements) or by transient stress changes (by the passing of seismic waves) is still unclear [Walter et al. 2007]. It is accepted that static stress changes decay with the cube of the distance away from the main

shock; so far away they are usually negligible. Instead, dynamic stress changes caused by propagating seismic waves can reach such large distances.

The triggering effect may act at large distances, as very small changes of the stress field may activate a system that is in a near critical state [Manga and Brodsky 2006]. In mud volcanoes, transient stresses can rearrange unconsolidated material and increase the pore fluid pressure to overcome that of the weight of the overburden. The effects are those of liquefaction and possible eruptions of mud volcanoes. In magmatic areas, such stress changes in general may cause failure of rocks surrounding stored magma or alter the fluid flow within the shallow crust. The gas phase within the magma-hydrothermal system may be affected by passing seismic waves. Gas bubbles can undergo volume expansion and increase the pressure [Walter et al. 2007]. In an established magma conduit, it can be expected that the pressure transient causes a readjustment of the gas fraction to overcome the static load of the magmatic column [Brodsky et al. 1998]. Otherwise only the bubble growth and ascent can be activated, indirect effects of which can be measured by means of fumaroles temperature (as in Merapi 2001 earthquake) and increased dome extrusion and dome collapse (as in 2006).

The 2006 eruption of Merapi volcano is only the most recent example of an eruption primed by a tectonic event. Unfortunately, its history demonstrates that in these situations, the volcanic and the seismic risks are intimately related and not well managed.

The comprehension of how stress triggering works at is important for the interpretation of precursors, early warning and hazard assessment, especially for a volcano, such as that of Deception Island, which has a eruptive history scarcely known.

The relationship between regional earthquakes and volcanic eruptions is even more crucial when, as in Deception Island, observations indicate a short interval time between seismic shocks and onset of the eruptions. Interestingly, on the base of descriptions previous to the eruptions, the only observed precursors were large earthquakes: no geochemical, or clear thermal evidences or deformation are described [Baker et al. 1975].

Therefore a similar behavior could be expected in the future. A regional tectonic event close to Deception Island could trigger a new eruptive phase in the island.

References

- Aristarain, A. J., and Delmas, R. J., 1998, Ice record of a large eruption of Deception Island volcano (Antarctica) in the XVIIIth century,: *Journ. Volcan. Geotherm. Res.*, v. 80, p. 17-25.
- Baker, P. E., McReath, I., Harvey, M. R., Roobol, M. J., and Davies, T. G., 1975, The geology of the South Shetland Islands: volcanic evolution of Deception Island, *Scientific Reports, British Antarctic Survey*.
- Brodsky, E. E., Sturtevant, B., and Kanamori, H., 1998, Earthquakes, volcanoes, and rectified diffusion: *J. Geophys. Res.*, v. 103, p. 23827-23838.
- Ibañez, J. M., Morales, J., Alguacil, G., Almendros, J., Ortiz, R., and Del Pezzo, E., 1997, Intermediate-focus earthquakes under South Shetland Island (Antarctica): *Geophys.Res. Lett.*, v. 24, p. 531-534.
- Lees, J. M., and Malin, P. E., 1990, Tomographic images of P wave velocity variation at Parkfield,California: *J.Geophys.Res.*, v. 95, p. 21793-21804.
- Linde, A. T., and Sacks, I. S., 1998, Triggering of volcanic eruptions: *Nature*, v. 395, p. 888-890.
- Manga, M., 2007, Did an Earthquake Trigger the May 2006 Eruption of the Lusi Mud Volcano?: *EOS*, v. 88.
- Manga, M., and Brodsky, E., 2006, Seismic Triggering of Eruptions in the Far Field: Volcanoes and Geysers: *Annu. Rev. Earth Planet. Sci.*, v. 34, p. 263-291.
- Mellors, R., Kilb, D., Aliyev, A., Gasanov, A., and Yetirmishli, G., 2007, Correlations between earthquakes and large mud volcano eruptions: *J. Geophys. Res.*, v. 112.
- Pelayo, A. M., and Wiens, D. A., 1989, Seismotectonic and relative plate motions in the Scotia Sea Region: *J. Geophys. Res.*, v. 94, p. 7293-7320.
- Robertson Maurice, S. D., Wiens, D. A., Shore, P. J., Vera, E., and M. Dorman, L. M., 2003, Seismicity and tectonics of the South Shetland Islands and Bransfield Strait from a regional broadband seismograph deployment: *J. Geophys. Res.*, v. 108.
- Simkin, T., Siebert, L., McClelland, L., Bridge, D., and Newhall, L., 1981, *Volcanoes of the World*: Stroudsburg, Hutchenson Ross, 232 p.
- Talandier, J., and Okal, E. A., 1987, seismic detection of underwater volcanism: the example of French Polinesia: *Pure Appl. Geophys.*, v. 125, p. 919-950.
- Walter, T. R., Wang, R., Zimmer, M., Grosser, H., Luhr, B., and Ratdomopurbo, A., 2007, Volcanic activity influenced by tectonic earthquakes: Static and dynamic stress triggering at Mt. Merapi: *Geophys Res. Lett.*, v. 34.
- Zhao, D., and Kanamori, H., 1993, The1992Landersearthquake sequence: earthquake occurrence and structural heterogeneities: *Geophys.Res.Lett.*, v. 20, p. 1083-1086.

Acknowledgements

During these remarkable years at Instituto Andaluz de Geofísica I have worked, learnt, discussed, talked and spent good time with a lot of people. Many of them contributed to my work, helped me from a scientific point of view but also encouraged and supported me with their friendship. I am very grateful to all of them.

I would like to thank Prof. Jesús Ibañez for the guidance during the Ph.D. work. I appreciated his generous support, encouragement, his patient explanations, and the example of his enthusiasm.

In my daily struggle with inversions, mathematical problems and nasty programs, I could always count on the precious and friendly help of Javier Almendros and on his intellectual curiosity.

Andrew Barclay was also essential for the progress of my project, from code understanding to the tireless fight against English grammar.

I am very grateful to Gilberto Saccorotti, William Wilcock and Maria José Blanco for supplying me with tomography codes, electronic devices, the roof during my visits and friendly support.

I express my gratitude to Bernard Chouet who welcomed me in the fascinating world of volcano-seismology at the beginning of my project.

Finally, I thank Rafa Abella, Graziella Barberi, Tami Ben-Zvi, Enrique Carmona, Norma Damiano, Phil Dawson, Antonio Martos, Enzo Nisii, Nicolau Wallenstein, Luciano Zuccarello, and all the members of the Instituto Andaluz de Geofísica, of the IGN of Tenerife, INGV of Naples and Catania and the personnel of the vessels *Hespérides* and *Las Palmas*.

The seismic surveys were founded by the projects *e_Ruption* (EVRI-CT-2001-40021) and *TOMODEC* (ANT2001-3833). Partial support also came from the project REN2002-12536-E/ANT, CGL2004-2002-E, CGL2004-05744-C04-01 and CGL2005-05789-C03-02/ANT of the Spanish Ministry of Education, and from the European Project VOLUME (FPG2004-GLOBAL-3-018471).